Photonic Integrated Shot-reach Transmitter for Optical Networks

Ankit Sharma

B. Tech, M.S. by research

A dissertation submitted in fulfilment of
the requirements for the award of
Doctor of Philosophy (Ph.D.)

School of Electronics Engineering
Faculty of Engineering and computing
Dublin City University

Supervisor: Dr. Prince Anandarajah
External supervisor: Dr. Aleksandra Kaszubowska-Anandarajah (Trinity college Dublin)
Industrial supervisor: Dr. Frank Smyth (Pilot photonics Ltd.)

August 24

Declaration

I hereby certify that this material, which I now submit for assessment on the programme of study leading to the award of Doctor of Philosophy is entirely my own work, and that I have exercised reasonable care to ensure that the work is original, and does not to the best of my knowledge breach any law of copyright, and has not been taken from the work of others save and to the extent that such work has been cited and acknowledged within the text of my work.

Signed: 

ID No.: 18214731

Date: 24/08/2024

To my papa, mammi, Alka, Aavyukt and brother and sisters.

“Arise! Awake! and stop not until the goal is reached.”

-Swami Vivekananda

Acknowledgement

I want to convey my gratitude to all group members of the photonic system and sensing lab who supported me and contributed their knowledge and efforts throughout the last four years of this research. It would not have been possible to conduct this research without their contribution and guidance. Firstly, I would like to express cordial thanks to my supervisor, Prof. Prince Anandarajah and Prof. Aleksandra Kaszubowska, for giving me the opportunity to pursue a Ph.D. in his research group and for his expert knowledge and continuous suggestions. His valuable guidance and substantial support helped me in various research and writing the thesis. I thank Professor Pascal Landais for discussing technical concepts and for his advice and comments that have substantially improved this work.

I will be highly grateful to Pilot Photonics, who provided me the opportunity to work as a research engineer and helped me at the early stages of my professional career in photonics, where I enjoyed working and enhanced my skills. My heartfelt appreciation goes to Dr. Frank Smyth and William Oppermann, who has been exceptionally supportive mentor. His continual advice, inspiration, motivation, understanding, and trust have always encouraged me, even during the complicated parts of the industrial PhD. I thank Jules Braddell and Michael Wallace for contributing to device design, sharing knowledge, and conducting research-oriented discussions. Both have deeply shared their efforts in this work with novel PIC designs and provided me with training and research materials, which significantly helped me achieve the research goals.

I would also like to thank Gaurav, Desi, and other colleagues for their precious time and support during research and measurement. A special thanks go to Dr. Manas Srivastav and Dr. Syed Tajammul for their immense help and support through the research and their friendship and continuous help. My appreciation also extends to Dr. Mohab Hammad for his kind help and valuable time and assistance in experiments, who made the first part of this research so easy and exciting. I want to express my gratitude for this work to my parents and sister for their faith in me, encouragement, and support throughout my education and career. Lastly, I thank Alka, my wife, for your exceptional support and love. This PhD could not have been possible without the support of everyone. I'll always be grateful to all.

Contents

List of Acronyms

ADC	Analog to digital converter
AMZI	Asymmetric Mach-Zehnder interferometer
APD	Avalanche photodiode
AR	Antireflective
ASE	Amplified spontaneous emission
ATM	Asynchronous transfer mode
BER	Bit error rate
BT	Bias-Tee
CD	Chromatic dispersion
CSMA	Carrier sense multiple access
WDM	Wavelength division multiplexing
DAC	Digital to analog converter
DFB	Distributed feedback
DGD	Differential group delay
DML	Directly modulated laser
DWDM	Dens wavelength division multiplexing
EAM	electro-absorption modulator
ED	Error detector
EOM	Electro-optic modulator
ER	Error rate
ESA	Electrical spectrum analyzer
FEC	Forward-error correction
FFT	Fast Fourier transform
FP	Fabry-Perot
FR4	Fiberglass-reinforced 4
FSR	Free spectral range

FTTX	Fiber to the x
GDS	Graphic data stream
HR	Highly reflective
HSPON	High-speed passive optical network
IP FP	Index-pattern Fabry-Perot
ITUT	International Telecommunication Union Telecommunication
LED	Light emitting diode
MBW	Modulation bandwidth
ML	Master Laser
MMF	Multimode fiber
MMI	Multimode interference
MZM	Mach-Zehnder interferometer
NRZ	Non-return to zero
ODN	Optical distribution network
OFDM	Orthogonal frequency division multiplexing
OIL	Optical injection locking
OLT	Optical line terminal
ONU	Optical network unit
OOC	Out of channel
OOK	On-off keying
OSA	Optical spectrum analyzer
P2MP	Point to multipoint
P2P	Point to point
PAM	Pulse amplitude modulation
PCB	Printed circuit board
PIC	Photonic integrated circuit
PID	Proportional–integral–derivative
PMD	Polarization mode dispersion
PON	Passive optical network
PPG	Pulse pattern generator

PR	Partially reflective
PRBS	Pseudorandom binary sequence
PSD	Power spectral density
PWNE	Power when not enabled
QAM	Quadrature amplitude modulation
QPSK	Quadrature phase shift keying
RAN	Radio access network
RF	Radio frequency
RIN	Relative intensity noise
ROP	Received optical power
RSOA	**Reflective semiconductor optical amplifier**
RT	Remote terminal
SL	Slave laser
SMF	Single mode fiber
SMSR	Sidemode suppression ratio
SOA	Semiconductor optical amplifier
TDM	Time division multiplexing
TEC	Thermo-electric cooler
TIR	Total internal reflection
TWDM	Time wavelength division multiplexing
UWDM	Ultra dense wavelength division multiplexing
VCSEL	Vertical-cavity surface-emitting laser
VNA	Vector network analyzer
VOA	Variable optical attenuator

List of Tables

List of Figures

Photonic Integrated Shot-reach Transmitter for Optical Networks

Ankit Sharma

Abstract

Photonic integrated circuits (PICs) have garnered a lot of interest due to their ability to offer reductions in size, weight and power, improved performance and stability over discrete solutions. The biggest benefits of the implementation of PICs in telecommunication applications are reaped in the cost sensitive short reach networks that include access and datacenter networks. Passive optical networks (PONs) that utilize optical fiber links to provide the end-user connectivity, have become one of the predominant access network options. The PON standards are steadily evolving due to the ever-increasing demand for bandwidth. A relatively recent advance involves the use of wavelength division multiplexing (WDM) together with the more common time division multiplexed (TDM) approach. This format is known as time and wavelength division multiplexing (TWDM) and, while it enables bandwidth growth, it places stringent technical demands on the optical components, increasing the challenge of meeting the cost targets required in high-volume PON applications.

To date, externally modulated lasers (EMLs) have typically been required to meet the technical requirements of TWDM networks. However, EMLs are relatively costly when compared with typical PON transmitters. Furthermore, they require more expensive and higher power laser drivers. For these reasons, there is a lot of interest in a directly modulated laser (DML) alternatives to reduce the cost and complexity of TWDM transceivers. A key challenge with direct modulation is the frequency chirp imposed on the modulated signal. It makes the signal more susceptible to fiber dispersion effects, which in turn limits the transmission distance achievable by DML based transmitters.

This research thesis investigates the employment of multi-section PICs, designed to enable direct modulation and achieve high bit rate and long-distance transmission. These PICs, intendent of use in next generation optical access networks, are developed using a regrowth-free fabrication technique. In this work, a detailed analysis and characterization of a slot-laser is carried out. Subsequently, a few different PIC architectures are proposed, realized and fully characterized. Finally, the characterized PICs are employed in transmission tests to verify their suitability as PIC based transmitters for next generation optical access networks.

Chapter 1

Introduction

Humans have made astonishing progress in developing and realizing communications technologies for connecting users globally. In the early eighteenth century (1849), the invention of the telegraph [1] revolutionized communications, enabling fast local and intercontinental communication. Telegraph machines could send and receive text messages as an electrical signal mainly used for business and distributing news. After that, the telephone was invented, which could transmit and receive human voice: electrical signals flowing through copper wires. Fundamentally, early communications technologies used analog signals and transmitted these signals via a twisted pair of copper cables, which was the main medium used. In the late 20^{th} century, with the development of the computer and the internet, digital communication became the preferred approach for data transfer.

The need for faster internet services kept rising, and the communication industry moved away from the “twisted pair” due to its high attenuation and limited bandwidth. The use of fiber optic cables was preferred to deliver internet services as it overcame the afore-mentioned limitations of coaxial cables. The fiber optic cable is a thin silica glass with a high refractive index (core) encompassed with low refractive index glass (cladding) to enable total internal reflection (TIR). In an optical communications system, the electrical signal is first converted into an optical signal utilizing electro-optic converters and then launched into an optical fiber. Due to the TIR phenomenon, light travels from one end to another without experiencing significant loss. At the receiver, the optical signal is converted back to an electrical signal to extract the original information. Hence, three fundamental components are used in optical communication: an optical transmitter (source) to generate an optical

signal, an optical fiber to transmit the signal from source to destination, and a detector to interpret the received optical signal.

1.1 Evolution of optical fiber and optical sources

This thesis provides an introduction to two of the vital pieces required for building communications systems. For detailed information, the reader is referred to [2], [3] and [4].

1.1.1 Optical Fiber

The optical fibers are drawn from pure molten silica using several methods such as flame heating [5], [6], laser heating [7], electrical heating [8], [9] [10]. There are two fundamental types of optical fiber: multi-mode fiber (MMF) and single-mode fiber (SMF), and the main difference is the core diameter size.

1.1.1.1 Multimode fiber (MMF)

In the early days of using fiber, MMF was manufactured and commercialized to transmit optical signals. Typically, the core diameter of a MMF is between 50 µm to 62.5 µm, which has the benefit of low coupling loss. However, the transmitted information (optical pulse) can be simultaneously supported by a number of electromagnetic (EM) modes. Each of the EM modes can travel at a different velocity and reach the receiver at a different time resulting in pulse broadening, which leads to distortion and interference effects [11], [12]. This phenomenon is called modal dispersion [13]. As shown in the Figure 1.1.1, in MMF, the optical pulse traveling in higher order mode (ray in red) arrives at the receiver later compared to one traveling in a lower order mode (beam in blue), causing time domain spreading of the optical pulse.

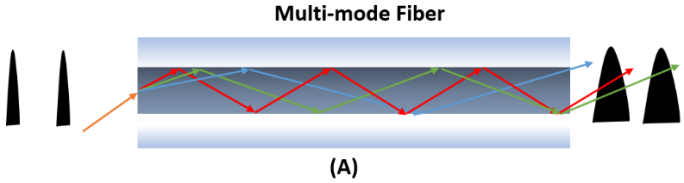

Figure 1.1.1. Pulse propagation in multi-mode fiber.

1.1.1.2 Single mode fiber (SMF)

In a further development of fiber, the intermodal dispersion caused by multimode fiber is resolved by narrowing down the diameter of the fiber core to between 4 and 10 µm [14], [15], [16]. A narrow core of the fiber restricts the propagation of higher order modes whilst allowing the transmission of the fundamental mode (as shown in Figure 1.1.2) and is hence referred to as single mode fiber (SMF). In addition, a reduction in the core diameter also affects the wavelength of operation of SM fiber. The relation between the cutoff wavelength (λ_{cutoff}) of fiber and fiber core diameter is given by equation 1.1.1, where a is the core radius, n_1 and n_2 are core and cladding refractive indexes.

$$\lambda_{cutoff} = \frac{2 \cdot \pi \cdot a}{2.405} \cdot \sqrt{(n_1^2 - n_2^2)} \qquad 1.1.1$$

Therefore, the SMF allows optical signal transmission if the wavelength lies within the wavelength band of 1260 nm to 1665 nm. For example, an SMF (G.652) having $a = 4.2\ \mu m$, $n_1 = 1.480$ and $n_2 = 1.475$ exhibiting a cutoff wavelength of 1334 nm [13].

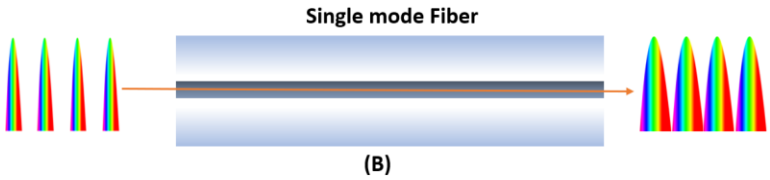

Figure 1.1.2. Pulse propagation in SMF.

It is important to note that SMF solved the problem of intermodal dispersion. However, the propagation of an optical pulse in such fiber is still degraded by other effects such as attenuation, dispersion (chromatic and polarization) and nonlinearity [3], [14], [17], [18], [19], [20], [21].

6.3.2.1 Attenuation

Attenuation is a phenomenon where the optical power of a transmitted signal is reduced while traveling through the fiber. It is predominantly caused by absorption and scattering of

photons in the optical fiber [22]. The attenuation coefficient of fiber (α) in dB is given by equation 1.1.2 where P_2 is the received power and P_1 is the launched power.

$$\alpha_{dB} = 10 \cdot \log_{10}\left(\frac{P_2}{P_1}\right) \quad 1.1.2$$

Attenuation introduced by fiber reduces the electrical signal-to-noise ratio (SNR) at the receiver; hence, the maximum distance of transmission of optical signal, in systems without optical amplification, is determined by the minimum signal power required at the receiver. In the early days, the SMF transmission loss was as high as ~20 dB/km. However, this has been reduced significantly ~ 0.2 dB/km. It is also important to note that the attenuation experienced by an optical signal depends on its wavelength. Figure 1.1.3 shows a plot of optical attenuation in dB/km as a function of the wavelength of optical signal in silica fiber. The high attenuation peak between the wavelength ranges of ~900 – 1200 nm, ~1200-1300 nm, and ~1350-1420 nm due to absorption caused by water molecules in the fiber.

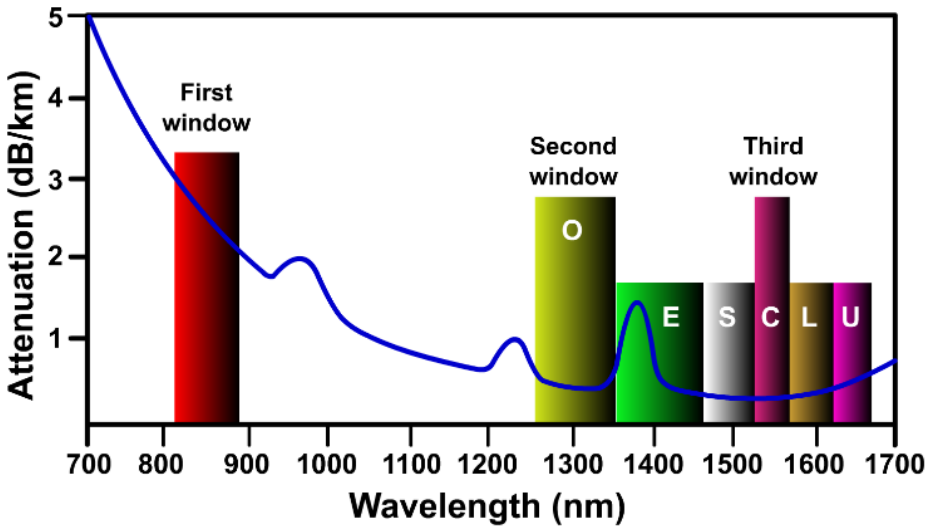

Figure 1.1.3. Fiber attenuation as a function of propagating wavelength in SMF.

Therefore, the regions with low attenuation are appropriate for optical signal transmission and are divided into three wavelength bands ranging from 800-900 nm (first band), 1270−1350 nm (second band), 1480−1600 nm (third band). The wavelength band with the lowest attenuation (~0.2 dB/km, wavelength between 1528−1565 nm), lies within C band,

and is suitable for long-reach optical communication. Within C band the wavelength ranging from 1550 nm to 1560 nm is reserved for the RF and video overlay. The spectrum allocated for the RF and video overlay carries the standard analog and digital for television. The video services are delivered on 1550 nm wavelength in coexistence with other passive optical network (PON) technologies. The video overlay running at 1550 nm suffers Raman cross-talk between caused downstream data running at 1490 nm wavelength [23].

6.3.2.2 Dispersion

As mentioned earlier, the broadening of a pulse in time is known as dispersion, and in the case of SMF, there are two types of dispersion: chromatic dispersion and polarization mode dispersion. Typically, an optical pulse comprises multiple wavelengths that experience different refractive indexes while traveling in the fiber. As the optical signal velocity depends on the wavelength, according to the relation $v = \frac{c\ (\text{speed of light})}{n\ (\text{referective index})}$, different wavelengths will travel at different speeds. Hence this effect is referred to as chromatic dispersion (CD). The longest wavelength has higher velocity than the shorter wavelengths, thus it arrives earlier at the receiver leading to a temporal broadening of the optical pulse. The schematic in Figure 1.1.4 (a) shows the effect of CD on an optical pulse (containing different wavelengths) traveling through fiber.

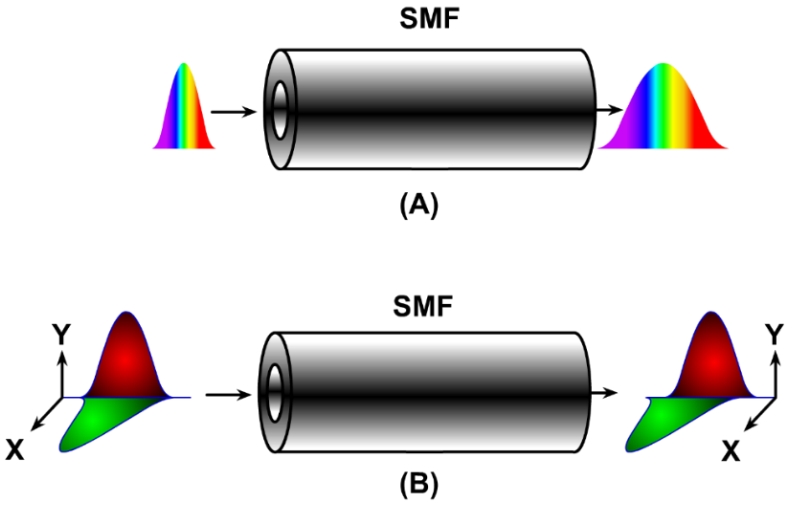

Figure 1.1.4. Pulse broadening in SMF caused by (a) chromatic dispersion and (b) polarization mode dispersion.

Another type of dispersion that occurs in optical fiber is polarization mode dispersion (PMD) [24], [25], [26], [27], [28], [29], [30]. In SMF, the non-uniform distribution of refractive index, known as birefringence [31], causes a signal in two polarizations to propagate at distinct speeds. Hence, such a signal suffers polarization-dependent group delay leading to temporal broadening of the pulse (as shown in Figure 1.1.4(b)). The temporal broadening results in a transmission penalty in terms of bit error rate [32], [33], [34]. The main factors causing PMD are non-perfect concentricity and inhomogeneity in fiber core, stress/strain on fiber.

As mentioned, the optical signal travels into the fiber in two polarization states at different speeds due to birefringence. The time delay between the transmission of signal occurring in two polarizations is called differential group delay (DGD). The PMD in fiber is defined by mean DGD and PMD coefficient $\Delta\tau_c$.

$$\text{Mean DGD} = \Delta\ \tau\ \ (\text{ps}) \tag{1.1.3}$$

$$\Delta\ \tau\ = \Delta\ \tau_{\,c} \cdot \text{L} \tag{1.1.4}$$

Another parameter that defines the PMD is the second order PMD delay (DGD_2) and second order PMD coefficient. The second order DGD is defined by rate of change of DGD with respect to wavelength. The second order DGD further reduces the limitation imposed by CD. However, high speed transmission is affected by DGD_2.

1.1.2 Optical sources

In the early days of communication, gas lasers were used as an optical source [35], [36], [37]. Later, light-emitting diodes (LED) were used mainly due to their smaller footprint and enhanced energy efficiency [22]. The early optical communications system used LEDs that emitted at a wavelength between 800 nm and 900 nm. With the advancement in semiconductor technology and LED fabrication, emission at longer wavelengths of 1100 nm to 1600 nm was achieved. However, the optical signal generated by an LED is incoherent and suffers severe dispersive effects. Hence it is not suitable for long-distance communications. Subsequently, the use of semiconductor lasers (SLs) as the optical source

enabled service providers to overcome the disadvantages of earlier light source. The main advantages of SLs are:

- Coherent optical source – reduces the impact of chromatic dispersion.
- High output power (>1 mW)
- Improved fiber (SMF) coupling efficiency due to low beam.
- An SL can be configured to lase at O to U band of fiber optic channel that significantly reduce the optical attenuation.

The most commonly used semiconductor lasers in fiber optic communications systems are: Fabry-Perot (FP) laser [38], [39], [40], [41], [42], distributed-feedback (DFB) laser [43], [44], [45], [46], [47], distributed Bragg reflector (DBR) laser [48], [49], [50], [51], and vertical-cavity surface emitting laser (VCSEL) [52], [53], [54], [55], [56]. The broad spectrum of an FP laser, consisting of multiple resonant longitudinal modes, makes it impractical for high-speed and long-distance transmission. A DFB laser is constructed with an internal grating that enables single mode lasing. The wavelength of a DFB laser can be varied over a small range (~ 2/3 nm) by altering operating temperature (typically 0.1 nm/℃) and bias current (by changing the carrier density in the laser cavity). However, applications requiring fast and large wavelength switching would use a distributed Bragg reflector (DBR) laser or a variant of its structure.

1.2 Types of optical networks

The hair-thin fiber optic fabric infrastructure is designed to handle ultra-high speed data traffic [57]. The optical broad-band network architecture that serves the internet consumer is coarsely divided into three categories: core, metropolitan, and access network. The fiber infrastructure of a core network, also known as the backbone network, connects and serves various sub-networks. This is the highest speed part of the telecommunication system, interconnecting cities and countries.

The core network is accountable for ultrahigh-speed routing and switching, acting as a gateway for accessing other networks and providing high reliability. The metro optical network is designed to cover a large area, typically several hundred kilometers. It acts as a

bridge connecting core (long-haul) to access (last mile) network. The access networks connect subscribers to the service provider via core and metro network. Access networks can be categorized in three ways: Wired, radio (wireless) and optical access network. Asynchronous digital subscriber line (ADSL) [58], [59], [60] is a popular wired broadband access network mainly designed for small businesses. ADSL is an entry level broadband service provider that uses copper cables to provide broadband access hence it is very cost efficient. However, the data rate of the ADSL in downstream and upstream is limited to 24 Mb/s and 8 Mb/s, respectively. Radio access networks (RAN) are designed to establish a seamless connectivity with terrestrial devices [61]. RAN is capable of serving airborne and fixed devices such as vehicles, mobiles, and drones via LTE, 3G, 4G, 5G and Wi-Fi [62], [63], [64], [65]. In optical access networks, users are directly connected to service provider via a fiber optic cable hence these services are labeled as fiber-to-the-home (FTTH) and fiber-to-the-building (FTTB) [66], [67], [68], [69]. The fiber-to-the-crub (FTTC) and fiber-to-the-node (FTTN) are established with hybrid connection of fiber and copper cables.

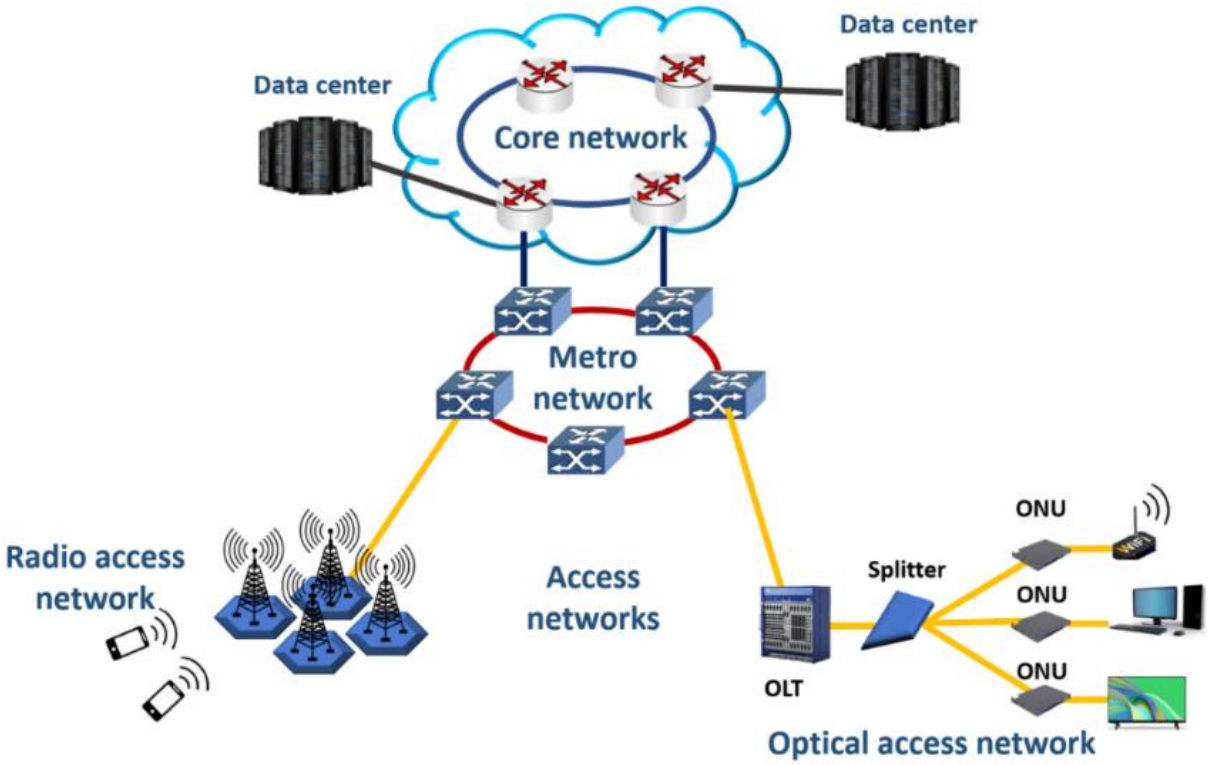

Figure 1.2.1. Categorization of optical networks.

All types of access network mentioned above establish long-haul or short haul connectivity. However, this thesis deals with short reach network and thus we will be focusing on optical access network. The passive optical network is a renowned technology that establishes a shot-reach communication infrastructure for providing services to data consumers.

1.3 Passive optical networks

The PON is a communication infrastructure that uses fiber optic cables to connect multiple users to a single service provider for delivering broadband services. In a PON, the service provider site and user endpoint are termed as optical line terminal (OLT) and optical network unit (ONU), respectively. In general, the optical links established between the OLT and ONUs are done so with passive optical components (as shown in Figure 1.3.1) and therefore referred to as a PON.

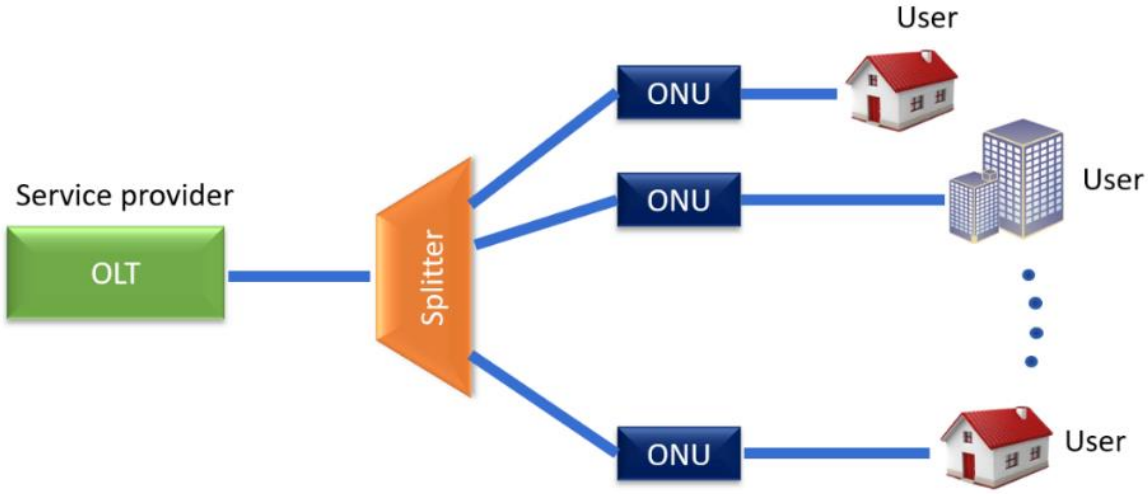

Figure 1.3.1. The typical architecture of a passive optical network (PON).

The optical-line-terminal (OLT), mainly handles the optoelectronic conversion of data, network handling and multiplexing [70], [71], [72]. On the other hand, the optical-network-unit (ONU) is the user endpoint of the optical access network that avails the services delivered by an OLT. They are designed to be energy-efficient and low-cost, relying on passive and low-cost optical splitters. In addition, the PON standards are designed with

backward compatibility in mind, providing an upgrade path for enhanced performance without disrupting services already in place.

1.4 Multiplexing techniques for PON

In PONs, there are three main technologies used to increase the channel capacity and handle a greater number of subscribers: time-division multiplexing (TDM), wavelength division multiplexing (WDM) and time and wavelength division multiplexing (TWDM).

1.4.1 Time-division multiplexing (TDM)

In TWDM the data packets destined for each user are assigned individual time slots (as shown in Figure 1.4.1) and broadcast to all ONUs using a power splitter in downstream operation [73]. Each signal contains the user address for correct reception. In the upstream direction, each ONU is given a particular slot to transmit data. To avoid collisions between data packets sent by different users, an accurate time synchronization control is required at the OLT. This is particularly important, as the distances between the OLT and ONUs vary, resulting in different propagation delays.

To solve this problem a ranging technique [74] is used to calculate the exact delay in transmission and the delay information is passed on to the remote terminal (RT) to enable an adjustment of the time window [75]. Most of the commercial schemes in a PON such as APON, BPON, EPON, and GPON use TDM for data transmission.

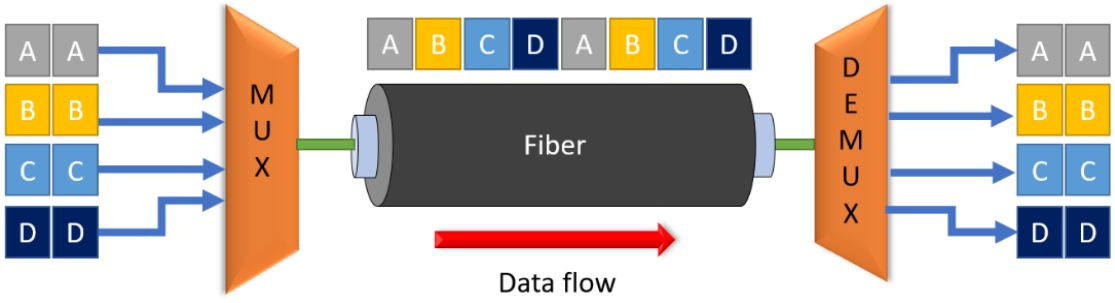

Figure 1.4.1. Simplified schematic to show the downstream operation of the TDM technique employed in a PON.

1.4.2 Wavelength division multiplexing (WDM)

WDM is a technique in which multiple optical channels, each at a different wavelength, can be transmitted simultaneously over a single optical fiber. Figure 1.4.2 depicts a typical architecture of WDM PON, where a unique wavelength for downstream and upstream operation is assigned to each ONU for establishing a point-to-point (P2P) connection to OLT [76], thus avoiding channel congestion. The wavelengths generated by the source at the OLT are combined together using an optical coupler and transmitted over a single fiber. A P2P connection between OLT and ONU enables full channel capacity so both can operate at full data rate.

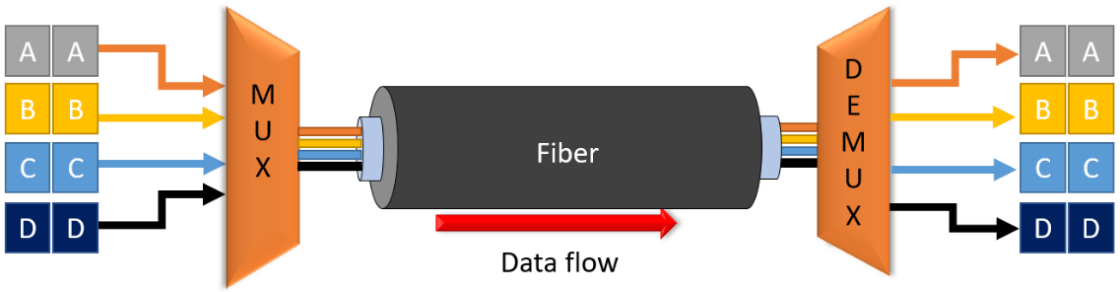

Figure 1.4.2. Simplified schematic diagram of downstream WDM technique.

Early WDM PONs employed a coarse wavelength division multiplexing (CWDM), with a 20 nm wavelength grid [77]. Such large channel spacings makes the WDM PON immune to wavelength drift of the transmitters. As a result, they do not require thermoelectric cooler (TEC), which lowers their cost and enhances energy efficiency. The drawback of the CWDM is its poor spectral efficiency and limited number of available wavelengths. Generally, the channel separation in the course WDM are limited [78], [79]. The number of channels can be increased by reducing the spacing between wavelengths. An alternative WDM scheme is dense WDM (DWDM) [80] and ultra-dense WDM (UWDM) [81], which utilises a wavelength spacing less than 100 GHz. An immediate advantage of DWDM is the extra number of channels that are available to connect more Early However, it requires a narrow band filter and temperature-controlled laser source, resulting in an increased cost of the system [82].

1.4.3 Time and wavelength division multiplexing (TWDM)

In TWDM PON architecture several wavelength channels are time multiplexed. It utilizes the advantages of both TDM and WDM technologies that depict high channel capacity and capable of serving vast numbers of users. The hybrid property of this architecture is cost-effective and supports coexistence with other PON standards. In this architecture (presented in Figure 1.4.3), multiple wavelengths are assigned for upstream and downstream data traffic. AT OLT, a multiplexer combines all the wavelengths and launches into fiber connecting to ONUs.

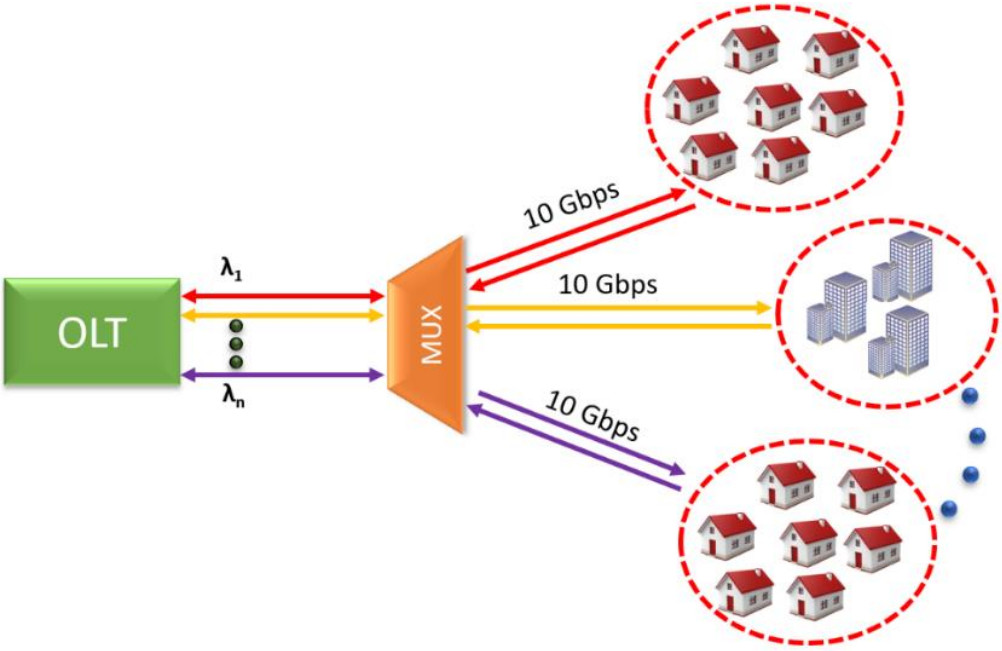

Figure 1.4.3. TWD multiplexing technique.

A group of ONUs form a cluster and each cluster is assigned a unique wavelength in the downstream and another in the upstream direction. A power splitter separates the optical signal and transmits to the cluster. Within a cluster, all the ONUs are time-multiplexed together, with a fixed time slot assigned for each user. The use of power splitter for the realization of TWDM PON increases the power budget. As mentioned, the ONU operates at specific wavelength however the channel can be switched for the load balancing [83] in case of congestion in the network. Hence, the ONU transceiver should be independently tunable in wavelength.

1.4.4 Code division multiple access (CDMA) PON

In CDMA PON the OLT recognizes ONUs with the help of the Walsh code and PN sequence [84] for multiplexing and demultiplexing. The advantages of CDMA PON are flexibility in user allocation, offer variable bit rates, and robustness against unauthorized users. Figure 1.4.4 shows the architecture of CDMA PON. The wavelength of operation for transmission in upstream and downstream direction are 1550 nm and 1310 nm [85]. In addition, all ONU use identical upstream wavelengths. At OLT, the data bits are encoded by multiplying the unique Walsh code and PN sequence and transmitted to ONUs after electro-optic conversion. Thereafter, a power splitter distributes the signal to all ONUs. The ONU recovers the data by multiplying the Walsh code and PN sequence used at the time of encoding to decode the signal [86]. In upstream, the coded signal from all the ONUs are multiplexed and sent to the multiple decoders of the OLT for data reception.

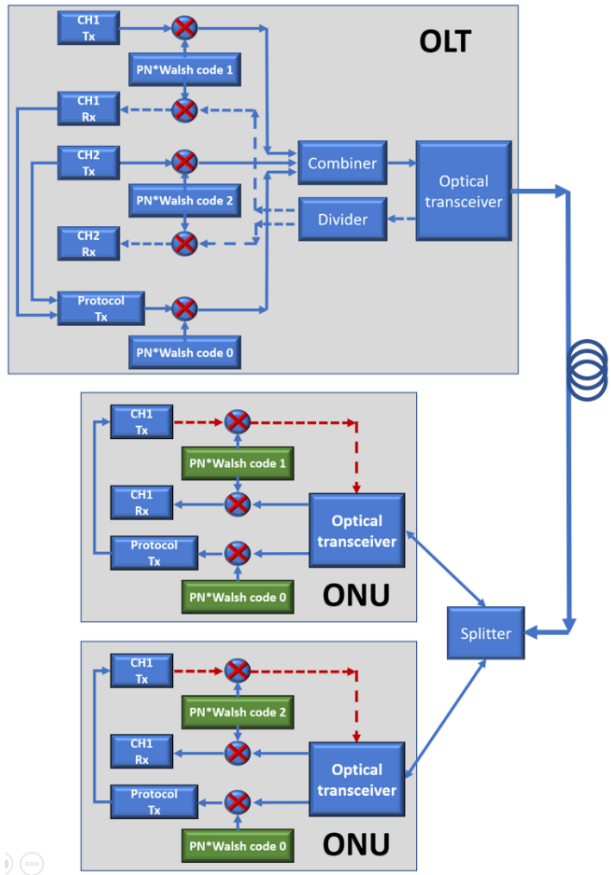

Figure 1.4.4. Architecture of CDMA PON.

1.4.5 Orthogonal-frequency division multiplexing (OFDM) PON

OFDM is a multicarrier technique, in which non-interfering orthogonal sets of RF frequencies are modulated and multiplexed over a single channel [87]. An optical OFDM signal is generated by modulating an optical carrier with the RF OFDM signal using an optical modulator. This technique is considered for PON due to its efficient use of spectrum, as well as the tolerance to chromatic dispersion. It can handle many users, especially in the hybrid OFDM/TDM scheme. Figure 1.4.5 shows a basic architecture of an OFDM transmitter and receiver. The transmitter and receiver require a real-time fast inverse fast Fourier transform (IFFT) and Fourier transform (FFT), respectively. These algorithms can be realised in real time using FPGAs. However, the size of the FFT is limited by the number of logical gates. In addition, the system also requires high speed digital to analog converter (DAC) and analog to digital converter (ADC). However, FPGAs, high speed DAC, and ADC are expensive and energy-consuming components. Moreover, the OFDM system also suffers from the problem of synchronization and peak to average ratio. The loss in carrier frequency synchronization may lead to loss in data signal. Furthermore, the OFDM transmitter multiples the carrier frequency by scaling factor that increases the peak to average ration. The signal with high peak to average ratio suffers nonlinear distortion when it passes through the amplifier at the receiver.

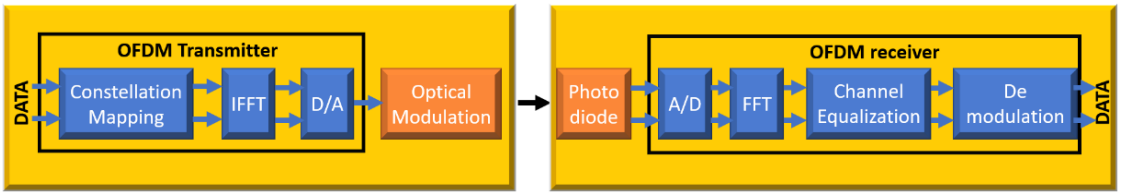

Figure 1.4.5. A simplified block diagram of an OFDM transmitter and receiver.

1.5 Evolution of the passive optical networks

The PON standard has undergone several changes as shown in Figure 1.5.1. The quest of providing higher bandwidth has been the main driver for these modifications. On-off keying is the commonly used modulation technique adapted by each standard. However, each

standard differs by downstream and upstream data rate; therefore, various generations can share the deployed optical infrastructure, with minor alteration and addition of components.

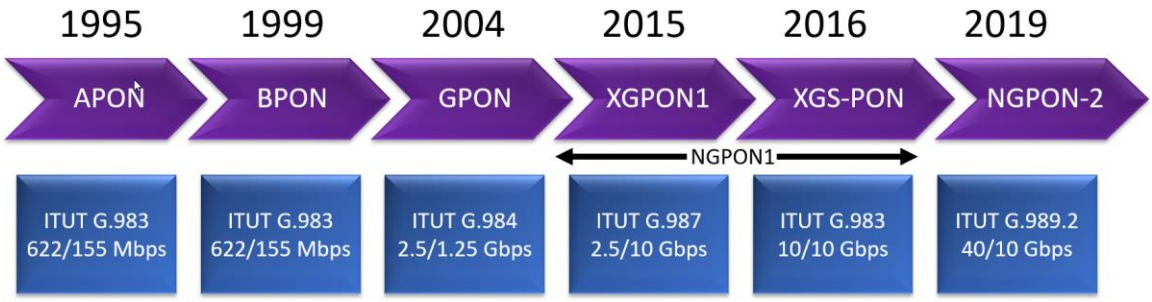

Figure 1.5.1. Evolution of the passive optical network architecture.

1.5.1 APON/BPON

Asynchronous PON (APON) was introduced as the first passive optical network, and it used multiplexed asynchronous transfer mode protocol (ATM). ATM uses asynchronous time division multiplexing to connect multiple users with P2P links [88]. In an early realization, the architecture had a P2P connection established by connecting N transceivers of the OLT to N transceivers of the ONU through N × L length of fiber (Figure 1.5.2). Later, a remote switch was used in the middle of the OLT and ONU to reduce the excessive use of fiber. However, this technique proved to be quite complex and expensive because it required 2N+2 transceivers to connect N users.

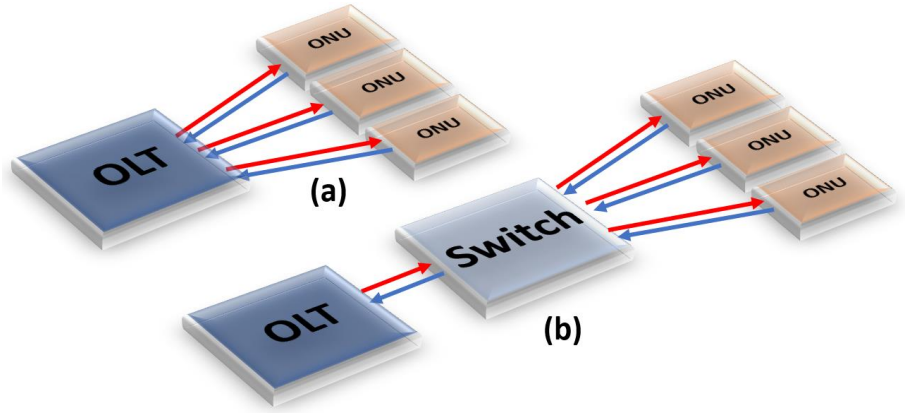

Figure 1.5.2. APON/BPON passive optical network (a) P2P connection and (b) P2P connection with reduced fiber length.

In APON, the data is divided into small, fixed size packets to transmit asynchronously to the ONUs [89]. Later, APON was upgraded to Baseband PON (BPON) by introducing wavelength division multiplexing (WDM) to establish a P2P link [88]. In addition, BPON had the capability to allocate the bandwidth according to the need of the end-user. BPON could achieve data rates of 155 Mbps upstream and 622 Mbps downstream, which enabled it to support services such as video, voice, and Ethernet access.

1.5.2 EPON

Despite the use of multiple wavelengths, BPON failed to deliver services such as high-quality video and high-speed internet to a large number of users. Ethernet passive optical network (EPON) was introduced to overcome these limitations. Figure 1.5.3 shows a typical network architecture of EPON. It uses the frame format to support point to multipoint connection. A single optical fiber connects the OLT to a passive optical splitter to reduce the length of optical link required to connect to multiple ONUs. The EPON encapsulates the data in the form of Ethernet frames and the later advancements in the protocol gave it the capability to handle voice, data, and video [90]. The EPON data packet contains a sender's and receiver's address to auto resolve the source and destination. EPON works in full-duplex mode and is based on IEEE802.3 standards which define the medium sharing using carrier sense multiple access with collision detection (CSMA/CD). The EPON evolved from providing 100 Mbps point-to-multipoint (P2MP) links (based on IEEE802.3-ah standard) to 10 Gb/s P2MP using the IEEE802.3-av standard [91].

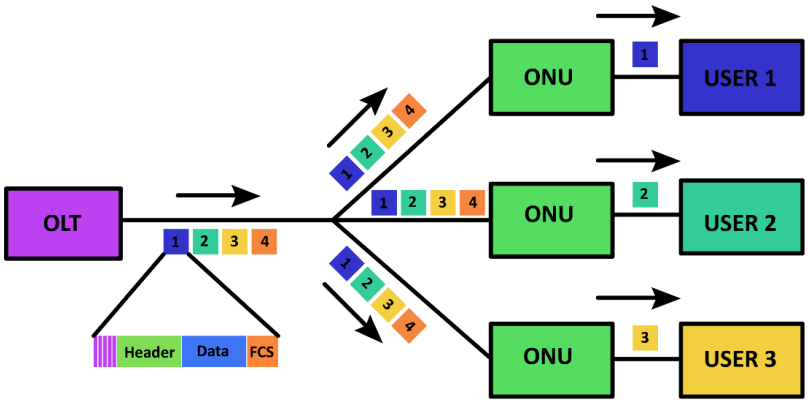

Figure 1.5.3. Schematic of a typical EPON network architecture.

1.5.3 GPON

The ever-increasing demand for higher data rates led to the development of the gigabit passive optical network (GPON), which was standardized by International telecommunication union (ITU) as G.984.1, 2, 3, 4, and 5. Figure 1.5.4 illustrates the architecture of a basic GPON system. Here, a traffic handler accepts the upstream data and the OLT performs the traffic scheduling, buffer control, and bandwidth allocation. Users are connected to an optical distribution network (ODN) that can support up to 64 users with a fiber length of up to 20 km. A user network interface (UNI) works as a bridge between the users and the ODN. The user's equipment connected to the ONT can be a setup box, personal computer, phone, etc. The GPON was mainly designed for handling voice, internet, video, and high-definition television (HDTV) services. GPON system uses two wavelength bands: 1230−1360 nm is allocated for the upstream and 1480−1500 nm for the downstream transmission. The major advantage of the GPON is its tree structure, which can support up to 64 users, who access the network with the aid of TDM. GPON uses an identical protocol for the upstream and downstream link, with the transmission rates highlighted in Table 1.5.1. In GPON the commonly used data rate to deliver FTTH services is 1.2 Gb/s upstream and 2.4 Gb/s downstream [92], [93].

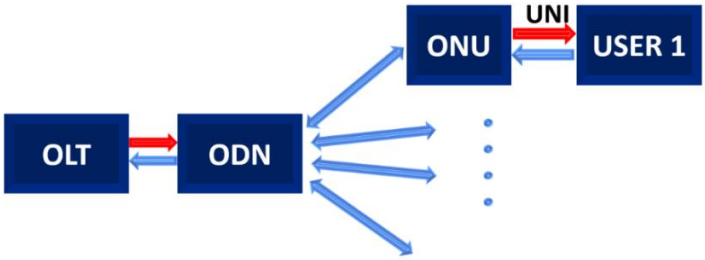

Figure 1.5.4. GPON architecture.

Upstream	Downstream
155 Mb/s	1.2 Gb/s
155 Mb/s	2.4 Gb/s
622 Mb/s	2.4 Gb/s
1.2 Gb/s	2.4 Gb/s
2.4 Gb/s	2.4 Gb/s

Table 1.5.1. Implemented upstream and downstream data rates in the GPON architecture.

1.5.4 XGPON1

XGPON1 was introduced as an upgrade to enhance the data speed up to 10 Gb/s in the downstream operation and extend the number of users. It is based on the G.987 ITU-T standard and gained popularity over GPON because of its simplicity and cost-effectiveness. The XG-PON infrastructure is merged with the GPON network without affecting the existing GPON subscribers [94]. Figure 1.5.5 shows the architecture of a typical XGPON system. In the architecture, simple or complex optical distribution networks (ODNs) are used to extend the number of users. In the simple architecture, a power splitter is used to connect multiple ONUs. On the other hand, in the complex ODN, a reach extender (RE) is used to compensate high splitting loss [95]. The RE comprises an optical amplifier and a repeater that allow for an increased link budget. However, since these are active components (energy consuming) this architecture is usually classified as a quasi-passive network. Figure 1.5.5 shows how the split ratio can be extended from $1{:}n$ to $1{:}p$ with the help of two REs. XGPON uses two wavelength bands: 1575 – 1580 nm for downstream and 1260 – 1280 nm for upstream transmission. It offers an asymmetric TDM PON by supporting downstream bit rates of 10 Gb/s and upstream bit rates of 2.5 Gb/s. However, multiple XGPON systems can be multiplexed in a single fiber using dense WDM, named DWDM/XGPON to increase the data rate further [96].

The DWDM uses closely spaced wavelength channels that allows operation of a large number of channels in the assigned band. Hence, the DWDM/XGPON requires highly stable drift free light sources, which are relatively expensive [97], [98], [99]. Apart from high channel capacity, XGPON1 also provides secrecy in data communication. The XGPON offers secure communication by using encryption technique and user authentication method [100]. XGPON1 upgrades to offers symmetrical transmission rate of 10 Gb/s in upstream and downstream direction in coexistence with XGPON1 and named as XGPON2.

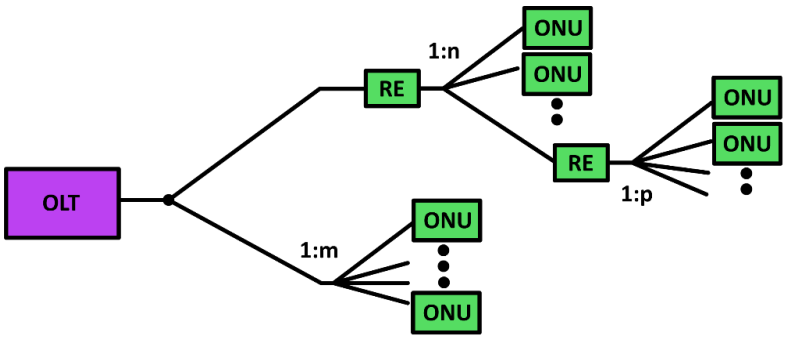

Figure 1.5.5. XGPON network architecture with reach extender (RE).

1.5.5 NGPON1

In this architecture, the XGPON1 and XGPON2 are collectively implemented and referred to as the next generation passive optical network-1 (NGPON1). Multiple XGPON1 and XGPON2 services running on different wavelengths over a single fiber implements NGPON1 architecture. NGPON1 uses forward error correction (FEC) and to accommodate the additional redundancy the downstream and upstream data rates of XGPON2 are reduced from 10.3125 Gb/s and 2.577 Gb/s to 9.985 Gb/s and 2.488 Gb/s, respectively. For the transmission and reception of 10 Gb/s signal NGPON1 requires high-speed transmitter and receiver at the user end, which adds cost at the time of upgrading the system. In addition, the NGPON1 supports split ration from 1:128 to 1:256. Hence, NGPON1 requires power budget from 29 dB to 31 dB [101].

1.5.6 NGPON2

In 2015, the TWDM was standardized as a fundamental architecture for a 40 Gb/s capable passive optical network-2 (NGPON2). It supports both a point-to-point and a point-to-multipoint link between the OLT and ONU [83]. The proposed architecture for the next generation passive optical network-2 (NGPON2) standard is shown in Figure 1.5.6, which essentially enables a low-cost implementation by replacing the ODN components. Here, the optical link is split into two parts: the OLT to ODN connection and subsequently the ODN to ONU/s links. The spectrum allocated for the NGPON2 allows for the coexistence with

deployed and in-service GPON, XG-PON, radio frequency video overlay for the distribution of digital and analog TV signal over FTTH as illustrated by Figure 1.5.7.

The wavelength plan for upstream and downstream operation is shown in Table 1.5.2. To implement a 40 Gb/s downstream link, 4 wavelength channels selected from the downstream wavelength band, each carrying a data rate of 10 Gb/s, are used. Similarly, 4 wavelength channels, within the upstream band, to realize the upstream connection with per channel transmission rates of 2.5 Gb/s and 10 Gb/s [102] are used. In the NGPON2 architecture, the allowed spacing between the four wavelengths selected for the upstream and downstream is 50 GHz, 100 GHz, and 200 GHz.

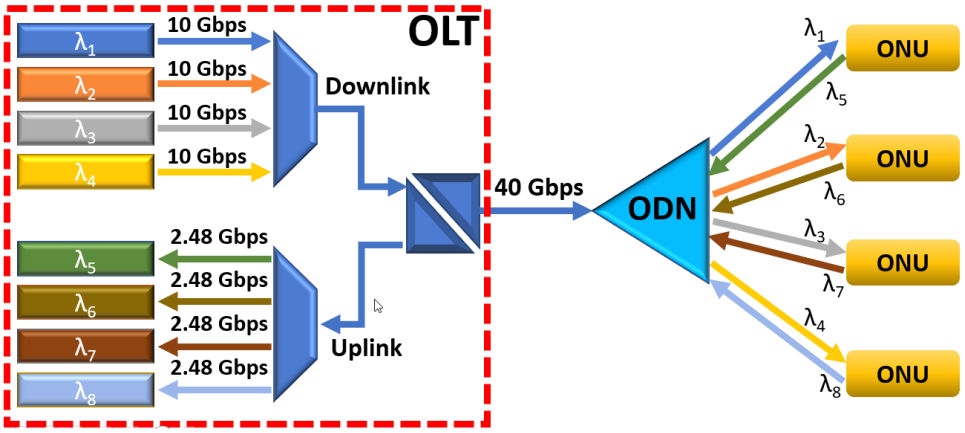

Figure 1.5.6. NGPON2 network architecture.

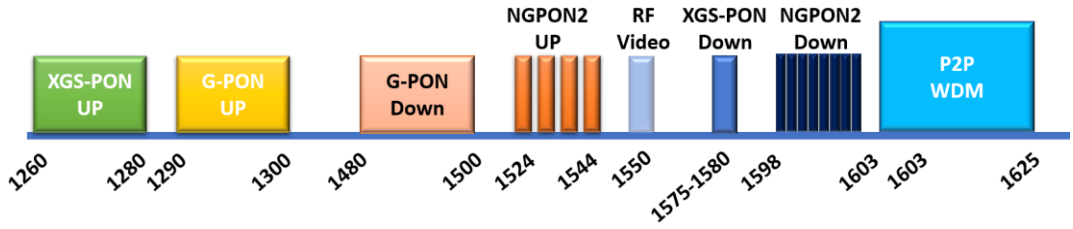

Figure 1.5.7. Wavelength plans for passive optical network architectures.

TWDM PON spectrum allocation		
Downstream	**Upstream**	
1596 nm – 1603 nm	Wide band option	1524 nm – 1544 nm
	Reduced band option	1528 nm – 1540 nm
	Narrow band option	1532 nm – 1540 nm

Table 1.5.2. Wavelength plan for NGPON2 standard.

1.5.7 G.HSP (50-G PON)

ITU-T standardized G.9804.3 in 2022, also called 50-G PON or high-speed PON (HS-PON), can deliver 50 Gb/s downstream and 25 Gb/s in the upstream direction. Unlike NGPON2, 50-GPON uses single wavelength channel and TDMA multiplexing technique to connect users [103]. In 50G-PON, the downstream and upstream wavelength channels lie in the O band. Previous standards such as GPON and XGS-PON are already running in the O band hence 50-G PON does not allow coexistence with it. In comparison to NGPON2, the architecture of the 50-G PON is designed to serve users over upto 60 km with a minimum split-ratio of 1:256. It is also important to note that the 50-G PON needs a very high-power budget to support a 1:256 split ratio. Hence, the OOK modulation scheme is considered for implementation [104].

1.6 Challenges for high-speed PON

1.6.1 Capacity crunch

The number of subscribers and the volume of traffic flowing through PONs continues to increase. In a recently published statistics it is estimated that the number of users and growth in global internet has increased to 7.9 billion and 1,416 %, respectively [105]. This puts huge pressure on the network infrastructure, making it difficult to meet the service requirements and forcing the network operators to invest in new technologies. A significant effort has been put into enhancing the channel capacity of the existing fiber infrastructure for enabling large data transfer at high speed. The Figure 1.6.1 shows the trend of channel capacity depicted by various multiplexing technique and forecast up to 2030. For example, WDM offered multiple wavelengths with each one offering itself as a high-speed link to carry vast amounts of data. Later, the channel capacity in SMF was further increased by using dense WDM (DWDM) [82]. However, the maximum transmission capacity of 1-10 Tb/s is achievable in SMF using WDM technique with space division multiplexing [106]. The transmission capacity limit can be extended up to 100 Tb/s by using higher order modulation techniques such as pulse

amplitude modulation (PAM), quadrature-phase shift keying (QPSK), 16-quadrature-amplitude modulation (QAM), etc. As per the trend, the channel capacity of the optical link needs to be increased by 40 % every year and the service providers would have to deal with the problem, known as capacity crunch.

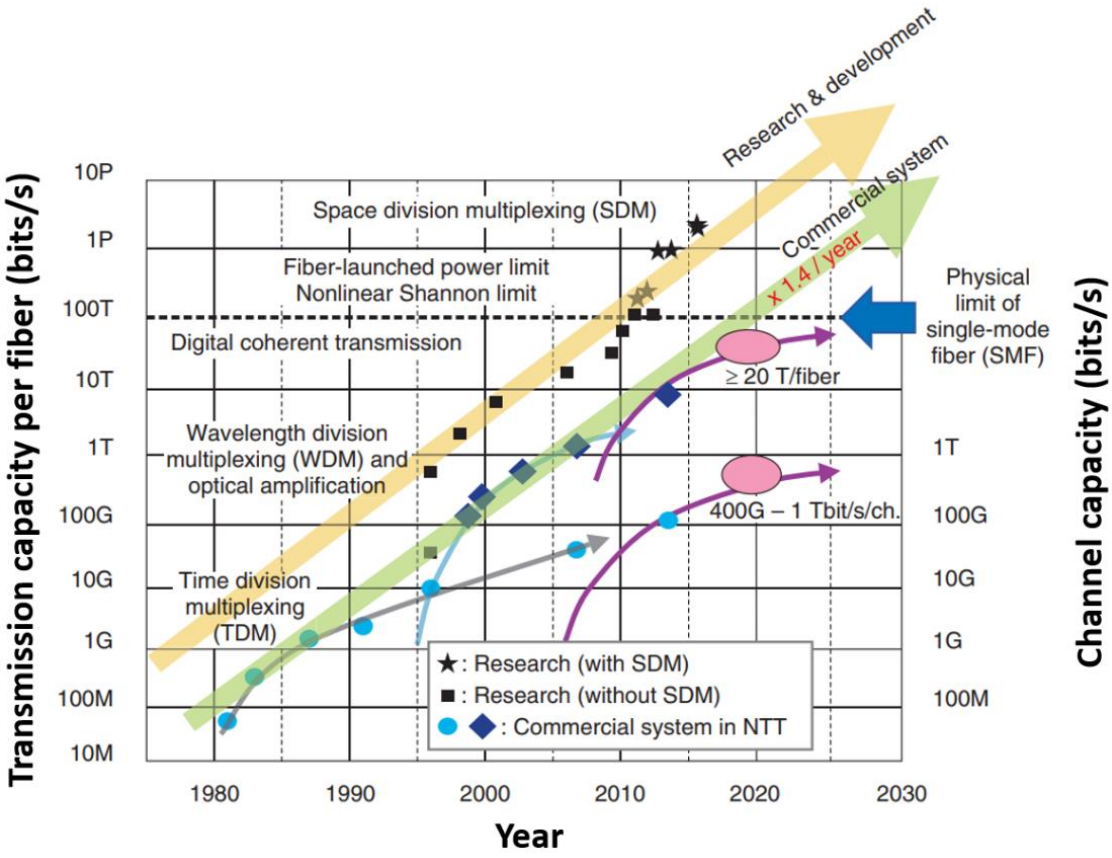

Figure 1.6.1. Trend of channel capacity [107].

1.6.2 Data rate limit

In On-off keying (OOK) modulation technique the intensity of optical signal directly modulated by a time varying electrical signal (data signal). As mentioned earlier, an optical pulse suffers broadening while traveling through fiber due to dispersion. Hence, to avoid overlapping of pulses for a specific fiber length and modulation rate, the broadening of the pulse must be at most 10% of initial pulse width [22]. The maximum rate of modulation supported by single-mode fiber is given by

$$t_T = \sqrt{(t_{mod})^2 + (t_{CD})^2 + (t_{PMD})^2} \quad 1.6.1$$

Where, $$t_{mod} = 0 \ \ for\ single\ mode\ fiber \quad 1.6.2$$

$$t_{CD} = D_{CD} \times L \times \Delta\lambda \quad 1.6.3$$

$$t_{PMD} = D_{PMD} \times \sqrt{L} \quad 1.6.4$$

D_{CD} is chromatic dispersion, L is length of SMF, $\Delta\lambda$ is spectral width of the optical signal, and D_{PMD} is the polarization mode dispersion. The chromatic and polarization mode dispersion depicted by a SMF fiber are $17\ ps/nm \cdot km$ [108] and $0.2\ ps/\sqrt{km}$, respectively. The maximum modulation rate using OOK scheme can be calculated by Eq (1.6.1). The highest modulation rate supported by a 50 km SMF transmitting OOK modulated optical source of $0.01\ nm$ linewidth is ~11.6 Gb/s [22]. The equation 1.6.1 also represents the inverse proportionality between modulation rate and length of transmission, which means the transmission length decreases with an increase in the modulation rate (or data rate in case of an OOK modulation scheme).

1.6.3 Wavelength stability

The transmission capacity of SMF over a single wavelength (channel) using TDM is limited to ~40 Gb/s because of the limitation of high-speed electronics, and to increase the data rate further number of channels need to be increased [109]. The limitation can be overcome by using optical time domain multiplexing (OTDM) [110]. However, the speed of the OTDM is limited due to distortion in optical pulse caused by chromatic dispersion [111]. The channel capacity can further be enhanced by using WDM system that offers data transmission over several channels multiplexed and transmitted through fiber. An array of lasers emitting closely spaced wavelength acts as a WDM source [112]. The operating condition of the laser is highly sensitive to thermal change. As mentioned in the section 1.1.2, the emission wavelength of the laser depends on the operating temperature. Hence, the change in operating

wavelength can lead to a misalignment with the passband of the demultiplexer which in turn may result in performance degradation or failure. The temperature instability can be tackled by using a closed-loop temperature controller that maintains the operating temperature of the lasers. In addition, the wavelength drift can be minimized by using wavelength-monitored temperature controller [113] and wavelength referencing and locking schemes [114].

1.6.4 Wavelength tunability

In a WDM PON, the wavelength-tunable optical source plays a vital role in coping with the issue of channel congestion by load balancing [115]. In this technique, the OLT generates several wavelengths and assigns a dedicated wavelength to each ONU. In load-balancing, the OLT allows the ONU to change from heavily congested to less busy wavelength channels to avoid congestion, both in the upstream and downstream operations [116] [117]. To this effect, the OLT and ONU are equipped with a wavelength tunable laser and filter to enable wavelength switching in NGPON2 architecture. In addition, the channel switching time is critical for avoiding congestion and providing a seamless service [102]. However, a transceiver manifesting wavelength switching and rapid tunability requires sophisticated electronics that increase the cost of the system.

1.6.5 Power budget and split ratio

The power budget is the maximum loss a data link can tolerate without using a repeater to maintain the quality of service. Generally, there is also an allowed minimum link loss to avoid overloading of the detector (detector saturation). A safety margin is considered to cope with ageing and any temporal variations in the system performance. The typical value of the safety margin is 8 to 10 dB [22]. The link budget can be determined by the equation 1.6.5.

$$P_i = P_0 + \left(\alpha_{fc} + \alpha_j\right) \cdot L + \alpha_{SL} + D_L + M_a(dB) \qquad 1.6.5$$

Where P_i, P_0 , α_{fc}, α_j, α_{SL}, D_L, M_a are the average input power at the receiver (minimum value determined by the detector sensitivity), the average output power at transmitter, fiber

attenuation, splice loss, split loss, dispersion equalization penalty, and safety margin, respectively.

The leading cause of signal loss in an optical link is attenuation imposed by fiber and the splitter. The loss can be compensated either by increasing the launch power or using a repeater in the fiber link. However, increasing the fiber input power may cause nonlinear effects, resulting in a crosstalk between neighboring wavelength channels (in WDM) [118], [119], [120]. Hence, the power level of the optical signal must be optimized to keep the nonlinear effect negligible. On the other hand, the use of repeaters or an optical amplifier (an active component) makes PON less energy- and cost- efficient.

1.6.6 Coexistence of different PON generations

It is critical that the newly introduced PON standards support backward compatibility. This allows for an installation of multiple PON technologies over the same fiber infrastructure and migration between different generations without service disruption. As mentioned earlier, each PON technology uses a unique wavelength band; hence, all PON services can be multiplexed using one or more wavelength multiplexers. For example, the fiber link supporting GPON, XG-PON, and XGSPON also facilitates NGPON2.

1.7 Role of photonic integration in PON design.

Photonic integration is a technique of interconnecting photonic components (laser, modulator, detector, etc.) on a single substrate to form a functional circuit. Photonic integrated circuits (PIC) bring benefits such as miniaturization, reduced energy consumption, reduced optical coupling losses, protection from thermal variation and electromagnetic interference, and ultimately, the cost of the system.

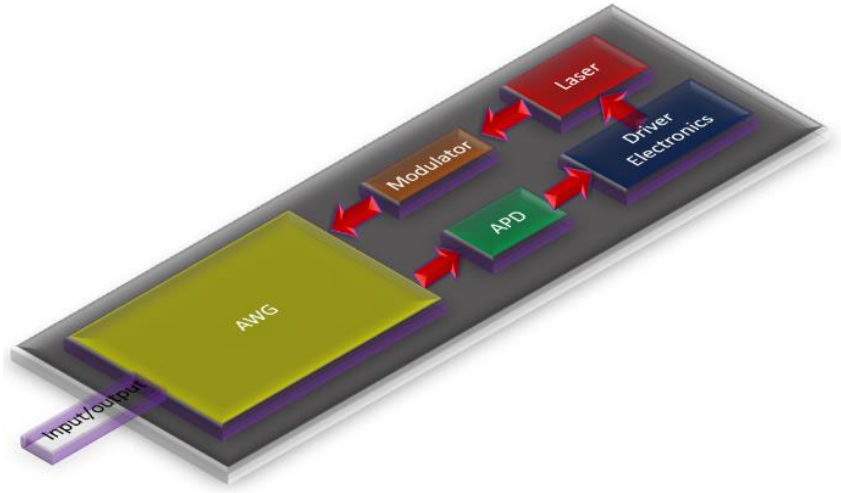

Figure 1.7.1 Basic architecture of an optical transceiver.

The transmitter and receiver are elementary components of all communications technologies. In the PON system, an OLT and ONU are equipped with an optical transmitter and receiver for sending and receiving an optical signal. The fundamental architecture of a transmitter consists of an optical source followed by a modulator and a wavelength multiplexer/demultiplexer to support WDM. A DFB, FP, SGDBR, and DBR lasers could all be considered as potential photonic integrated optical sources. In terms of the modulators, the electro-absorption and Mach-Zehnder modulators are the preferred candidates. Similarly, arrayed waveguide gratings are the most common (de)multiplexing components. Finally, a photodetector (PIN and APD) can be easily integrated within the receiver. All photonic components can be arranged and integrated in a single chip to realize an optical transceiver as shown in Figure 1.7.1.

As this thesis is focused on implementing the transmitter for short reach application, photonic integration plays a crucial role in fabricating a small-sized cost-effective optical transmitter. Generally, the photonic integration of optical components such as laser, modulator, optical waveguides, etc., differ in epitaxial composition requires multiple steps for fabricating a transmitter. However, regrowth-free fabrication offers minimized steps of fabrication that allows fast manufacturing of chips at a very low cost.

1.8 Conclusions

In this chapter we discussed the issue of growing demand of superfast and seamless connectivity to large number of users in the access network. This issue has been sustained for the past several years and optical network architecture has undergone several changes to solve the problem of capacity crunch. In the access network sector, the PON sustainably upgraded for providing increased data rates to end users without interrupting previously running technology. All proposed PONs, such as APON/BPON, EPON, GPON, XG-PON, and NGPON1, have supported coexistence and used previously deployed optical components. Recently, a newer architecture, NGPON2, has been standardized to solve issues of high bandwidth demand and increasing number of users. It supports the backward compatibility with previous standards and allows easy upgrades. The requirements and specifications for NGPON2 technology have been finalized and documented by ITU-T as Rec. G.989.2 (02/2019). The main goal of the thesis is to design a cost-effective optical transmitter in a small footprint for NGPON2 architecture. Photonic integration technology together with regrowth free technique can play a vital role in realizing an optical transmitter for the NGPON2 architecture. As the laser is a as a crucial part of an optical transmitter, in the next chapter, the design technique, optimization, and fabrication are discussed.

Chapter 2

Design and characterization of regrowth-free laser

2.1 Introduction

The previous chapter delves into the evolution of PON architectures designed to deliver high-speed data and services. However, the previously deployed PON technologies like EPON, GPON, XGOPON, and XGSPON, operating concurrently, need help to keep up with the increasing demand for data traffic and number of subscribers. A more advanced architecture, NGPON2, has been introduced to address this challenge. NGPON2 is designed to coexist with the existing PON standards seamlessly and allows straightforward upgrades to meet the growing bandwidth demands and cater to a large user base. As previously mentioned, the NGPON2-specific optical transmitter needs to be cost-effective and compact in design, which can be achieved through photonic integration techniques.

The process of photonic integration, which combines small-sized optical components like lasers, modulators, and detectors, has emerged as an economically efficient approach to manufacturing transmitters. Among these components, the laser, which acts as the source of optical signals, plays a pivotal role in optical transmitters. DFB, DBR, and SG-DBR lasers are popular optical sources available in integrable packages. However, the fabrication of these lasers involves several intricate steps, including lithography, etching, and regrowth, making the process time-consuming and less cost-efficient [121]. Single mode Index-Pattern Fabry-Perot (IP FP) lasers can be a viable replacement for DFB or DBR lasers that simplifies the fabrication and photonic integration [122], [123], [124]. The IP FP laser can be realised using a low-resolution photolithography and requires few fabrication steps [125]. Such lasers

exhibit similar characteristics to DFB and DBR lasers but also portray a low linewidth and high side mode suppression ratio (SMSR) [126]**.** Furthermore, they support regrowth-free fabrication offering merits such as minimized fabrication cycle and development time, and substantial cost reduction [127], [128], [129], [130], [131]**.** So, in this chapter we describe the step-by-step procedure for the design and optimization of a single mode IP FP laser.

We begin by utilizing an open-source software tool called "modesolver.py" [132] to identify the optimal width of the ridge. Subsequently, we turn our attention to the design parameters of the slot reflectors, which are generated by the periodic index pattern on the ridge waveguide. The characteristics of IP FP laser, such as threshold, SMSR, and linewidth, are critically dependent on the design parameter of the slot reflectors. In our simulations, using an open-source software "CAvity Modelling FRamework (CAMFR)" [133], we meticulously examine the impact of slot width and depth on the reflection coefficients. We then extract the reflectance band of the slot grating while varying slot widths. Subsequently, the gain characteristics of the material (used to fabricate the laser) are determined. Once the vital design parameters such as the ridge width, net modal gain, and reflection coefficient are determined, we employ a rate equation model to assess the laser's performance, using slot width as the control parameter. Finally, we conduct experimental characterization and performance comparison on IP FP lasers fabricated with distinct slot widths. To validate our findings, we compare the rate equation simulation model results with those from the experimental characterization tests, obtaining the best-performing laser variant.

2.2 Design of regrowth free laser

As previously mentioned, the IP FP laser offers the advantages of regrowth-free fabrication. There are two primary methods for implementing the IP FP laser using regrowth free fabrication technique: lateral patterning [134], [135], [136], [137], [138], [139], [140], [141] and vertical patterning [142], [143], [144], [145] of the refractive index on the ridge waveguide. In this discussion, our emphasis is on the implementation of IP FP achieved through the vertical patterning of refractive index on the ridge waveguide. In this design, a gain section can either be positioned between two slot-based reflectors [146], or

alternatively, between group of slots and a reflective coated facet [147]. We focus on the design of IP FP where the gain section is placed between a group of slots and a reflective coated facet. Figure 2.2.1 provides a step-by-step visual representation of fabrication cycle of IP FP laser.

The fabrication commences with the selection of a standard wafer grown on an InP substrate, exhibiting a spectral peak at 1545 nm, as depicted in the three-dimensional structure of the wafer. The wafer comprises a five quantum well active layer, with a p-doped AlGaInAs layer on top and an n-type AlGaInAs layer at the bottom, as illustrated in Figure 2.2.1(a)). The effective refractive indices for the p-type, active region, and n-type layers are 1.53, 3.28, and 1.68, respectively. This configuration places a high refractive index layer between two layers with lower refractive indices. This arrangement is crucial as it effectively confines the optical emission field of the laser along the z-axis.

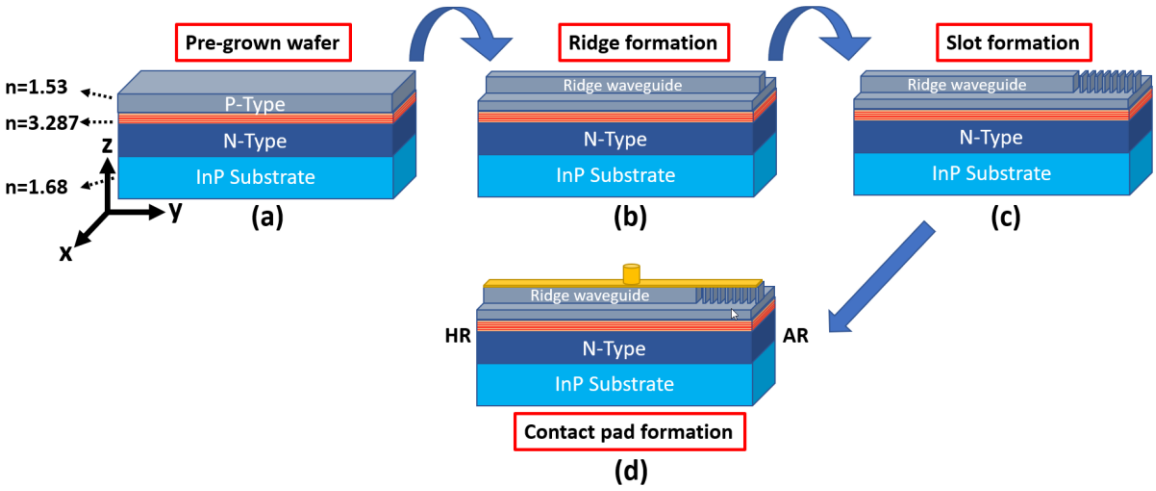

Figure 2.2.1. Fabrication steps for implementing a laser using regrowth free technique.

In the fabrication process, a ridge structure is created on the upper P-layer, as depicted in Figure 2.2.1(b). This ridge structure effectively confines photons within the active region along the x-axis, resulting in two-dimensional photon confinement on the z-x plane. This confinement forms an optical mode, illustrated in Figure 2.2.2. Subsequently, reflectors are introduced at both ends of the structure. To achieve this, slots are formed into the ridge structure at one end using photolithography and an etching process with precision of ~0.1 nm, as shown in Figure 2.2.1(c). These periodically etched slots, according to the Bragg

wavelength [148], play a critical role by reflecting a specific wavelength back into the active region, thereby functioning as reflectors. The second reflector is facilitated by applying a high-reflective coating to the rear facet. Finally, an anti-reflective coating is applied on the front facet, as shown in Figure 2.2.1(d). Metal contact is then grown through a metallization process to complete the structure. This sequence of steps is fundamental to the laser's functionality and optical properties.

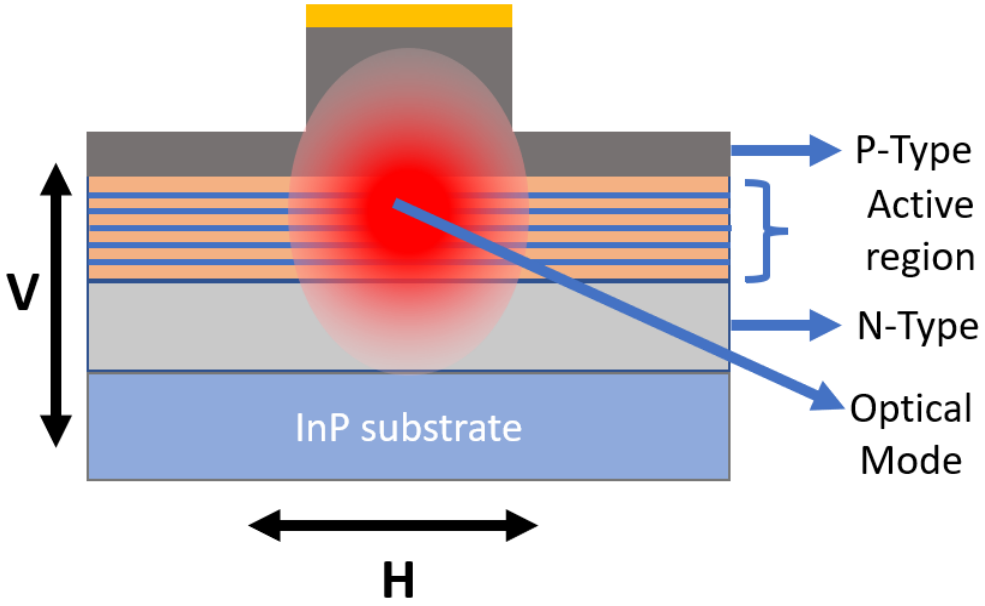

Figure 2.2.2. The cross-sectional view of two-dimensional confinement of optical mode, V: vertical and H: horizontal.

The width of the ridge plays a crucial role in optimizing the efficient transfer of optical power into a single-mode fiber. To identify the ideal dimension for fabrication, we conducted an analysis of the mode field distribution pattern across various ridge widths. For this analysis, we employ modesolver.py, an open-source Python-based simulation tool. Through this process, we determine the ridge width that offers the best confinement of the optical field within the waveguide.

Subsequently, we proceed to create the reflectors on the waveguide by etching a pattern of slots onto the ridge. Using another open-source simulation platform, CAMFR, we extract essential data, including the reflection coefficients and reflectance bands, for a range of slot widths. These estimations are of paramount significance in the laser's design and will be explored in greater detail in upcoming sections.

2.2.1 Optimization of ridge width

As mentioned earlier, the ridge structure fabricated on top layer confines the optical modes along x-axis. A shallow etched ridge waveguide, fabricated on the top layer by an etching process, results in optical confinement in the horizontal direction (x-direction). Figure 2.2.3(a) depicts a ridge structure of width W, where the material is removed along z-direction up to a depth of H by etching. The width (W) and etch depth (H) must be optimised to allow coupling of the fundamental mode between the active layer and the ridge, while suppressing the higher order spatial modes. The reason for minimizing the intensity of the higher-order modes in the waveguide is to minimize the coupling losses to single mode fiber and reduce the threshold for the fundamental mode that contributes to lasing. For optimization of W and H, the 2-dimensional (2-D) full vectorial algorithm solving a Laplace equation (modesolver.py) is employed [149], [150]. The solver returns the transverse optical modes with their respective E-field distribution on the cross-sectional area of the waveguide. The ridge waveguide structure is constructed by defining the thickness of layers, refractive index profile, W and H. For the shallow etch ridge waveguide, the value of H is chosen as 1.35 µm [151] because it is the maximum allowed etch depth for the chosen wafer. However, the optimization of W can be performed for any suitable value of H. The angle of the side walls of the ridge is defined as 80^{o} (as shown in Figure 2.2.3(a)) to account for fabrication errors.

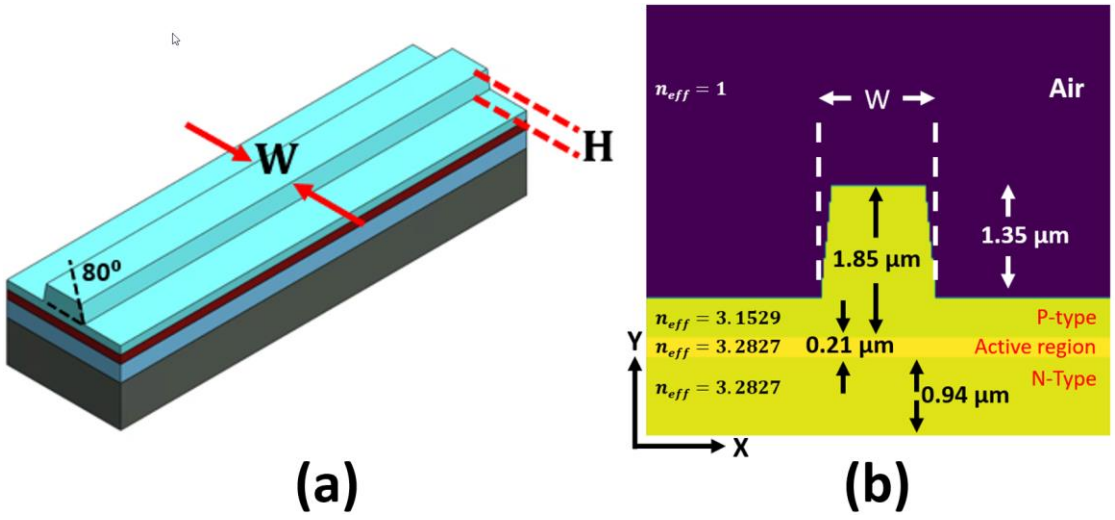

Figure 2.2.3. (a) Three- dimensional view of ridge waveguide structure and (b) definition of structure in the software to solve supported modes.

The optimization of the ridge width is carried out by performing the simulation for various values of W. While the solver provides the solution for all the modes supported in the waveguide, we consider only the first three modes (TE_{00}, TE_{01}, and TE_{02}) for the optimization process. This is because a significant amount of the total optical power (~95 %) is distributed in these modes. Figure 2.2.4(a), (b), (c), and (d) shows the plots of the power distribution pattern ($|E|^2$) for the first three TE modes for three different values of ridge width. In the case of W = 4 μm, the higher order modes, TE_{10} and TE_{20}, are seen to be coupled into the ridge waveguide. The power of TE_{10} and TE_{20} modes coupled to the waveguide decreases as W is reduced to 2 μm. Hence, the mode TE_{10} and TE_{20} doest not contibute to the lasing due to the low coupled power. In addition, the power of TE_{10} and TE_{20} coupled into the ridge is suppressed further for W = 1 μm. However, the coupled power of the fundamental mode also reduces, as can be seen in Figure 2.2.4(e), (f), (g). The primary reason for the reduction in the coupled power is the leakage of the electric field outside the ridge waveguide due to scattering loss [152]. As shown Figure 2.2.4 (g), the peak power of the TE_{00} mode coupled into the ridge is highest in the case of $W = 2$ μm, while the higher order modes are suppressed. Hence, a 2 μm wide ridge is chosen for design and fabrication.

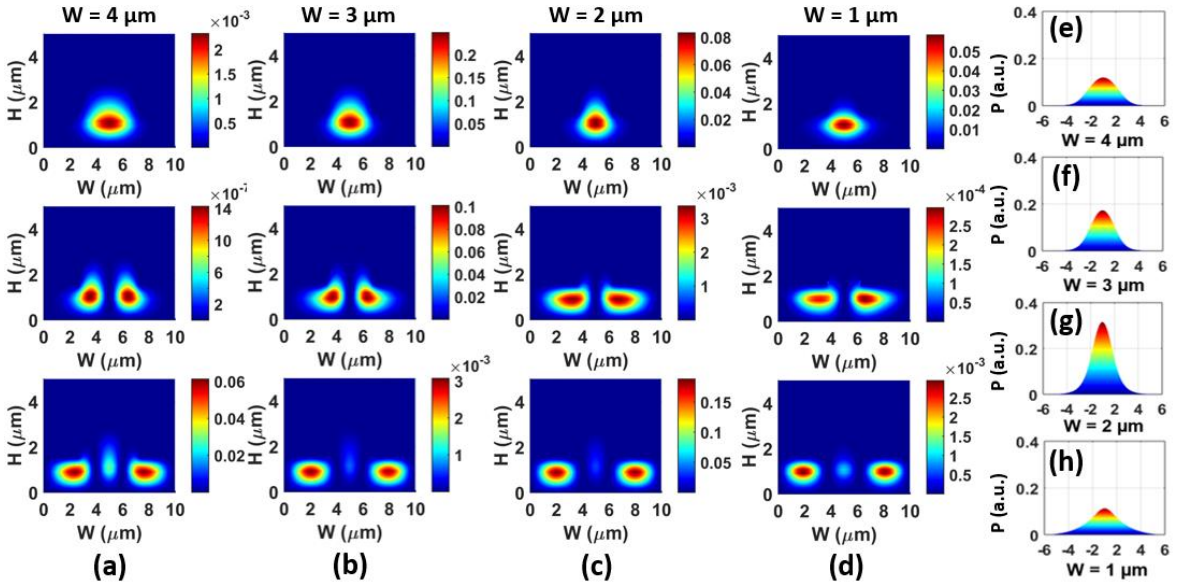

Figure 2.2.4. The power distribution patterns in TE_{00}, TE_{10} and TE_{20} modes for (a) $W = 4$ μm, (b) $W = 3$ μm, (c) $W = 2$ μm, and (d) $W = 1$ μm respectively, and the comparison of power level (arbitrary unit) of the TE_{00} mode for the varying ridge widths (e) $W = 4$ μm, (f) $W = 3$ μm, (g) $W = 2$ μm, and (h) $W = 1$ μm.

2.2.2 Optimization of surface grating

The performance of the reflector section (slot grating) is studied, as the next step. The slot grating is implemented by periodically etching slots on the ridge waveguide, as shown in Figure 2.2.5. These slots create a discontinuity in the refractive index that causes wavelength-specific reflections of the electromagnetic wave, and therefore contribute to the wavelength selectivity of the resonant modes in the laser cavity. The reflection coefficient of the grating depends on the geometry (slot width and depth) and the number of slots. In addition, the wavelength selectivity is controlled by the spatial period between the slots and can be determined by Bragg's equation given in Equation 2.2.1.

$$\Lambda = \frac{k \cdot \lambda_{Bragg}}{2 \cdot n_{eff}} \qquad 2.2.1$$

Where Λ, k, λ_{Bragg}, n_{eff} are the grating period, period order, Bragg peak wavelength, and effective refractive index of the grating respectively. The effective refractive index (n_{eff}) of the grating is obtained from the simulation discussed in the previous section and is calculated as ~3.19.

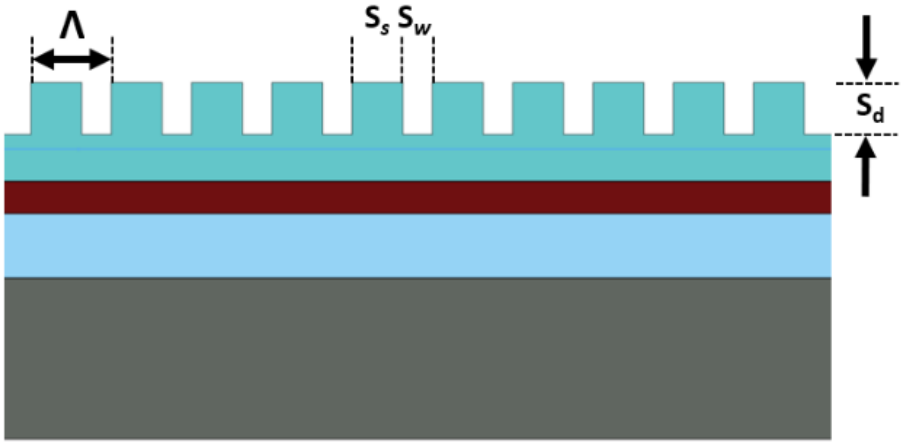

Figure 2.2.5. Schematic of the design of slot reflectors. Here: Λ is the grating period, S_w is slot width, and S_s is slot spacing.

The perfomance of the index-pattern laser relies on the slot reflector hence, the slots need to be carefully patterned on the ridge waveguide. Before patterning slots the slot width,

depth, and perriod need to be detrmined carefully. Several methods have been proposed to simulate the performance of slot reflectors [153], [154], [155], [156], [157], [158], [159]. We use an open-source CAMFR to carry out the analysis and estimate the behaviour of the slot reflectors. The grating is realised as a 1-D slot structure created by defining the thickness of layers (p-type, active region, and n-type), slot width (S_w) and slot spacing (S_s) (as shown in Figure 2.2.5), and period Λ defined as $\Lambda = S_w + S_s$. The period of the slot grating, calculated by setting the grating order at $k = 42$, $\lambda_{Bragg} = 1545$ nm (as the spectral peak of the material is at 1545 nm), results in a value of ~10.17 μm. The period order of 42 provides a 36.8 nm free spectral range which leads to successive Bragg wavelengths at 1508.2 nm and 1581.8 nm (peaks a and c in Figure 2.2.7). The net modal gain at 1508.2 nm and 1581.8 nm are much lower than 1545 nm and does not contribute in lasing. Thereafter, the reflection and transmission coefficients are extracted for 8, 10, and 12 cascaded slots by varying $S_w$while keeping the period constant. Figure 2.2.6 shows the trend of the reflection coefficient with varying S_w and S_d (slot depth) for a different number of slots. The plot reveals that the reflectivity increases with an increase in the number of slot reflectors, S_w, and S_d. It is seen that a high reflection coefficient is obtained for the combination of values $S_w = 0.3$ μm and $S_d = 1.35$ μm, as pointed out in Figure 2.2.6. It should be noted here that the maximum possible value of S_d is equal to the etch depth of the ridge waveguide (H), which is 1.35 μm (as specified by the fab.).

As the next step, we examine the dependence of the reflection coefficient on the operational wavelength. Here again using CAMFR, we extracted the reflection coefficients for a wavelength range of 1.5 μm to 1.6 μm (at a resolution of 0.1 μm). For this simulation, $S_d = 1.35$ μm (maximum etch depth) and S_w is varied between 0.2 μm and 1.4 μm. The value of Λ is kept unchanged throughout the simulation. Figure 2.2.7 shows the reflectance band for various vlaues of S_w. The plot reveals the presence of three reflectance bands at the Bragg peaks for each value of the slot width. Moreover, 0.3 μm and 0.7 μm slot widths give the highest and lowest reflectivity at the lasing wavelength of 1545 nm, respectively. For the fixed period order, the 0.3 μm slot attains ~40 % reflectivity at an operating wavelength of 1545 nm. We attribute the poor performance of the 0.7 μm slot to the high scattering loss at the Bragg wavelength.

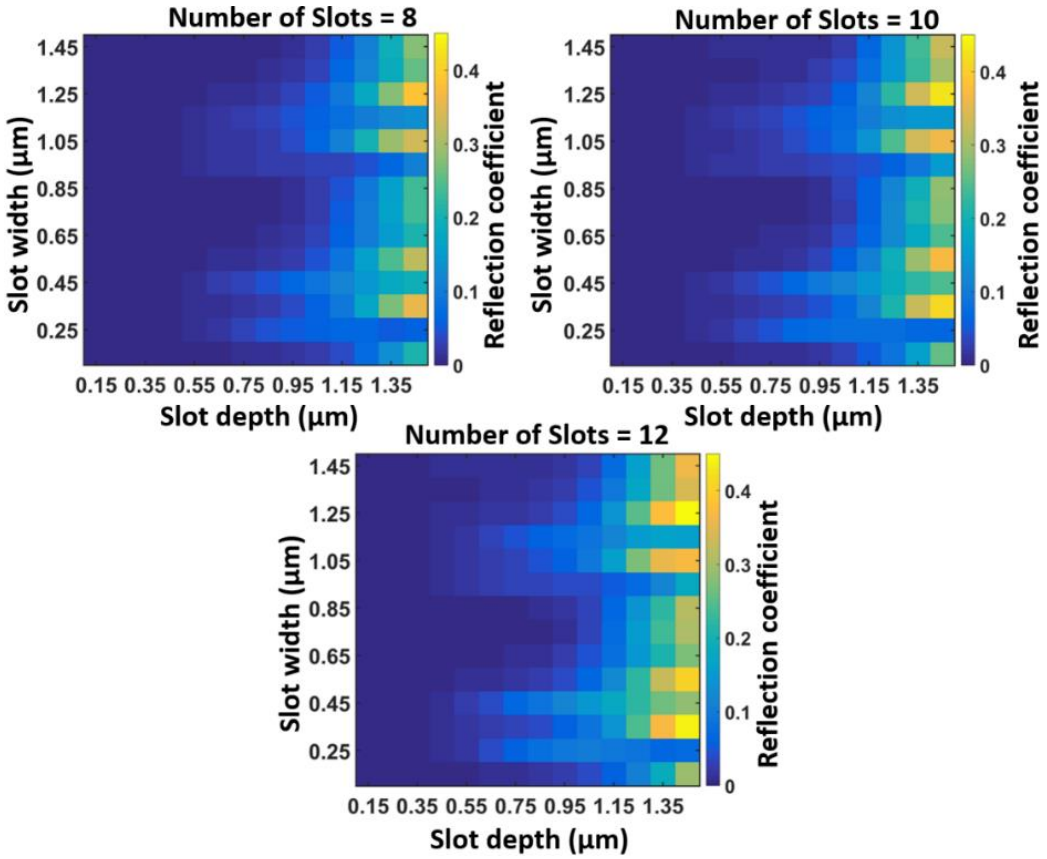

Figure 2.2.6. A plot of the variation of the reflection coefficient with respect to slot width and slot depth for various numbers of slots.

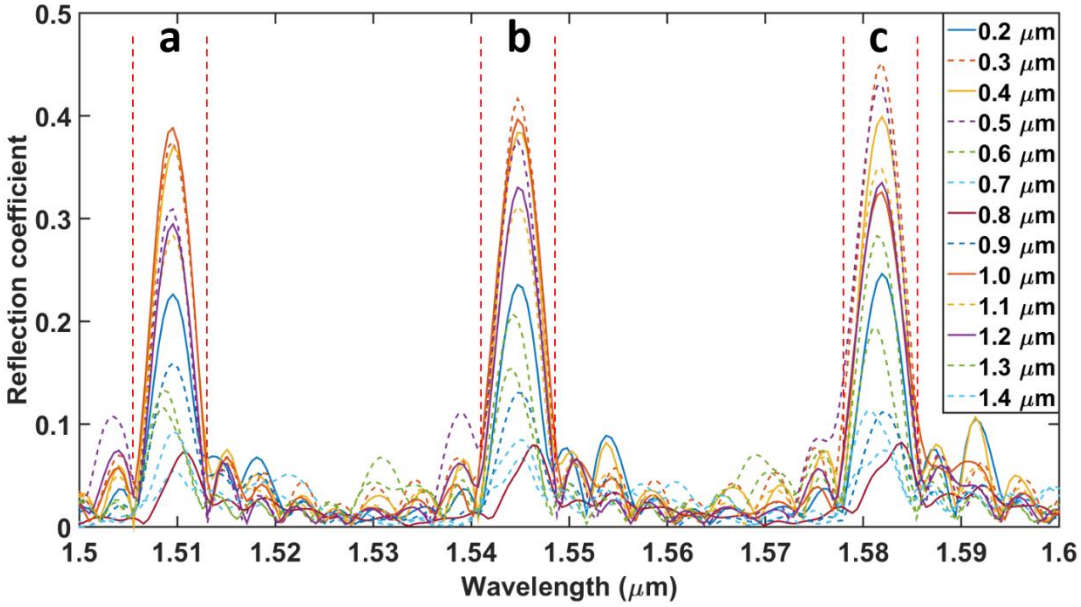

Figure 2.2.7. Trend of reflection coefficient with respect to wavelength for different values of slot width.

2.2.3 Extraction of gain coefficient

The gain section of the laser is essentially a semiconductor optical amplifier (SOA), and hence the performance metrics of the laser such as L−I characteristics, optical spectrum, etc., rely on the gain parameters of the material. Moreover, the dependence of gain on injection current is critical to predict the characteristics of the laser. The net gain (g) provided by the SOA is a combination of the gain caused by the stimulated emission of photons and optical loss caused by material defects. Additionally, the injection of carriers into the gain medium alters the refractive index of the medium, which has an impact on the spectral characteristics of the gain media. Hence, it is important to establish a correspondence between the injected current and the gain spectrum of the SOA. In this section, we describe the procedure for extracting the dependence of gain characteristics on the carrier density and wavelength, which is in turn is dependent on the injected current.

Several methods have been proposed to measure the gain parameter of the material used in the SOA, such as the optical transmission method [160], Hakki−Paoli method of analysis of amplified spontaneous emission (ASE) spectrum [161], [162], [163], [164], [165], comparison of ASE spectrum of distinct length SOA [166], and segmented SOA [167]. The method described in [161], [162], [163], [164], [165], [166], shows limited accuracy in gain measurements due to the requirement of a high-resolution (0.02 nm) optical spectrum analyser (OSA) and poor optical coupling. The method proposed in [167] is an improved method for the gain measurement that overcomes the mentioned drawbacks. Hence, we used the multi-section SOA method by comparing ASE spectra taken at various injection currents and extracting the gain profile at distinct values of carrier density.

The effective carrier density (N) that contributes to spontaneous emission in an SOA can be calculated by finding the roots of Equation 2.2.2 for N at various supplied current (I). Later, the obtained N is used to calculate the differential gain of the SOA.

$$C \cdot N^3 + B \cdot N^2 + A \cdot N - \frac{\eta \cdot I}{e \cdot V} = 0 \qquad 2.2.2$$

Where, C, B, A, η, I, q, V are the Auger coefficient, bi-molecular coefficient, nonradiative recombination coefficient, current injection efficiency, current, electronic charge, and the volume of active region respectively.

The net modal gain $g(\lambda)$ as a function of wavelength can be extracted from the measurement of the ASE spectrum by using Equation 2.2.3.

$$P_{ASE}(\lambda) = \eta_c \frac{p_{sp}(\lambda)}{g(\lambda)} \left(e^{g(\lambda)\cdot L} - 1\right) \quad 2.2.3$$

where $P_{ASE}(\lambda)$ and, $p_{sp}(\lambda)$ are the total output optical power from an SOA of length L and, spontaneous emission power per unit length at wavelength λ respectively, η_c is the output power coupling efficiency, and L is the length of the gain section. $P_{ASE}(\lambda)$ is measured for two SOA sections of different lengths L_1 and L_2 driven by the same value of current, which can be expressed using Equation 2.2.3 as

$$P_{ASE}^{L1}(\lambda) = \eta_c \frac{p_{sp}(\lambda)}{g(\lambda)} \left(e^{g(\lambda)\cdot L1} - 1\right) \quad 2.2.4$$

$$P_{ASE}^{L2}(\lambda) = \eta_c \frac{p_{sp}(\lambda)}{g(\lambda)} \left(e^{g(\lambda)\cdot L2} - 1\right) \quad 2.2.5$$

Where $P_{ASE}^{L1}(\lambda)$ and $P_{ASE}^{L2}(\lambda)$ are the output optical power of an SOA of length L_1 and L_2. Taking the ratio of Equation 2.2.4 and 2.2.5, and rearranging, we get Equation 2.2.6.

$$\frac{P_{ASE}^{L1}(\lambda)}{P_{ASE}^{L2}(\lambda)} = \frac{\left(e^{g(\lambda)\cdot L1} - 1\right)}{\left(e^{g(\lambda)\cdot L2} - 1\right)} \quad 2.2.6$$

and subsequently equation can be represented as,

$$\frac{\left(e^{g(\lambda)\cdot L1} - 1\right)}{\left(e^{g(\lambda)\cdot L2} - 1\right)} - \frac{P_{ASE}^{L1}(\lambda)}{P_{ASE}^{L2}(\lambda)} = 0 \quad 2.2.7$$

In Equation 2.2.7, $g(\lambda)$ is an unknown quantity and it can be determined by finding the roots of the equation.

To begin the measurement, we used an integrated two-section SOA (gain section) of lengths ~244 µm (SOA_1) and ~200 µm (SOA_2). The chip is mounted on the test station for gain measurement. Electrical isolation is maintained between gain sections to restrict the flow of current from one section to another. Initially, the front section (SOA_1) is biased at 25 mA to confirm the presence of ASE emission. Then, optical power from the output facet of the device is coupled into a lensed fiber with the help of an auto-aligner for maximizing the coupled power and maintaining the alignment. The current applied to SOA_1 is swept from 1 mA to 175 mA and an optical spectrum ($P_{ASE}^{L_1}(\lambda)$) is recorded for each value of current. Next, the current input to the sections SOA_1 and SOA_2 are tied together, and the current is swept again from 1 to 175 mA and the optical spectrum ($P_{ASE}^{L_2}(\lambda)$) is measured.

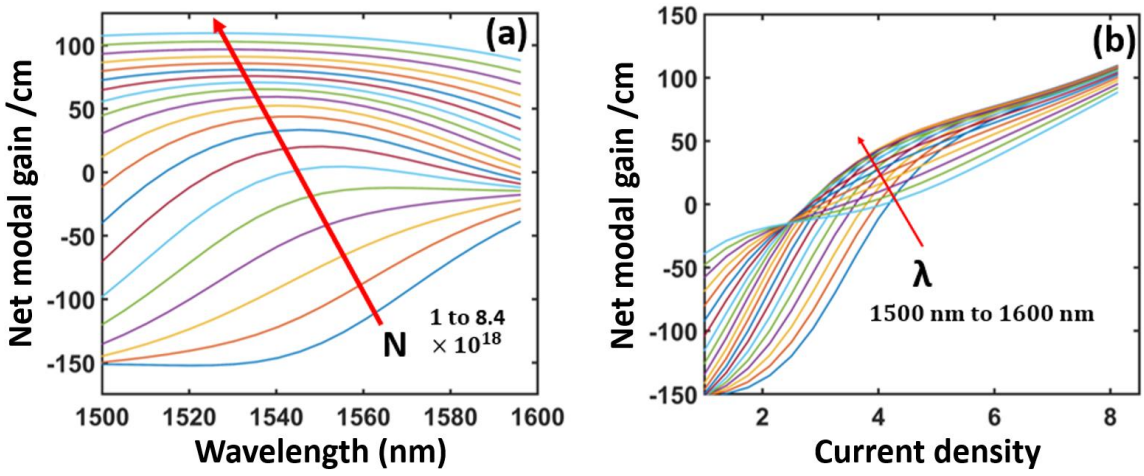

Figure 2.2.8. (a) Net modal gain vs wavelength for distinct carrier density and (b) Net modal gain vs carrier density for various wavelengths.

Thereafter, the values of the net modal gain are extracted using Equation 2.2.7 by substituting $L_1 = 244$ µm and $L_2 = (244 + 200)$ µm, and the respective $P_{ASE}(\lambda)$ for all values of carrier densities. The range of current used for this measurement corresponds to carrier density values ranging from $1 \times 10^{18}\ \mathrm{cm}^{-3}$ to $8.42 \times 10^{18}\ \mathrm{cm}^{-3}$ in steps of $1.21 \times 10^{18}\ \mathrm{cm}^{-3}$. Figure 2.2.8 (a) and Figure 2.2.8(b) shows the net modal gain as a function of wavelength and net modal gain as a function of carrier density for a wavelength range of 1500 nm to 1600 nm. Thus, a relationship between the carrier density and the gain spectrum of the medium is established, which is essential for implementing the rate equation model of the laser, as discussed in the next section.

2.3 Rate equation model of single mode and multi-mode laser

The performance of the laser can be simulated using the rate equations, where a set of three differential equations represents the time variation of the carrier density (N), photon density (P_i), and phase (ϕ_i). The P_i and ϕ_i are the density of photons and phase of the i^{th} longitudinal mode. The Equations 2.3.2, 2.3.3, and 2.3.4 show the laser rate equation for the five modes where P_0 is central mode and, P_{-2}, P_{-1}, P_1, P_2, are side modes as shown in Figure 2.3.1 The spacing between the longitudinal modes with respect to central wavelength (λ_o) is dependent on the length of the gain section and can be determined by Equation 2.3.1.

$$\Delta\lambda = \frac{\lambda_0^2}{2 \cdot n_{eff} \cdot L} \qquad 2.3.1$$

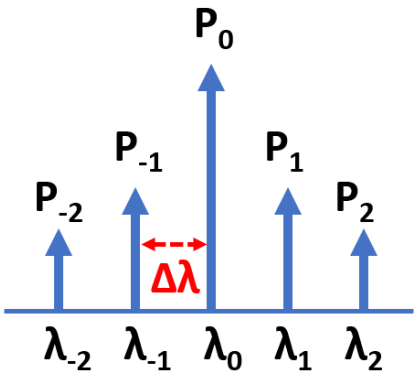

Figure 2.3.1. Simplified spectrum of a laser showing five modes.

The calculated wavelengths of the longitudinal modes in a 380 µm long laser with respect to the central mode at 1545.0 nm are 1543.03 nm, 1544.01 nm, 1545.98 nm, 1546.96 nm, respectively. As discussed in Section 2.2.2, the reflection coefficient depends on the wavelength of operation. Hence, the reflection coefficients (R_i) are extracted from the reflectance band (shown in Figure 2.2.7). Subsequently, the differential gain (dg_i/dN) of each longitudinal mode (P_0, P_{-2}, P_{-1}, P_1, P_2,) are extracted from the plot shown Figure 2.2.8 (b). The simulation is carried out by putting the values of dg_i/dN and constants given in Table 2.3.1 in the rate equation model.

$$\frac{dN}{dt} = \frac{I}{e \cdot V} - \sum_{i=-n}^{n} G_i \cdot (N - N_0) \cdot \frac{P_i}{1 + \epsilon \cdot P_i} - N_k + F_N \qquad 2.3.2$$

$$\frac{dP_i}{dt} = \Gamma \cdot G_i \cdot (N - N_0) \cdot \frac{P_i}{1 + \epsilon \cdot P_i} - \frac{P_i}{\tau_{p_i}} + \Gamma \cdot \beta_{sp} + F_{p_i} \qquad 2.3.3$$

$$\frac{d\phi_i}{dt} = \frac{\alpha_h}{2} \cdot \left(\Gamma \cdot G_i \cdot (N - N_0) - \frac{1}{\tau_{p_i}} \right) + d\omega_{c_i} + F_{\phi_i} \qquad 2.3.4$$

where

$$N_k = A \cdot N + B \cdot N^2 + C \cdot N^3 \qquad 2.3.5$$

$$G_i = \frac{dg_i}{dN} \cdot v_g \qquad 2.3.6$$

$$\tau_{p_i} = \frac{1}{v_g} \cdot \left(\alpha_i + \frac{1}{2 \cdot L} \cdot \ln \frac{1}{R_1 \cdot R_i} \right)^{-1} \qquad 2.3.7$$

$$D_{pp_i} = \Gamma \cdot \beta_{sp} \cdot B \cdot N^2 \cdot P_i \qquad 2.3.8$$

$$D_{nn_i} = \frac{D_{pp_i}}{\Gamma} + \frac{N_k}{V} \qquad 2.3.9$$

$$D_{\phi_i} = \frac{\Gamma \cdot \beta_{sp} \cdot B \cdot N^2}{4 \cdot P_i} \qquad 2.3.10$$

$$F_N = \sqrt{\sum_{i=-n}^{n} \frac{2 \cdot D_{nn_i}}{t_s}} \qquad 2.3.11$$

$$F_{p_i} = \sqrt{\frac{2 \cdot D_{pp_i}}{t_s}} \quad 2.3.12$$

$$F_{\phi_i} = \sqrt{\frac{2 \cdot D_{\phi_i}}{t_s}} \quad 2.3.13$$

Symbol	Parameter	Value
N_0	Threshold carrier density	2.08×10^{18} /cm^3
L	Length of the laser	380 µm
w	Width of ridge waveguide	2×10^{-4} cm
d	Thickness of active region	0.03×10^{-4} cm
I	Current	30 mA
e	Electronic charge	1.6×10^{-19} C
n_{eff}	Effective refractive index	~3.19
v_g	Group velocity	9.39×10^{7} m/s
ϵ	Gain compression factor	5×10^{-17} cm^3
Γ	Confinement factor	0.05
C	Auger constant	3.5×10^{-29} cm^3/s
B	Bimolecular recombination coefficient	1×10^{-10} cm^6/s
A	Non radiative recombination coefficient	0.1×10^{9}
η	Injection efficiency	0.8
β_{sp}	Spontaneous emission factor	3.2×10^{-5}
α_h	Linewidth enhancement factor	2
t_s	Sampling time	5 ns
α_i	Internal loss	40 /cm
R_1	Reflection coefficient of back facet	0.95
R_i	Reflection coefficient of grating	-

Table 2.3.1. Parameters used in rate equation model.

F_N, F_{P_i}, F_{ϕ_i} are the Langevin noise source for carrier density, photon density, and phase of N, P_i, and ϕ_i, respectively, and are calculated using Equations 2.3.8, 2.3.9, and 2.3.10 [152], [168]. The set of ordinary differential Equations 2.3.2, 2.3.3, and 2.3.4 are solved using the Runge-Kutta numerical technique. The N_k and G_i are total carrier density and net modal gain calculated using 2.3.5, 2.3.6. τ_{p_i} is the photon lifetime that depends on the length of cavity, reflectance of both mirrors, internal loss, and group velocity and calculated by using Equation 2.3.7. The value of $\alpha_h = 2$ is used in the simulation as in [169]. Only five modes are considered in the simulation to study the static behavior such as L−I, threshold and SMSR of the laser. The reason for considering only five modes is to analyze

the effect of the reflectance band b as presented in 2.2.7 on the suppression of sidemodes. The longitudinal modes lying outside of pass band b are not considered. The modes under the passbands a and c attain low gain (approximately $\frac{0}{\text{cm}}$ at 30 mA as depicted in Figure 2.2.8(a)), hence does not contribute to lasing. Moreover, the longitudinal modes which are outside of passbands a, b, and c are suppressed due to low reflectivity ($R < 0.1$). The simulation is carried out by using values of R_i for various slot widths and values obtained from Equations 2.3.8−2.3.12. In addition, the value of $\frac{\mathrm{d}g_i}{\mathrm{dN}}$ is obtained by calculating the slopes from the net modal gain versus carrier density presented in Figure 2.2.8(b) for all five longitudinal modes at carrier density = 4.27×10^{18}/cm, at $\mathrm{I} = 30$ mA. The calculated dg_i/dN for the mode $\lambda_0, \lambda_1, \lambda_{-1}, \lambda_2,$ and λ_{-2} are 2.13×10^{-17}, 2.11×10^{-17}, 2.10×10^{-17}, 2.08×10^{-17}, and 2.07×10^{-17}. Initially, the simulation is performed to analyze the effect of the slot width on L−I characteristics by calculating the output power with respect to the supplied current. Figure 2.3.2 shows the L−I data obtained from the simulation. It reveals that the 0.3 µm, 0.4 µm, 1.0 µm wide slots reach the lowest threshold current and the 1.4 µm, 0.7 µm, and 0.8 µm long the highest laser thresholds. In addition, the threshold of the laser for each of the slot widths lies between 15 mA to 21 mA. The 0.3 µm wide slot is considered for further investigation since it exhibits the lowest threshold.

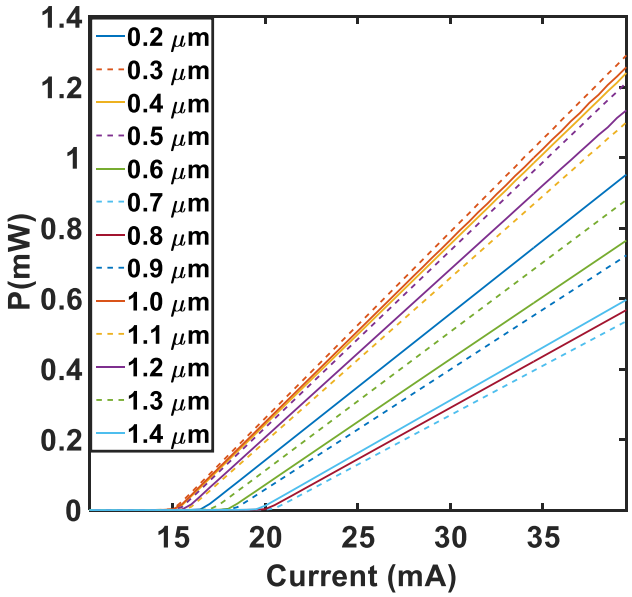

Figure 2.3.2. Simulated L − I plot of IP FP for slot width varying from 0.2 µm to 1.4 µm.

In the next simulation, we compare the SMSR performance of the IP FP laser and a conventional FP laser using the rate equation model by extracting the time variation of the photon density for each longitudinal mode. The architectures of an FP and IP FP are shown in Figure 2.3.3. The FP structure is defined by L = 380 µm, $R_1 = 0.95$ (HR coated back facet) and $R_2 = 0.33$ (front facet). Similarly, the structure of IP FP keeps the same length and R1 as for FP. However, the IP FP used slotted grating of $S_w = 0.3$ µm, which makes R_2 wavelength dependent, as shown in Figure 2.2.7.

Moreover, the Figure 2.3.4 and Figure 2.3.5 represents the comparison of the time trace of the emitted photon density obtained from the simulation for five modes of the FP and the IP FP. The simulation reveals that the photon density in steady state for the λ_0 mode is ~2.8 higher in the case of the indexed-patterned FP than that of the conventional FP. In addition, we see a 3.4×10^2, 4.7, 8.1, 5.6 times reduction in the number of photons in $\lambda_1, \lambda_{-1}, \lambda_2$, and λ_{-2} modes for the IP FP compared to the conventional FP. The reason for the higher photon density in the central mode is the suppression of the side mode. From the simulations, the SMSR is calculated by taking the logarithm of the ratio of the steady-state number of photons lying in the central mode and sidemodes. The simulation returns SMSR values of ~7.1 dB and ~37 dB for the conventional FP and the IP FP lasers, respectively, showing a notable improvement in SMSR provided by the IP FP.

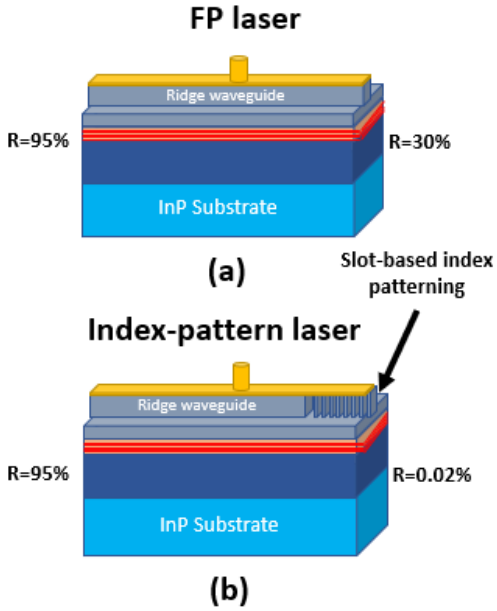

Figure 2.3.3. Schematic of the (a) structure of an FP and (b) an IP FP. Here: R is reflectivity.

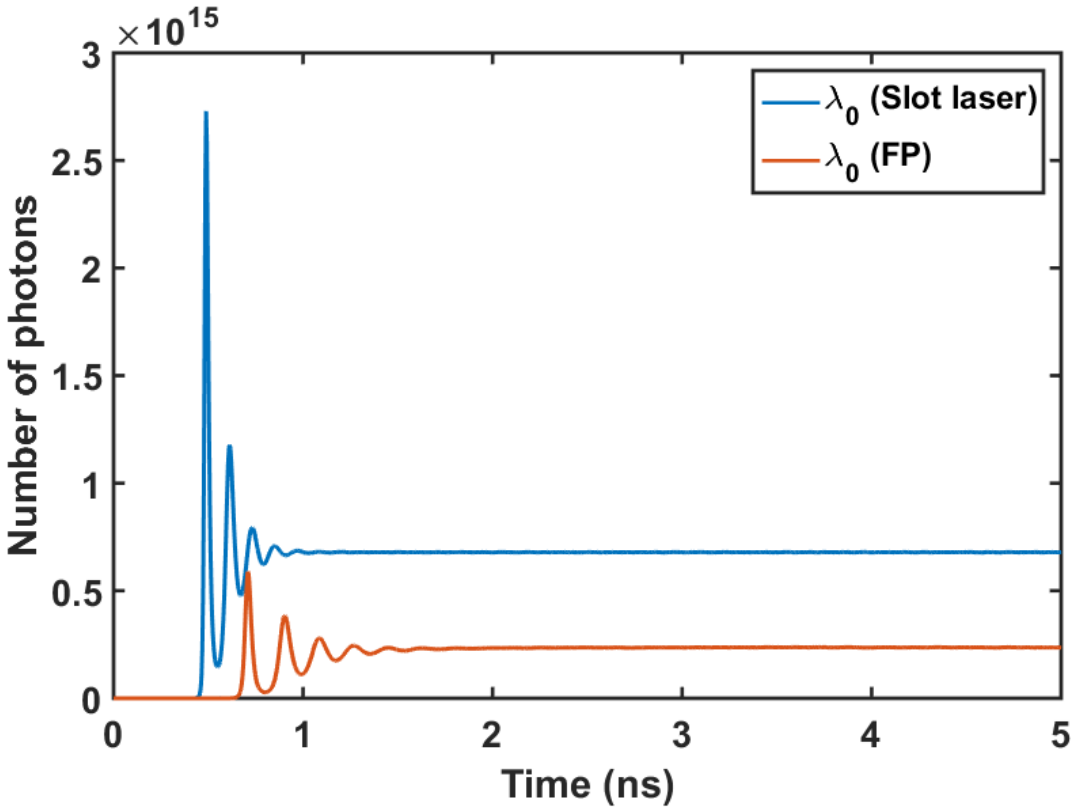

Figure 2.3.4 Comparison of photon dynamics of index-pattern laser with FP laser for central mode.

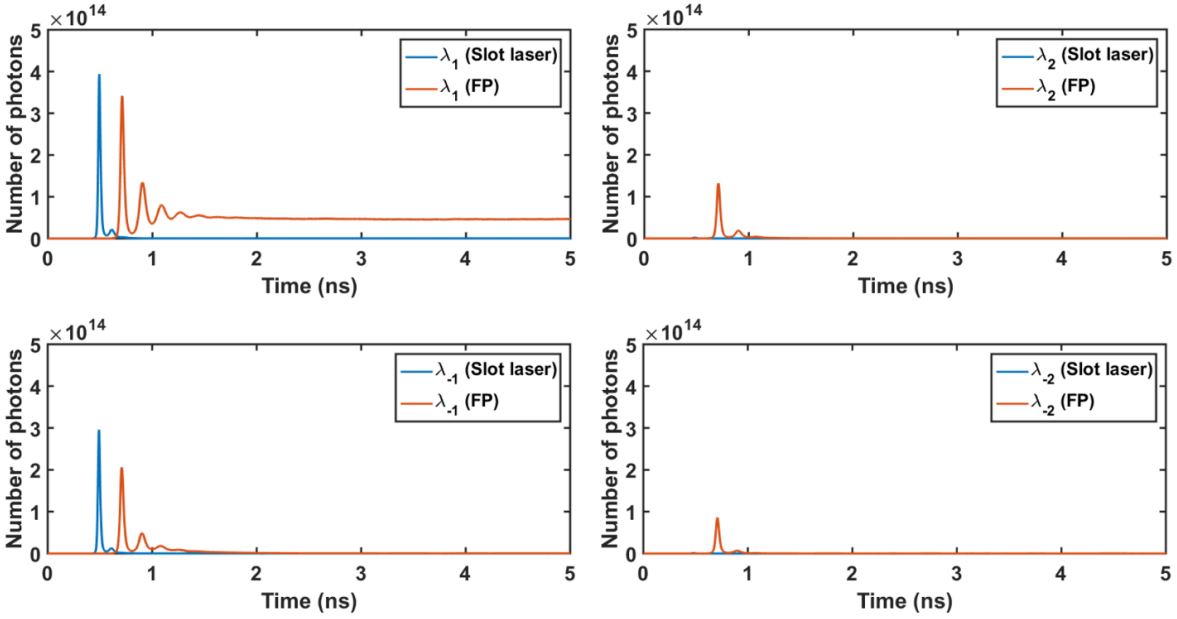

Figure 2.3.5. Comparison of photon dynamics of index-pattern laser and FP laser for sidemodes modes.

2.4 Layout of IP FP laser using Nazca and KLayout

In the following step, we initiate the design and fabrication of the IP FP laser, building upon the parameters acquired from the ridge waveguide and slot reflectors discussed in previous sections. To start this process, we employ open-source Nazca design software [170] to create layout. This layout is then visualized using the KLayout Graphic Data Stream (GDS) visualization tool [171]. The layout defines individual layers representing various components, including ridge trench, oxide, slots, and metallization. The width of the trench is determined using Equation 2.4.1 [152], resulting in a calculated trench width of 21 µm. Based on this calculated value, we define the specific trench area on the ridge trench layer.

$$\frac{\text{Trench width}}{\text{Ridge width}} > 10 \qquad 2.4.1$$

Subsequently, we define the oxide openings and exposed regions on the oxide layer, which facilitate the flow of current exclusively through non-isolated areas. Notably, the colored region on the P-layer signifies where SiO2 insulation hasn't been deposited. Following this, we create slots, represented as colored rectangular bars, with dimensions ranging from 0.2 µm to 1.4 µm and spaced at a 10.16 µm period on the slot layer. In the final stages, we define contact pads on a metal layer. To aid in the wafer cleaving process and obtain individual chips, we place cleaving marks (in the form of plus marks) on the metal layer. The Figure 2.4.1 serves as an illustrative example of a GDS layout for the IP FP laser, showcasing 1 µm wide slots. This approach is consistently applied to design all the variations of the IP FP laser. In the zoomed image, you can observe the fully refined layout of the IP FP laser, highlighting key components such as metal pads, ridge trench, slots, oxide regions, and cleaving points.

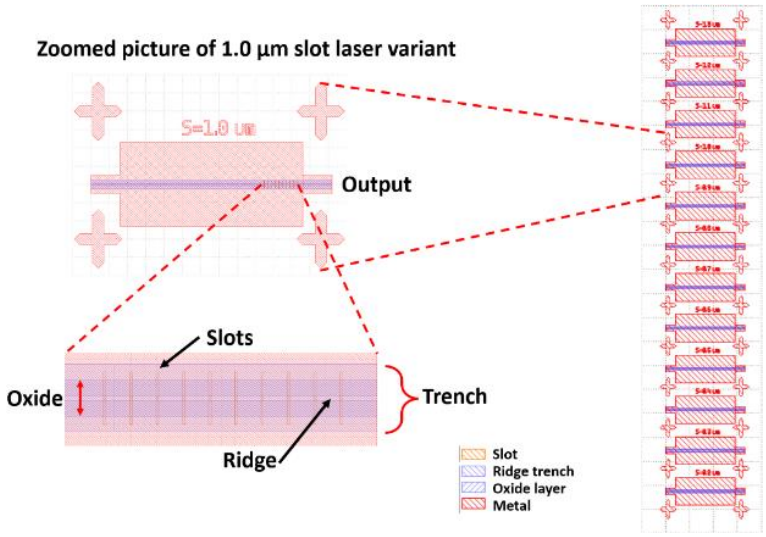

Figure 2.4.1.Generated GDS layout of IP FP laser using Nazca design.

2.5 Characterization of index-pattern laser with varying slot width

After creating the layout of different variants using the Nazca design the IP FPs are fabricated using a regrowth free technique [122]. A photograph of the fabricated lasers on a cleaved bar is shown in Figure 2.5.1. The back and front facets of the laser are highly reflective (HR) and antireflective coated (AR), respectively. The back and front facets of the laser are highly reflective and antireflective coated, respectively. To initiate the characterization, the laser bar is mounted on a subcarrier printed circuit board (PCB) and a DC current is supplied to the contact pads of the laser by using DC current probes. To obtain the L-I curve of the laser, the applied current is swept from 0 to 100 mA and the output optical power is measured using a wide area photodetector with a responsivity of 0.95, A/W. The measurements are carried out on 6 bars and for 13 different slots widths, varying between 0.2 µm and 1.4 µm.

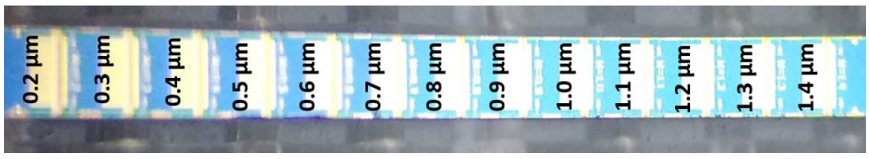

Figure 2.5.1. Picture of fabricated lasers on a bar of varying slot width.

2.5.1 L − I characteristic

Figure 2.5.2 shows the L−I plot of IP FP lasers with varying slot widths (0.2 µm to 1.4 µm). The data shows that the laser having 0.3 µm wide slot exhibit the lowest threshold. Moreover, the L−I measurement is repeated on 6 bars containing all 13 variants. From each bar, the lasers with a 0.3 µm slot width exhibits the lowest threshold. The measured threshold of a 0.3 µm slot laser is ~16 mA. The 0.9 µm and 1.1 µm slot width lasers show the highest threshold and low slope efficiency which attribute to high scattering loss at 1545 nm wavelength.

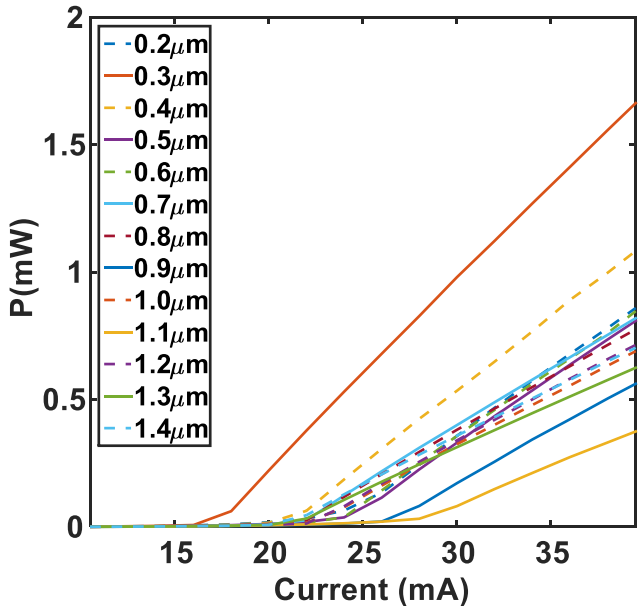

Figure 2.5.2. Plot of measured L−I data of IP FPs for varying slot width from 0.2 µm to 1.4 µm.

2.5.2 SMSR and Wavelength Map

Further investigation is carried out on all the variants of IP FP laser by measuring the optical spectrum and extracting the SMSR. To measure the optical spectrum, the optical power from the output facet of the laser is coupled into a lens-ended fibre and fed to an optical spectrum analyser (OSA). The laser current is swept from 0 to 100 mA at a resolution of 0.2 mA and the SMSR is measured. The extracted heat maps of wavelength and SMSR are shown in

Figure 2.5.3(a) show that the IP FP having 0.3 µm wide slot, attains an SMSR greater than 30 dB for bias currents higher than 24 mA. An example of the optical spectrum for 0.3 µm IP FP biased at 30 mA and featuring SMSR > 35 dB is shown in shown in Figure 2.5.3(b).

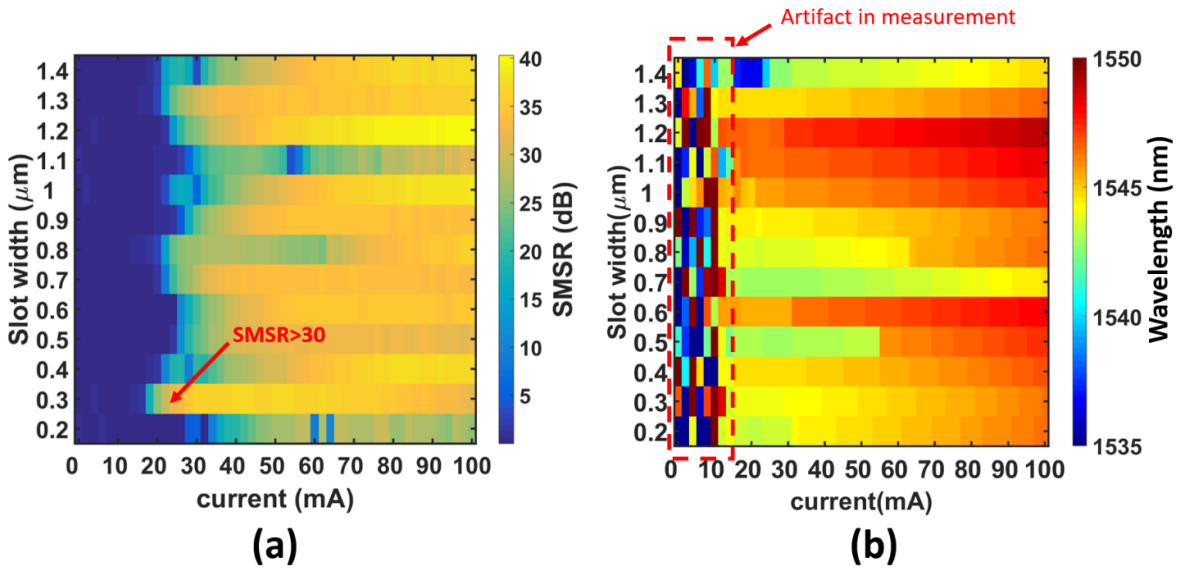

Figure 2.5.3. SMSR and wavelength map for all variants of laser.

2.5.3 Linewidth performance

Finally, the linewidth of each variant of the IP FP laser is measured using delayed self-heterodyne method (DSH) [172]. The DSH technique for measuring linewidth involves the process of beating the signal with a decorrelated replica on a photodiode and then observing the resulting RF beat tone. Figure 2.5.4. illustrates the experimental setup used for this linewidth measurement. The optical signal emitted by the laser is divided into two equal parts using a 50:50 passive optical splitter. The first part is connected to an electro-optic phase modulator (PM), while the second part is routed through a fiber delay. The length of the fiber is set to 25 km that provides resolution of ~10 kHz while measuring the linewidth and ensures sufficient decorrelation of signal. This is important to prevent the cancellation of optical phase noise during the homodyning process. For the linewidth measurement all laser variants are biased at current of 65 mA. The results, displayed in Figure 2.5.5, shows that all the variants exhibit linewidth between 1 and 5 MHz with the lowest linewidth of ~1 MHz

attained by 0.3 µm and 1.0 µm. Such low performance (in both simulation and experimental results) can also be linked to the low threshold, high SMSR and high slope efficiency.

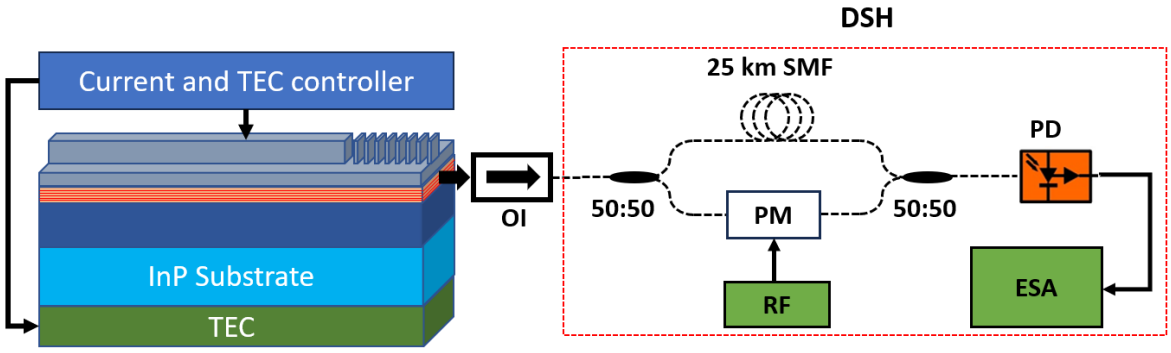

Figure 2.5.4. Schematic diagram of experimental setup for linewidth measurement.

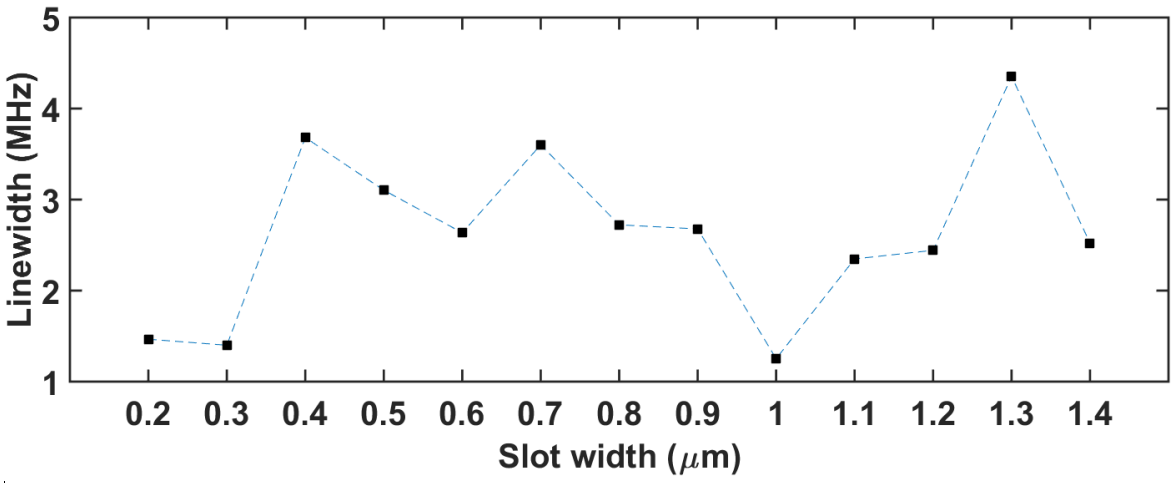

Figure 2.5.5. Linewidth measurements of IP FPs for slot width varying from 0.2 µm to 1.4 µm.

2.6 Results and discussion

The initial phase of the study involved optimizing the dimensions of a ridge laser, specifically focusing on the ridge height and width. Through our analysis, we found that the power coupled into a ridge structure with a width of 2 µm was the highest. This is because the fundamental mode of the laser reached its maximum power, and the higher order modes were effectively suppressed. Conversely, ridge waveguides narrower than 2 µm exhibited lower coupling power because the fundamental mode leaked outside of the ridge.

Another crucial element within the index pattern FP is the slot grating, achieved by etching slots onto the ridge's surface. Our simulations indicate that reflectivity rises as the number of slots and their depth increase. Moreover, when maintaining a constant period order and slot depth, the 0.3 µm slot reaches approximately 40% reflectivity at the 1545 nm operating wavelength, outperforming all other variants ranging from 0.2 µm to 1.4 µm. The excellent performance of the 0.3 µm slot can be attributed to its minimal scattering loss.

In the third phase, we applied the previously established design parameters to a rate equation model for simulating the static characteristics of the laser (L-I) and its SMSR performance. All the different versions of the IP FP laser exhibit threshold values ranging from 15 mA to 21 mA. Once again, the simulation results highlight that the IP FP laser with a 0.3 µm wide slot has the lowest threshold and the most efficient slope performance among all the variants. This lower threshold can be attributed to its high reflectivity and minimal transmission loss at a wavelength of 1545 nm. Furthermore, the 0.3 µm wide slot IP FP achieves an SMSR of over 36 dB when supplied with a current of 30 mA.

The experimental characterization of all the slot laser variants reveals a consistent pattern. We compared the simulated and experimental results for threshold current and SMSR. However, the order of threshold currents varies, and this discrepancy can be attributed to the inadequate definition of the slot during the fabrication process. Nevertheless, in both cases, the 0.3 µm slot laser stands out with the lowest threshold, approximately 15 mA in simulation and around 16 mA in the experimental data. The 0.3 µm slot laser also achieves an SMSR of roughly 36 dB in simulation and approximately 37 dB in the experimental characterization. The disparity between the simulated and measured threshold values can be attributed to inaccuracies in gain measurement.

2.7 Conclusions

In conclusion, we describe a step-by-step procedure for designing and optimizing a low threshold laser using open-source software and a rate equation model. The simulation on optimization of ridge width reveals that the fundamental mode attains maximum power coupled into the 2 µm wide and 1.35 µm thick ridge at 1545 nm wavelength hence chosen

for fabrication. Subsequently, the characteristics of the reflector such as the reflectivity and reflectance band are determined using CAMFR software. The simulation shows that 0.3 μm wide 1.35 μm deep slot exhibits highest reflectivity. Thereafter, the performance of all the variants of IP laser is evaluated by simulation of rate equation model and experimental characterization. We see a good agreement between simulation and experimental characterization. The 0.3 μm IP FP shows best performance in terms of low threshold and linewidth, and high SMSR. The findings presented in this chapter could serve as a crucial foundation for creating a highly precise laser suitable for use in NGPON2 transmitters. Therefore, the next chapter will delve into the strategies for constructing an optical transmitter through a regrowth-free fabrication process.

Chapter 3

Transmitter Design Methodology

3.1 Introduction

The previous chapter contained a discussion on the design and optimization of a laser supporting regrowth-free fabrication. Such a fabrication technique significantly simplifies the manufacture of semiconductor lasers, which in turn reduces the cost of optical transmitters to be employed in cost sensitive short reach networks. As mentioned in Chapter 1, the main thrust of this thesis is the realization of an optical transmitter for access networks (focussing on the NGPON2 standard), which requires low cost, easily manufacturable, and wavelength tunable transmitters.

In this chapter, first, the architecture and implementation methodology of NGPON2 are discussed to determine the critical requirements of the transmitter. Next, choice of modulation techniques used for implementing an optical transmitter for access networks are discussed, as it directly affects the implementation cost. As direct modulation is the most cost-efficient technique, a discussion on the challenges associated with the direct modulation scheme is provided. This also includes a section on optical injection locking (OIL). Finally, a transmitter architecture incorporating the OIL that can be fabricated using a regrowth-free fabrication process is investigated.

3.2 Implementation of NGPON2

The NGPON2 system (Figure 3.2.1) can typically be divided into five blocks: an optical line terminal (OLT), a wavelength multiplexer (WM), a fiber link, a branch node (BN), and an

optical network unit (ONU). As mentioned in section 1.5.6, the NGPON2 delivers a capacity of 40 Gb/s. In the downstream (DS), the transmitter at the OLT generates a set of four wavelengths with a channel spacing (CS) of 50 GHz, 100 GHz, or 200 GHz, and each channel modulated at a data rate of 10 Gb/s. The choice of the CS typically depends on the available optical spectrum. At the OLT, the modulated wavelengths are multiplexed, with the aid of a WM, to generate an aggregate data rate of 40 Gb/s. The multiplexed signal is then transmitted over a single optical fiber link. At the receiver side, the multiplexed optical wavelengths are filtered by a BN and distributed to the respective ONUs. In the upstream direction, data from multiple ONUs, transmitting on the same channel, is time multiplexed. A BN assigns a time slot to each ONU, which enables synchronous transmission from the ONU to the OLT in the upstream direction. The time multiplexed wavelengths transmitted in US direction are then filtered out by a wavelength filter present at OLT. The transceivers, both at the ONU and OLT, use tunable lasers for a point-to-point (P2P) connection. At the ONU, they are initially set to a specified wavelength (channel) to communicate with the OLT. However, in case of congestion, the wavelength of ONU can be tuned to other channel to avoid overloading. Before tuning to another channel, the ONU informs the OLT about changing the channel by sending a message to the OLT.

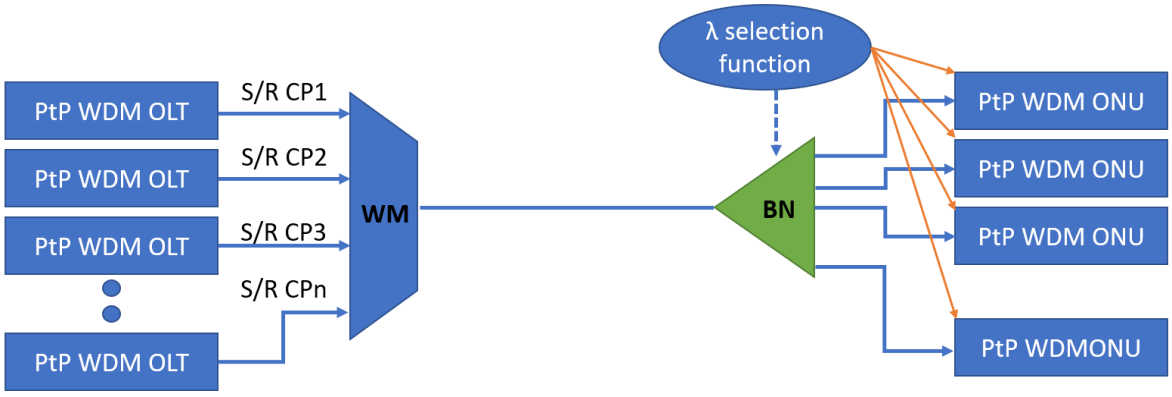

Figure 3.2.1. Block diagram describing the architecture of an NGPON2 system. Here: S/R is the sender/receiver, CP is the channel pair, WM is the wavelength multiplexer, and BN is the branch node.

As mentioned earlier, the wavelengths assigned for the uplink and downlink connections are distinct and form a channel pair (as described in chapter 1). This way, both

the wavelengths received and transmitted at the OLT and ONU do not interfere. Hence, to realize a transceiver suitable for the NGPON2, wavelength band and emission wavelength are aspects that need to be considered. However, this aspect is outside the scope of this work. Here, I focus on the design of a transmitter operating at NGPON2 specific wavelengths, its characterization, and the verification of system performance. Finally, all these aspects are compared to the NGPON2 specification.

3.3 Modulation techniques

In general, optical transmitters use a time varying electrical signal to modulate the intensity, phase or polarization of a light source. The most common form entails on-off modulation, which is used to convert high-speed binary signals to light pulses. Modulation can be broadly classified into two different types namely using external modulation and direct modulation.

3.3.1 External modulation

There are various types of external modulators, with the main types being electro-optic modulators (EOM) and electro-absorption modulators (EAM).

3.3.1.1 EOM

In electro-optic modulators, the refractive index of a material can be altered through an applied electric field (modulating signal) [173], [174], [175], [176], [177], [178], [179], a phenomenon called Pockels effect [179], [180]. This change in refractive index ($\Delta\, n_{eff}$) can cause a change in the phase ($\Delta\phi$) of the light wave passing through it. The Equation 3.3.1 shows relation between $\Delta\phi$ and Δn_{eff} where λ, L and $u(t)$ are wavelength, length of electrode (arm) and driving signal, respectively.

$$\Delta\phi = \frac{2\pi}{\lambda} \cdot \Delta n_{eff} \cdot \mathrm{L} \cdot u(t) \qquad 3.3.1$$

Hence the relation between phase modulated output ($E_{out}(t)$) and input ($E_{in}(t)$) signal in one arm can be expresses as Equation 3.3.2.

$$E_{out}(t) = E_{in}(t) \cdot e^{j\frac{u(t)}{V_\pi}\cdot \pi} \quad 3.3.2$$

The V_π is the driving voltage achieving π phase shift. The electro-optic material subjected to an electric field modulates the phase of the optical signal and acts as a phase modulator. Moreover, to realise an amplitude modulator, the light from a laser is split equally into two different paths (as shown in Figure 3.3.1l). An electric field can be applied to one or both paths to shift the phase of the waves so that they arrive at the far end, either in phase to give a pulse of light or out of phase to give no light. The transfer function (ration of output electric field to input electric fields) of the modulator can be written as Equation 3.3.3.

$$\frac{E_{out}(t)}{E_{in}(t)} = \frac{1}{2} \cdot \left(e^{j\phi_1(t)} + e^{j\phi_2(t)}\right) \quad 3.3.3$$

When the $\phi_1(t) = \phi_2(t)$ are in phase a pure phase modulation is achieved. In addition, if $\phi_1(t) = -\phi_2(t)$ then a pure intensity modulation is achieved. These devices are commonly referred to as Mach-Zehnder modulators (MZM) and the material most used to fabricate such a device is Lithium Niobate ($LiNbO_3$). The transfer function of MZM for intensity modulation is expressed as Equation 3.3.4.

$$\frac{E_{out}(t)}{E_{in}(t)} = cos\left(\frac{\pi \cdot u(t)}{2 \cdot V_\pi}\right) \quad 3.3.4$$

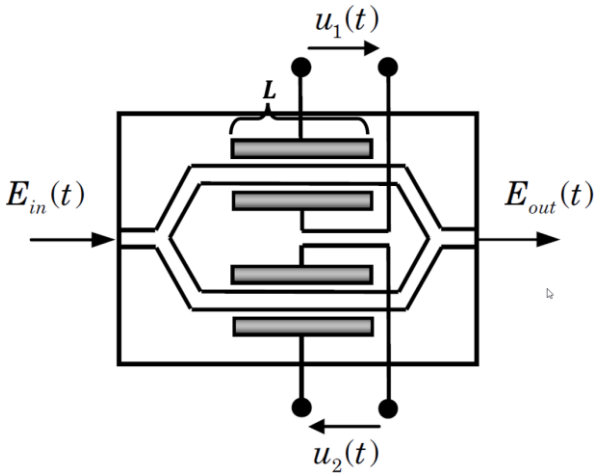

Figure 3.3.1. Schematic of the architecture of a Mach-Zehnder modulator [181].

The $LiNbO_3$ based external modulator poses outstanding properties such as good temperature stability, wide window of transparency and exhibits highly efficient linear Pockel effect [182]. However, the material used to implement EOMs does not allow for monolithic integration resulting in small form factors/packages [183].

3.3.1.2 EAM

Electro-absorption modulators (EAMs) unlike their counterparts (EOMs) can be easily integrated with semiconductor lasers they are to be used with. This stems from the fact that EAMs are made of similar materials to semiconductor lasers (as shown in Figure 3.3.2).

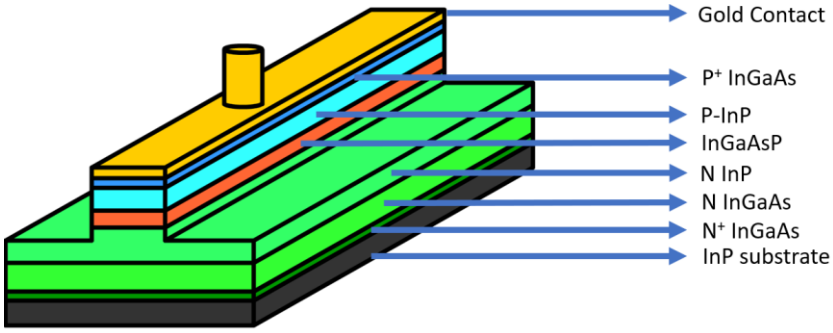

Figure 3.3.2. Schematic showing the architecture of an electro absorption modulator (EAM).

EAMs exploit the Franz-Keldysh effect [184], [185], [186], [187], [188], [189], [190], [191] and quantum-confined Stark effect [192], [193], i.e., the phenomenon of change in a energy gap, thus its optical attenuation, in response to applied electric field. With no voltage, EAMs are transparent and when a reverse voltage is applied, they exhibit an almost logarithmic attenuation/absorption of optical power (due to Stark effect) at the laser wavelength they are designed for. Hence, to represent a logic high (bit '1'), the EAM needs to allow light through, and so no voltage (or a low reverse bias) is applied thereby making it transparent to the laser light. The logic '0' is generated by subjecting EAM to an electric field that absorbs all the photons and passes no light to the output. The transfer function of EAM can be expressed as Equation 3.3.5 [194].

$$P_{out} = P_{in} \cdot \Gamma \cdot e^{(-\alpha_i \cdot L)} \qquad 3.3.5$$

Where P_{out}, P_{in}, Γ, α_i, and L are output optical power, input optical power, confinement factor, absorption coefficient, and length of device (or electrode), respectively.

The benefits of using EAM as an external modulator are high modulation bandwidth, low power consumption, optical bandwidth and switching speed. Nevertheless, the development of EAM requires sophisticated fabrication process and also it shows limited thermal stability [195], [196], [197].

3.3.2 Direct modulation

Semiconductor lasers portray a unique property, unlike other solid state and liquid lasers, where the modulating signal can be "added" to the bias current to directly control the optical output of the semiconductor laser [198]. As a laser diode is a current-driven device, a time-varying current signal can be directly applied to the laser to convert it to a time-varying optical signal, as shown in Figure 3.3.3(a). The realisation of direct modulation (electrical to optical conversion), as illustrated in Figure 3.3.3(b), is typically achieved by driving (modulating) the laser with a high frequency signal in conjunction with a direct-current (DC). The maximum frequency of modulating electrical signal that can be imposed on to a laser depends on the 3-dB limit of the frequency response of the laser [199], [200], [201].

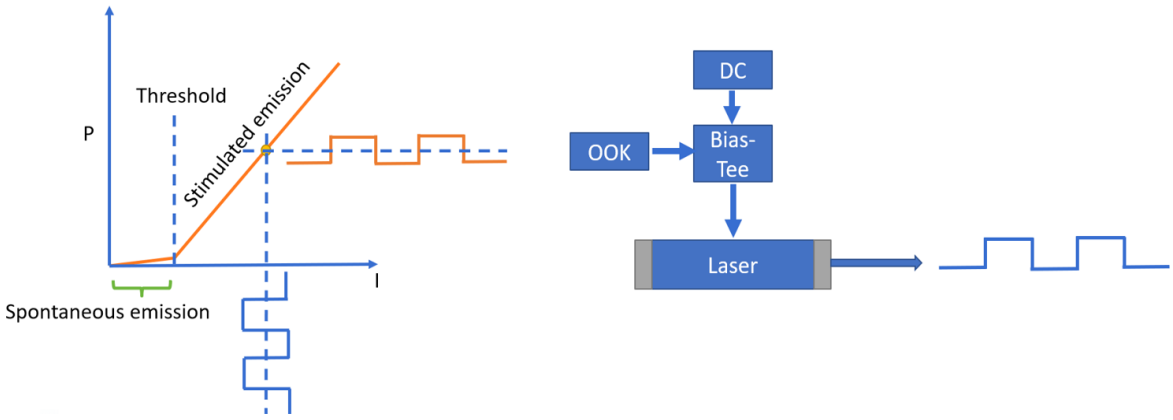

(a) (b)

Figure 3.3.3. Schematic to show the (a) principle of direct modulation of a semiconductor laser and (b) setup of a directly modulated laser.

The advantage of the direct modulation is the simplicity and the cost efficiency of implementation, rendering is attractive for employment especially in the cost sensitive sectors of an optical communications network.

3.4 Issues with direct modulation technique

There are some challenges associated with the direct modulation that degrade the quality of the modulated optical signal. Some of these issues that severely affect the performance of a directly modulated laser (DML), when employed as a transmitter, are listed below.

3.4.1 Modulation bandwidth limitation

It is much easier to obtain a high speed modulated optical signal using the external modulation in comparison to direct modulation of laser. As demonstrated in [202], data rates of 100 Gb/s are easily achievable using an external modulator. However, the modulation bandwidth of a DML is limited. Commercially available semiconductor lasers typically exhibit bandwidths of about 10-15 GHz. However, in research work, studies have shown modulation bandwidths up to 18 GHz [30] [33] [34]. The modulation response of semiconductor laser mainly depends on the coupling between the atomic population and photon density in the gain medium [152]. The resonant frequency (ω_r) is proportional to number of photons (N_p), compressed differential gain (a), and group velocity (v_g). ω_r is expressed in Equation 3.4.1.

$$\omega_r^2 \approx \frac{v_g a N_P}{\tau_p} \tag{3.4.1}$$

The compressed gain is defined as

$$a = \frac{a_0}{1 + \epsilon N_P} \tag{3.4.2}$$

ϵ is gain compression coefficient. Combining Equation 3.4.1 and 3.4.2 we get

$$\omega_r^2 = \frac{\nu_g a_0 N_P}{\tau_P(1 + \varepsilon N_P)} \quad 3.4.3$$

When N_p is equal to $\frac{1}{\varepsilon}$, the ω_r^2 reaches the maximum value and defined by Equation 3.4.4

$$\omega_r^2 = \frac{\nu_g a_0}{\tau_P} \times \frac{1}{\varepsilon} \quad 3.4.4$$

This means that the resonant frequency ω_r is independent of N_p and cannot be enhanced by increasing number of photons in the cavity. The modulation response can be increased by reducing τ_P and ε, and increasing a_0 [36].

3.4.2 Frequency chirp

Chirp is a negative effect that is generated when the laser is subjected to direct modulation. The types of frequency chirp originated due to direct modulation are adiabatic and transient chirp. The adiabatic chirp is defined as change in laser frequency due to instantaneous power of the laser. The transient chirp is change in lasing frequency due to modulation of photon number [207]. When a time varying signal is applied to the laser, it modulates the carrier and photon density in the cavity. This varies the effective refractive index and consequently, optical path length. The variation in optical path length shifts the resonant wavelength back and forth. This causes a broadening of the emission optical spectrum, which in turn worsens the chromatic dispersion effects, when the modulated signal is propagated through standard single mode fiber (SSMF) [152].

3.4.3 Relative intensity noise

The relative intensity noise (RIN) is the ratio of variation in the laser power to its average power. This is mainly occurring because of random changes in carrier and photon density in the laser cavity even if the laser is not modulated. The fluctuation in carrier and photon

density also leads to change in effective index of laser and subsequently variation in emission wavelength. However, this variation in emission wavelength is much smaller than chirp [152].

3.4.4 Extinction ratio

The extinction ratio (ER) achieved by DML is significantly lower than externally modulated lasers because of low modulation bandwidth [30] [33] [34] and frequency chirp introduced in the optical signal [208], [209], [210], [211], [212], [213], [214]. The $LiNbO_3$ MZM [215], [216], [217], [218], [219], [220], [221], [222] and InP based MZM [223], [224], [225], [226], [227], [228] exhibits high modulation bandwidth. Hence, MZM based external modulation can easily achieve an ER of about 30 dB [229], whereas with direct modulation, it is very difficult to achieve an ER of 8 dB [230]. It is also important to note that the chirp and ER are in some ways directly proportional to each other (if ER is increased then chirp also increases). The increase in bias current reduces the chirp and simultaneously increase in average power, which results in a reduced ER.

3.5 Design options for an NGPON2 transmitter.

In the previous section the types of modulation techniques and their pros and con are discussed. Both, external and direct modulation technique are used to implement transmitter for NGPON2. Typically, external modulators show better performance when it comes to parameters such as extinction ratio and frequency chirp. However, they introduce a substantial insertion loss and increase the cost of the transmitter. Hence, the direct modulation technique can be used as an alternative solution to realise a transmitter for an NGPON2 system. Several implementations of a transmitters for NGPON2 using a DML have been demonstrated [231], [232], [233], [234], [235]. Here, we focused on direct modulation based photonic integrated transmitter. An ODN compatible TWDM-PON is demonstrated in [236] using a thermally tuned DML. All DMLs used in this architecture are thermally tuned i.e., the wavelength of each DML can be set to the desired wavelength by changing the operating temperature. The four DMLs, each carrying a data rate of 10 Gb/s, are operated at

wavelength spacing of 100 GHz and are multiplexed together to achieve an aggregate data rate of 40 Gb/s. The transmission reach achieved is 50 km, 75 km, and 100 km at a split ratio of 1:1024, 1:256, and 1:64, respectively. [32] and [33] demonstrates a 40 and 100 Gb/s symmetric PON using a thermally tuned DML at both the OLT and ONU. In addition, reflective semiconductor optical amplifiers (RSOA) are used to pre-amplify the upstream and downstream signal. In this scheme, an external wavelength filter is used to filter the desired wavelength and mitigate the effects of chirp. A split ratio of 1:256 using passive splitter is achieved after 25 km fiber transmission. The inline amplifier for the upstream and downstream transmission improves the power budget, but simultaneously increases the implementation cost. As can be seen from the above-mentioned articles, most of the work carried out thus far on the TWDM-PON scheme, has been designed and demonstrated using discrete components.

From the integrated transmitter point of view, the most relevant reports involve devices based on the external modulation. An externally modulated OLT transmitter is realised by integrating the distributed Bragg reflector (DBR) laser, Mach-Zehnder modulator (MZM), and arrayed waveguide grating (AWG) [239]. In this work, the transmitter consists of two DBR lasers that are externally modulated and multiplexed using an AWG. As mentioned earlier, even though all the components can be integrated, the hybrid integration (interconnection of active and passive photonic components) is challenging. In addition, this process becomes even more complex and unreliable when there are multiple fabrication steps required [240]. The PICs integrated with passive and active materials are highly sensitive to temperature and thermal changes affect the emission wavelength of the device [152]. To maintain the stability of a wavelength, a thermoelectric cooler (TEC) is used to restrict the variation in operating temperature.

The transmitters mentioned in the paragraph above are all based on the external modulation. However, as mentioned before, direct modulation-based transmitters are promising in terms of easy implementation and cost effectiveness. Hence, in this section, a brief review of the most relevant work on directly modulated integrated transmitters is included. The authors in [203], demonstrate the design and fabrication of a monolithically integrated four channel, high-speed thermally tunable DML transmitter. In this design, the

output of four directly modulated and thermally tuned DFB lasers are multiplexed through optically integrated MMI couplers. This chip shows an aggregate transmission capacity of 240 Gb/s. The drawback of this design is the complexity of fabrication. The fabrication of the PIC requires hybrid integration [241] of DFBs, passive waveguides and the MMI.

3.6 Overcoming the challenges associated with direct modulation

3.6.1 Optical injection locking

Optical injection locking (OIL) [234], [242], [243], [244], [245], [246], [247], [248], [249], [250] is a technique that can be used to synchronize the phase of two resonant optical cavities. Typically, it entails injecting light from one laser (master/leader laser) being run in continuous wave (CW) mode into another laser (slave/follower laser) which is going to be modulated. Figure 3.6.1 show arrangements of master-slave architecture implementing OIL using discrete optical components.

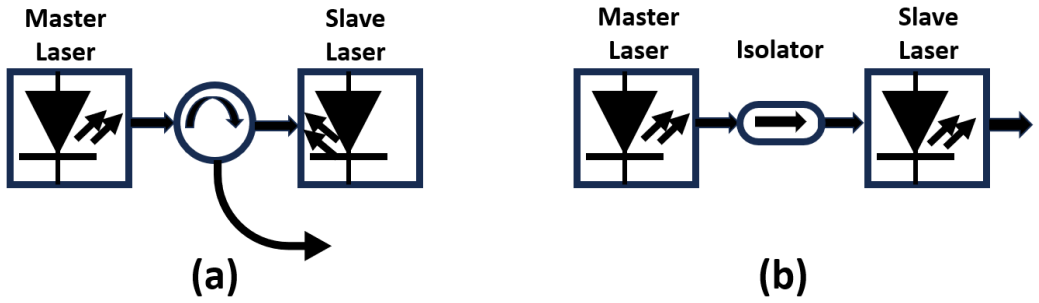

Figure 3.6.1. Schematic diagram of (a) reflection and (b) transmission type optical injection locking system.

The optical injection from master to slave laser is provided via an optical circulator or inline optical isolator. The optical circulator or isolator prevents back-reflection to master laser. The phase and frequency of slave laser is forced to synchronized with master laser when the emission wavelength of master is close to that of the slave laser. Also, the slave laser follows any slow drift ($\Delta\omega$) in master wavelength. For the stable injection looking, the range of $\Delta\omega$ must be in the rage defined in Equation 3.3.1.

$$-\kappa\sqrt{1+\alpha^2}\cdot\sqrt{\frac{P_{inj}}{P_o}} < \Delta\omega < \kappa\cdot\sqrt{\frac{P_{inj}}{P_o}} \qquad 3.6.1$$

Where κ, α, P_{inj}, P_o, are coupling coefficient, linewidth enhancement factor, and injection intensity and the intensity of free running laser respectively.

The OIL has been demonstrated with discrete components [234], [242], [243], [244], [245], [246], [247], [248], [249], [250] as well as implemented by using photonic integration method [251], [252], [253], [254]. The stable injection locking is dependent on the polarization of injected light. Since the locking range is proportional to injected optical power [255], variation in polarization may reduce the injected optical power and cause unlocking of slave laser. The change in polarization also introduce nonlinear dynamics in the cavity of laser [256]. This issue can be resolved by photonic integration [257], [258], where the polarization of light is maintained by an integrated optical waveguide. The challenge in the realisation of a photonic integrated master-slave architecture is the thermal cross-talk and poor optical isolation between slave and master laser [259], [260], [261]. The effect of OIL on the SL are described below.

3.6.1.1 Bandwidth enhancement

The modulation response of the laser is directly proportional to the bias current [262] and relation between the cut-off frequency (f_{3dB}) and bias current (I) can be approximated in Equation 3.6.2. As a result, increasing the bias current enhances the modulation bandwidth of a laser. However, a laser operated at a high bias current may suffer facet damage.

$$f_{3dB} = \left(\frac{3}{4\pi^2 q}\frac{\Gamma v_g \sigma_g}{V}(I - I_{th})\right) \qquad 3.6.2$$

where q, Γ, v_g, σ_g, V, I, and I_{th} are electronic charge, confinement factor, group velocity, differential gain, volume of active region, bias current, and threshold current, respectively.

In addition, the modulation bandwidth can be increased if laser cavity length is reduced, which shortens the photon lifetime. However, a short cavity laser results in a reduced output

power. An alternative solution entails the employment of the OIL technique. It has been shown that OIL enhances the bandwidth without the need to increase the bias current or shortening the cavity of laser [263], [264], [265]. The increase in the modulation bandwidth can be attributed to the reduction in the number of carries in the active region by ΔN ($\Delta N = (N - N_0)$, N – Number of carriers in active region, N_0 – threshold number of carriers) [264], [266]. This in turn enhances the resonant frequency of laser from ω_0 to $\omega_0 + \frac{\alpha}{2} g\Delta N$, where α is linewidth enhancement factor and g is net modal gain. The range of α is between 2 and 3 [267] and it cannot be changed or manipulated when designing the laser hence, the increment in resonant frequency can be obtained by increasing g and ΔN. The gain of the material can be improved by increasing number of quantum wells in active region [268] and intensity of optical injection [74].

3.6.1.2 Chirp reduction

As mentioned earlier, a DML suffers from a large amount of frequency chirp, caused mainly by the rapid change in refractive index of the laser, which in turn alters the emission wavelength [269], [270], [271], [272], [273]. A laser under high level of optical injection shows a significant reduction in frequency chirp as described in [274], [275]. The reason of chirp reduction is the master laser locks the slave laser's frequency under stable injection locking condition [276], [277]. Moreover, the injection of light increases the number of photons in slave laser cavity thereby act as an optical resonator as well as an optical amplifier. The total chirp in the signal is contributed by transient and adiabatic chirp (as defined in Equation 3.6.3). The α, $P(t)$, and κ are linewidth enhancement factor, instantaneous power of the laser, and coupling coefficient, respectively. The transient chirp dominates while laser is directly modulated with high-speed electrical signal. The transient chip is inversely proportional to instantaneous power $P(t)$ (Equation 3.6.4) hence increment in number of photons in the cavity due to optical injection reduces the frequency chirp.

$$\Delta\nu = \frac{\alpha}{4\pi}\left(\frac{1}{P(t)}\frac{dP}{dt} + \kappa P(t)\right) \qquad 3.6.3$$

$$\Delta\nu \propto \frac{1}{P(t)} \qquad 3.6.4$$

3.6.1.3 Reduction in relative intensity noise

As mentioned earlier, the RIN arises from a random transition of carriers in the active region, which leads to a fluctuation of photons. This leads to a change in the output power and a degradation in the signal to noise ratio of an output signal [278]. This issue can be resolved by using OIL, which significantly reduces the RIN in the output signal [279], [280] by suppressing the random phase change of the photons (spontaneous emission) and a fluctuation in the carrier density [281].

3.7 Realization of an OIL based regrowth-free PIC

As mentioned above the OIL can be implemented with discrete components and using photonic integration method. Also, there are pros and cons of photonic integration of OIL techniques (as stated above). The manufacturing process of a photonic integrated circuit (PIC) is analogous to the manufacturing of an electronic integrated circuit. In a standardised PIC fabrication process, the integration of photonic components follows sequential regrowth and etching of the material. The process becomes more sophisticated in hybrid integration [241], [282], [283], [284]. Conversely, in regrowth-free manufacturing of PICs, all the required layers are first grown on the InP substrate, which then undergoes multiple etching processes to replicate the mask layout with the defined depth at necessary places. The regrowth-free manufacturing process offers a fast and robust method to manufacture PICs. This improves the yield of the manufacturing process.

The master-slave arrangement can be integrated on the same InP substrate to realize OIL. As described in chapter 2, the device consisting of a master and slave laser, as well as the connecting optical waveguide can be built using regrowth-free fabrication. This thesis focusses on the use of this technique for the realisation of all the transmitters.

3.7.1 Architecture of OIL based DML PIC transmitter

The architecture of the OIL based transmitter (as shown in Figure 3.7.1) is built by integrating a high speed DML with a master laser (CW operation) and connecting them via an optical waveguide and isolator. The rib [285] and ridge waveguides [286] are the commonly used structures to transport light in PICs that shows attenuation of 0.1 dB/cm and 0.81 dB/cm, respectively. The optical isolator prevents unwanted back reflection to laser cavity.

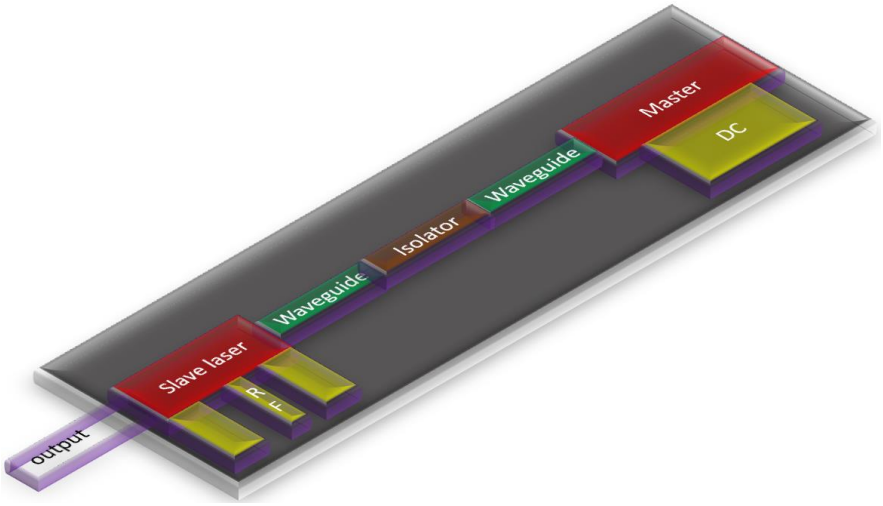

Figure 3.7.1 Architecture of OIL based PIC transmitter.

The photonic integrated isolator can be implemented by fabricating magneto-optic waveguide, Mach–Zehnder structure, and micro ring resonator. While the integration of lasers and optical waveguides can be realised through the regrowth fee fabrication, integration of optical isolator requires sophisticated fabrication steps. Hence, in regrowth-free fabrication the OIL transmitter is built without isolator and allowed mutual injection locking between master and slave lasers [261], [287].

3.7.2 Fabrication of OIL based DML PIC transmitter

Figure 3.7.2 illustrates the main manufacturing steps involved in a regrowth-free fabrication process of a multi-section PIC. The first step entails a prefabricated wafer undergoing an

initial stage of etching that forms a ridge structure on the p-layer. The resulting structure is a single section PIC, in which the optical mode is coupled throughout the ridge waveguide.

At the second stage of fabrication, a deep isolation slot is etched that bisects the ridge waveguide and converts the single section to a multi-section PIC. Subsequently, the individual contact pads for each section are formed by gold deposition. The standalone contact pads ensure an independent operation of each section. This method of fabrication can be used to implement master-slave architecture on the same substrate.

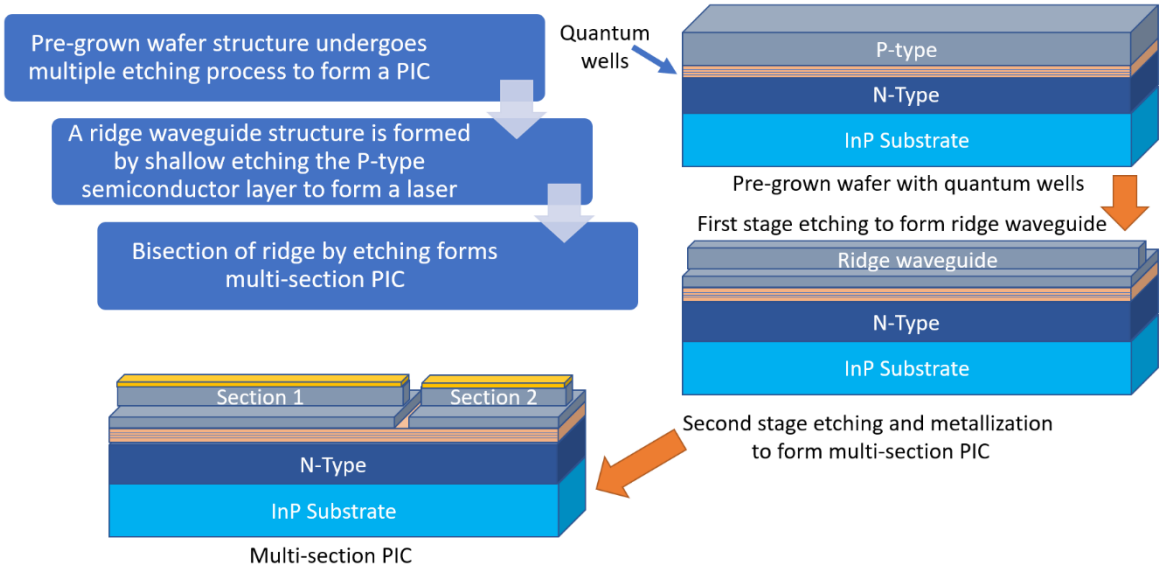

Figure 3.7.2. Flow chart showing the steps in a regrowth-free fabrication of a multi-section PIC.

As it is well known, a laser is a cavity formed by inserting a gain medium between two reflectors. Chapter 2 contains a description of how a laser could be formed by etching the slots in the ridge waveguide at one end and applying HR coating at the other end. However, it is important to note that a laser can be formed by etching slots on the ridge and applying AR coating at both ends. Hence, to implement a laser, a gain medium is placed between two reflectors as in Figure 3.7.3. The reflectors are designed by etching multiple grating slots on the ridge waveguide at a period defined by the Bragg condition. The variation in etch depth changes the effective refractive index and thereby acts as a reflector. The effective refractive index can be further varied by injecting current (carriers) into the reflector sections, thereby achieving wavelength tunability. Equation 3.7.2 shows that the change in

the peak wavelength is proportional to change in effective refractive index with respect to change in number of carriers [288]. It is apparent that an increase in bias current changes the carrier density and subsequently the refractive index of the reflector section. The change in refractive index of the reflector section alters the effective refractive index of the laser.

$$\Delta\lambda = \frac{dn}{dN}\frac{(N-N_0)}{n_g}\,\lambda \qquad 3.7.1$$

$$\Delta\lambda \propto \frac{dn}{dN} \qquad 3.7.2$$

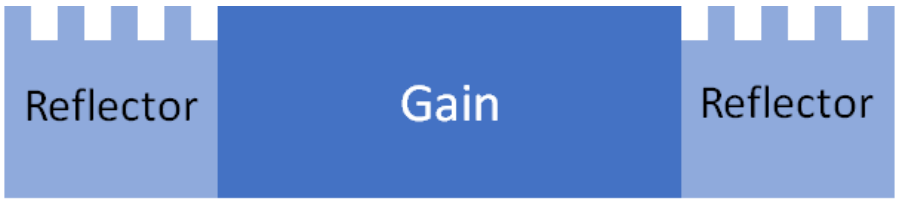

Figure 3.7.3. Structure of slotted grating-based laser.

The drawback of using a grating-based reflector is a high transmission loss in the form of scattering of the electromagnetic wave at the edge of the reflectors. This loss can therefore prevent the laser from attaining a threshold condition and lasing at the Bragg wavelength. Designing the reflectors in an active material overcomes this problem by equalizing the gain and loss. The latter is achieved by DC biasing the reflectors. Overall, the implemented laser is essentially a three-section device with three independent bias controls. Finally, in order to realise OIL, a master-slave configuration can be implemented by cascading two lasers (with one overlapping/shared section) as shown in Figure 3.7.4.

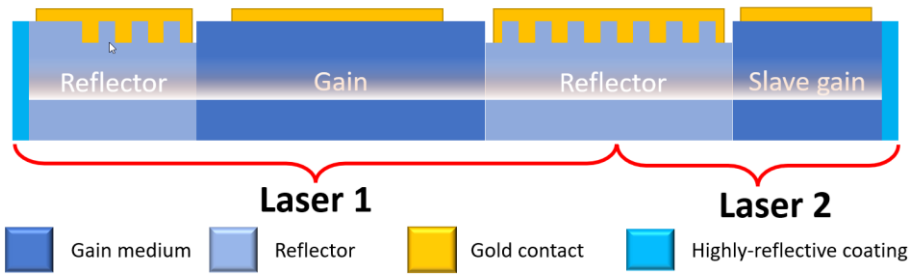

Figure 3.7.4. Architecture of a monolithically integrated two-section PIC.

Such a regrowth-free four-section device was fabricated and reported in [289] and demonstrated an enhancement in the modulation bandwidth and a reduction in chirp, which enabled 10 Gb/s data transmission over 37 km. The device was fabricated on an InP substrate containing 5-AlGaInAs quantum wells in the active region. The device had a HR coating at the back facet and an AR coating at the front facet. Wavelength tunability was achieved by changing the bias of both reflectors and the gain section. Even though this device availed of low manufacturing cost, it suffered from the lack of independent control of the laser sections. Essentially, this translates to a difficulty in achieving OIL as the common middle reflector between the master and slave sections affects the emission wavelength of both lasers. My contribution, as discussed in next chapter, involves achieving independent control of emission wavelengths of master and slave laser as well as introducing a mechanism of controlling the level of optical injection without affecting operating condition of slave laser.

3.8 Conclusions

In this chapter, the standards of NGPON2 architecture are discussed and the requirements of a transmitter that could be used to satisfy these standards examined. The transmitter specifically built for NGPON2 architecture must satisfy requirements such as wavelength tunability, 10 Gb/s data rate generation, low spectral excursion, and burst mode transmission. Many transmitters have been implemented using either external or direct modulation. The direct modulation is simple and cost efficient because it requires minimum electronics to build a transmitter. However, the impairments of direct modulation are: introduction of frequency chirp in optical signal; high relative intensity noise; and limited modulation bandwidth. These drawbacks can be mitigated by using OIL. The photonically integrated device implementing OIL is particularly attractive as it reduces the manufacturing cost and can be minimized further by using regrowth-free fabrication. However, some of the transmitters implementing OIL suffered the lack of accurate control of the optical injection due to shared sections causing leakage of current that results change in characteristics of the device. In the next chapter the design of the multi-section PIC transmitter implemented using regrowth- free fabrication that overcomes the issues involved in 4-section PIC.

Chapter 4

Six-section photonic integrated transmitter

4.1 Introduction

The previous chapter discussed the design and implementation methodology of a transmitter that is to be employed in an access network scenario (specifically suited to meet the NGPON2 standard). As mentioned, the transmitter can be implemented using both external and direct modulation schemes. However, the direct modulation scheme simplifies the transmitter's architecture and significantly reduces building costs, thereby making it very attractive to the cost sensitive access networks. As discussed in detail, the direct modulation scheme suffers from drawbacks such as low modulation bandwidth (MBW) and frequency chirp, both of which can be overcome by employing the OIL technique. The previous chapter also highlighted how OIL, using two lasers in a master-slave configuration, can be implemented on a single chip. The photonic integration of the master-slave arrangement using a regrowth-free fabrication technique further reduces the cost and fabrication time.

This chapter discusses the design and fabrication of a six-section directly modulated transmitter, which allows independent wavelength control of each section (unlike the device in [290]). The chapter is organized in such a way that the architecture of the fabricated transmitter is discussed first. Subsequently, a complete characterization of the slave laser, under free running and injection locking conditions, is carried out. Static characterization results include the measurement of L-I characteristic, linewidth, wavelength tunability, and RIN. Dynamic tests entail measuring the modulation as well as the frequency chirp characterization of the PIC directly modulated with a 2.5 Gb/s data signal. Finally, the

transmission tests are carried out in which the device is directly modulated with a 10 Gb/s pseudo random bit sequence (PRBS) data and the signal transmitted over various lengths of standard single mode fiber (SSMF). The performance of the transmitter is then verified via bit error ratio measurements under an injection locked and free running scenarios.

4.2 Architecture of the six-section transmitter

The 3-dimetional schematic in Figure 4.2.1 depicts the architecture of the 6-section transmitter. The device is manufactured using a prefabricated standard 1550 nm wafer, containing a five quantum well active layer sandwiched by a p-doped AlGaInAs layer (at the top) and an n-type AlGaInAs layer (at the bottom). In the first step of the fabrication, a 2 µm wide optical waveguide is defined by pattering the ridge structure on the top layer and removing the unwanted material through an etching process. The ridge waveguide confines the fundamental optical mode into the active region in the horizontal direction. In the second step, the master and slave lasers are created.

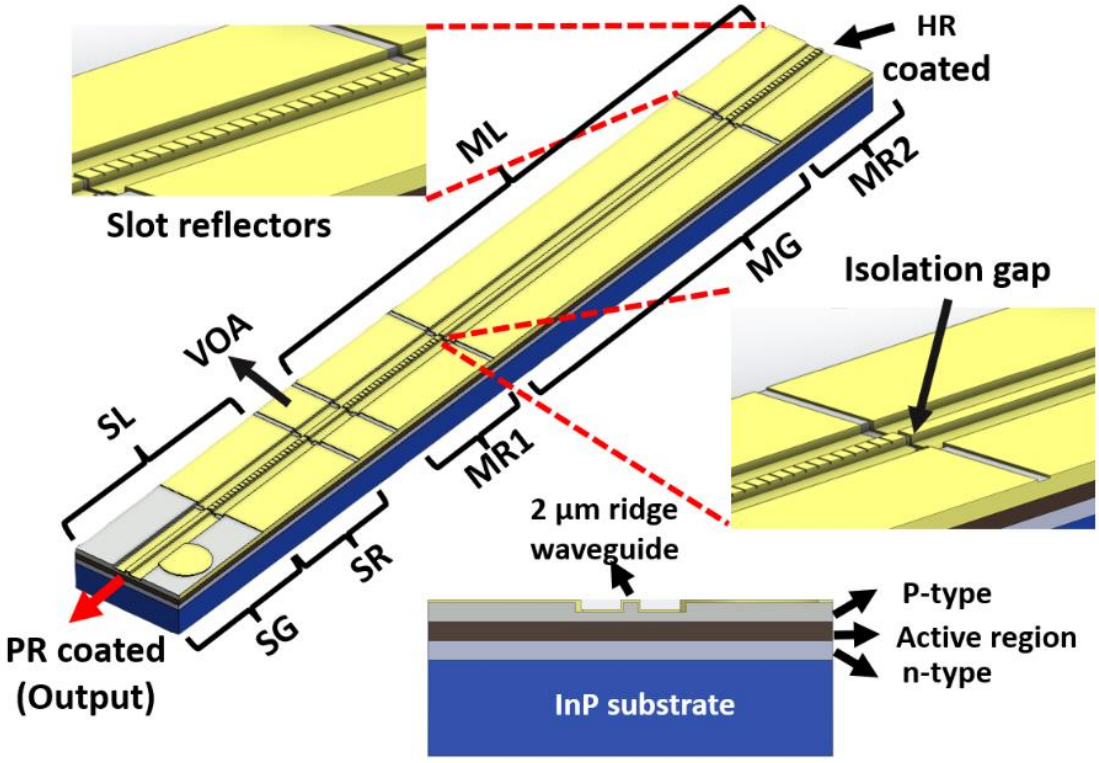

Figure 4.2.1. 3-D schematic of the architecture of the six-section PIC.

The master laser (ML) is made up of three sections: a long gain section (MG) between two grating-reflector sections named as master reflector 1 and 2 (MR1 and MR2). The design parameters for MR1 and MR2 are similar, consisting of slot gratings fabricated by etching three groups of eight-slots (total 24 slots) of period order 37, 42, 47 on the ridge. The slot grating of three distinct periods improves the SMSR by supressing the sidemodes [291]. One difference between MR1 and MR2 are the slot depth and width, which are designed to be 1.35 µm and 1.15 µm respectively. The slave laser (SL) is composed of two sections: the slave gain (SG) and slave reflector (SR). The rear section of the SL, i.e., the SR, is identical to MR1 and consisting of 3-groups of slots. Each group has 8-slots and a period of 37, 42, 47. All slot depths and width are equal to 1.35 µm and 1.15 µm, respectively. The latter value is chosen to ease the fabrication process using the photolithographic technique. In addition, as highlighted in the chapter 2, this slot width delivers the lowest threshold current. To implement a second reflector of the SL, the front facet of the PIC is coated to be partially reflective (PR), providing 33 % reflectivity. Another important feature of note in this six-section PIC is a short gain section that separates the ML and SL. This section is used as a variable optical attenuator (VOA), which provides accurate control of the optical power injected into the slave laser. In addition, the physical separation provided by it allows the independent operation of the ML and SL. To further decouple the operation of each of the lasing sections, a slot with 1.35 µm depth and 1.0 µm width is defined between them. Finally, a gap of 10 µm is maintained between the contact pads of adjacent sections, which provides an electrical isolation of approximately 10 kΩ. The image of a fabricated six-section PIC is shown in Figure 4.2.2.

Figure 4.2.2. Microscopic image of the fabricated six-section PIC.

4.3 Static characterization

To carry out the testing of the PIC, a subcarrier using a fiber reinforced 4 (FR4) printed circuit board (PCB) with a radio frequency (RF) transmission line is designed and fabricated. The bare chip is placed and glued on to the PCB, after which electrical contact pads (direct current (DC) and RF) are wirebonded to the respective electrical contacts, as shown in Figure 4.3.1. Thereafter, a 34 Ω resistor is placed in series with the SG section (with a dynamic resistance of 16 Ω) in order to achieve an equivalent resistance of 50 Ω. Finally, the SG section and the matching resistance is wirebonded to the 50 Ω RF track of the subcarrier PCB.

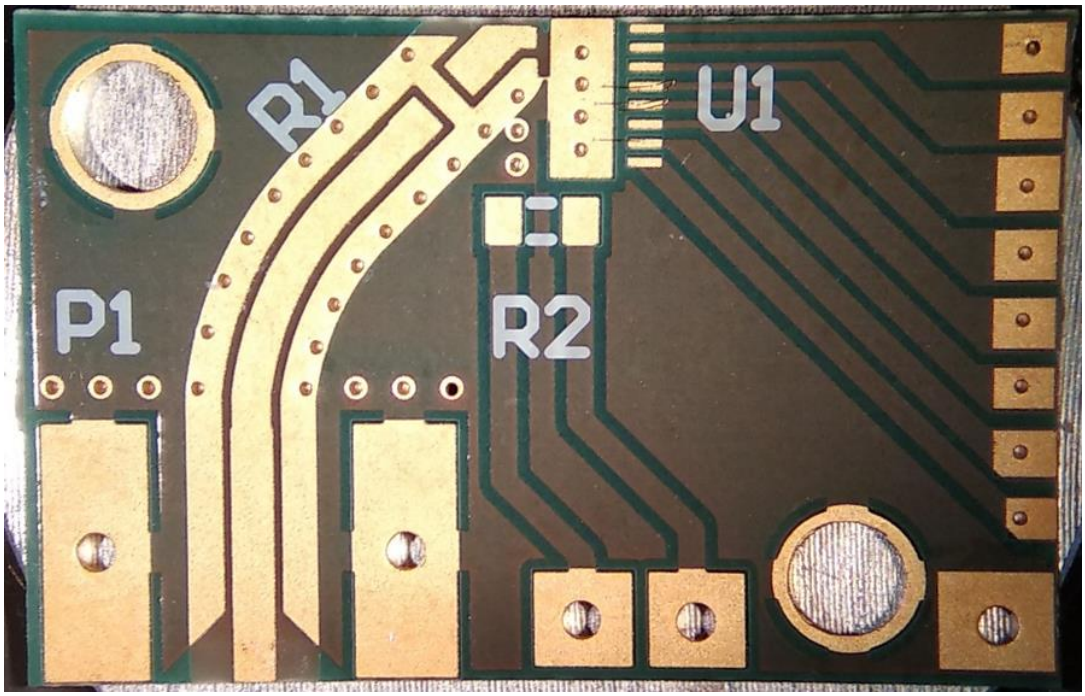

Figure 4.3.1. Image of subcarrier PCB.

In order to maintain the PIC at a fixed temperature of 20 °C [292], a thermoelectric cooler (TEC) is placed under the PCB together with a temperature sensor (thermistor). The TEC is driven with a proportional-integral-derivative (PID) temperature controller. The DC pads of the PCB are connected directly to low noise DC current sources, while the pad on the SG section is connected to a wideband bias tee (BT) with a bandwidth of 10 GHz. The BT enables applying a DC in conjunction with a modulation signal. The light emitted by the

PIC is coupled to the fibre with the aid of a conical lensed fibre, mounted on an auto-aligner. The output of the lensed fibre is split using a 90:10 coupler, with the 10% used as feedback to the auto-aligner controller and 90% used for the static and dynamic characterization, and for the transmission experiment. The results from the testing are presented in the sub-sections below.

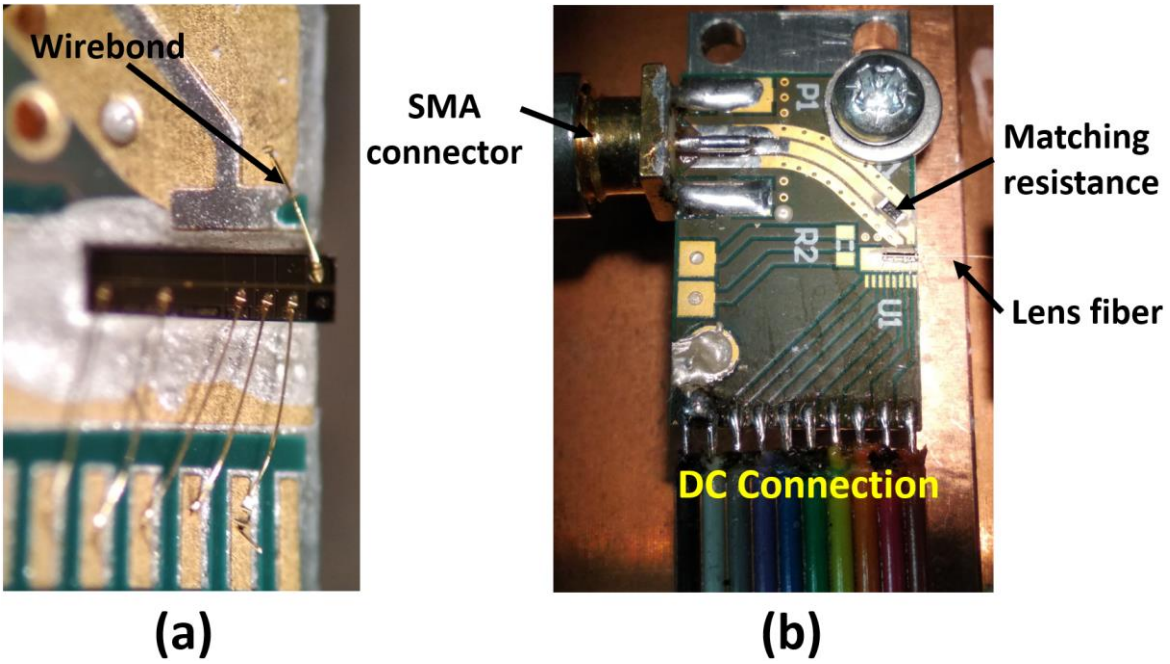

Figure 4.3.2. Images of (a) wirebonded PIC and (b) mounted PIC on a subcarrier and coupled to a lens-ended fiber.

4.3.1 L-I characteristic

This section outlines the results from the voltage, current and power measurements taken on the slave laser part of the PIC, which enables the determination of the dynamic resistance and the threshold current. The dynamic resistance is calculated by measuring the slope $(\frac{\Delta V}{\Delta I})$ of the V-I plot above the threshold current. The calculated value of the dynamic resistance is ~16 Ω. As mentioned earlier, the SL comprises two sections: SG and SR. Initially, the chip is kept at room temperature and equal currents, swept from 0 to 60 mA, are supplied to both the SG and SR sections. Then, the output power is measured using an optical power meter. The results are shown in Figure 4.3.3(a). The plot reveals that the threshold current of the

laser is ~22 mA and that there is a steady increase in the output power up to a current of 40 mA. However, at a bias current above 42 mA, the output power reduces. The main reason for this is a mode hop to another longitudinal mode [293]. The longitudinal mode and gain peak wavelengths rely on the temperature of active region, which rises with increase in injection current. The heating of active region alters the gain peak wavelength and longitudinal wavelength mode. However, the gain peak wavelength changes at a faster rate comparing to longitudinal mode wavelength and results mode hopping.

To further investigate the behaviour of the SL, its L−I is measured for different values of currents applied to SG and SR sections. The current in the SG section is swept from 0 to 80 mA at resolution of 4 mA, while the current in the SR section is swept from 0 to 60 mA in steps of 4 mA. The resulting three-dimensional L−I dependency, plotted in Figure 4.3.3(b), clearly shows that the SL exhibits a mode hop from 1544 nm to 1546 nm, for SR currents between 18 mA and 40 mA. The plot also shows that the SL emits a maximum power of 0.5 mW (for SG bias at 42 mA and SR at 56 mA) and exhibits a linear region suitable for direct modulation, when the SR section is biased at 56 mA and the SG section at 40 mA. Beyond the SG bias of 42 mA, the output power drops, because of generation of another mode and sharing power, and misalignment of lens fiber.

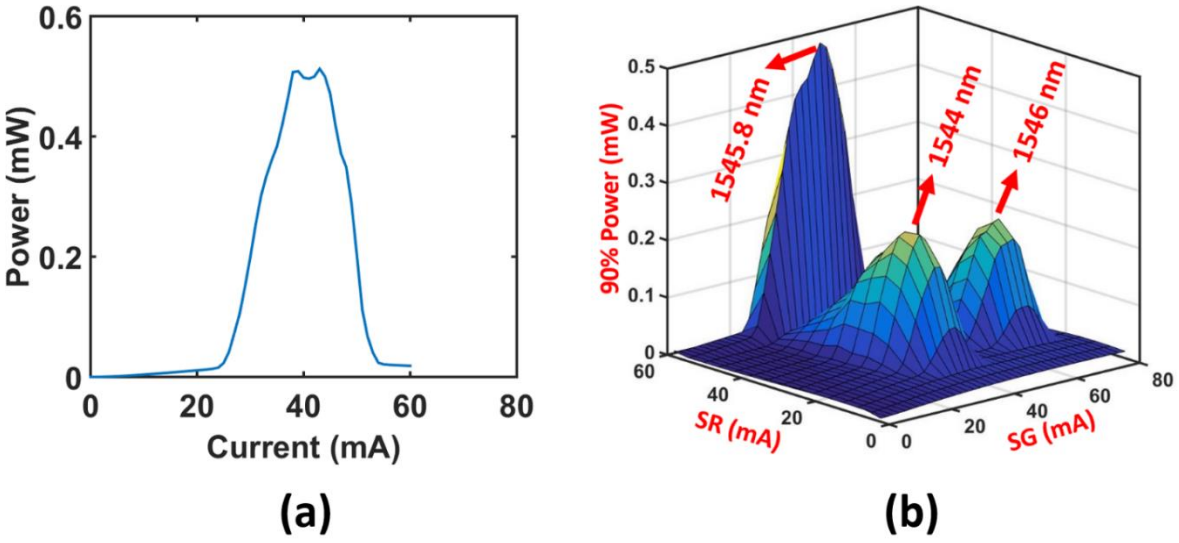

Figure 4.3.3. L-I characteristic of the slave laser when the slave gain and reflector sections are kept at (a) equal current and (b) different currents.

4.3.2 Wavelength and SMSR map of SL

The subsequent characterization step entailed obtaining heat maps of the wavelength and the side mode suppression ratio (SMSR) of the SL as a function of the SR and SG currents. This was achieved by sweeping the SG current from 0 mA to 80 mA and SR current from 10 mA to 80 mA at a resolution of 2 mA and measuring the SMSR and peak wavelength using an optical spectrum analyzer (OSA). Figure 4.3.4(a) shows a plot of the wavelength as a heat map. It reveals that the SL is tunable from 1540 nm to 1548 nm, and that the SL wavelength increases for higher SR and SG currents. Furthermore, the abrupt change in wavelength (dotted line) shows the mode hop.

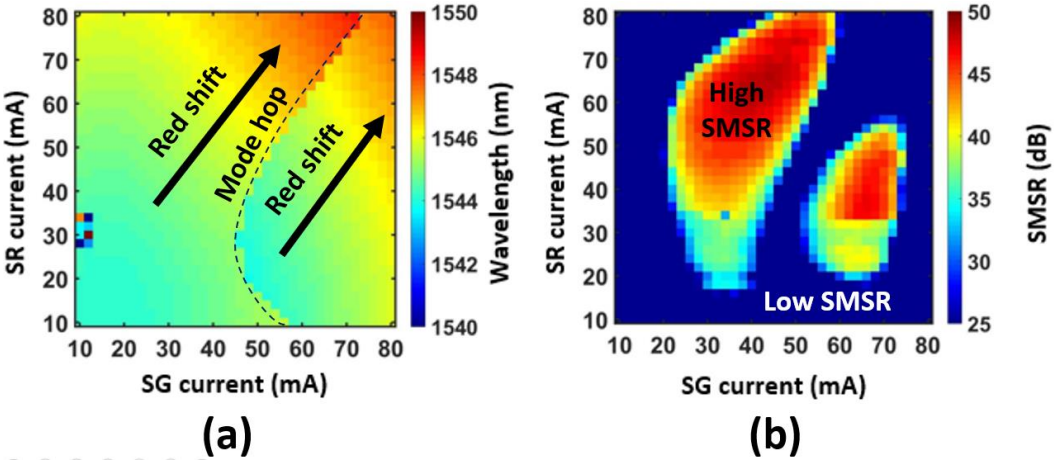

Figure 4.3.4. Heat maps of (a) wavelength and (b) SMSR of slave laser.

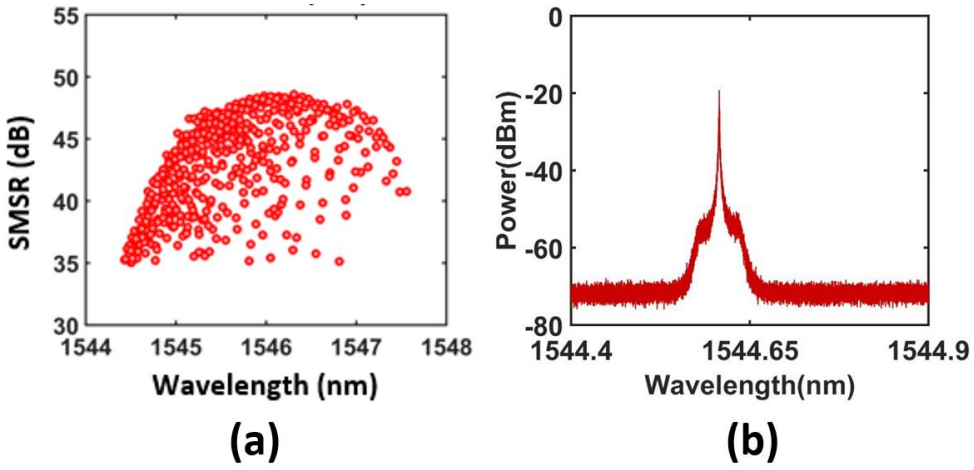

Figure 4.3.5. Plots of SL (a) wavelengths for the SMSR $>$ 35 dB and (b) optical spectrum of the SL biased at SG $=$ 38 mA and SR $=$ 40 mA.

The SMSR as a function of SG and SR currents is plotted in Figure 4.3.4(b), revealing the regions of single-mode operation ($SMSR > 35$ dB) of the laser while tuning SL wavelength from 1540 nm to 1550 nm. The two distinct high SMSR regions visible in Figure 4.3.4(b), confirm the mode hop behaviour exhibited by the SL. In addition, the SL achieves an SMSR more than 35 dB, when the SR and SG are biased between 20 mA and 80 mA, and 20 mA to 60 mA, respectively. The highest SMSR achieved by the SL is ~48 dB. Using both plots in Figure 4.3.4, the range of wavelengths with SMSR > 35 dB is identified and plotted in Figure 4.3.5. From the figure it can be seen that the SL can generate wavelengths between 1544.5 nm and 1547.5 nm with $SMSR > 35$ dB, while the wavelength range between 1545 nm and 1547 nm achieves an SMSR of more than 45 dB. The optical spectrum of the SL emitting at 1544.58 nm with an SMSR > 45 dB, when biased at $SG = 38$ mA and $SR = 40$ mA, is plotted in Figure 4.3.5(b).

4.3.3 Optical injection locking of the slave laser

Having tested the free running SL, next the ability to injection lock the SL to ML is verified. The first step here entailed confirming the lasing of master laser, which requires biasing of the SL and VOA sections at transparency. Hence, the SR, SG and VOA sections are biased at 14 mA, 14 mA, and 10 mA respectively. Thereafter, the ML sections (MR1, MG, MR2) are biased at 52 mA, 100 mA, and 60.33 mA, respectively. At these bias currents the emission from ML is dominant over that of the SL and the ML is seen to be lasing at ~1547 nm, as shown in Figure 4.3.6. From this figure, it can also be noticed that the linewidth of the ML is much narrower than the SL, which is due to the ML having a longer cavity length than SL [294], [295].

After confirming the lasing of the ML laser, the next step entails verifying the ability to achieve optical injection locking (OIL) of the SL by the ML. This is process is started by turning-on all the SL sections and the VOA (SG, SR, and VOA biased at 50 mA, 60 mA, and 10 mA, respectively) and measuring the SMSR using the OSA, while tuning the ML wavelength from 1545.48 nm to 1547.56 nm. The latter is achieved by varying the bias currents of both gratings (tied together) and the MG sections between 0 mA to 68 mA (in

2 mA steps). The results achieved are plotted, as a heat map of the SMSR as a function of the MR and the MG currents, in Figure 4.3.7(a).

The high SMSR regions (red areas in Figure 4.3.7(a)) indicate a high probability of achieving OIL. Based on these results, a bias current of 35 mA is selected and applied to the MG. To find an optimum set of currents for MR1 and MR2 sections, the biases supplied to MR1 and MR2 are varied individually from 0 to 68 mA in steps of 2 mA. The results achieved are then plotted as a heat map of the SMSR as a function of the two MR currents with a fixed MG current and shown in Figure 4.3.7(b). The regions with an SMSR > 55 dB (dark red region in Figure 4.3.7(b)) clearly indicate that OIL is achieved. Hence, a set of bias currents, which lead to OIL, can be deduced from Figure 4.3.7(b). An example of the optical spectrum of the injection locked SL for bias currents given in Table 4.3.1 (gleaned from Figure 4.3.7(b)), is shown in Figure 4.3.8. The injection locked wavelength shows 58 dB SMSR.

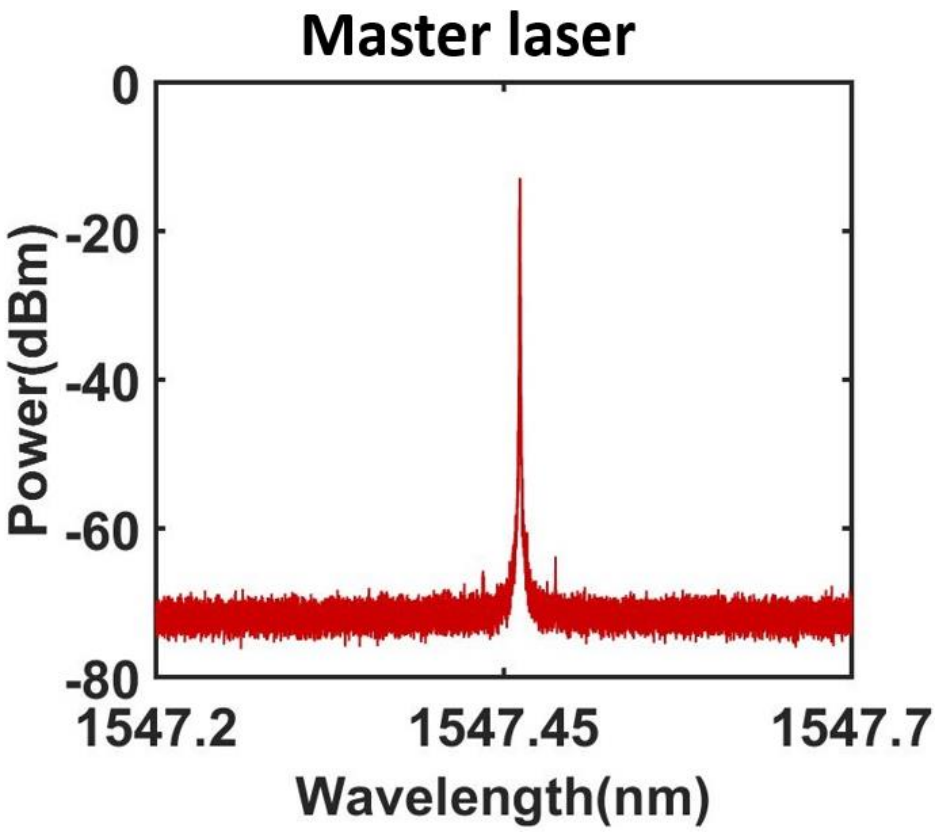

Figure 4.3.6. Optical spectrum of the master laser (OSA resolution set at 0.16 pm).

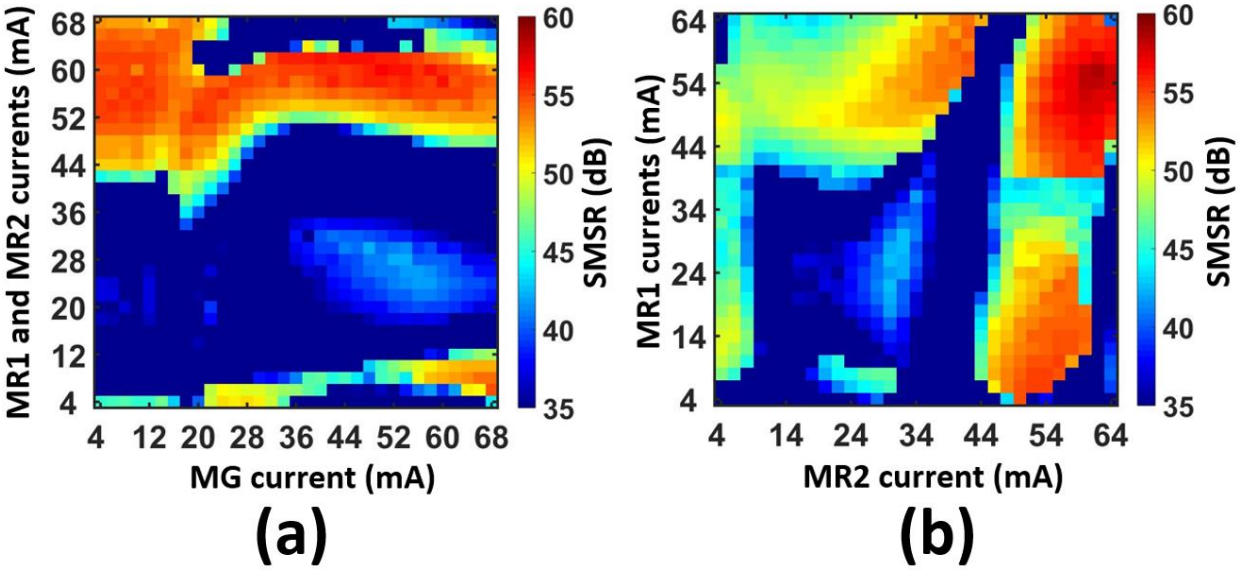

Figure 4.3.7. Heat maps of SMSR versus (a) MG and MRs currents (MR1 and MR2 tied together), and (b) MR1 and MR2 at fixed MG current of 100 mA.

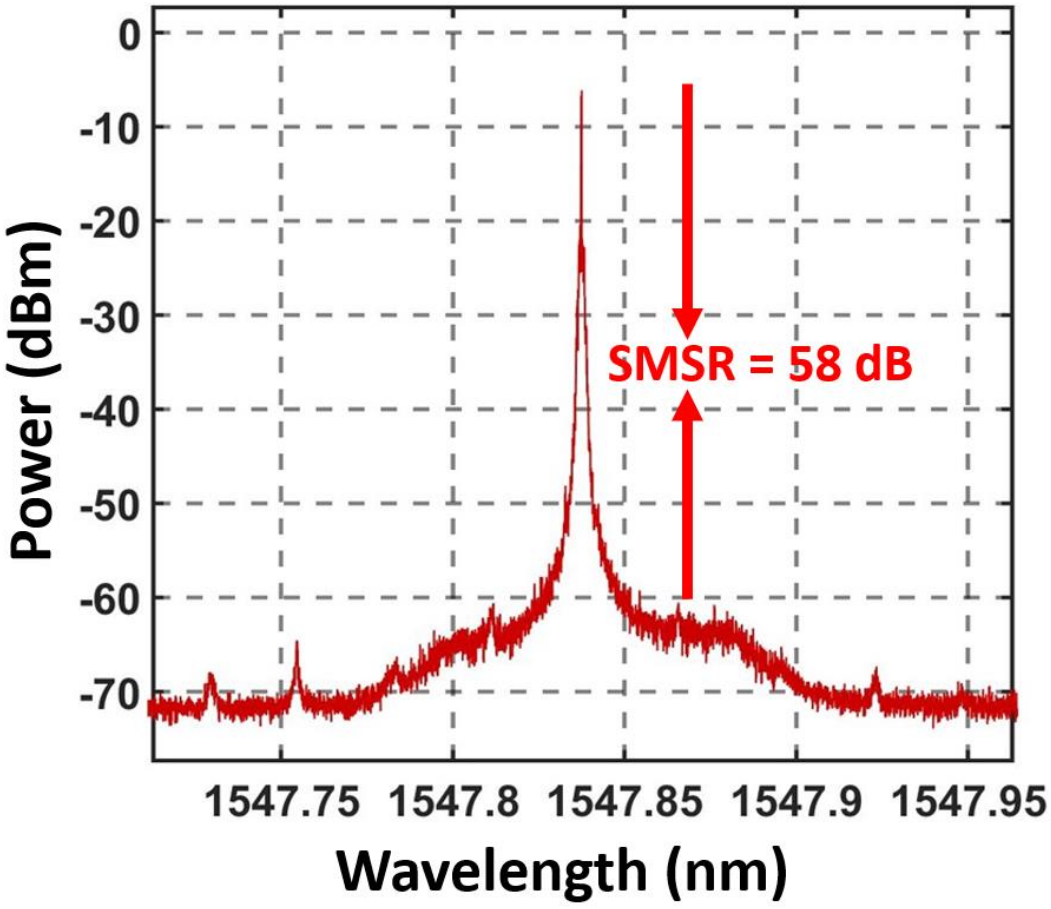

Figure 4.3.8. Optical spectrum of the injection locked slave laser (OSA resolution set to 0.16 pm).

Section	Current (mA)
SR	50.72
SG	57.54
VOA	10
MR1	54.12
MG	35
MR2	56.17
Temperature	18 °C

Table 4.3.1. Bias currents applied to the various sections for OIL as in Figure 4.3.8.

4.3.4 Wavelength stability of injection locked slave laser

This section outlines results achieved when studying the wavelength stability of the slave laser when it is optically injection locked. For this test, the SL is set to 1546.76 nm and its wavelength is measured at one-minute intervals over 60 minutes, using a high resolution (0.16 pm) OSA. From the results, plotted in Figure 4.3.9, the maximum deviation in the lasing wavelength, observed over the 60-minute time span, is found to be ± 4.56 pm (560 MHz). The main cause of this variation is the limited thermal control of the chip. However, it is important to note that this deviation in the lasing wavelength is much lower than maximum allowed deviation of ±20 GHz as described in the NGPON2 specification [83].

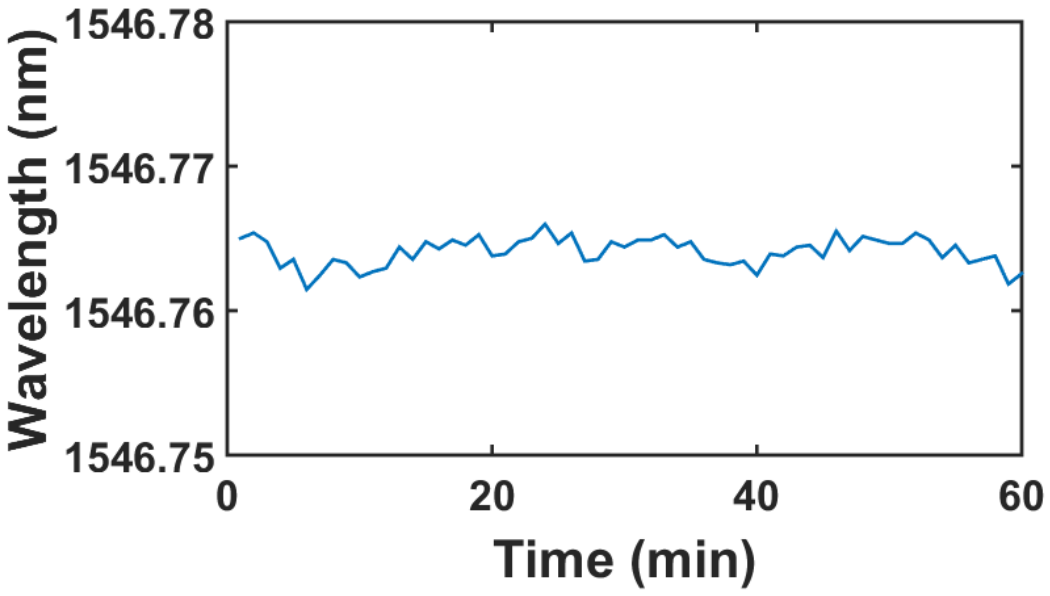

Figure 4.3.9. Variation of the peak wavelength over a 60 min of time span when slave laser is injection locked.

4.3.5 Wavelength tunability of the injection locked slave laser

Here, the wavelength tunability of the injection locked slave laser is studied. The SL and ML are multi-section lasers, whose wavelength can be tuned by controlling the currents applied to their individual reflectors, while keeping the bias of the other sections (SG, VOA, and MG) unchanged. Table 4.3.2 shows the bias points used to achieve four different wavelengths when the slave laser is injection locked. The overlapped optical spectra of these four wavelengths, on a 25 GHz grid, and showing stable injection locking of SL, are plotted in Figure 4.3.10.

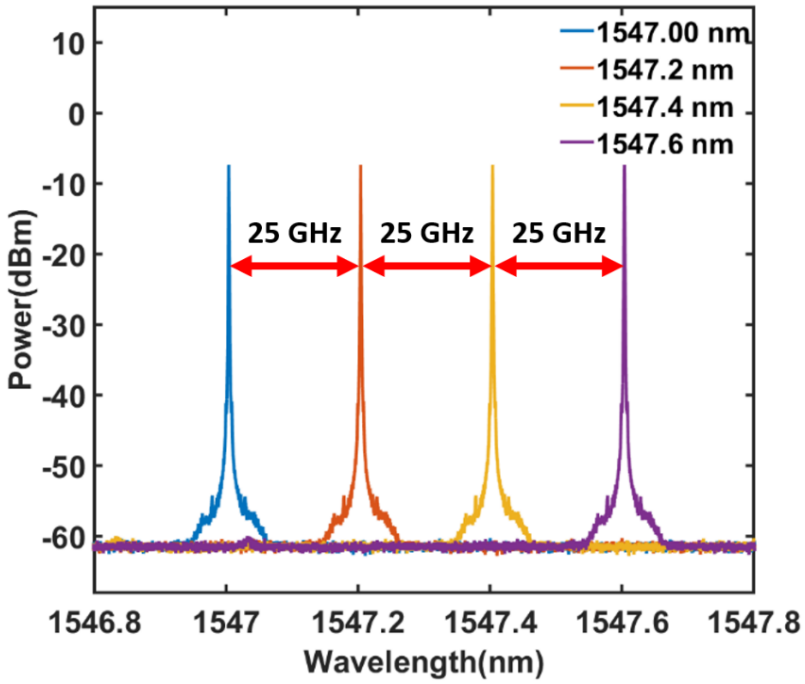

Figure 4.3.10. Tunability of injection locked slave laser on 25 GHz grid.

Wavelength	SR	SG	VOA	MR1	MG	MR2
1547.0 nm	40.71 mA	58.02 mA	11 mA	46.95 mA	54 mA	45.76 mA
1547.2 nm	44.80 mA	58.02 mA	11 mA	47.76 mA	54 mA	51.59 mA
1547.4 nm	51.13 mA	58.02 mA	11 mA	50.65 mA	54 mA	53.36 mA
1547.6 nm	55.17 mA	58.02 mA	11 mA	52.19 mA	54 mA	59.17 mA

Table 4.3.2. Bias data for achieving wavelengths on 25 GHz grid in the injection locked regime.

4.3.6 Linewidth characterization

As a part of the static characterization, this section reports on the optical linewidth of the SL and ML. The measurement is performed using the delayed self-heterodyne (DSH) method [296], a well-known DSH technique involving beating the signal with its decorrelated replica on a photodiode and observing the linewidth of the RF beat tone. The experimental setup used for linewidth measurement is shown in Figure 4.3.11. The optical signal from the laser is split using a 50:50 passive optical splitter, whose first arm is connected to an electro-optic phase modulator (PM), while the second to a fiber delay. The length of the fiber needs to be sufficient to decorrelate the signals in both arms, thus preventing the cancellation of the optical phase noise during the homodyning process.

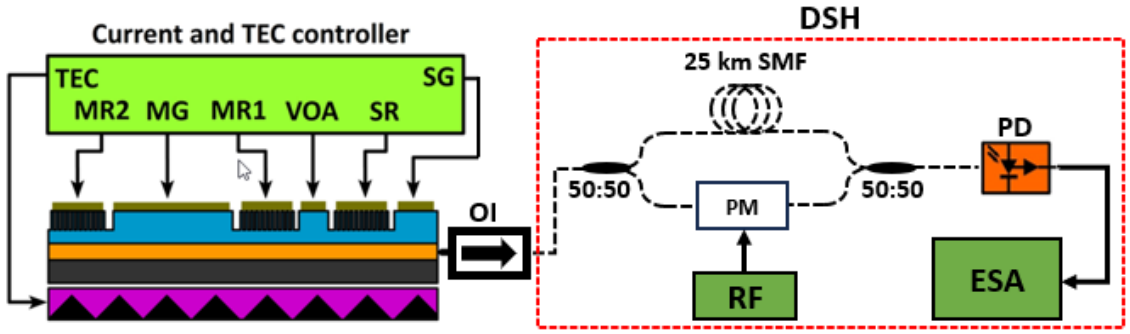

Figure 4.3.11. Experimental setup for linewidth measurement. DSH: delayed self-heterodyne, OI: optical isolator, SMF: single mode fiber, RF: radio frequency, PM: phase modulator, PD: photodiode, ESA: electrical spectrum analyser.

In the tests described here, a 25 km SMF is used, providing 122 µs delay and resolution of ~10 kHz in measurement. The output of both arms is combined using a passive optical power combiner and detected using a high bandwidth photodiode to generate the beat tone. The spectral shape of the tone is measured using an electrical spectrum analyser (ESA). The peak of beat tone frequency is centered at DC for unmodulated PM and can be shifted to an arbitrary frequency by modulating the signal fed to PM. To obtain the laser linewidth, the line shape of the beat tone is captured and the curve fitting using a Voigt profile is carried out. While the 3 dB spectral width is affected by 1/f noise and returns inaccurate measurement of linewidth, the 20 dB spectral width mainly contains information of

Lorentzian shape [296]. Hence, the 20 dB spectral width is measured, and the 3 dB optical linewidth is extracted by dividing it by $2\sqrt{99}$ [296].

It is well known from literature that the linewidth of a semiconductor laser is inversely proportional to length of the laser [295]. The cavity length of the ML (~590 µm) is approximately three times longer that the cavity length of SL (200 µm). First the linewidth of the SL is measured using the DSH method mentioned above. Initially, the SR and SG section current of SL are set to 40.70 mA and 58.02 mA, respectively (arbitrary set of currents that lead to the emission signal exhibiting an SMSR > 35 dB). The other sections of the PIC are kept unbiased. The optical signal is supplied to the DSH measurement setup, and the electrical spectrum of the beat tone is recorded using ESA (at 100 Hz resolution). Figure 4.3.13(a) shows the measured electrical spectrum of the beat signal with a Voigt profile fitted over it. This is used to extract a 3 dB linewidth of the SL, which is 56.4 MHz. Next, the MR1, MG, and MR2 sections of the ML are biased at 46.95 mA, 54 mA, and 45.76 mA, respectively. It is important to note that access to the ML emission is attained from the front facet. Hence the SR1 and SG sections are biased at transparency (12 mA). The emitted optical signal is once again fed to the DSH setup and the Voigt curve fitting is superimposed on the measured ESA spectrum (as shown in Figure 4.3.13(b)), which then allows the extraction of the linewidth of ~18 MHz. The measurement confirms that the linewidth of ML is approximately 3 times better than SL.

Subsequently, the linewidth of the injection locked SL is also measured. It is well known that the linewidth of the injection locked SL follows the linewidth of the ML [295], [297]. OIL of the SL is achieved at 1547 nm wavelength by biasing all the sections with currents described in Table 4.3.1. Figure 4.3.13(c) shows the electrical spectra of the beat tone with the superimposed Voigt curve fit. The measured linewidth of the injection locked SL is ~18 MHz, which verifies that the SL is injection locked by the ML (inherits the linewidth of the master).

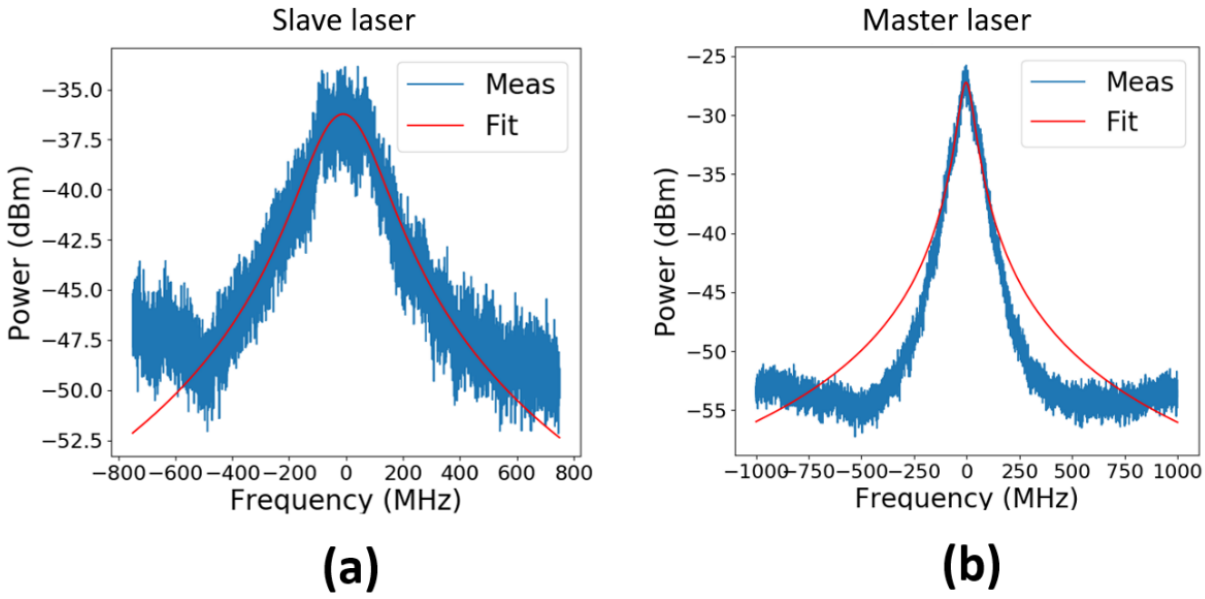

Figure 4.3.12.The ESA spectra and Voigt fit to measure linewidth of the (a) SL and (b) ML.

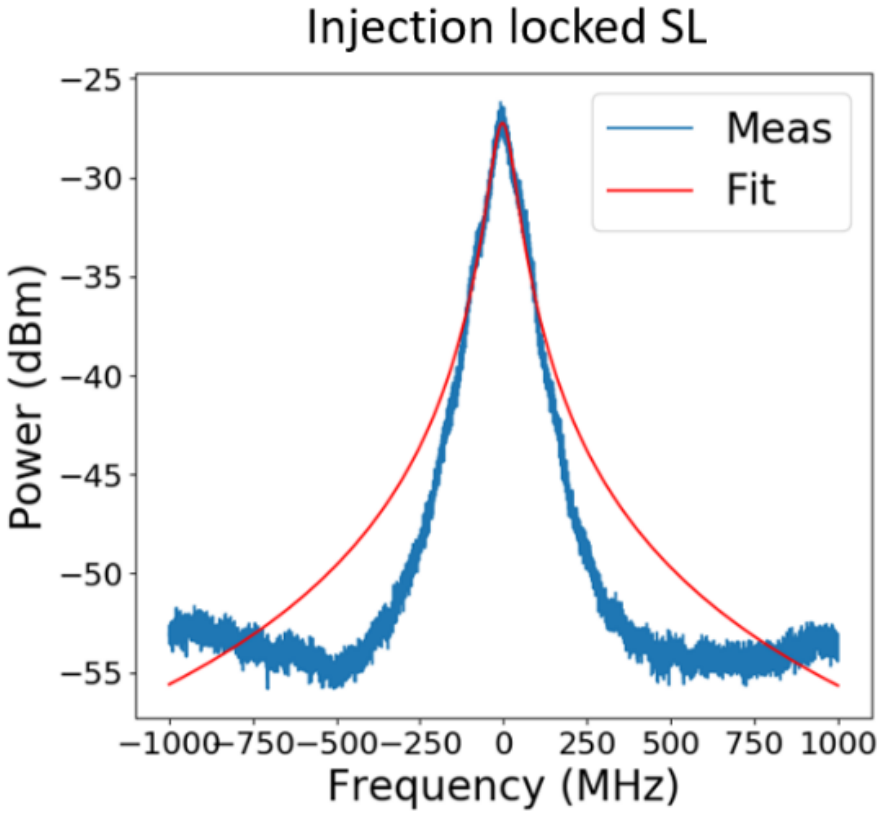

Figure 4.3.13. The ESA spectra and Voigt fit to measure linewidth of IL SL.

4.3.7 RIN measurement

The last test performed within the static characterisation of the device involved measuring the relative intensity noise (RIN), which is defined as the ratio of the ensemble average fluctuations ($\langle \delta P(t)^2 \rangle$) to the squared average power of the laser (P_0^2). The RIN in semiconductor lasers is typically caused by the random generation/recombination of carriers and photons resulting in a random variation of the carrier and photon density. The random fluctuation in photons is due to spontaneous emission and recombination of electron-hole pair, also called shot noise. The spontaneous emission dominates over shot noise, which adds noise in both the intensity and phase of photons [298]. The perturbation in intensity is characterized as RIN that directly affects signal-to-noise ratio (SNR). It also contributes to distortions of the modulated signal, which can result in a worsening bit error rate [278] [299] [300]. The RIN can be expressed by Equation (4.3.1).

$$\mathrm{RIN} = \frac{\langle \delta P(t)^2 \rangle}{P_0^2} \tag{4.3.1}$$

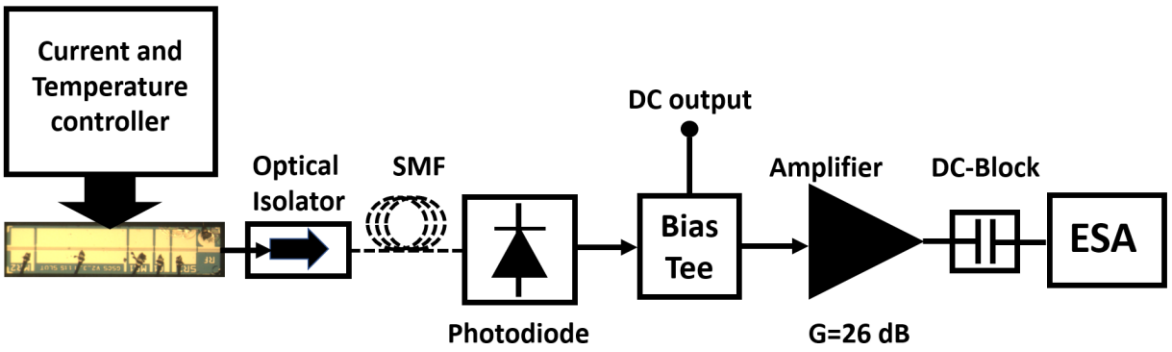

Figure 4.3.14. Schematic of the experimental setup for the RIN measurement.

The RIN of the six-section PIC is measured using the set up shown in Figure 4.3.14. The output of the biased device is fed to a high-speed photodetector (20 GHz bandwidth) via inline isolator and SMF. The detected electrical signal containing both the DC (average signal) and the AC component (fluctuations) is split via a bias-tee (BT). The DC port of BT is connected to a voltmeter to read the average output voltage. The RF output of BT (noise) is amplified and measured using electrical spectrum analyser (ESA). As the ESA-detected

signal is made up of contributions from the RIN in the optical signal, thermal noise, and shot noise, to extract the RIN, the thermal (background noise) and shot noise must be subtracted from the measurement. The final value of the SL RIN is thus calculated using in Equation (4.3.2). Here, P_{off} is the background noise (measured with no optical signal connected to the photodiode) and P_{on} is the optical signal measured with background noise.

$$RIN = P_{total} - P_{thermal} - P_{shot} - P_{dc} \tag{4.3.2}$$

where

$$P_{total} = \frac{10^{\frac{P_{on}}{10}} \times 10^3}{RBW} \tag{4.3.3}$$

$$P_{therm} = \frac{10^{\left(\frac{P_{off}}{10}\right)} \times 10^3}{RBW} \tag{4.3.4}$$

$$P_{shot} = 2 \cdot q \cdot V_{dc} \cdot \frac{R_1}{R_{out}} \tag{4.3.5}$$

$$P_{dc} = \left(\frac{V_{dc}}{R_{out}}\right)^2 \times R1 \times V \tag{4.3.6}$$

$$V = 10^{G_{amp}/10} \tag{4.3.7}$$

The RBW, q, V_{dc}, G_{amp}, R_1, R_{out}, V are resolution bandwidth, electronic charge, DC output of bias-tee, gain of amplifier, input and output resistance of amplifier, and output voltage of amplifier. The values of parameters used in the equation is shown in Table 4.3.3.

Parameter	Description	Values
RBW	Resolution band width	100 kHz
$\boldsymbol{q}$	Electronic charge	1.6×10^{-19} C
G_{amp}	Gain of amplifier	26 dB

R_1	Input impedance of amplifier	50 Ω
R_{out}	Output impedance of amplifier	50 Ω

Table 4.3.3. The description and values of parameters used in the RIN calculation.

The level of RIN present in the output optical signal is determined for SL without optical injection (free running) and injection locked SL. The latter is measured for various levels of injected power (various bias currents of the VOA section). The results are plotted in Figure 4.3.16. The average RIN of the free running SL over a 1 GHz to 6 GHz frequency span is −121.8 dBc/Hz. It can be seen that the RIN is highest at frequency of ~2.3 GHz due to the relaxation oscillation frequency peak being at ~2.3 GHz at the given bias (as shown in Figure 4.3.15). The average RIN of the IL SL are −142.75 dBc/Hz, −143.77 dBc/Hz, and −145.54 dBc/Hz, when VOA is biased at 2 mA, 3 mA, and 10 mA, respectively. The main reason of low RIN in IL SL is the reduction in spontaneous emission [301], [302], [303] and suppression in nonlinear distortion due to photon and carrier interaction [304].

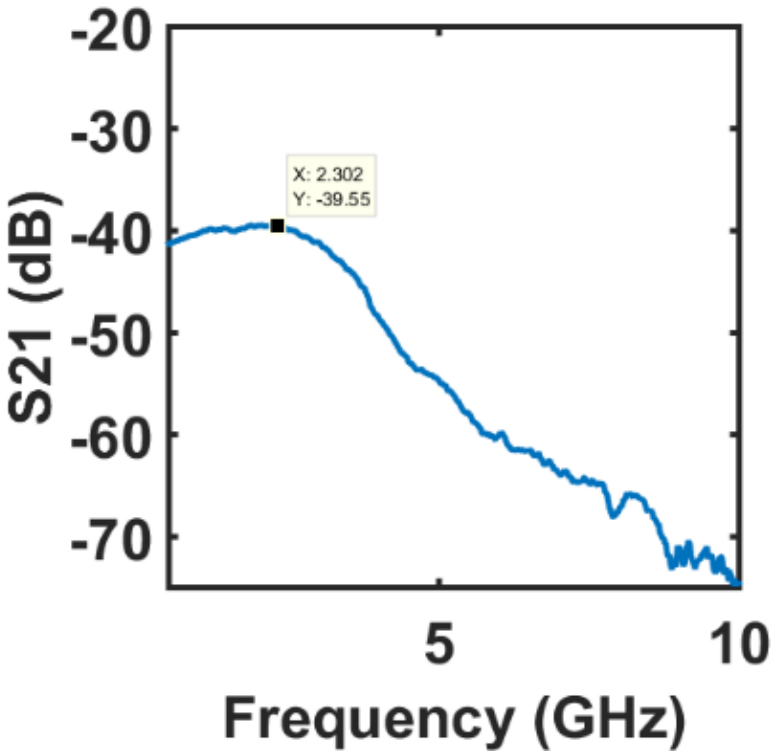

Figure 4.3.15. Modulation response of free running SL.

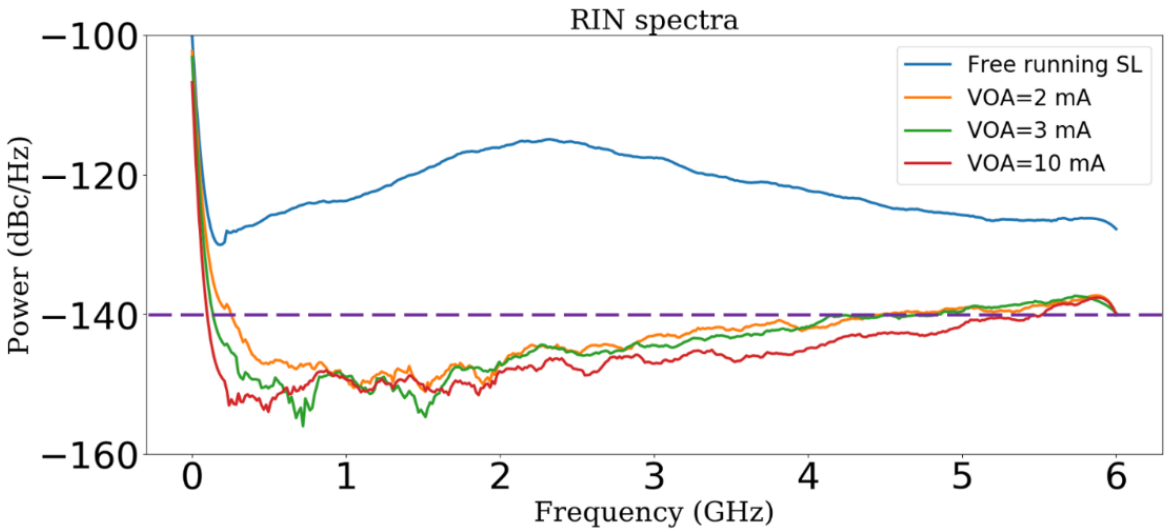

Figure 4.3.16. Plot of the RIN of the free running SL (blue) and the injection locked SL when the VOA is biased at 2 mA (orange), 3 mA (green), and 10 mA current (orange).

4.4 Dynamic characterization

The first phase of the dynamic characterization of the SL involves the determination of its frequency response in both the free running and OIL regimes. The latter is carried out at different levels of power injected into the SL. Subsequently, the effect of optical injection, when slave laser is modulated with a data signal, is characterized by studying the optical spectrum and the eye diagrams (with and without injection). Finally, the frequency chirp imposed due to direct modulation is investigated and its reduction when the SL is injection locked, is studied.

4.4.1 Frequency response

As mentioned in chapter 3, the frequency response of most semiconductor lasers, especially free running, is limited. It was also mentioned that OIL can improve the modulation bandwidth based on the frequency detuning and the optical power injected [305], [306], [307], [308], [309]. In this section, the modulation bandwidth of the SL, both in the free running and under optical injection regimes, are investigated. Figure 4.4.1 shows the setup used for measuring the frequency response. The sections with DC pads are supplied with a

DC current, and the SG section is supplied with a DC current in conjunction with an RF signal from the output port of the vector network analyzer (VNA). Then, the modulated optical output is coupled to a lensed fiber followed by an inline optical isolator and finally detected by a high-speed photodetector connected to the input port of the VNA.

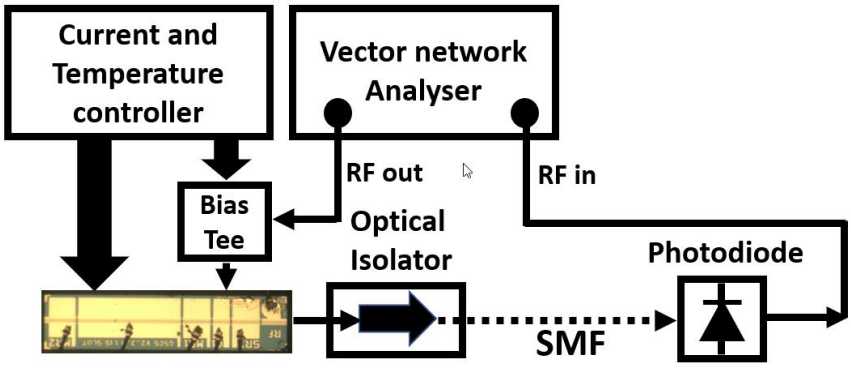

Figure 4.4.1. Schematic of the experimental setup used for measuring the frequency response.

It is well known that the relaxation oscillation frequency of the SL under optical injection is directly proportional to the fractional change in injected optical power with respect to power of the free running SL [310]. Hence, the measurements are carried out for different levels of injected power. It is important to note that the optical injection in this device can be varied in two ways: by changing the MG current, which results in a change of the ML output power, or by changing the bias applied to the VOA section, which changes the level of attenuation (absorption).

The first step involves determining the effect of changing the MG current, whilst keeping the MR1, MR2 and VOA (10 mA) currents unchanged, on the frequency response of the SL. The results obtained are displayed in Figure 4.4.2 and clearly show that the modulation response of the SL improves, when the current applied to the MG section increases. A minimum bias current of 23 mA on the MG section is required to achieve lasing. Hence, the MG current is swept from 23 mA to 38 mA in steps of ~3 mA. The modulation bandwidth (3 dB) of the SL increases from ~4.2 GHz at 23 mA to ~7.8 GHz at 38 mA, as a result of the increased level of optical injection.

However, as mentioned earlier, a change in the bias current applied to the MG section also results in a change of the emission wavelength. Hence, the positive attribute brought by

the six section PIC architecture is taken advantage of by varying the injection level using the VOA current (keeping the MG constant). Hence, as a subsequent step, the bias current applied to the VOA section is tuned to change its transmission response from being opaque to becoming more transparent. As the VOA section is made of an active material, the state of transparency is achieved by supplying current to compensate the waveguide loss (the level of absorption is varied). Thus, by changing the bias to VOA section, the level of the optical injection from the ML to the SL can be varied. The frequency response of the SG section is then recorded at different biases applied to the VOA section and shown in Figure 4.4.2(b). The blue line depicts a case where the SL section has little or no injection from the ML (VOA section bias is set to 0 mA i.e., maximum attenuation). The 3 dB MBW in this operating condition is measured to be ~3.6 GHz. When the current to the VOA section (thus the optical injection level) is increased, the 3 dB MBW of the SL improves to 4.6 GHz (orange line), when the VOA section current is set at 1 mA, to ~7.8 GHz (cyan line) for VOA current of 12 mA. Moreover, the modulation response is uneven and shows high roll-off in both scenarios i.e., changing MG and VOA current. The behaviour is due to reflection caused by the matching resistor and wire bond connected to SG. In addition, the RF track is designed using a PCB having FR4 material as a substrate, thus causing a high loss in transmission of RF signal.

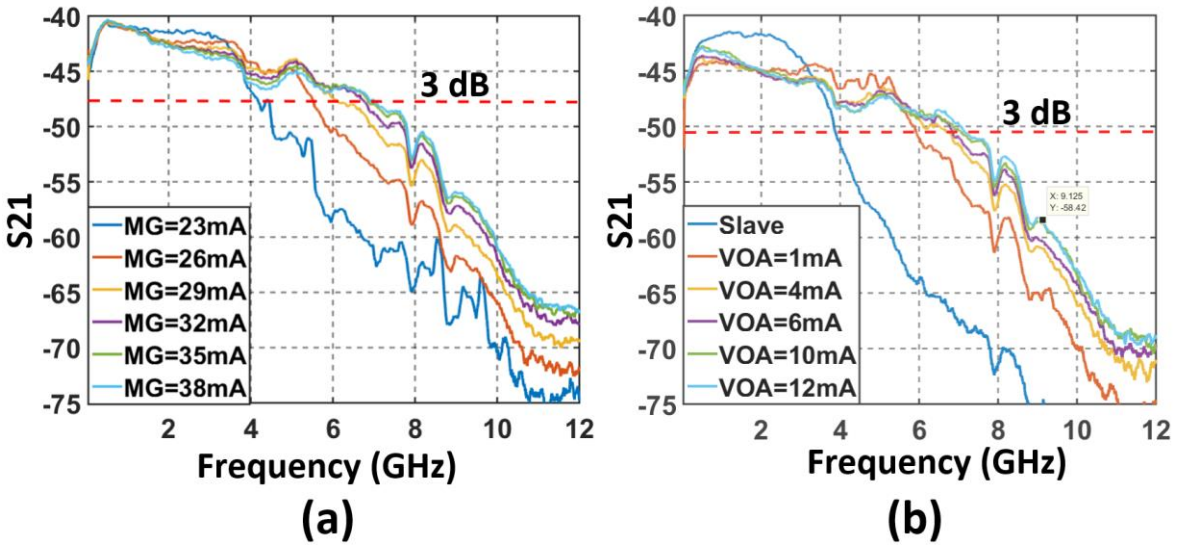

Figure 4.4.2. Plot of the frequency response of the SL under different levels of optical injection controlled by (a) MG current and (b) VOA current.

4.4.2 Chirp measurement

The final measurement in the characterisation of the device is the chirp measurement using the experimental setup illustrated in Figure 4.4.3. For this test, the slave laser is operated in the optical injection locked and biased to achieve ~1547.2 nm wavelength using values listed in Table 4.3.2. Subsequently, a 10 Gb/s non-return-to-zero (NRZ) data signal with a pseudo random bit sequence (PRBS) of order 2^{15}–1 with a peak-to-peak voltage of 2 V, sourced from a pulse pattern generator (PPG), is applied to the gain section of the SL.

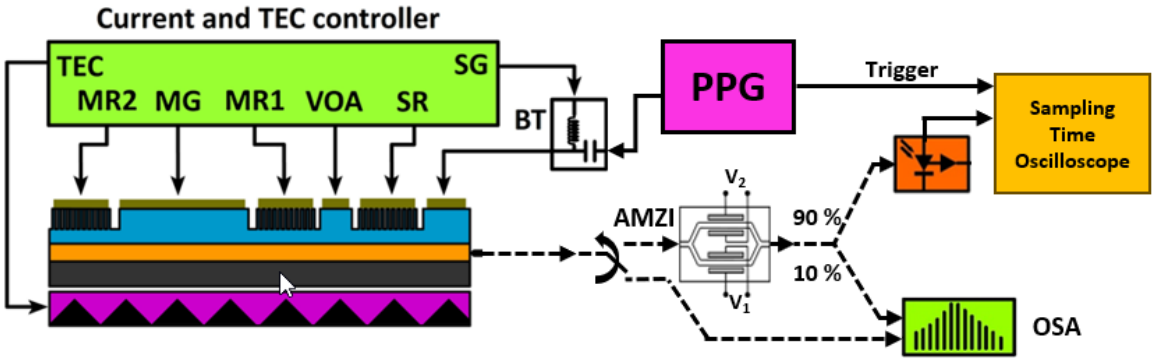

Figure 4.4.3. Experimental setup used for the measurement of chirp of directly modulated six-section PIC. AMZI: asymmetric Mach-Zehnder interferometer, BT: bias-tee, OSA: optical spectrum analyser, PPG: pulse pattern generator, PD: photodetector.

The output signal of the PIC is either directly connected to OSA or fed to an asymmetric Mach-Zehnder interferometer (AMZI) filter. Then the output of AMZI filter split using a 90:10 coupler, with the 10% tap connected to an OSA and the 90% supplied to a high-speed photodetector (20 GHz). The electrical output of the photo detector is connected to a sampling time oscilloscope synchronized to PPG.

As discussed in chapter 3, direct modulation of a laser can introduce a relatively large amount of frequency chirp in the resultant (modulated) optical signal. This chirp can be minimized by optical injection locking of the modulated laser [311], [312]. The reduction in chirp depends on various parameters including the level of optical injection as described in section 3.6.1.2. As seen above, one of the positive attributes of this PIC, is its ability to control the level of optical injection into the SL, from the ML, by simply changing the current applied to the VOA section.

4.4.2.1 Measurement of chirp using OSA

Initial characterization of the chirp is done by observing the optical signal on a high resolution (0.16 pm) OSA. To see the change in chirp as a function of the level of optical injection, the current applied to the VOA section is varied. As highlighted earlier, a higher bias current to this section reduces the level of attenuation (increases the level of injection) and vice versa. The optical spectrum of the modulated signal at three different VOA current is plotted in Figure 4.4.4.

The result shows that when the VOA is biased at 2 mA, it allows a very low level of optical injection, which essentially means that the incurred frequency chirp (spectral broadening) is not reduced (spectrum in blue). The measured spectral broadening (~30 dB below the peak) for 2 mA, 6 mA, 10 mA VOA currents are 1.4 nm, 0.12 nm and 0.1 nm. The spectral width of the directly modulated laser significantly reduces at 6 mA VOA current (spectrum in orange) and further narrows down when VOA current increased to 10 mA (spectrum in yellow). This measurement clearly shows that the chirp is reduced significantly by increasing the level of injection. It is also important to highlight that the emission wavelength doesn't change - which is a key feature of this PIC design.

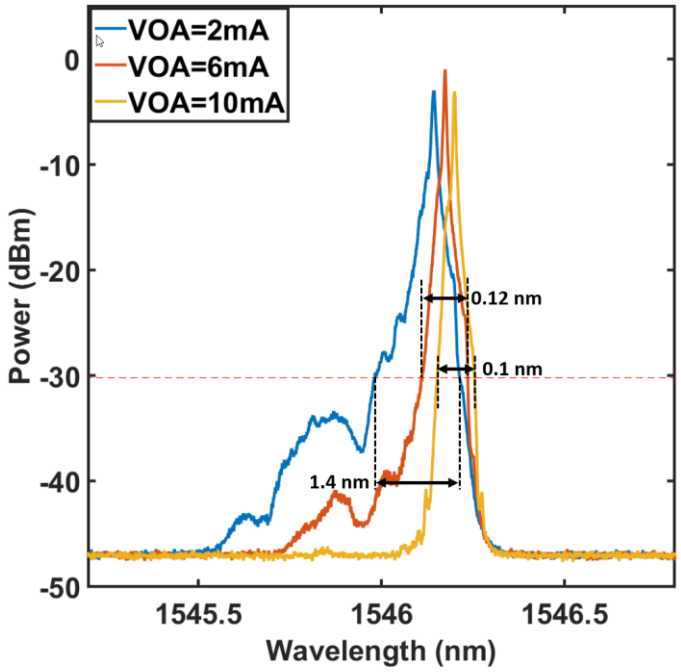

Figure 4.4.4. Optical spectrum of modulated SL under different level of optical injection.

4.4.2.2 Measurement of chirp using frequency discrimination method

Further to the qualitative spectral measurements, a more extensive characterization is performed to quantify the chirp. This measurement of the chirp in the optical signal is carried out by using the well frequency discriminator technique [313], [314], [315], [316]. Specifically, in this experiment an AMZI based filter is used as the frequency discriminator [316], [317], allowing for the conversion of the frequency fluctuations to an intensity modulation, providing a more accurate chirp measurements than traditional methods (e.g., fiber transfer function method [318]). The procedure used for the chirp measurement is as follows:

- The transfer function of the filter is characterized and plotted. The key points such as A, B, C, D, and E are labelled (see Figure 4.4.5).

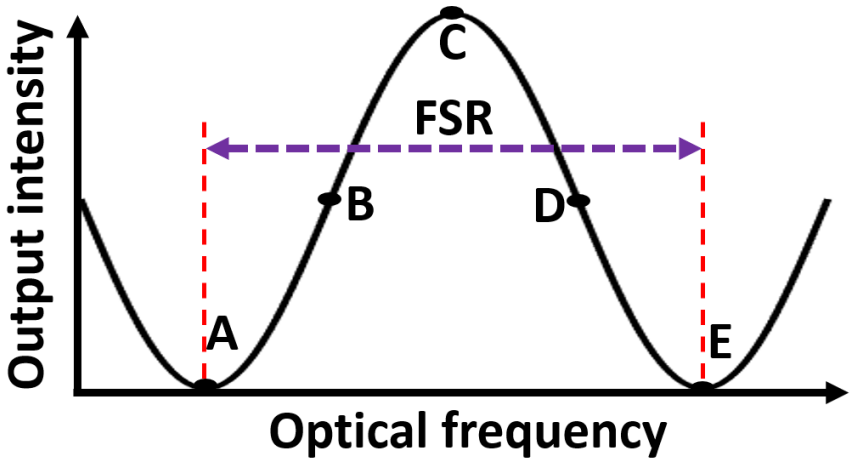

Figure 4.4.5. Transfer function of the AMZI.

- The spectrum of the modulated signal is aligned to point C (maximum) of the AMZI filter response, and the time traces are recorded using a wideband photodetector (20 GHz bandwidth) connected to a sampling oscilloscope.
- The modulated spectrum is aligned to point B (center of the rising edge) of the AMZI filter response, and the time traces are recorded and named as P_2 trace.
- The modulated spectrum is aligned to point D (center of the falling edge) of the AMZI filter response, and the time traces are recorded and named as P_1 trace.
    - The free spectral range (FSR) is calculated by obtaining frequency difference between point A and point E where the output intensity is zero.

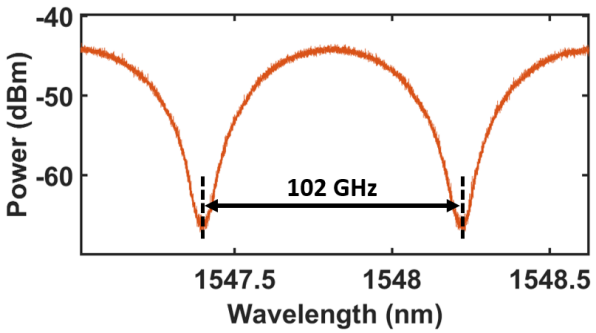

Figure 4.4.6. Measured AMZI filter response.

- The chirp is calculated using Equation (4.4.1).

$$\Delta f = \frac{FSR}{2\pi} Sin^{-1}\left(\frac{P_1 - P_2}{P_1 + P_2}\right) \tag{4.4.1}$$

Thus, the chirp measurement starts with the characterization of the AMZI filter response, carried our passing the amplified spontaneous emission (ASE) generated from an Erbium dopped fiber amplifier through the AMZI and measuring the optical spectrum of the output signal. The response of the AMZI used in the test is shown in Figure 4.4.7(a) in yellow. Subsequently, the FSR is extracted by finding difference between two subsequent nulls (here is 102 GHz). Next, a 2.5 Gb/s PRBS of 2 V pk-pk was applied to the slave gain section of the free running SL in conjunction with a DC current of 50.54 mA. The spectra of the free running (blue) and modulated SL (orange) are shown in Figure 4.4.7(a).

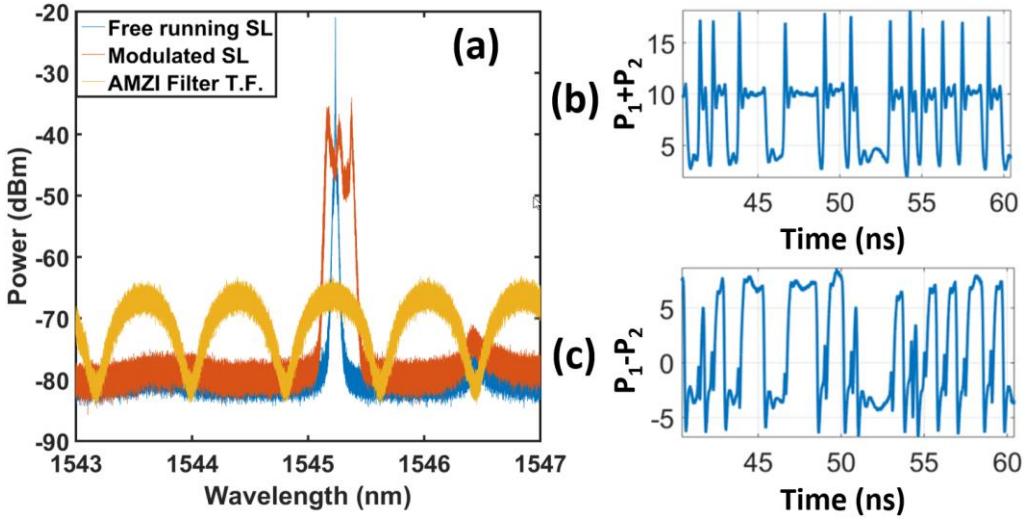

Figure 4.4.7. (a) AMZI filter transfer function (yellow), spectrum of the SL in CW (blue) and modulated with 2.5 Gb/s data (orange); time traces of $P_1 + P_2$ (b) and $P_1 - P_2$ (c).

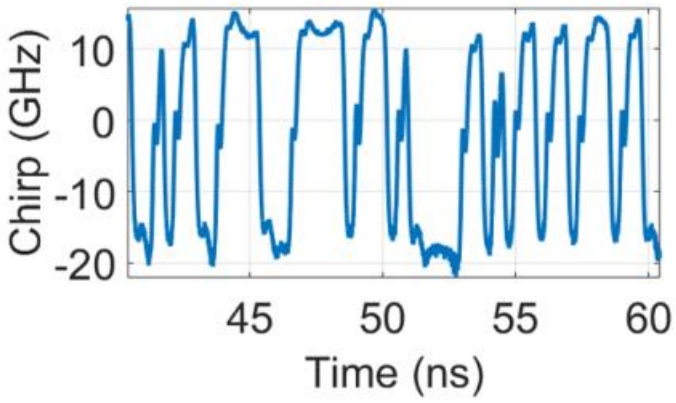

Figure 4.4.8. Extracted chirp of the modulated SL.

The P_1 and P_2 traces are extracted by aligning the spectrum of the modulated SL to the center of the rising and falling edges of the filter response. Then the time traces are added and subtracted to find $P_1 + P_2$ and $P_1 - P_2$ and plotted as Figure 4.4.7(b) and (c). Using Equation (4.4.1) the chirp is extracted and plotted in Figure 4.4.8. The figure shows the frequency is varying from -20 GHz to +15 GHz, thus giving the peak frequency chirp of 35 GHz.

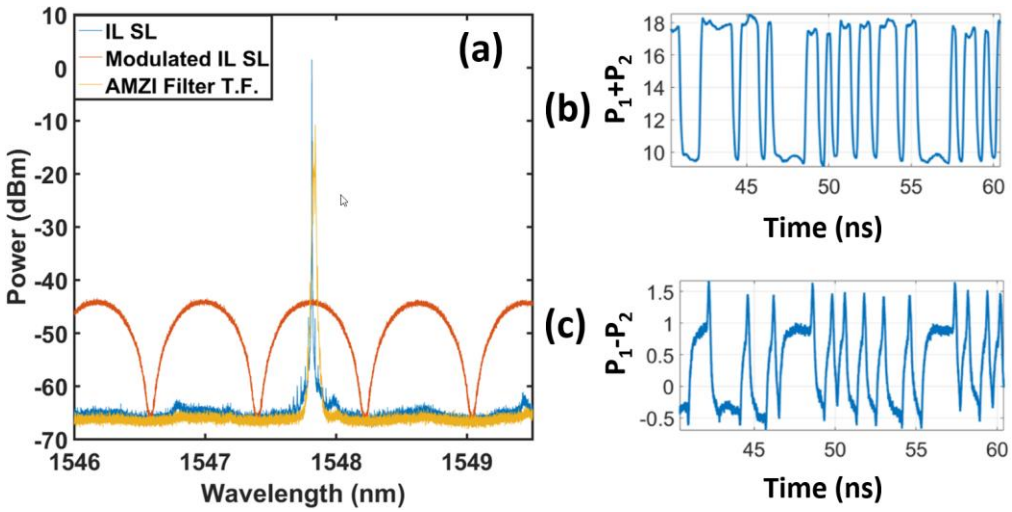

Figure 4.4.9. (a) AMZI filter transfer function (orange), optical spectra of the injection locked CW (blue), and modulated SL (yellow), traces of (b) $P_1 + P_2$ and (c) $P_1 - P_2$.

Having measured the chirp of the free running laser, the next step entails measuring the chirp of the SL while injection locked (VOA biased at 2 mA). Again, a 2.5 Gb/s PRBS

(2^{15}−1) was applied to the slave gain section of the laser in conjunction with a DC current of 50.54 mA. The same procedure mentioned above is followed and the AMZI filter response (orange) and the optical spectra of the modulated (yellow) and unmodulated (blue) injection locked SL are shown in Figure 4.4.9(a).

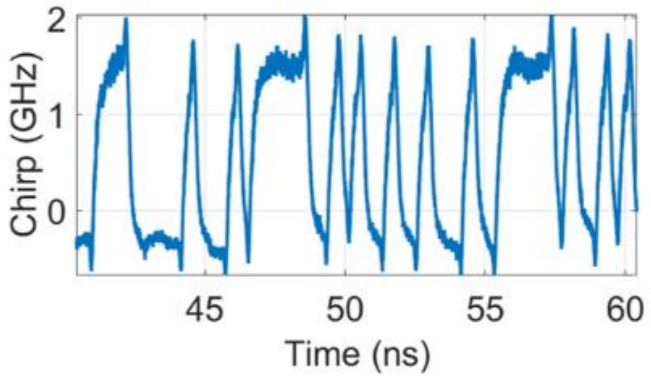

Figure 4.4.10. Measured chirp of modulated SL under optical injection.

Similar to the previous measurement, the time traces P_1 and P_2 are extracted, after which the frequency deviation (chirp) is calculated using Equation (4.4.1). Figure 4.4.10 shows the plot of the extracted chip, which reveals that the maximum positive and negative deviation in chirp, of the injection locked directly modulated SL are 2 GHz and 0.5 GHz. This is a reduction in the frequency chirp of more than ten times, which clearly shows that the chosen architecture is effective. Hence, such a PIC may be viable for employment in directly modulated communications systems.

4.5 Data transmission

The previous section clearly showed that the six section PIC can be potentially employed as a directly modulated transmitter in an optical communications system. Hence, the next step involves the verification of such a scenario in a short reach network.

The experimental setup used is illustrated in Figure 4.5.1. For this measurement, the slave laser is operated in the optical injection locked regime, achieved by supplying the different sections with the bias currents shown in Table 4.3.1. Subsequently, a 10 Gb/s NRZ

data signal with a PRBS of order $2^{15}-1$ with a of 2 Vpp, sourced from a pulse pattern generator (PPG), is applied to the gain section of the slave laser. The output signal of the PIC is split using a 90:10 coupler, with the 10% tap connected to an OSA and the 90% tap initially launched into a patch cord (for back-to-back tests), and subsequently into a 25 km or a 50 km reel of SSMF. At the receiver, the signal is passed through an external VOA, to change the received optical power (ROP), prior to being fed to an avalanche photodiode (APD). The output of the APD is connected to the error detector (ED) for bit error rate (BER) analysis.

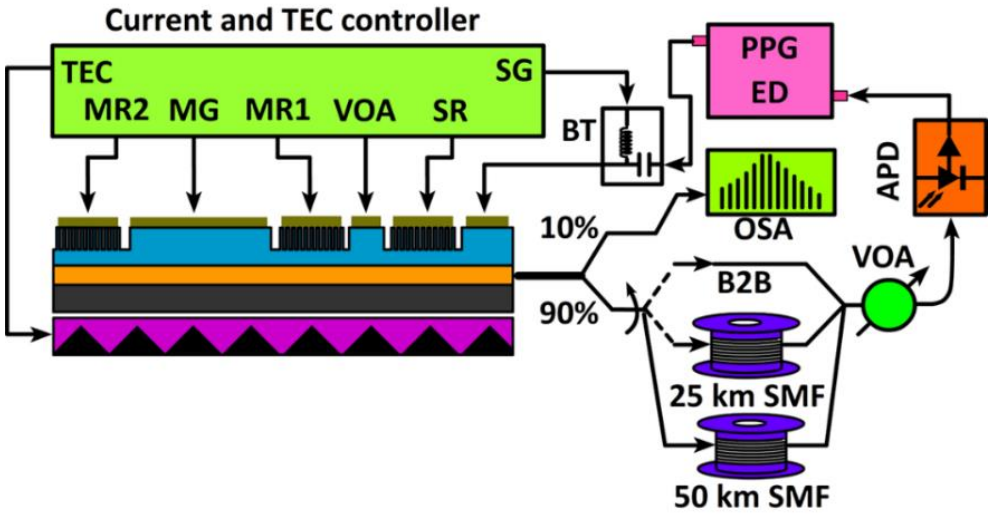

Figure 4.5.1. Experimental setup used for the direct modulation of the PIC.

The first test is the back-to-back (B2B) scenario where a patch cord connects the transmitter to the receiver. The eye diagram and the BER as a function of the ROP are then measured. Figure 4.5.2 shows the B2B eye diagram from which the extinction ration (ER) of the signal is measured to be ~5 dB. The patch cord is then replaced with a 25 km and subsequently a 50 km reel of SSMF. The BER plots of the transmission are superimposed with the B2B case and shown in Figure 4.5.3. It is important to note that error free transmission ($1e^{-9}$) is achieved for all three scenarios. In the B2B case, the transmission is error-free at -20 dBm received optical power. In addition, the receiver sensitivity ($1e^{-9}$) for the 25 km fiber transmission is measured to be −22 dBm and for the 50 km fiber transmission is −15 dBm. This corresponds to a power penalty, with respect to the back-to-back case, of ~2 dB (25 km) and ~5 dB (50 km), which can be mainly attributed to the chromatic dispersion incurred in the fiber.

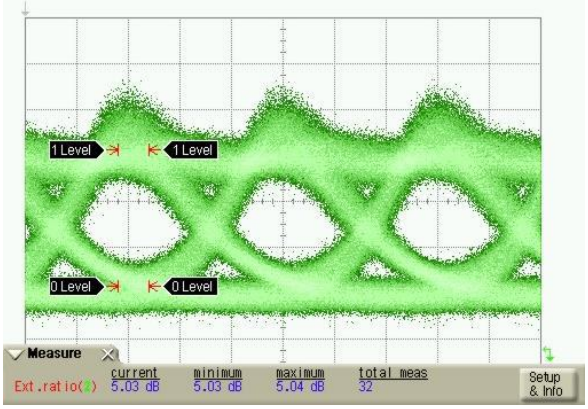

Figure 4.5.2. Eye diagram of the received signal in a B2B case and the measurement of its ER.

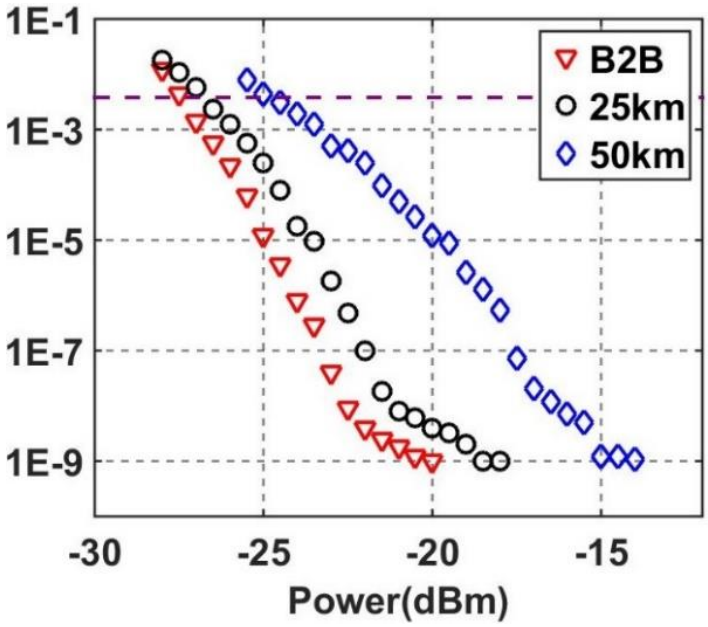

Figure 4.5.3. BER vs. ROP for back-to-back and after transmission over 25 and 50 km of SSMF.

Finally, to demonstrate the efficacy of the VOA and the advantage of varying the level of optical injection, measurements of varying the VOA current on the BER performance for the two transmission distances is carried out. From the results, plotted in Figure 4.5.4, it can be seen that by increasing the VOA bias, thus the injection level, a significant improvement in the performance of the system can be achieved. In the case of the 25 km transmission, changing the VOA section current from 4.5 mA to 10 mA reduces the BER from $1e^{-3}$ to $1e^{-9}$, while in the case of the 50 km transmission, the best performance

(BER of $1e^{-9}$) is achieved for the VOA section current of 12 mA. This improvement stems from the reduction of the chirp induced by the optical injection. It also shows that for the longer fiber length, optimizing the system performance requires a higher level of injection (higher VOA current). It is important to note that the optical injection also results in a reduction of the extinction ratio (ER) of the modulated signal. Hence, there is a trade-off between the level of chirp compensation and the degradation of the ER. In other words, a shorter transmission distance (less dispersion) could benefit from a reduced level of optical injection (better ER).

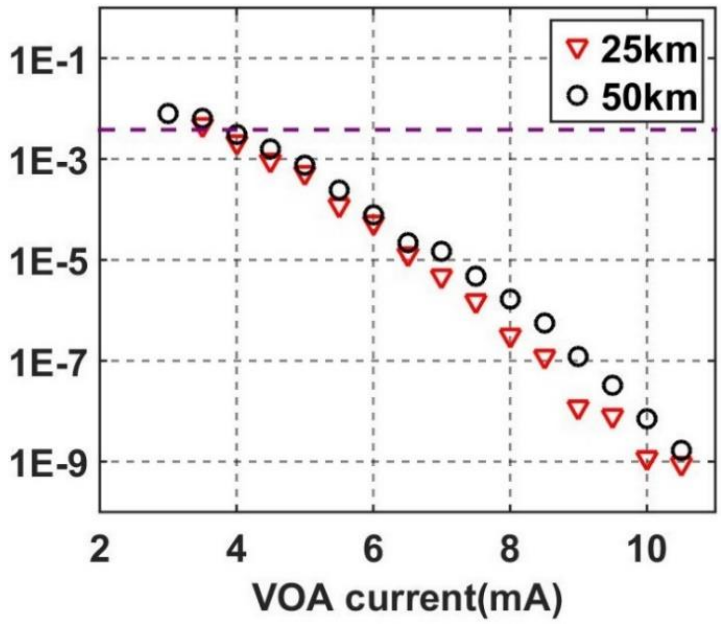

Figure 4.5.4. BER vs. VOA current after transmission over 25 km and 50 km.

4.6 Conclusion

A novel six-section PIC consisting of a master slave architecture is fabricated using a re-growth free technique. The overall objective of this design is to achieve a device that can be directly modulated at a bit rate of 10 Gb/s thereby being able to support the latest standards of an access network.

The device's unique architecture is based on introducing an integrated VOA between the master and slave laser sections. The implemented PIC demonstrates the phenomenon of

OIL and its merits, such as reduction of RIN, decrease in linewidth, and improvement in modulation response. Having an independent contact pad for each section helps to compensate for thermal crosstalk with bias control. In addition, the intensity of optical injection can be precisely controlled by varying the current of the VOA section. Moreover, the SL under the OIL condition shows a significant reduction in frequency chirp that minimizes the effect of chromatic dispersion while transmitting over SSMF. The direct modulation of PIC achieved an ER of 5 dB under OIL conditions. The optimized injection-locked device shows an error-free transmission of a directly modulated 10 Gb/s signal over 25 km and 50 km of SSMF. The features such as mitigation of frequency chirp, ER of 5 dB, and modulation bandwidth of 7.8 GHz by the PIC make this device suitable for short-reach network. However, the proof-of-concept device does not comply with the specification of NGPON2. So, in the next chapter an improved version of six-section pic is discussed that is designed to meet the standards of NGPON2.

Chapter 5

Eight-section photonic integrated transmitter

5.1 Introduction

The previous chapter demonstrated a six-section directly modulated transmitter fabricated using a regrowth-free method. The transmitter is realized by integrating master-slave architecture on the same wafer to implement the OIL [242]. The design of such a PIC supports, with the help of the VOA section introduced between the master and slave lasers, an accurate control of the level of optical injection [319], [320], and independent bias control of the laser sections (reflector and gain). Thus, this structure supports the achievement of optimum OIL of the SL, which manifests as an improvement in the modulation response [266], and a reduction of the frequency chirp [276]. These attributes enable the use of cost-efficient direct modulation on the PIC thereby making it more attractive for use in the cost sensitive short reach networks, as demonstrated in section 4.5. However, as outlined earlier in this thesis, a primary objective of this research work is to realise a transmitter suitable for the NGPON2 standard [83]. This requires improvements to the six section PIC in terms of the wavelength tunability, burst mode operability, low cross channel interference, and transmitter enable/disable features.

Hence, this chapter discusses an eight-section PIC (an improved version of the six-section device). The architecture of the improved PIC brings a suite of benefits similar to the six-section PIC [319], such as improved dynamic response and reduced frequency chirp. In

addition, it can generate four OIL wavelength channels, each capable of being directly modulated with an on-off keyed (OOK) data signal at 10 Gb/s. Moreover, the PIC meets the NGPON2 power-when-not-enabled (PWNE) requirements and features low adjacent channel interference while operating in burst mode.

5.2 Architecture of transmitter

The PIC transmitter is manufactured using same wafer as used for the six-section PIC (as described in Chapter 4). In addition, the fabrication process of the ridge waveguide for the confinement of the optical mode is the same as that described for the six-section PIC [319].

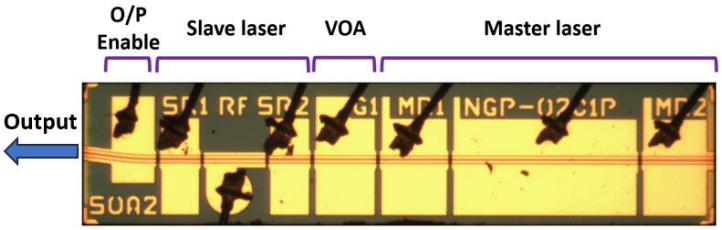

Figure 5.2.1. A microscope image of the eight-section PIC fabricated.

The entire device is ~2 mm long and it is divided into four main sections: ML, VOA, SL, and an SOA (as shown in Figure 5.2.1). The front and back facets are anti-reflective (AR) and high reflective (HR) coated, respectively. The waveguide at the front section is angled at 7° to minimize optical feedback [321].

Figure 5.2.2 represents a detailed 3-dimensional architecture of the eight-section PIC. ML are formed by introducing gain sections that are each sandwiched between two reflector sections. In six-section PIC the SL was implemented by placing a gain section between PR coating and a reflector section. However, in this PIC the SL adapts architecture of ML (reflector-gain-reflector). The length of the ML and SL are 1126 µm and 485 µm respectively. The reflectors MR1, and MR2 are formed by making 24 slots of three distinct periods (as shown in Figure 5.2.3(a)). Similarly, the slave gain (SG) between the SR1 and SR2 sections forms the SL. The slave reflectors have a single period order grating structure as depicted in Figure 5.2.3(b). Since we need shorter SL and single period gratings are shorter than the multi-period grating with the same number of slots. of slots, the SL uses single period grating (as depicted in Figure 5.2.3(b)). Like six-section PIC the length of the SG

section and size of contact pad is optimised to achieve high modulation bandwidth.

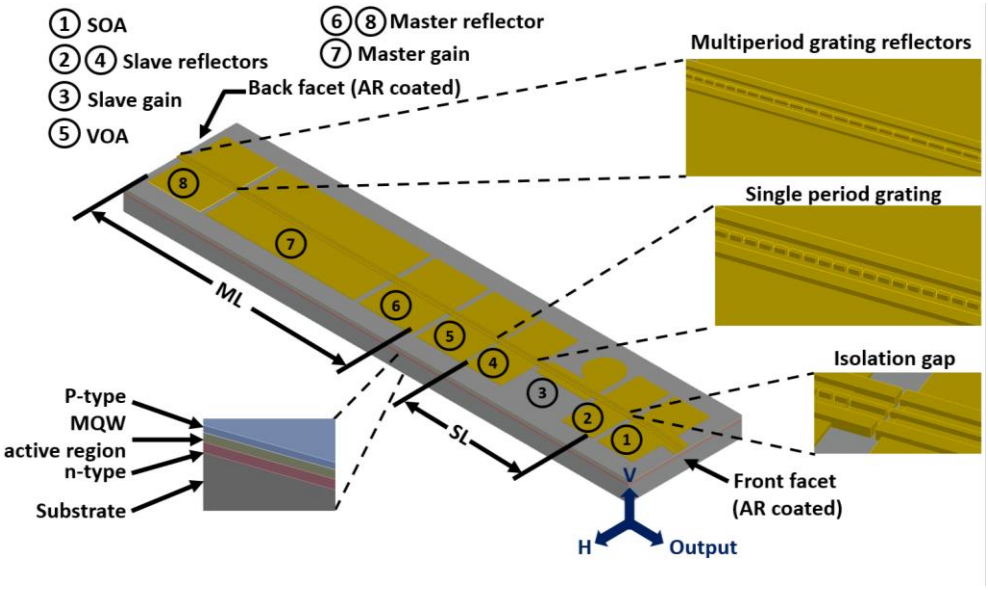

Figure 5.2.2. 3-dimensional architecture eight-section PIC transmitter.

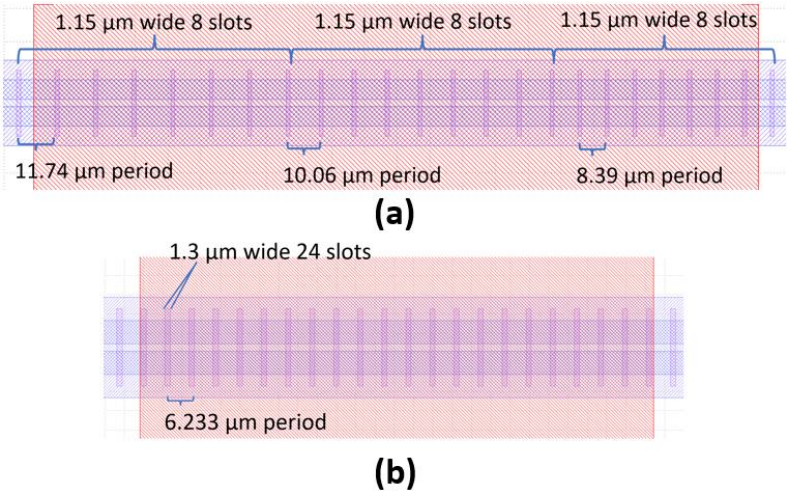

Figure 5.2.3. Figure of a (a) three-period and (b) single-period grating structure.

For the same reason, the contact pad of the SG section is kept small (150 µm diameter) thereby reducing the RC time constant (lowering the effect of parasitic capacitance). A short (221 µm) gain section, introduced between the ML and SL, serves as a VOA. Finally, the last section close to the output facet, is a 230 µm long semiconductor optical amplifier (SOA) to enable absorption, amplification, and optical gating. The SOA

section is kept short to support fast turn on/off operation. To isolate the flow of current between adjacent sections, a slot in the p-region with a depth of 1.35 µm and width of 1.15 µm is introduced. In addition, a 10 µm gap is also maintained between all the contact pads that provides 10 kΩ resistance to further restrict the flow of current to adjacent sections.

5.3 Static characterization

To begin the characterization of this new eight-section PIC, a subcarrier realised as a PCB is manufactured containing a 50 Ω grounded coplanar waveguide-based transmission line and DC contact pads. After that, the chip is mounted on the PCB, with each section (except the SG section) wire bonded with the DC gold pads of the subcarrier. The contact pad of the SG section is wirebonded to a matching resistance (34 Ω) that is soldered on a 50 Ω radio RF track [322]. To maintain the PIC at a constant temperature of 18°C throughout the entire characterisation and system experiments, a TEC, driven with a PID temperature controller, is placed under the PCB together with a temperature sensor. The output of the transmitter is coupled to a conical lens fiber mounted on a 3-axis auto-aligner, which plays a crucial role in maintaining optimum coupling of the light to the lensed fiber. Initially, only the SOA, SR1, SG and SR2 sections are biased to determine the standalone performance (L−I and spectrum) of the SL.

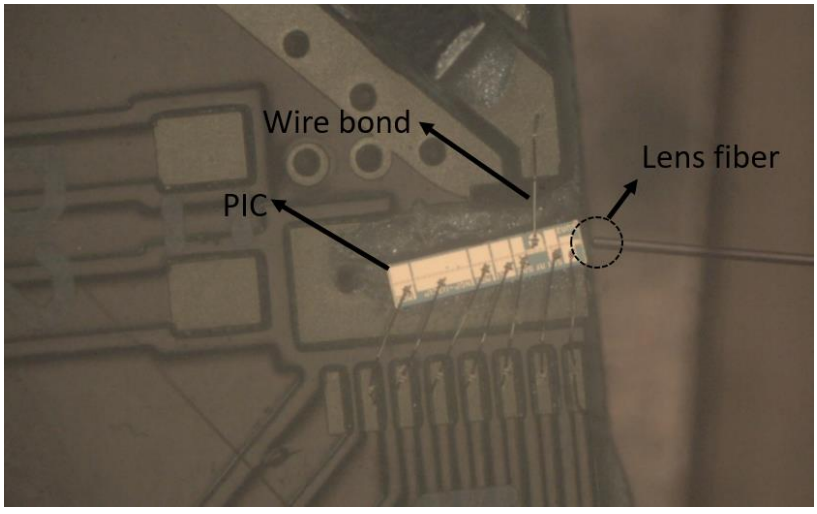

Figure 5.3.1. (a) A photograph of the subcarrier with mounted and wirebonded PIC. Also seen on the RHS of the image is lensed fiber (circled) for the coupling of light.

5.3.1 L−I Characteristic of SL

To measure the L−I curve, the bias currents of the SOA, SR1 and SR2 are set to 21 mA, 45 mA and 45 mA, respectively. The SL exhibits single mode operation when SR1 and SR2 are biased above 40 mA. As typical slot-based reflectors introduce a high loss due to scattering, here SR1 and SR2 act as active DBRs thereby compensating the loss [323], [324]. Hence a minimum current of 21 mA is required to allow traveling of light through the reflector sections. The DC current of the SG section is swept, from 0 to 90 mA in steps of 1 mA, and the output power of the device is recorded using a wide area photodiode. Figure 5.3.2 shows that the threshold of the SL is ~12 mA and that the L−I exhibit a sublinear behavior, which can be linked to gain compression [325]. As the generation of light increases with an increase in injection current, a high number of carriers are consumed at the lasing wavelength. This leads to spectral hole-burning, which reduces the gain available at that wavelength and in turn leads to a less efficient lasing process. Hence, for the higher injection current, a reduction in the number of generated photons causes the sublinear L−I characteristics. Another interesting observation from Figure 5.3.2, is the kink observed at a bias current of ~70 mA. This can be attributed to a mode-hop.

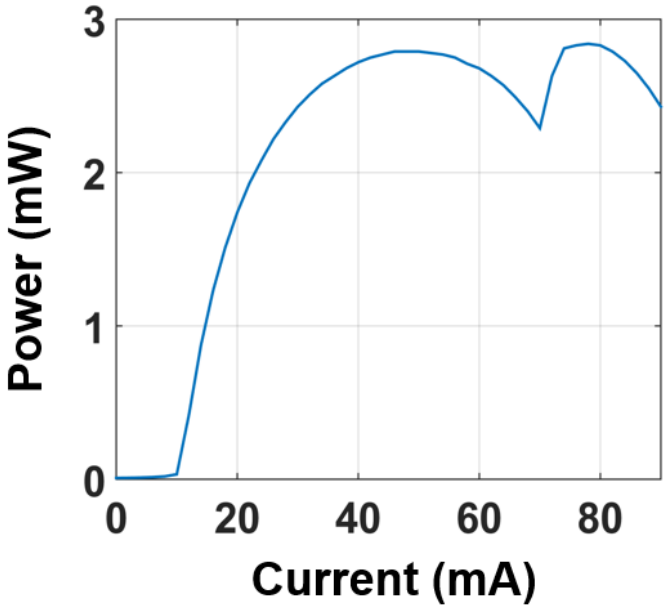

Figure 5.3.2. L−I characteristic of the slave laser with SR1 biased at 45 mA and SR2 at 45mA.

5.3.2 Wavelength and SMSR maps of the SL

In the next phase, the wavelength and SMSR maps of SL are measured to identify the wavelength range, over which a single mode operation of the SL can be attained. To this effect, the current in the SG section is swept from 10 mA to 70 mA (at steps of 1 mA), the bias to SR1 and SR2 (same current applied to both) is swept from 5 mA to 65 mA (with an increment step of 1 mA), and the SOA section is biased at 21 mA. The measured peak wavelength and SMSR maps are shown in Figure 5.3.3(a) and Figure 5.3.3(b), respectively. The plots demonstrate a wavelength tunability of the SL from 1529.5 nm to 1533 nm at the SMSR $>$ 30 dB. Figure 5.3.3(c) shows the SMSR as a function of the slave laser emission wavelength (from 1529 to 1534 nm) and is achieved by extracting all wavelengths that exhibit an SMSR more than or equal to 35 dB. Thereafter, an optical spectrum (shown in Figure 5.3.3(d)) is captured for sections biases SR1 $=$ 45 mA, SR2 $=$ 45 mA, and SG $=$ 40 mA, i.e., currents for which the SL portrays the lowest threshold current and an SMSR $>$ 42 dB.

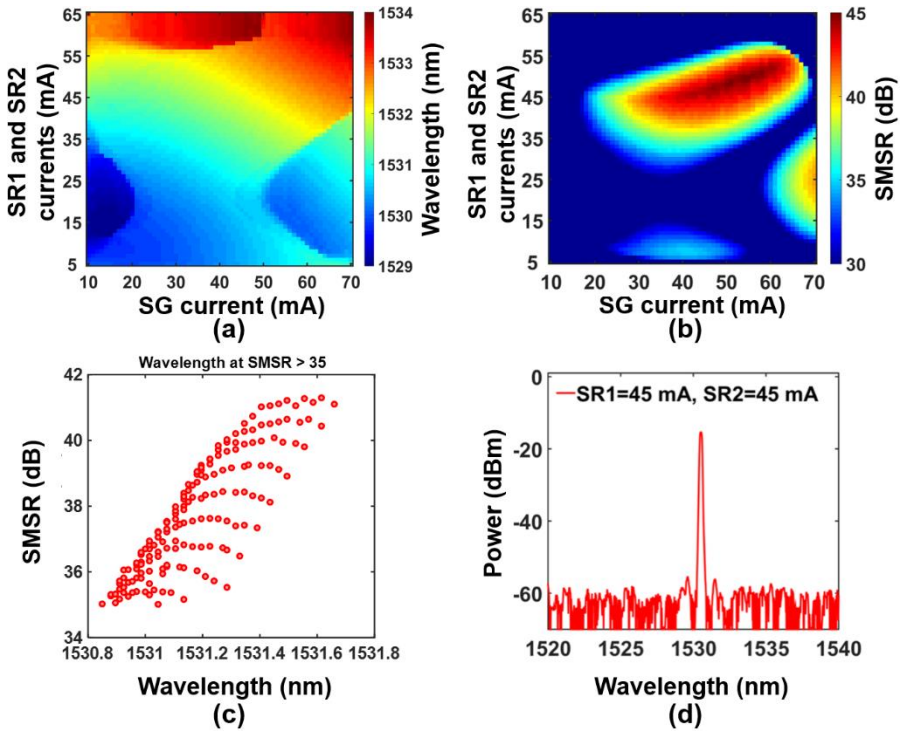

Figure 5.3.3. Heat maps of (a) wavelength and (b) SMSR of slave laser, (c) wavelengths at SMSR $>$ 35 dB, and (d) spectrum of SL at SR1 $=$ 42 mA, SR2 $=$ 45 mA, SG $=$ 40 mA.

Subsequently, we proceed to confirm the independent lasing of the ML and SL. To do this, we apply the following currents to the device: SR1 = 42 mA, SR2 = 45 mA, SG = 40 mA, MR1 = 20 mA, MR2 = 45 mA, MG = 40 mA, VOA = 4 mA. The optical spectrum in Figure 5.3.4 shows ML and SL lasing at 1531 nm and 1532 nm, respectively. At the output facet the peak power of ML is lower than SL, which results from the fact that the access to ML output facet is via SOA, SL and VOA, all of which attenuate the optical output from ML.

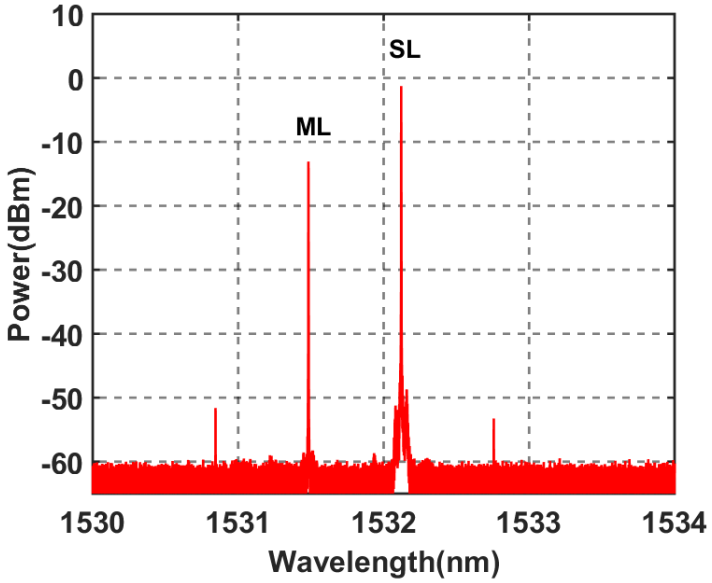

Figure 5.3.4. The optical spectrum of the SL and ML lasing independently.

5.3.3 Optical injection locking

The injection locking of the SL is achieved by gradually increasing the currents of the ML sections; namely MR1, MG, and MR2, until a single mode optical spectrum with a high SMSR is obtained. As shown in Figure 5.3.5, the wavelength at which OIL is achieved portrays an SMSR of 60 dB which proves the ability of the PIC to achieve OIL at a single wavelength. However, to verify the compatibility of the PIC based transmitter with the NGPON2 wavelength grid, a more comprehensive test is performed. The procedure of finding the wavelengths where the SL is under OIL is showed as a flowchart in Figure 5.3.6. It consists of two main steps: a coarse-tuning and fine-tuning of the ML.

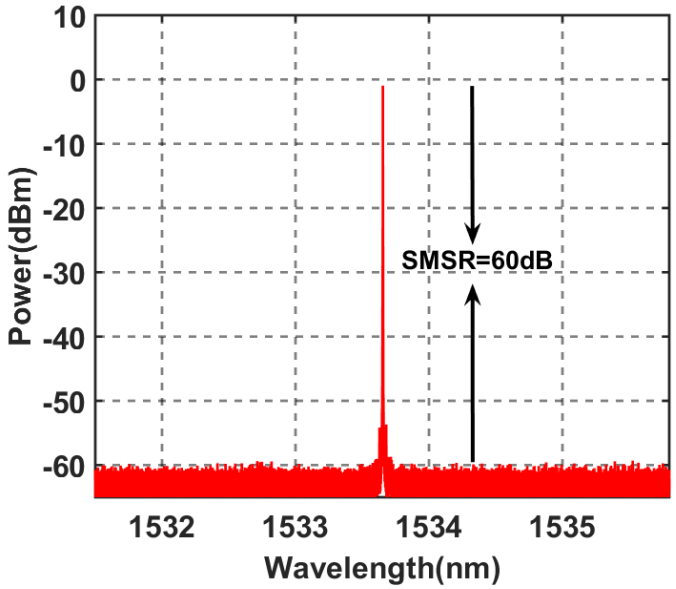

Figure 5.3.5. Optical spectrum of the SL when under OIL (measured at 0.16 pm resolution).

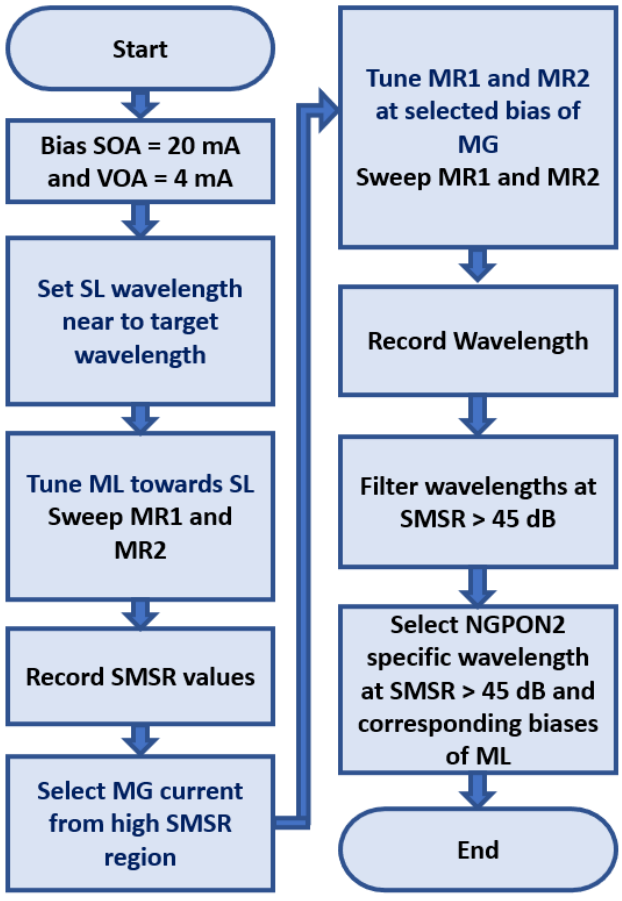

Figure 5.3.6. Flow chart for finding the wavelengths at which the SL is under OIL.

The steps applied to find OIL at a target wavelength (e.g., 1533.46 nm) are as follows; first, the SL is tuned to one of the NGPON2 wavelengths and a coarse tuning operation is performed. To initiate this operation, the sections SR1, SG and SR2 are biased at which point the SL lases close to the target wavelength (for 1533.47 nm the biases are 37.82 mA, 50 mA, and 46 mA, respectively). The SOA section is driven at transparency (21 mA) and kept unchanged in further measurements.

Subsequently, the ML sections MR1, MG, and MR2 are biased at 35 mA, 85 mA, and 35 mA. At this bias, the ML is at a slightly lower wavelength than the SL (1532.8 nm). Thereafter, the current in the MG section is swept from 85 mA to 115 mA in steps of 1 mA, while the currents applied to MR1 and MR2 are simultaneously varied from 35 mA to 60 mA in steps of 1 mA. This two-dimensional scan (MR1 & MR2 current vs MG current) tunes the ML wavelength (from shorter to longer wavelength) towards that of the SL. As soon as ML enters the injection locking range, the ML pulls the SL to its wavelength. The OIL condition is maintained when ML and SL are in locking range during tuning operation of ML and produce several wavelengths at high SMSR. By measuring the SMSR during this current sweep and identifying the regions with an SMSR value exceeding 40 dB, it is possible to identify all wavelengths at which OIL can be achieved (the red region in Figure 5.3.7(a)).

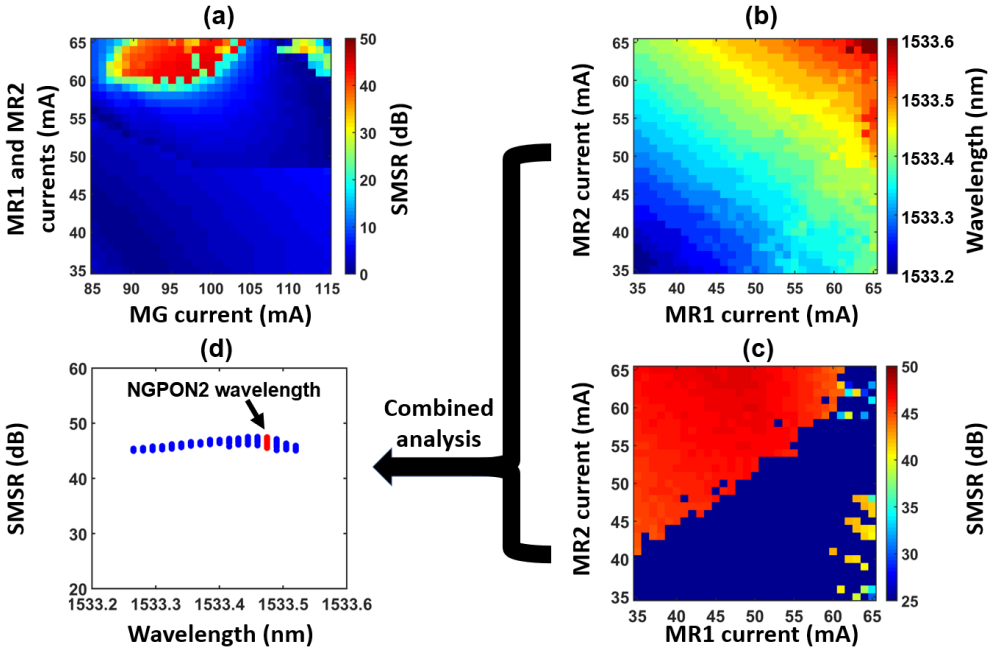

Figure 5.3.7. (a) SMSR map of SL in coarse tuning of ML, (b) wavelength and (c) SMSR

map in fine tuning operation of ML at $MG = 100$ mA, and (d) extracted OIL wavelengths (blue) and NGPON2 specific wavelength (red).

Figure 5.3.7(a) shows that the SL tends to be injection locked when the MG section is biased between 90 mA to 102 mA. In the second step (fine-tuning operation), the same investigation is carried out by biasing the MG at 100 mA and carrying out a two-dimensional current sweep of the MR1 and MR2 sections. Again, the wavelength and SMSR are plotted as heat-maps, which are shown in Figure 5.3.7(b) and Figure 5.3.7(c) respectively. In Figure 5.3.7 (c), the region in red shows all the possible wavelengths, where OIL could be achieved. To find the settings for the desired channel (1533.46 nm), all achievable wavelengths with SMSRs $>$ 45 dB are extracted and plotted in Figure 5.3.7(d). The red dots in Figure 5.3.7(d) corresponds to the target IL wavelength, showing that there are several bias current combinations delivering the target channel. Amongst these, the operating point providing the highest SMSR is chosen for further characterization.

5.3.4 Wavelength tunability

Our focus is on designing a transmitter to operate in the upstream direction in NGPON2 network. Hence, the transmitter must comply with the upstream transmission standards described in [83] such as wavelength spacing and tunability. As mentioned in section 1.5.6, the NGPON2 upstream transmitter generates four wavelengths with allowed spacing of 50 GHz, 100 GHz, and 200 GHz. Therefore, the procedure of finding OIL wavelengths (process mentioned above) is repeated for the remaining three NGPON2 wavelengths (1532.68 nm, 1534.25 nm, 1535.02 nm). The overlaid spectrum of all four wavelengths (labelled OIL1 to OIL4) on the 100 GHz grid, measured with the aid of a high resolution (0.16 pm) OSA, are shown in Figure 5.3.8.

The output power of the PIC at OIL1, OIL2, OIL3, and OIL4, when the SOA is biased at 21 mA, is 3.16 dBm, 2.71 dBm, 2.94 dBm, and 2.42 dBm, respectively. The power can be enhanced to 7.02 dBm, 7.46 dBm, 7.51 dBm, and 7.05 dBm by increasing the SOA bias current to 30 mA. The difference in peak power between the wavelength channels is due to a misalignment of the lens fiber (mounted on 3-axis translation stage) caused by minor thermal variations that are not compensated for by the temperature control arrangement used.

Table 5.3.1 shows the bias currents applied to different sections of the transmitter for the four wavelengths shown in Figure 5.3.8.

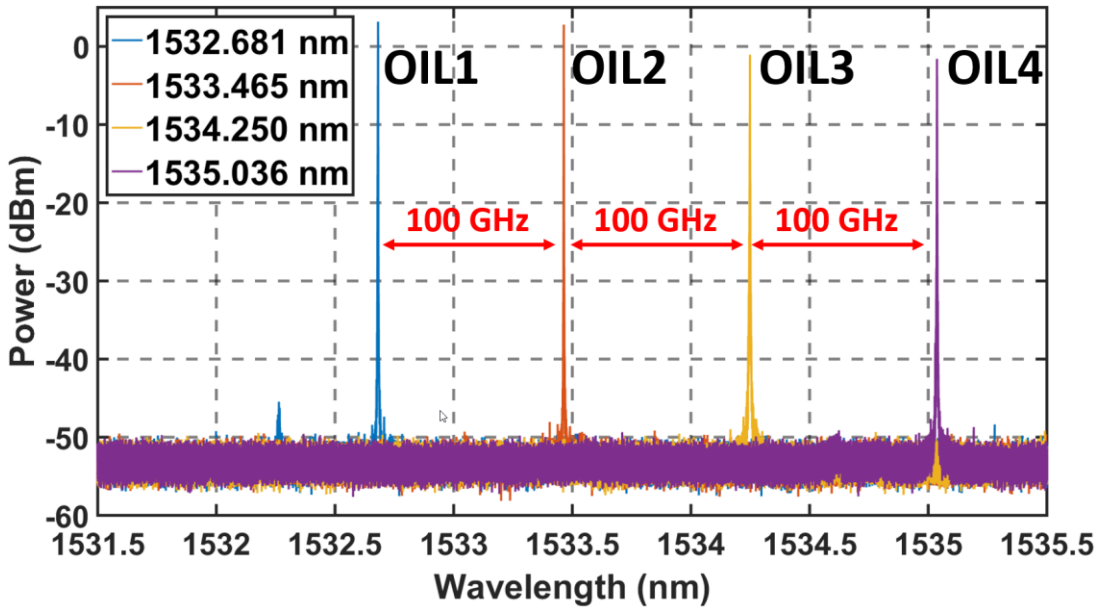

Figure 5.3.8. Optical spectrum of the four wavelengths, on 100 GHz grid, where OIL is achieved.

Sections	OIL1	OIL2	OIL3	OIL4
SOA	21 mA	21 mA	18 mA	18 mA
SR1	24 mA	37.82 mA	46 mA	46 mA
SG	51 mA	50 mA	56.38 mA	56.38 mA
SR2	40 mA	46 mA	51 mA	51 mA
VOA	1 mA	2 mA	1 mA	2 mA
MR1	62.42 mA	60 mA	80 mA	88 mA
MG	78 mA	108 mA	94 mA	96.4 mA
MR2	50 mA	61 mA	70 mA	70 mA
Temp	17 ºC	18.5 ºC	17.5 ºC	24 ºC

Table 5.3.1. Bias data for achieving 4 wavelengths, on 100 GHz grid, with OIL.

5.3.5 Linewidth measurement

In further characterization the linewidth performance of the SL and ML is determined to confirm the effect of OIL. The optical linewidth is measured using method described in chapter 4 [296] and the experimental setup used for linewidth measurement is shown in Figure 5.3.9.

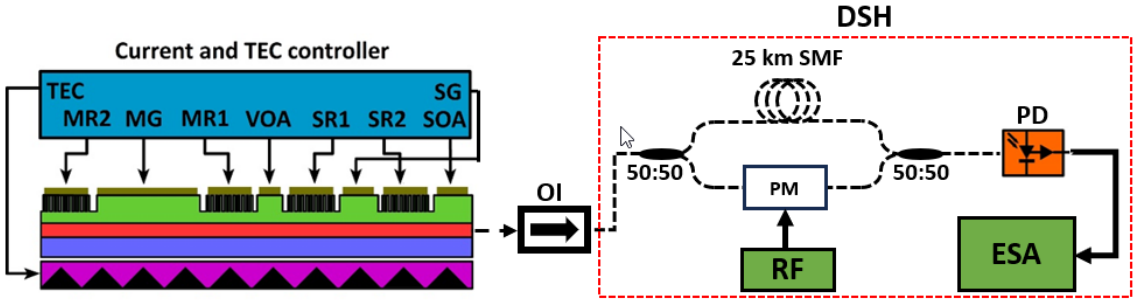

Figure 5.3.9. Schematic of the experimental setup for linewidth measurement. DSH: delayed self-heterodyne, OI: optical isolator, SMF: single mode fiber, RF: radio frequency, PM: phase modulator, PD: photodiode, ESA: electrical spectrum analyser.

The description and procedure of the linewidth measurement is mentioned in section 4.3.6 (Chapter 4). As the optical linewidth of a semiconductor laser is inversely proportional to its length [295], we expect better linewidth from ML in comparison to SL. As mentioned earlier, the length of the ML and SL are 1068.5 µm and 494.5 µm, respectively. Initially, the linewidth of the SL is measured for the SOA, SR1, SR2, SG sections biased at 17.5 mA, 45 mA, 52 mA, and 52 mA, respectively. The VOA and ML sections are left unbiased. The chosen SG bias current is about 3 times the threshold of the SL at which the lasing mode exhibits an SMSR > 35 dB. Figure 5.3.10(a) depicts the electrical spectrum of the measured beat tone signal using PD together with a superimposed Voigt fit [326]. The linewidth of the SL is measured to be 38.4 MHz. After that, the linewidth of the ML is measured with MR1, MG, and MR2 biased at 61 mA, 95.88 mA, and 49.32 mA, respectively.

As the optical emission of the ML flows through the SL and VOA (back facet is HR coated), the SL and VOA section are biased at transparency (SOA=18.56 mA, SR1=15 mA, SG=15 mA, and SR2=15 mA). The optical signal is fed to the DSH setup, and the measured electrical spectrum superimposed with the Voigt fit is shown in Figure 5.3.10(b). The optical linewidth of the ML at the given bias is measured to be 4.4 MHz. The measurement confirms

that the linewidth of the ML is nine times better than the SL. As previously mentioned, the linewidth of SL when injection locked follows the linewidth of the ML. Hence, the linewidth of the SL when injection locked is measured for two wavelengths; namely IL2 and IL4 and the results are shown in Figure 5.3.11. The measured linewidth of IL2 and IL4 are 6.125 MHz and 9.87 MHz, respectively. The linewidth of IL4 in comparison to IL2 is approximately 1.5 time and this attribute to thermal effect [295] and low level of optical injection.

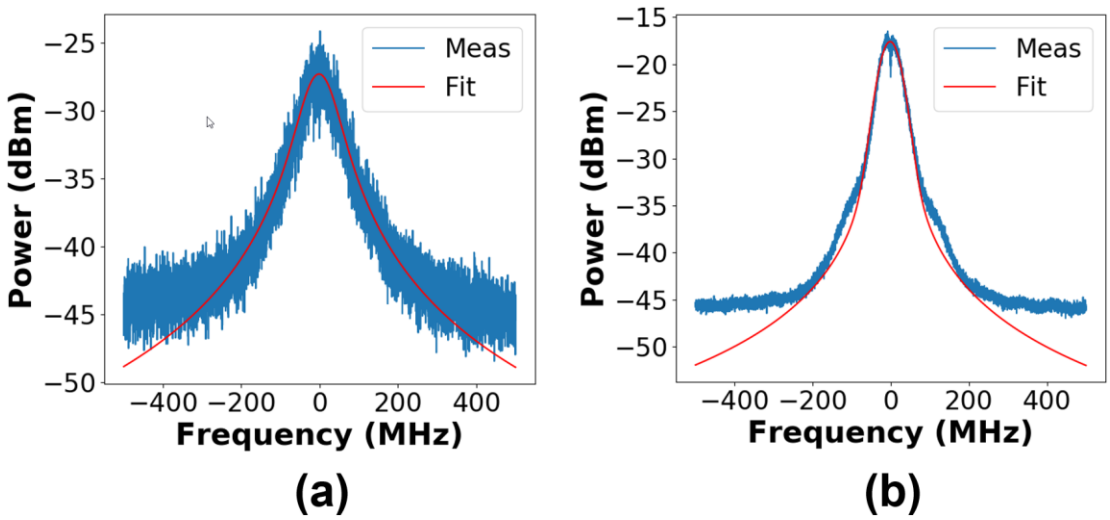

Figure 5.3.10. The electrical spectra of beat tone and Voigt fits to measure linewidth of (a) SL and (b) ML.

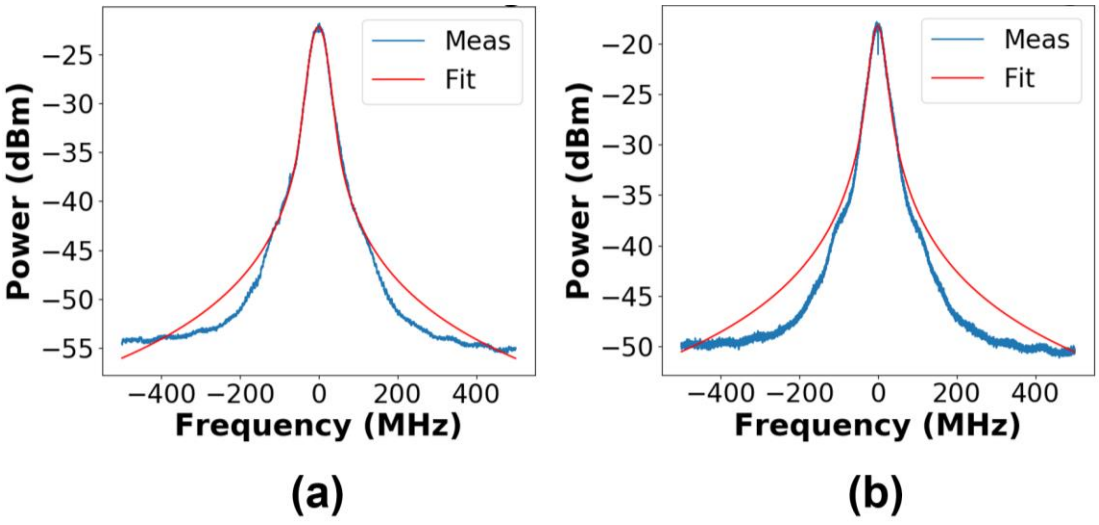

Figure 5.3.11. The electrical spectra of beat tone and Voigt fits to measure linewidth of (a) IL2 and (b) IL4.

5.3.6 RIN measurement

The RIN of the free running and OIL laser is measured using the method [296] described in section 4.3.7. The schematic of the experimental set-up used is depicted in Figure 5.3.12. The total noise present in the optical signal of the laser is RIN, thermal noise, and shot noise. Hence, the RIN of the laser is determined by subtracting the noise contributed by thermal noise and shot noise from the total noise.

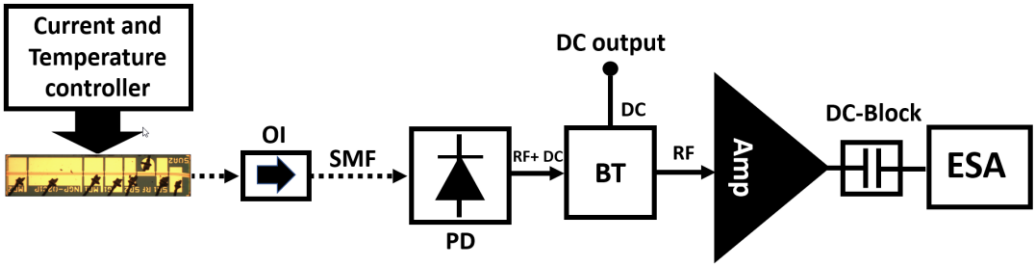

Figure 5.3.12. Schematic of the experimental setup for the RIN measurement. OI: optical isolator, SMF: single mode fiber, RF: radio frequency, DC: direct current, PM: phase modulator, PD: photodiode, ESA: electrical spectrum analyser, Amp: amplifier.

The RIN of the SL is determined by measuring electrical spectrum and plotted in Figure 5.3.13 for the free running case and OIL with different optical injection levels. From the figure it can be seen that the average RIN of the free running SL over 1 to 6 GHz span is lower than -130.6 dBc/Hz.

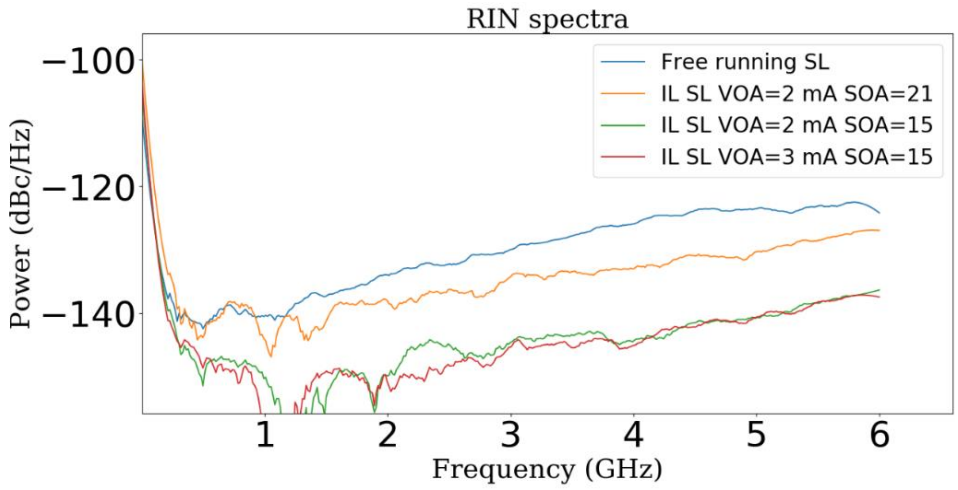

Figure 5.3.13. Measured RIN spectrum of the free running SL (blue) and OILed SL at 2 mA (orange), 3 mA (green), and 10 mA current (orange) VOA currents.

The RIN of the SL is significantly lower when the laser is injection locked due to the reduction in spontaneous emission. Moreover, the RIN of the IL SL is further reduced for higher levels of the optical injection (achieved by increasing the bias of the VOA section to allow more light from ML). The RIN decreases from −135 dBc/Hz to −137 dBc/Hz when the VOA current is increased from 2 mA to 3 mA. In addition, it is observed that the RIN of SL also reduces when the SOA current is reduced, from −134 dBc/Hz at SOA current of 21 mA to −144 dBc/Hz for the SOA current of 15 mA. We attribute this to the change in the ASE noise generated by the SOA [327] and the increased back-reflection from output facet to SL [328].

5.4 Dynamic characterization

Since the PIC is to be employed in a direct modulation set-up, the next step entailed the dynamic characteristic of the SL. As in the case of the six-section device, all measurements here are carried out in two regimes: free running and OIL. The first dynamic characteristic to investigate is the frequency response of the SL. Subsequently, the optical spectra and eye diagrams are examined and finally, the frequency chirp is explored.

5.4.1 Measurement of modulation response

The setup used for measuring the modulation response is shown in Figure 5.4.1. In addition to DC bias currents applied to all sections, an RF signal from a vector network analyser (VNA) is supplied to the SG using a bias tee. Then, the modulated optical output is coupled, with the aid of a lensed fiber followed by an inline optical isolator, to a high-speed photodetector. The detected RF signal is passed into the input port of the VNA for the S21 measurements.

First the modulation response of free running SL is measured for SOA, SR1, SG, and SR2 biased at 21 mA, 37.82 mA, 50 mA, and 46 mA, respectively. The ML (MR1, MG and MR2) and VOA sections are turned-off. The result is plotted in Figure 5.4.2 in blue colour. The figure shows that the modulation bandwidth of the free running SL is limited to ~5.8 GHz. The next step entailed biasing the PIC sections to achieve the OIL2 operating point

(VOA, MR1, MG, and MR2 sections biased at 2 mA, 60 mA, 108 mA, and 61 mA, respectively). The modulation bandwidth, measured at this operating point (OIL2) is 8.8 GHz (shown in orange in Figure 5.4.2). The modulation response of SL is significantly improved from ~5.8 GHz to ~8.8 GHz that clearly depict the merit of OIL.

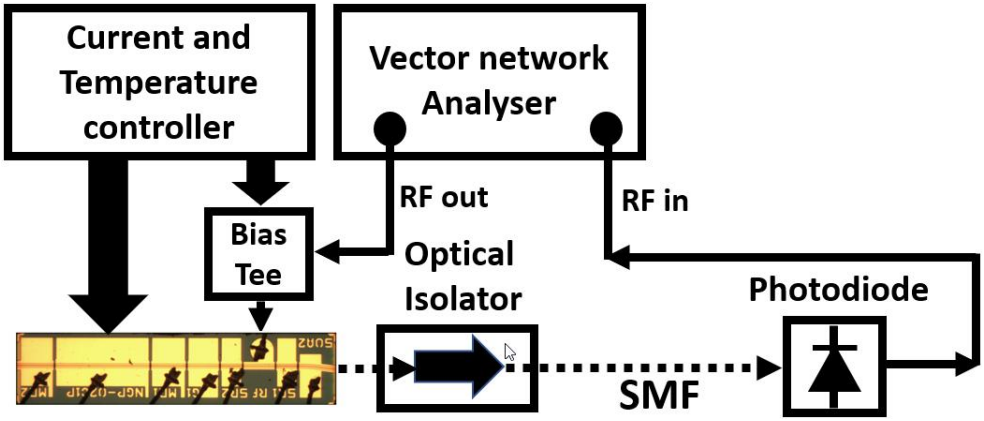

Figure 5.4.1. Schematic of the experimental setup used for measuring the frequency response of eight-section PIC.

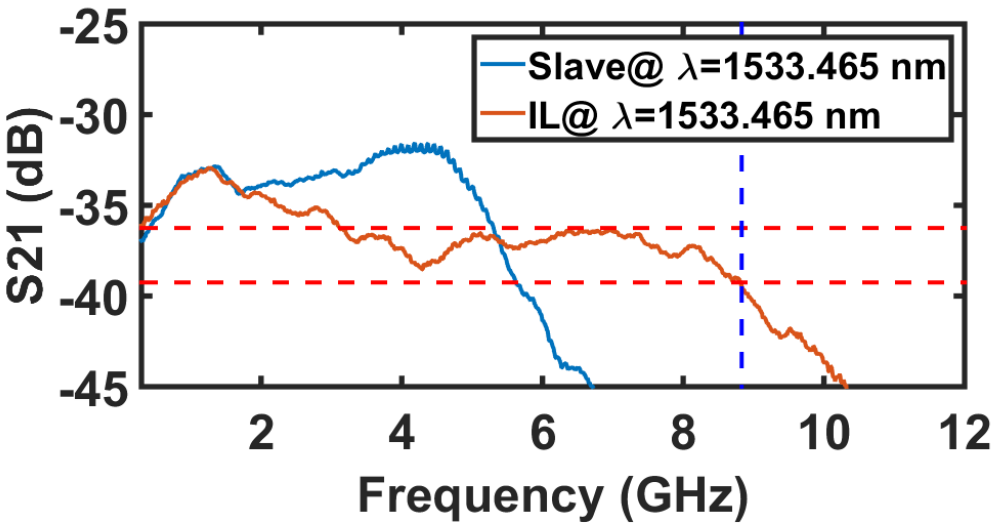

Figure 5.4.2. Frequency response of the SL in free running (in blue colour) and under OIL condition (in orange colour).

5.4.2 Chirp measurement

Another step in the dynamic characterisation is the measurement of chirp imposed on the signal due to direct modulation of the multi-section PIC. The experimental setup used for the

chirp measurement is shown in Figure 5.4.3, while the technique is described in the section 4.4.2. The slave gain section of the PIC is directly modulated with a PRBS of length $2^{15}-1$, sourced from a PPG. The bit rate of the modulating signal is set to 5 Gb/s (because the modulation response of SL is limited to ~5.8 GHz) with a peak-to-peak voltage of 1.5 V and applied to the laser in conjunction with a DC bias current. The output signal of the PIC is either directly connected to OSA (0.16 pm resolution) or fed to an AMZI filter. Then the output of AMZI filter is split using a 90:10 coupler, with the 10% tap connected to an OSA and the 90% supplied to a high-speed photodetector (20 GHz). The electrical output of the photodetector is connected to a sampling oscilloscope synchronized to PPG. Firstly, the amount of chirp is estimated from the spectral width and subsequently measured using the filter technique [316], [317].

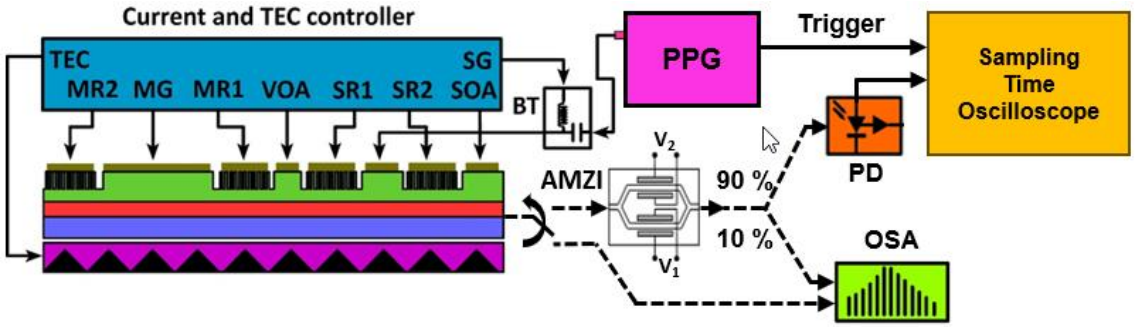

Figure 5.4.3. Schematic of the experimental setup used for the chirp measurement. AMZI: asymmetric Mach-Zehnder interferometer, BT: bias-tee, OSA: optical spectrum analyser, PPG: pulse pattern generator, PD: photodetector.

5.4.2.1 Measurement of chirp using OSA

Initially the chirp imposed by direct modulation of SL is observed by inspecting the optical spectra on a high resolution OSA (0.16 pm). The impact of the injection level on the spectral width of the SL for all four OIL operating points are investigated by varying the bias of the VOA section.

As mentioned earlier, an increase in the VOA bias current reduces the optical attenuation thus increases the optical power injected from the ML into the SL. The higher level of optical injection leads to a reduction of the frequency chirp and thereby the overall spectral width [329]. Figure 5.3.4(a), (b), (c), and (d) shows the optical spectra emitted by

the PIC when operating at OIL1, OIL2, OIL3 and OIL4, respectively, for three values of the VOA bias current. It is important to point out that the wavelength of the SL remains almost constant for all three VOA biases used, indicating the ability to optimize the injection level without affecting the operating point of the SL. The plots clearly show that, at all OIL operating points, the spectral width (thus the chirp) is reduced significantly as the level of injection is increased (as the VOA current is increased). For example, the measured spectral width (20-dB below the spectral peak [330]) at the OIL2 operating point at VOA bias currents of 1 mA, 2 mA, and 4 mA are ~98.7 pm, ~94 pm, and ~92 pm, respectively. In addition, the appearance of the "rabbit ears" in the spectrum, indicating the presence of transient chirp [331], is also reduced. The transient chirp is dominant over adiabatic chirp when the laser is directly modulated at high bit rate (> 2 Gb/s). The lowest spectral width is obtained when the VOA bias is set at 4 mA.

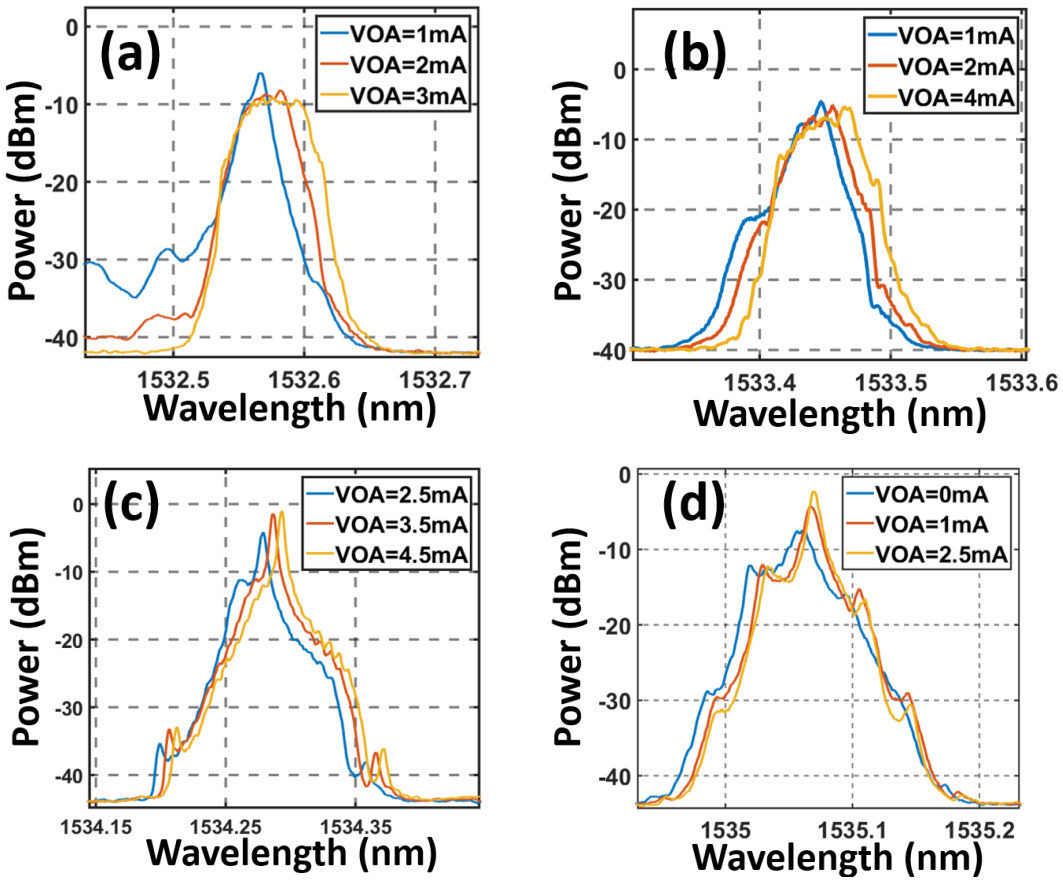

Figure 5.4.4. Optical spectra of the modulated SL operating points at different levels of optical injection (a) OIL1, (b) OIL2, (c) OIL3, and (d) OIL4.

Next, the effect of frequency chirp on spectrum together with eye pattern is investigated for 10 Gb/s directly modulated. As the previous characterizations are done on OIL2 operating point, we chose the same for further investigation. An optical spectrum of the modulated SL is captured at the transmitter and compared under two cases: without and with the optical injection (see Figure 5.4.5(a)). In the first case, the spectrum (blue line) is broader because of the presence of frequency chirp induced by direct modulation. However, we clearly see a reduction in the spectral width in the second case (orange line). The wavelength of the OIL SL is red-shifted due to the induced change in the effective refractive index cause by the injection. In addition, we see an improved eye diagram when the SL is injection locked in comparison to the free running SL. This can be attributed to the damped relaxation oscillations and improved modulation response, and the reduced amplitude fluctuations.

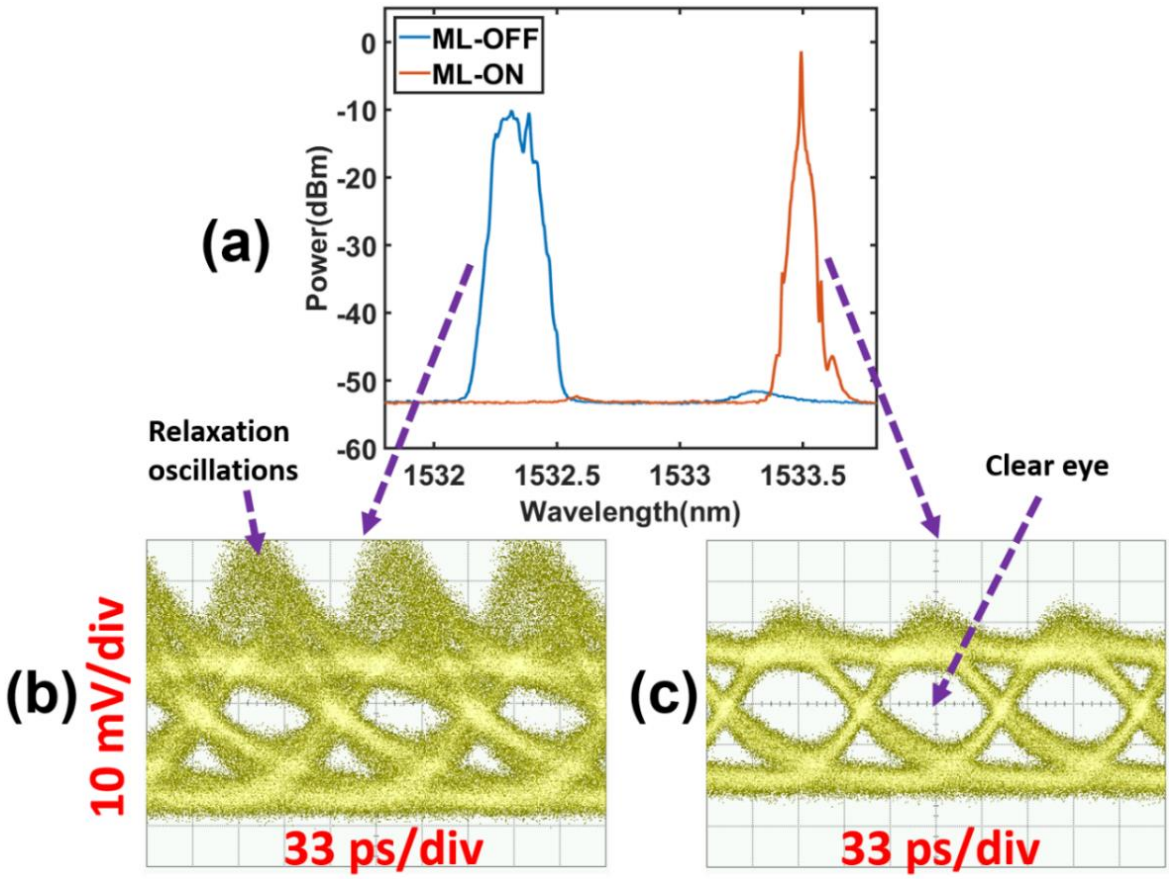

Figure 5.4.5. A comparison of optical spectrum of modulated SL: without the injection (blue) and IL (orange), eye diagrams of free running (b) and optically injected (c) SL.

It is important to note that a high level of optical injection provides a major boost to direct modulation by significantly reducing the chirp. However, at the same time it also has a negative impact by reducing the threshold of the laser, which results in a degraded extinction ratio (ER) [332], [333], [334], [335]. The latter was thus measured by feeding the output of the PIC transmitter to a DC-coupled photodiode at the front end of a sampling oscilloscope. The test was carried out for VOA bias current of 1 mA to 2 mA, and 4 mA, and the ER was measured to be ~3.9 dB, ~3.8 dB, and ~3.6 dB respectively. Hence, the VOA plays an important role in managing the trade-off between the reduction of the chirp and ER. The ER is then verified for all the four wavelength channels at the OIL operating points of OIL1, OIL2, OIL3, and OIL4 and found to be 3.6 dB, 3.8 dB, 4.1 dB, and 4.8 dB, respectively. The corresponding average output power levels were 6.0 dBm, 5.66 dBm, 5.81 dBm, and 4.81 dBm, respectively. From these measurements, it is apparent that the ER at OIL3 and OIL4 are 0.1 dB and 0.8 dB higher than the specified limit of 4 dB. However, at OIL1 and OIL2, the ER requires a marginal improvement of 0.4 dB and 0.2 dB, respectively.

The ER of the PIC in future designs could be improved by changing some design parameters. One such avenue could be through the shortening of the SL cavity length to improve the frequency response [336]. Other potential paths are by reducing the internal [337], and mirror losses [278] to enhance the slope efficiency, and by optimizing the slot width, slot depth, and period order of slot grating.

5.4.2.2 Measurement of chirp using frequency discrimination method

Further investigation of chirp present in the optical signal is investigated using filter technique described in chapter 4, section 4.4.2.2. Figure 5.4.6(a) and (b) shows the measured chirp for the free running (non-injected) and the IL scenarios. In the first instance, a data signal at 5 Gb/s was used. In the free running case, the maximum chirp is measured to be ~9.7 GHz. Next, the VOA, MR1, MG and MR2 sections are biased at 2 mA, 60 mA, 108 mA, 61 mA, respectively, to achieve OIL2 operating point. For these settings, peak to peak chirp is measured to be ~2.6 GHz. Next, the data rate is increased to 10 Gb/s. In this case, the chirp imposed by a non-IL SL cannot be measured due to limitation of modulation bandwidth (~5.8 GHz) of free running SL. When the directly modulated SL is biased at an

OIL2 point, the maximum chirp is measured to be ~2.9 GHz. This value is further reduced to 2.6 GHz and 2.5 GHz when the VOA is biased at 3 mA and 4 mA, respectively.

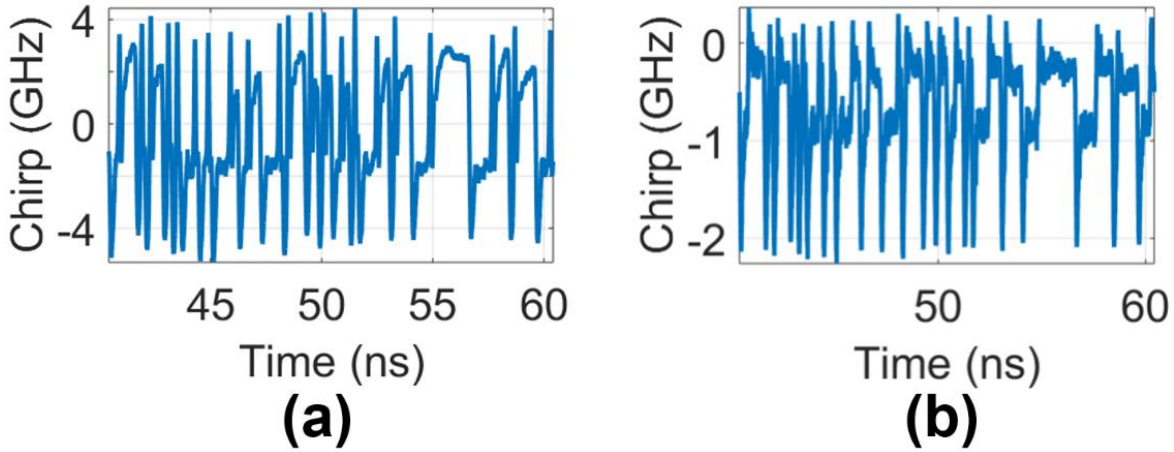

Figure 5.4.6. Frequency chirp of the SL modulated at 5 Gb/s when (a) free running and (b) set to OIL2 operating point.

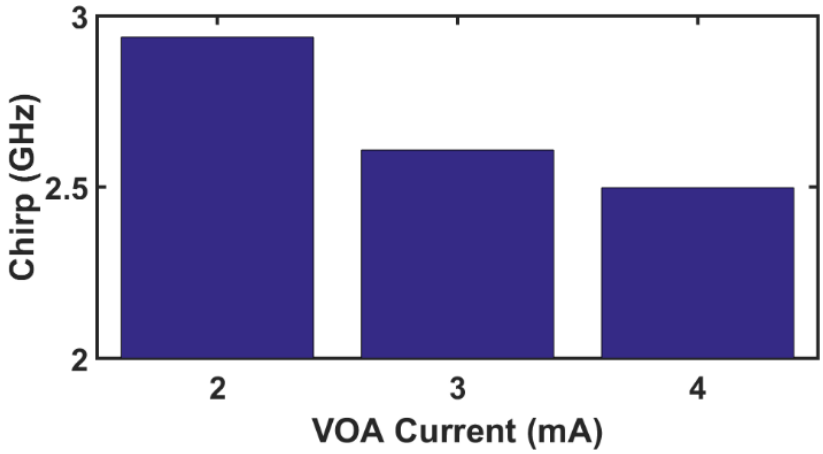

Figure 5.4.7. Reduction of the frequency chirp for increasing VOA bias current when the SL is directly modulated at 10 Gb/s.

5.5 Data transmission

One of the main objectives in this work is to ensure that the signal from the directly modulated eight-section PIC can be transmitted over the maximum transmission distance specified in the NGPON2 standards document [83] i.e., 40 km. Hence, we carry out a data transmission experiment using the setup shown in Figure 5.5.1. The bias currents to obtain

the four OIL operating points are chosen from Table 5.3.1. The SL gain section of the PIC is then directly modulated with a non-return-to-zero (NRZ) PRBS (2^{15}–1) signal at a data rate of 10 Gb/s and a peak-to-peak voltage of 2V. The output signal of the PIC is split using a 90:10 coupler, with the 10 % tap connected to an OSA (0.16 pm resolution) and the 90 % tap used for the data transmission. The received optical power (ROP) is controlled and measured using an external VOA with an inbuilt power meter. This signal is then passed into an APD whose output is connected to an error detector (ED) and the performance of the individual channels is measured via BER measurements. The tests are carried out in a B2B scenario and after 25 and 50 km SSMF transmission.

The resultant plots of the BER versus the ROP for all four channels are shown in Figure 5.5.2. From the figure it can be seen that all channels achieved BER of $1e^{-9}$ in the B2B scenario. Similarly, in the case of 25 km transmission, all channels also show error free performance (BER of ~$1e^{-9}$). For the 50 km transmission, OIL1, OIL2, OIL3 and OIL4 operating points show BER of $5e^{-8}$, $1e^{-9,}$ $1e^{-9}$, and $1e^{-9}$ with power penalties of ~1.5 dB, ~1 dB, ~0.5 dB, and ~2 dB, respectively. The performance of OIL1 is relatively poor and can be attributed to the low extinction ratio (~3.6 dB) caused by low modulation response (~7.8 GHz). On the other hand, the largest power penalty for 50 km transmission is observed for OIL4 (~2 dB at a BER of $1e^{-9}$). This could be ascribed to the lower level of optical injection used leading to the highest degree of chirp, thereby resulting in a larger dispersion penalty.

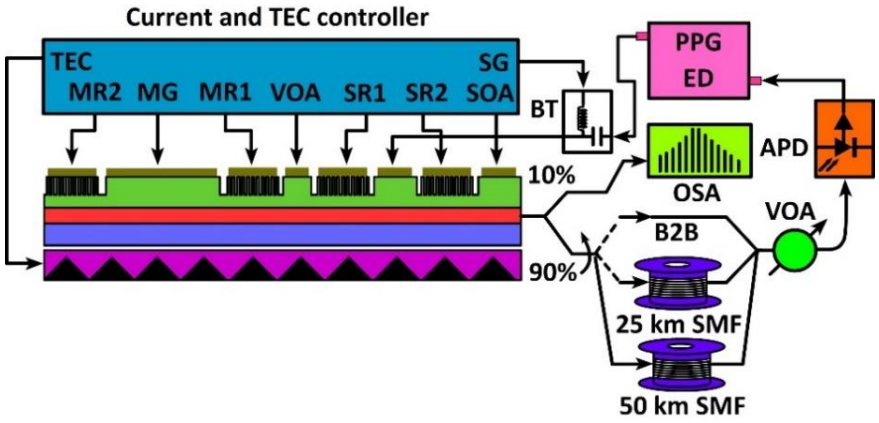

Figure 5.5.1. Schematic of the experimental setup to realise the fiber transmission of a direct modulated 10 Gb/s signal at four OIL operating points. BT: bias-tee, PPG: pulse pattern generator, ED: error detector, OSA: optical spectrum analyser, VOA: variable optical attenuator, APD: avalanche photodiode.

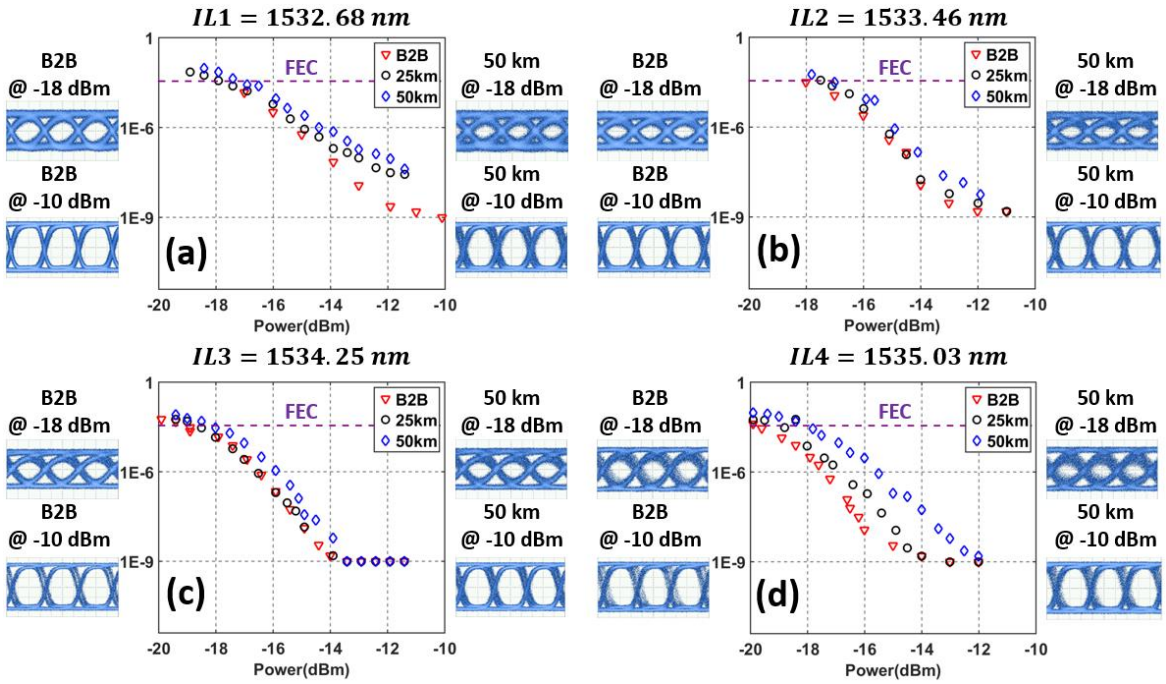

Figure 5.5.2. BER vs. ROP for back-to-back and after transmission over 25 and 50 km of SSMF, inset: eye diagrams at the indicated ROP.

Nevertheless, for all the OIL points are exhibiting BER better than $5e^{-8}$, even after 50 km of uncompensated fiber transmission, which is a significant result for a 10 Gb/s capable directly modulated transmitter. This is made possible by the realised master slave architecture which allows the reduction of frequency chirp thus enabling an extension of the transmission distance. The ability to transmit at 10 Gb/s at each of the four OIL points makes the PIC usable as a NGPON2 transmitter. In addition, comparing to two-section [338], four-section [290] and six-section [322] PIC that depict tunability less than 300 GHz, the current PIC archives wavelength tunability more than 300 GHz and longer transmission distance (50 km).

5.6 Out-of-channel power in burst-mode transmission

Another requirement of the NGPON2 standard, that we tested on the proposed transmitter, is the out-of-channel power-spectral-density (OOC-PSD) [83]. It sets the maximum level of the PSD that a transmitter can generate outside of the operational channel with an aim to minimize cross-channel interference. To verify the compliance with the OOC-PSD

requirement, the spectrum of the transmitter in burst mode is measured and compared with the NGPON2 specifications. For this test, the SOA is turned on and off during the burst mode operation. We start off by generating a 62.5 µs, 50% duty cycle, 2V pk-pk square wave (transmitter enable signal) and apply it to the SOA to enable/disable the output of the transmitter. A 10 Gb/s non-return-to-zero (NRZ) data signal with a $2^{15}-1$ PRBS is then applied to the SL, while the SOA is enabled. As the SOA settling time is 50 ns, the modulating signal to the SL is applied after a delay of 50 ns. The optical output is detected using a PIN PD and analyzed using a high-speed sampling oscilloscope. Figure 5.6.1(a) shows the received burst data signal after the PD and the corresponding eye pattern. The optical spectrum of the burst mode signal (Figure 5.6.1(b)) is observed using an OSA set in the maximum hold mode. The OSA resolution is set to 0.02 nm and spectrum is swept until no change in the spectral shape is detected.

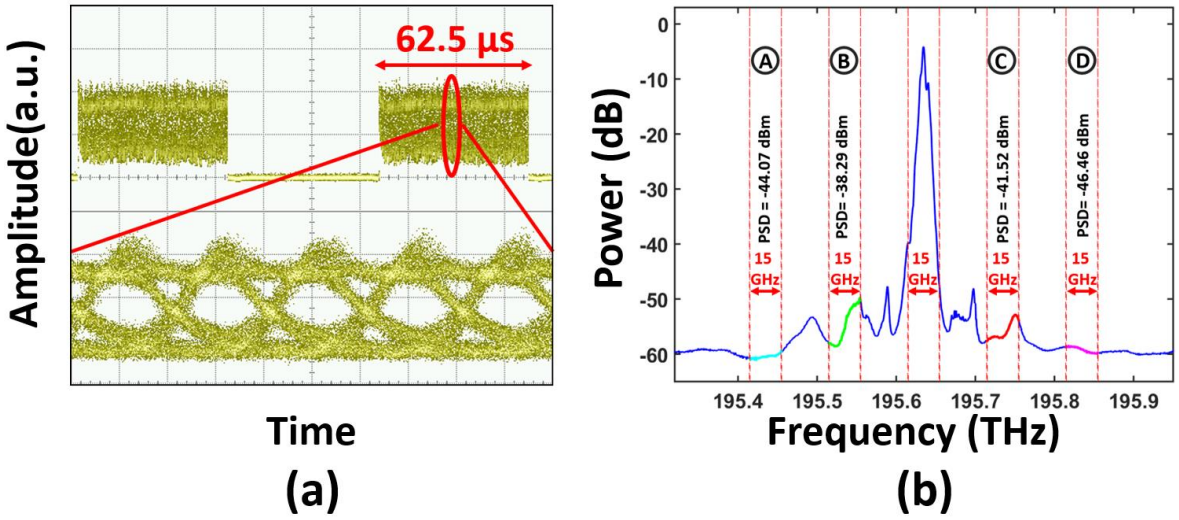

Figure 5.6.1. (a) Burst mode data transmission with a 62.5 µs burst length with a 50% duty cycle and (b) optical spectrum of the device operating in the burst mode (OSA in max. hold mode).

Then, post processing is performed to calculate the PSD at a resolution of 15 GHz (resolution used for defining OOC-PSD in NG-PON2 standard). The PSD values are calculated as −44.07 dBm (cyan), −38.29 dBm (green), −41.52 dBm (red), and −46.46 dBm (magenta) at different distances from the operational channel (blue). According to the specification, the maximum OOC-PSD must not exceed −40.5 dBm in case of a 100 GHz

channel spacing. All the OOC PSDs are within the limit specified in NGPON2 specification except channel B, which is 1.8 dB higher than the specification. The primary cause of higher PSD in channel B is the side mode of SL falling within the spectral slot of the neighbouring channel, the power of which is further increased when the SOA is directly modulated. The PSD in channel B can be reduced by suppressing the side mode power of SL which can be done by implementing SR1 and SR2 as multiperiod grating rather instead of single period grating.

5.7 Power-when-not enabled

As mentioned above, any transmitter that is to be employed in an NGPON2 system, needs to adhere to certain requirements as specified in the standards document [83]. One such criterion is the power-when-not enabled (PWNE), which introduces a limit on the maximum output PSD, when the burst is not being transmitted, to -62.6 dBm [339]. To meet this PWNE requirement, an SOA is integrated at the output of the PIC, to allow disabling the output of the transmitter when no data is being sent (blanking the output power without the need to turn off the laser). This is achieved by toggling the SOA section between transparency or amplification (bias current ≥ 18 mA) and absorption (bias current $= 0$ mA).

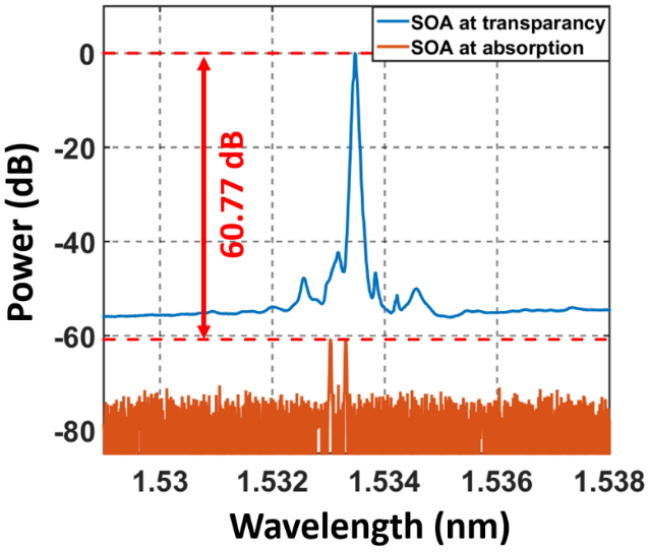

Figure 5.7.1. Optical spectrum of the PIC when the SOA is forward biased (blue) and unbiased (orange) SOA.

Figure 5.7.1 shows the comparison of the measured output optical spectrum, when the SOA is biased at 21 mA (blue trace) and 0 mA (orange trace), resulting in a change in the peak output power of the transmitter from 0 dBm to −60.77 dBm. As at 0 mA bias of the SOA, the transmitter doesn't meet the PWNE criterion, the SOA is reverse biased to increase the absorption of the light. In addition, the VOA is also turned off so as to attenuate the optical power from the ML. In such a configuration, the output power of the PIC drops below −62.6 dBm, which meets the specified PWNE limit for the NGPON2 transmitter. In future designs, an additional SOA section can be integrated at the output, which can provide further optical absorption when turned-off. The benefit of such a design would be that the desired PWNE can be obtained without turning off other sections of the PIC.

5.8 Wavelength switching

The wavelength switching in NGPON2 plays a critical role in resolving the issue of channel congestion by load balancing i.e., allowing the ONU to switch from heavily congested to less busy wavelength channels [115], [116], [117]. Thus, the PIC transmitter must comply with the channel switching standards set in NGPON2 specification document [83] which is described in Table 5.8.1.

Classes	Tuning time
Class 1	< 10 µs, any channel to any channel
Class 2	10 µs to 25 ms, any channel to any channel
Class 2R1	10 µs to 25 ms, any channel to a channel not more than 100 GHz away
Class 2R2	10 µs to 25 ms, any channel to a channel not more than 200 GHz away
Class 3	25 ms to 1 s, any channel to any channel

Table 5.8.1. Classes of transmitter/receiver wavelength channel tuning times.

To verify the compliance of the eight-section device with this requirement, the wavelength switching test is performed, during which the transmitter is switched between each of the OIL wavelength. As an example, to change the OIL2 point to OIL3, first, the bias currents of each section are determined at the same operating temperature, VOA, and SOA

current. The optimized values for OIL2 and OIL3 points are shown in Table 5.8.2. A software controlled multi-channel current source is used to bias the PIC. A python script is written to communicate with current controller and update the bias current. The bias data to achieve OIL2 and OIL3 are saved in a look-up table in the python script and then the code is initiated. The current controller updates the bias data that switches wavelength from OIL2 to OIL3 and vice versa. According to the NGPON2 specification, the transmitter qualifies for the class 3 type wavelength switching because the PIC supports switching of channel from any channel to any channel within 0.57 seconds (< 1 second).

OIL2 (1533.47 nm)		OIL3 (1534.25 nm)	
SOA	21 mA	**SOA**	21 mA
SR1	50 mA	**SR1**	54 mA
SG	47.86 mA	**SG**	54 mA
SR2	50 mA	**SR2**	57 mA
VOA	1 mA	**VOA**	1 mA
MR1	79.6 mA	**MR1**	83 mA
MG	57 mA	**MG**	103.29 mA
MR2	75 mA	**MR2**	74 mA
Temp	17.5 ºC	**Temp**	17.5 ºC

Table 5.8.2. Bias data for OIL2 and OIL3 operating points at equal temperature and currents applied to the SOA and VOA sections.

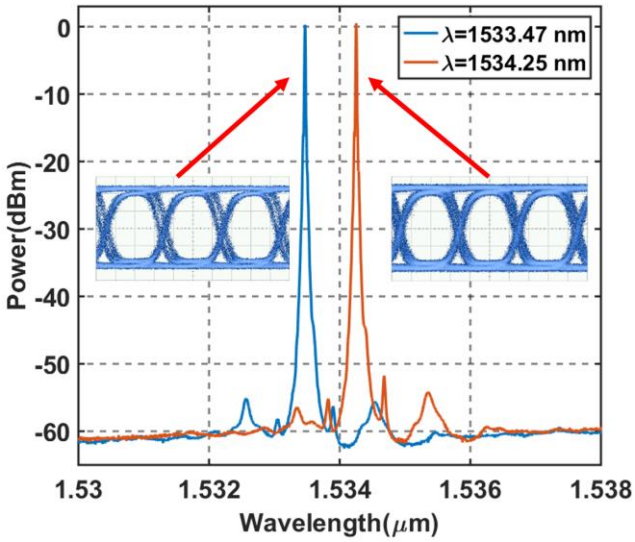

Figure 5.8.1. Optical spectrum showing the emission wavelengths at the OIL2 and OIL3 operating points when switching from one to the other. Inset shows the corresponding eye patterns.

Amongst previously demonstrated PIC transmitters, only few have shown the wavelength switching required for the NGPON2. For example, the PIC presented in [340] uses thermal tuning to switch between four wavelength channels. The device presented in [341] and [342] demonstrates high speed wavelength switching realised by turning on and off four individual lasers. In addition, both schemes use an external modulation that is inexpensive. The eight-section PIC shows merits over mentioned schemes such as a single tunable laser supporting wavelength switching between all four channels. Although its switching time is longer than shown in [342], the device fulfils class 3 switching criteria of NGPON2. The slow response time ($>$ 0.1 s to update channel currents) of multi-channel current controller causing slow wavelength switching.

5.9 Conclusions

This chapter discussed the design and characterization of a novel eight-section directly modulated integrated transmitter suitable for employment in a TWDM access network. The implemented PIC overcomes the limitations of six-section device (discussed in chapter 4) such as limited tunability and lack of burst mode transmission. The static characterization of the device reveals that the transmitter is able to achieve four OIL wavelengths on 100 GHz grid, which is a key required for NGPON2. All OIL operating points show high SMSR (SMSR $>$ 50 dB). Moreover, the average RIN depicted by the PIC transmitter is well below -140 dBc/Hz. Furthermore, the dynamic performance of the device is examined by measuring modulation response, chirp for free running and injection locked SL, and data transmission over SSMF. Analogous to six-section PIC, the enhancement in modulation bandwidth is observed for injection locked SL, achieving $>$ 7.8 GHz for each OIL operating point, sufficient for direct modulation with 10 Gb/s OOK signal. Additionally, the transmission reach is extended by controlling frequency chirp using an on-chip VOA. The PIC demonstrates a significant reduction in the frequency chirp from ~9.7 GHz to 2.6 GHz (similar to six-section PIC), when VOA is turned on and SL is injection locked. This lower chirp brings about an improved transmission performance of the device, verified by achieving a BER well below FEC limit (and $< 5e^{-8}$ for all channels) for 25 km and 50 km

SMF transmission of 10 Gb/s directly modulated signals. Furthermore, the integrated SOA at the output of the device enables the optical channel power on-off and burst mode transmission. The transmitter passes the PWNE requirement by showing output optical power below or equal to -62.6 dBm, while SOA is working in absorption mode. This PIC also exhibits a low level of interference (< -38.29 dBm at 100 GHz grid) while operating in burst mode. Finally, the transmitter also supports a class 3 wavelength switching operation that supports switching from one channel to any channel but at slower speed (more than 25 ms due to slow response of current controller). In conclusion, the features of PIC such as ease of fabrication, tunability, error free transmission, low cross channel interference, make it a potential candidate to be used as NGPON2 transmitter, given small improvements in ER and PWNE are made. The ER of the PIC can be enhanced by increasing the modulation bandwidth and slope efficiency of SL. The PWNE characteristic can further be improved by fabricating a two section SOA at device output that would increase the absorption resulting in a high attenuation to output optical signal.

Chapter 6

Conclusions and Future work

6.1 Conclusions

The continual rise in data consumption by both fixed and mobile broadband subscribers drives incessant industry innovation to meet this challenge. One of the innovations in fiber-built access systems is based on passive optical networks (PONs). Such solutions include the G-PON and EPON as standardized by the ITU-T and IEEE respectively. The standards bodies have also defined XG-PON1 and 10G-EPON that have been deployed. However, to deal with the unprecedented increment in the volume of data traffic in access networks, continuous innovation is required. One such step entails increasing the channel capacity on a single fiber by introducing the combination of multiplexing techniques of TDM and WDM to yield TWDM. According to current state of the art, TWDM is a well-established standard that offers an aggregate channel capacity of 40 Gb/s. Hence, the fiber access evolution defined by the ITU-T is known as the second next generation PON (NG-PON2), which uses four wavelengths each delivering 10 Gb/s.

Like the previously launched PON standards (EPON, GPON, XGPON, XGSPON) the OOK modulation scheme is preferred for NGPON2 that supports easy upgrade and use of a low-cost optical transmitter. Hence, the main thrust of this work was to design, characterize and optimize a cost-efficient laser that could satisfy all the requirements of the new standard.

6.2 Contribution to the state-of-the-art and research outcomes

6.2.1 Design and optimization of a regrowth free

The first key contribution of this thesis is the creation of an IP FP laser designed for use in a transmitter. This laser is fabricated using a regrowth-free method, which is essential for achieving a highly cost-effective laser. The laser's performance, including factors like threshold and SMSR (side mode suppression ratio), depends on the depth and width of slots periodically carved on the surface of the ridge waveguide. Two scenarios are considered to investigate the performance of a slot-based reflector. First, the study explores how slot width and depth affect reflectivity, finding that reflectivity is influenced by the number of slots and the etching depth. Next, the relationship between reflection and wavelength is examined for varying slot widths. Simulation results indicate that a 0.3 μm wide slot offers the best performance in terms of reflectivity and minimal scattering loss. The rate equation model reveals that the 0.3 μm wide slot IP FP laser performs better. Subsequent experimental characterization confirms that the IP FP laser with a 0.3 μm wide slot is the top-performing laser and depicts a low threshold (~15 mA) and SMSR > 35 dB. The data obtained from optimizing the index-patterned laser is then employed in creating a DML transmitter.

6.2.2 Design, implementation, and characterization of six-section DML laser

The Second key contribution is the implementation of a six-section DML transmitter built by cascading two IP FP lasers. The DML transmitter brings a suite of benefits, such as simplified driver circuitry and low cost. However, the optical signal from DML suffers from frequency chirp that shortens the transmission distance due to effect of dispersion. The impairments associated with DMLs are solved by adapting OIL technique. The six-section PIC implementing OIL phenomenon was created by implementing the SL-VOA-ML configuration that allows accurate control of optical injection. With this arrangement, the

PIC inherits the benefits of OIL and demonstrates improvement in modulation response, reduction in RIN and frequency chirp. We observe that the modulation bandwidth of SL improves from ~4.2 GHz to ~7.8 GHz; the average RIN over a 1 GHz to 6 GHz frequency span reduces from -121 dBc/Hz to -145 dBc/Hz; and frequency chirp decreases from 35 GHz to 2.5 GHz under OIL which is the significant improvements. The characterization results also prove the importance of having a VOA section to improve transmission quality. For example, the VOA section helps to maintain the balance between ER and Chirp. The on-chip chirp control delivers error-free (BER < $1e^{-9}$) while transmitting 10 Gb/s OOK signal over 50 km SMF with 5 dB ER. The characteristics demonstrated by the six-section DML transmitter make it suitable for short-reach applications and pave the way for developing a transmitter for NGPON2.

6.2.3 Design, implementation, and characterization of eight-section DML laser

The final and the main contribution is the implementation of the eight-section DML transmitter (an improved version of six-section PIC) that complies to NGPON2 specifications. The PIC is widely tunable and capable of generating four IL wavelengths on 100 GHz grid satisfying the wavelength band and channel spacing of NGPON2. Each channel can be modulated at 10 Gb/s. Like six-section PIC, the on-chip chirp compensation significantly reduces frequency chirp while directly modulated that helps extending transmission reach. The BER performance at each of the IL wavelengths, when transmitted over 50 km SMF, is well below the FEC limit and always below $5e^{-8}$. Furthermore, the integrated SOA at the output of the device enables the optical channel power on-off feature (output optical power below or equal to -62.6 dBm). This PIC also exhibits low level of interference (< -38 dBm) to the other equally spaced operational channels. In conclusion, the features of PIC such as ease of fabrication, tunability, error free transmission, low cross channel interference have a potential to be used as NGPON2 transmitter.

6.3 Future work

While the research work presented in this thesis has provided technical solutions (and the science behind it) to several challenges, there is still a large body of work that can be carried out to further the science and to pave the way towards the realization of an optimum transmitter for next generation access networks. Hence, we start by examining some of the enhancements that could be made to the proposed device. Subsequently, we look at other improvements that could be made to satisfy new standards.

6.3.1 Enhancements to eight-section DML transmitter

The existing PIC meets several NGPON2 requirements but requires enhancements in various areas, including improving ER, reducing cross-channel interference and PWNE.

6.3.2.1 Improvement in extinction ratio

Typically, there are many ways to improve the ER. However, the most poignant techniques that are applicable to the PIC developed in this work are:

6.3.2.1.1 Improvement in the slope efficiency of a laser

In direct modulation, the variation in the power of the optical signal is proportional to the time varying electrical signal. Hence, the slope efficiency of the laser would directly impact the extinction ratio achieved. Essentially, a laser with high slope efficiency archives high ER and vice versa. The slope efficiency relies on internal loss and can be minimized by reducing non radiative defects, mirror loss, and length of the laser. In the eight-section PIC, an ER of more than 4dB could not be achieved at each IL operating point because the SL depicts high internal loss. The ER performance can be improved by developing an eight-section PIC using a wafer depicting a low non-radiative effect and mirror losses (scattering loss). The mirrors are implemented as a group of slots so the losses can be lowered by choosing the dimension of the slot and period order appropriately.

6.3.2.1.2 Improvement in modulation response

Another reason for low ER in the eight-section PIC is limited modulation response. So, the ER can also be enhanced by improving the modulation response of the SL. This can be achieved by reducing the parasitic effects and effective length of the laser. The parasitic capacitance can be minimized by shortening the contact pads and the relaxation oscillation peak can be enhanced to $\sqrt{2}$ times by shortening the cavity length by 50%. In the eight-section PIC, the SL is implemented as reflector-gain-reflector so the length of the SL can be minimized by lowering down the period order of the slot reflectors and length of the gain section.

6.3.2.2 Improvement in OOC PSD

As mentioned in section 5.6, the device OOC PSD for one of the neighboring channels is slightly higher than the specified limit. High interference occurs because the power of one of the side modes with high power spectral density spills into the neighboring channel. The optical spectrum of slave laser (in black) is plotted in Figure 6.3.1. The power in the side mode L is higher than the side mode R. In the injection locking condition, the peaks of side mode L and R shift to channel B and C, respectively.

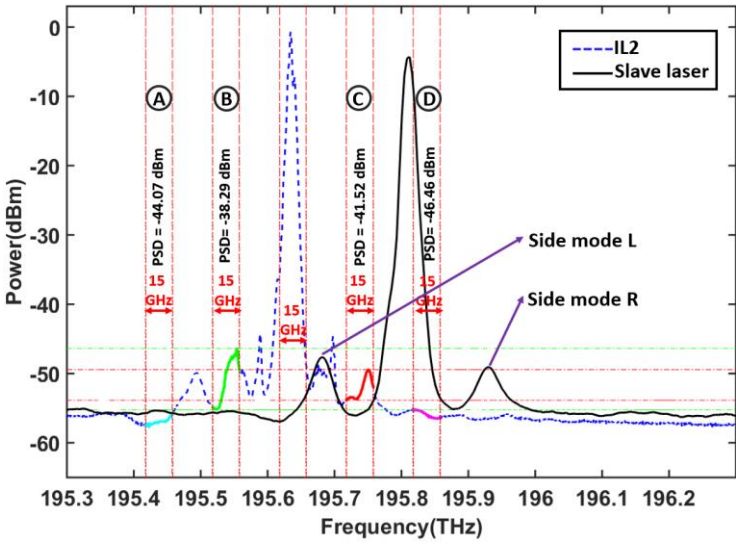

Figure 6.3.1. Optical spectrum of free running SL and injection locked SL.

We see a minor suppression of sidemodes when slave laser is injection locked. However, the power spectral density of side mode L remains higher than the side mode R. The level of interference further increases in channel B and C when the SOA is directly modulated with an OOK signal (as depicted in Figure 6.3.2). A time varying current leaks into the slave reflector, changing the effective refractive index, altering the lasing wavelength of the SL, and causing distortion in the optical spectrum. The level of interference in channel B can be minimized by improving the design of the reflectors to improve the suppression of the side mode.

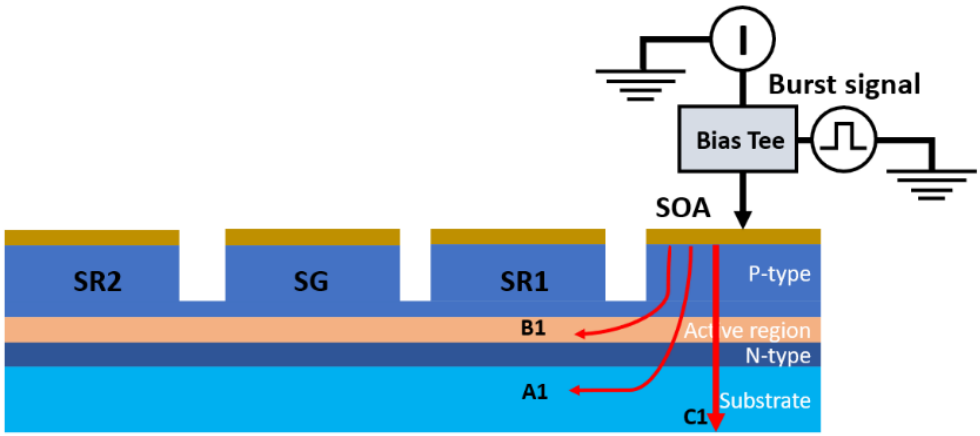

Figure 6.3.2. Current leakage from SOA supplied with burst signal.

6.3.2.3 Improvement in PWNE

In the current design, a short (230 µm) SOA section is integrated to enable fast burst mode switching and enable/disable the output optical power. However, it does not provide enough absorption when the SOA is turned off. A longer SOA section could solve this problem but will not be able to support fast switching. Hence, instead of a long SOA section, we proposed two electrically isolated short SOA sections (as shown in Figure 6.3.3) for two stage absorption. This would allow for the PWNE limit to be reached without switching off other sections of the PIC. When it comes to enabling burst mode, one SOA section can be driven at transparency and the other can be supplied with the burst signal.

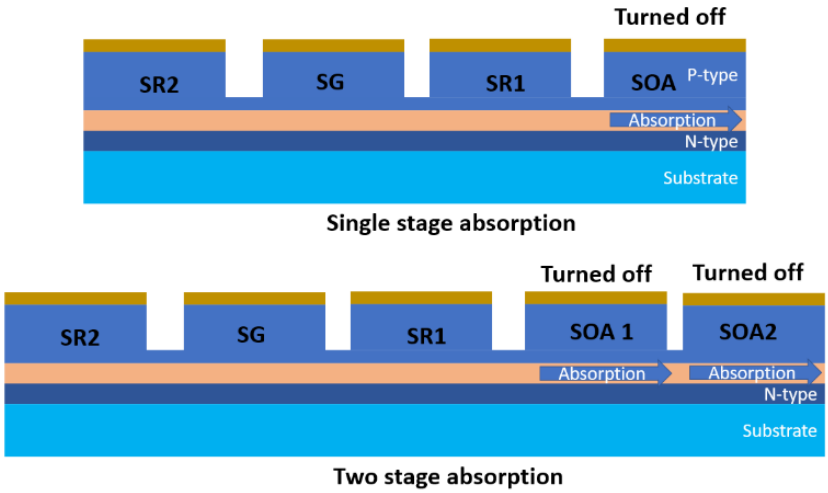

Figure 6.3.3. Single and double stage absorption in one-section and two-section SOA.

Overall, the successful development of a directly modulated transmitter system enabled by a multi-functional photonic integrated circuit is presented in this thesis. The scientific advancements and investigation presented in this thesis may play a vital role in the realization of a cost-effective transmitter to be employed in future high-capacity PONs.

6.3.2 Enhancement to satisfy new standards.

PON technology is constantly evolving to address the challenges posed by the existing standards. Presently, one of the most significant challenges in PON technology is the channel capacity enhancement.

6.3.2.1 Data rate enhancement

The NGPON2 specifications were established in 2015, but its commercial development has been hindered by the need for expensive tunable optical components. As a result, there is a possibility that its commercialization may be delayed or even abandoned in the future. The ITU-T has conducted research on next-generation high-speed PON technology, and it is currently considering the adoption of single-wavelength 50G PON as the primary industry standard for the next-generation optical access network, following the 10G PON technology.

The 50G PON has the potential to be a game-changer in PON technology, capable

of providing high data rates to many subscribers. For the seamless transition from 10G PON to 50G PON and ensure long-term coexistence, the OOK modulation scheme is preferred.

Although, 50G PON chose OOK modulation format because of hardware simplicity and its cost effectiveness. However, soon the capacity of PON needs to be increased up to 100 Gb/s or further (400 Gb/s). Attaining such a high data rate is impossible with OOK modulation format. As mentioned in chapter 1, the data rate of OOK modulation scheme is limited because of limitation in speed of electronic components and dispersion (CD and PMD) imposed by the fiber. One way to increase data rate is the use of higher order modulation schemes such as PAM-x, QPSK and m-QAM (advanced modulation format). Advanced modulation formats provide higher data rate for a given bandwidth in comparison to OOK signaling. For example, the symbol transmitted at the rate of 6.25 Giga-Samples/s (GSa/s) using 16-QAM modulation format generates aggregate data rate of 25 Gb/s. In this modulation technique the symbols are sent either in form of multi-level intensity (for example PAM-x) or combination of multi-level intensity and phase (also known as symbol). The extraction of bits from a symbol is done either by coherent detection or direct detection. A coherent detector in a combination of DSP algorithms portrays mitigation of channel interference and compensation of fiber dispersion and nonlinearities.

6.3.2.1.1 Coherent PON

The Coherent PON (CPON) is known for high-capacity data access achieved via coherent detection of signal modulated with advanced modulation formats and superior receiver sensitivity [343] and flexibility in terms of channel selectivity [344]. CPON can be a viable solution to implement a futuristic PON architecture that can achieve channel capacity beyond 400 Gb/s. In addition, CPON receivers are tolerant to fiber dispersion and nonlinearities that can be mitigated using digital signal processing and equalization schemes after optical to electrical conversion through photodetector [345]. In CPON, a coherent receiver is used that associates a laser acting as local oscillator or a phase reference followed by a balanced detector to extract both intensity and phase information [346], [347], [348], [349]. The CPON associate implementation complexity due to requirement of real-time processing units (ADC, DAC, and FPGA) which is expensive. The direct detection scheme can be a viable

replacement of coherent detection that can detect multi-level signal. In direct detection the phase information is first converted to intensity using an interferometry method and then detected by a photodiode.

6.3.2.1.1.1 DMT modulation

As mentioned, the direct detection scheme exhibits limited data transmission capacity, however it is popular for its cost effectiveness. In opposite to that multi-level signaling (like m-QAM) capable of handling high volume of data but require expensive hardware to implement. The DMT modulation scheme combines both the advantage of direct detection and high-capacity data transmission. The DMT scheme is based on OFDM multiplexing technique [350], [351]. The advantage of the DMT over OFDM is, it transmits only intensity information rather than transmitting intensity along with phase information [352]. The transmission of intensity information makes it suitable for direct modulation. Hence, we performed a data transmission experiment by applying DMT signal directly to SG section of SL in conjunction with DC current. We tested the transmission performance of the PIC by directly modulating the IL SL with DMT (discrete multitone) signal. The Figure 6.3.4 show the block diagram of DMT transmitter and receiver.

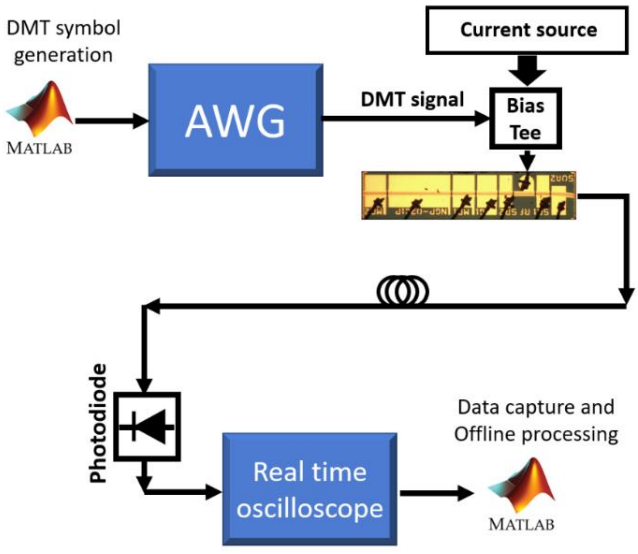

Figure 6.3.4. Block diagram of DMT transceiver system.

To generate the DMT signal, first the binary data is converted to N complex symbols of 16-QAM. Then the array of N complex symbols and their hermitic counterpart is formed. Thereafter, the 2-N point IFFT is calculated for [N, $N_{Hermatic}$] array that generated DMT symbol having only real values. Subsequently, the generated DMT symbols are loaded to arbitrary waveform generator (AWG) that generates output electrical signal at the rate of 6.25 GSa/s. The Figure 6.3.5(a) shows the generated electrical signal. After that, the quality of electrical signal in back-to-back (b2b) case is investigated. For the investigation the electrical DMT signal is supplied to real-time electrical oscilloscope and sampled at 100 GSa/s. The sampled signal is then supplied to the receiver implemented on MATLAB and post-processed to extract 16-QAM symbol. Figure 6.3.5(b) is plot of received 16-QAM electrical b2b signal. The calculated BER and Error vector magnitude (EVM) are $9.7e^{-5}$ and 0.076%, respectively.

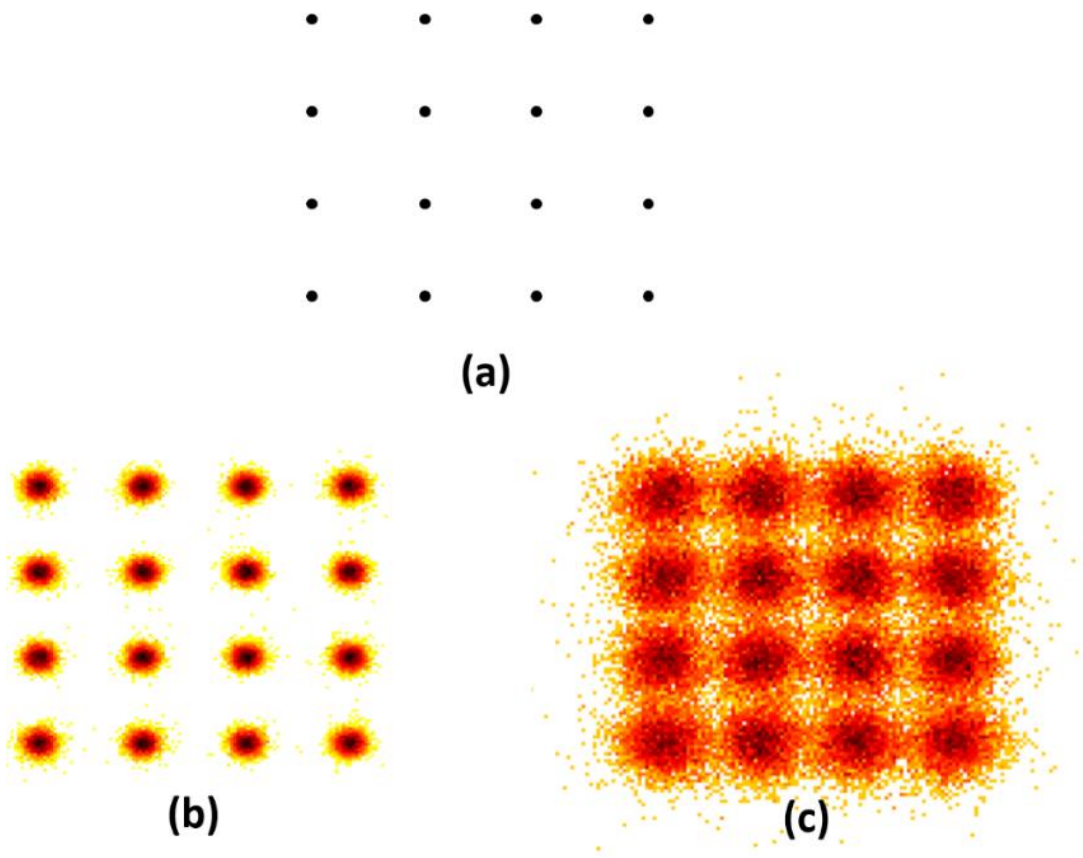

Figure 6.3.5. (a) Transmitted 16 QAM symbols. (b) electrical back-to-back and (c) Received optical back-to-back 16-QAM signal.

Next, the OIL is achieved to obtain 1533.47 nm IL wavelength. The DMT electrical signal is mixed with DC current using a bias-tee and supplied to SG section of SL for direct modulation. The DMT modulated optical signal is collected by a lens fiber and supplied to wideband photodiode for opto-electronic conversion. The electrical signal is fed to real-time oscilloscope and electrical samples are collected at 100 GSa/s. Figure 6.3.5(c) shows the received 16-QAM symbols. The calculated BER and Error vector magnitude (EVM) of received electrical symbol after optoelectronic conversion are $2.6e^{-2}$ and 0.23%, respectively. The optical b2b signal is degraded because the symbols suffer distortion due to non-flat modulation response, and noisy electrical input signal. In future, the transmission performance can be improved by equalizing electro-optic response to reducing the symbol distortion and reducing noise level of electrical signal supplied to SG section.

References

[1] R. Wenzlhuemer *et al.*, “The Development of Telegraphy, 1870–1900: A European Perspective on a World History Challenge,” *History Compass*, vol. 5, no. 5, pp. 1720–1742, 2007, doi: 10.1111/j.1478-0542.2007.00461.x.

[2] S. D. Personick *et al.*, *Optical Fiber Transmission Systems*. Springer Science & Business Media, 2013.

[3] M. Barnoski *et al.*, *Fundamentals of Optical Fiber Communications*. Elsevier, 2012.

[4] M. Arumugam *et al.*, “Optical fiber communication—An overview,” *Pramana - J Phys*, vol. 57, no. 5–6, pp. 849–869, Nov. 2001, doi: 10.1007/s12043-001-0003-2.

[5] H. Xuan *et al.*, “Highly birefringent optical microfibers,” *Opt. Express*, vol. 18, no. 4, p. 3828, Feb. 2010, doi: 10.1364/OE.18.003828.

[6] S. Pricking *et al.*, “Tapering fibers with complex shape,” *Optics express*, vol. 18, no. 4, pp. 3426–3437, 2010.

[7] T. E. Dimmick *et al.*, “Carbon dioxide laser fabrication of fused-fiber couplers and tapers,” *Applied Optics*, vol. 38, no. 33, pp. 6845–6848, 1999.

[8] G. Brambilla *et al.*, “Compound-glass optical nanowires,” *Electron. Lett*, vol. 41, no. 7, pp. 400–402, 2005.

[9] L. Shi *et al.*, “Fabrication of submicron-diameter silica fibers using electric strip heater,” *Optics express*, vol. 14, no. 12, pp. 5055–5060, 2006.

[10] W. A. Gambling *et al.*, "Optical fibre systems." *Philosophical Transactions of the Royal Society of London. Series A, Mathematical and Physical Sciences* 289.1356 (1978): 135-150.

[11] X. Zhao *et al.*, “Demonstration of 10-Gb/s transmissions over a 1.5-km-long multimode fiber using equalization techniques,” *IEEE Photonics Technology Letters*, vol. 14, no. 8, pp. 1187–1189, Aug. 2002, doi: 10.1109/LPT.2002.1022013.

[12] M. B. Shemirani *et al.*, “Higher-Order Modal Dispersion in Graded-Index Multimode Fiber,” *J. Lightwave Technol., JLT*, vol. 27, no. 23, pp. 5461–5468, Dec. 2009.

[13] G. Keiser *et al.*, *Optical fiber communications*. Vol. 2. New York: McGraw-Hill, 2000

[14] G. P. Agrawal *et al.*, *Fiber-optic communication systems*. John Wiley & Sons, 2012.

[15] K. Appaiah *et al.*, "Impact of fiber core diameter on dispersion and multiplexing in multimode-fiber links," *Opt. Express*, vol. 22, no. 14, p. 17158, Jul. 2014, doi: 10.1364/OE.22.017158.

[16] G. Yabre *et al.*, "Influence of Core Diameter on the 3-dB Bandwidth of Graded-Index Optical Fibers," *J. Lightwave Technol., JLT*, vol. 18, no. 5, p. 668, May 2000.

[17] D. Marcuse *et al.*, "Pulse distortion in single-mode fibers," *Appl. Opt., AO*, vol. 19, no. 10, pp. 1653–1660, May 1980, doi: 10.1364/AO.19.001653.

[18] A. R. Chraplyvy *et al.*, "Limitations on lightwave communications imposed by optical-fiber nonlinearities," *Journal of Lightwave Technology*, vol. 8, no. 10, pp. 1548–1557, Oct. 1990, doi: 10.1109/50.59195.

[19] R.-J. Essiambre *et al.*, "Capacity Trends and Limits of Optical Communication Networks," *Proceedings of the IEEE*, vol. 100, no. 5, pp. 1035–1055, May 2012, doi: 10.1109/JPROC.2012.2182970.

[20] M. DiDomenico *et al.*, "Material Dispersion in Optical Fiber Waveguides," *Appl. Opt., AO*, vol. 11, no. 3, pp. 652–654, Mar. 1972, doi: 10.1364/AO.11.000652.

[21] S. P. Singh *et al.*, "NONLINEAR EFFECTS IN OPTICAL FIBERS: ORIGIN, MANAGEMENT AND APPLICATIONS," *PIER*, vol. 73, pp. 249–275, 2007, doi: 10.2528/PIER07040201.

[22] J. M. Senior *et al.*, *Optical fiber communications: principles and practice*. Pearson Education, 2009.

[23] F. Coppinger *et al.*, "RF Video Overlay in an Ethernet Passive Optical Network," in *Optical Fiber Communication Conference and Exposition and The National Fiber Optic Engineers Conference (2006), paper OThK7*, Optica Publishing Group, Mar. 2006, p. OThK7. Accessed: Feb. 14, 2023. [Online]. Available: https://opg.optica.org/abstract.cfm?uri=OFC-2006-OThK7

[24] S. C. Rashleigh *et al.*, "Polarization mode dispersion in single-mode fibers," *Optics Letters*, vol. 3, no. 2, pp. 60–62, 1978.

[25] H. Kogelnik *et al.*, “Polarization-mode dispersion,” in *Optical Fiber Telecommunications IV-B*, Elsevier, 2002, pp. 725–861.

[26] J. P. Gordon *et al.*, “PMD fundamentals: Polarization mode dispersion in optical fibers,” *Proceedings of the National Academy of Sciences*, vol. 97, no. 9, pp. 4541–4550, 2000.

[27] N. Gisin *et al.*, “Polarization mode dispersion of short and long single-mode fibers,” *Journal of lightwave technology*, vol. 9, no. 7, pp. 821–827, 1991.

[28] N. Gisin *et al.*, “Combined effects of polarization mode dispersion and polarization dependent losses in optical fibers,” *Optics communications*, vol. 142, no. 1–3, pp. 119–125, 1997.

[29] A. Galtarossa *et al.*, *Polarization mode dispersion*, vol. 296. Springer, 2005.

[30] H. Kogelnik *et al.*, “Chapter 15 - Polarization-Mode Dispersion,” in *Optical Fiber Telecommunications IV-B (Fourth Edition)*, I. P. Kaminow and T. Li, Eds., in Optics and Photonics. , Burlington: Academic Press, 2002, pp. 725–861. doi: 10.1016/B978-012395173-1/50015-3.

[31] I. Kaminow *et al.*, “Polarization in optical fibers,” *IEEE Journal of Quantum Electronics*, vol. 17, no. 1, pp. 15–22, Jan. 1981, doi: 10.1109/JQE.1981.1070626.

[32] D. van den Borne *et al.*, “PMD-induced transmission penalties in polarization-multiplexed transmission,” *Journal of Lightwave Technology*, vol. 23, no. 12, pp. 4004–4015, Dec. 2005, doi: 10.1109/JLT.2005.858237.

[33] B. Frank *et al*., "Impact of first-and second-order PMD in optical digital transmission systems." *Optical Fiber Technology* 2.3 (1996): 269-280.

[34] G. Zhang *et al*., “Impact of fiber nonlinearity on PMD penalty in DWDM transmission systems,” *IEEE Photonics Technology Letters*, vol. 17, no. 2, pp. 501–503, Feb. 2005, doi: 10.1109/LPT.2004.839010.

[35] K. Iga *et al*., *Fundamentals of laser optics*, vol. 38. Springer, 1994.

[36] M. Endo *et al*., *Gas lasers*. CRC Press, 2018.

[37] V. N. Bagratashvili *et al*., “On the tunable infrared gas lasers,” *Optics Communications*, vol. 4, no. 2, pp. 154–156, 1971.

[38] M. Mohrle *et al*., "High-performance all-active tapered 1550 nm InGaAsP-BH-FP lasers," in *Conference Proceedings. 14th Indium Phosphide and Related Materials Conference (Cat. No. 02CH37307)*, IEEE, 2002, pp. 27–30.

[39] Q. Lu *et al*., "Design of slotted single-mode lasers suitable for photonic integration," *IEEE Photonics Technology Letters*, vol. 22, no. 11, pp. 787–789, 2010.

[40] E. Kotelnikov *et al*., "High-power single-mode ingaasp/inp laser diodes for pulsed operation," in *Novel In-Plane Semiconductor Lasers XI*, SPIE, 2012, pp. 178–183.

[41] Y. D. Jeong *et al*., "Tunable single-mode Fabry-Perot laser diode using a built-in external cavity and its modulation characteristics," *Optics letters*, vol. 31, no. 17, pp. 2586–2588, 2006.

[42] W.-H. Guo *et al.*, "Integrable slotted single-mode lasers," *IEEE Photonics Technology Letters*, vol. 24, no. 8, pp. 634–636, 2012.

[43] H. Zhu *et al.*, "The fabrication of eight-channel DFB laser array using sampled gratings," *IEEE Photonics Technology Letters*, vol. 22, no. 5, pp. 353–355, 2010.

[44] P. J. Williams *et al.*, "Design and fabrication of monolithically integrated DFB laser-wavelength duplexer transceivers for TPON/BPON access links," *Electronics Letters*, vol. 10, no. 27, pp. 809–810, 1991.

[45] H. Wenzel *et al.*, "Design and realization of high-power DFB lasers," in *Physics and Applications of Optoelectronic Devices*, SPIE, 2004, pp. 110–123.

[46] J. Rahimi *et al*., "Demonstration of a high-efficiency short-cavity iii-v-on-si c-band dfb laser diode," *IEEE Journal of Selected Topics in Quantum Electronics*, vol. 28, no. 3: Hybrid Integration for Silicon Photonics, pp. 1–6, 2021.

[47] Y. Nakano *et al*., "Analysis, design, and fabrication of GaAlAs/GaAs DFB lasers with modulated stripe width structure for complete single longitudinal mode oscillation," *IEEE journal of quantum electronics*, vol. 24, no. 10, pp. 2017–2033, 1988.

[48] J. W. Zimmerman *et al*., "Narrow linewidth surface-etched DBR lasers: fundamental design aspects and applications," *IEEE Journal of Selected Topics in Quantum Electronics*, vol. 19, no. 4, pp. 1503712–1503712, 2013.

[49] B. Mason *et al*., "Widely tunable sampled grating DBR laser with integrated electroabsorption modulator," *IEEE Photonics Technology Letters*, vol. 11, no. 6, pp. 638–640, 1999.

[50] K. Lawniczuk *et al.*, "InP-based photonic multiwavelength transmitter with DBR laser array," *IEEE Photonics Technology Letters*, vol. 25, no. 4, pp. 352–354, 2013.

[51] M. Fallahi *et al*., "Design and fabrication of circular grating coupled distributed Bragg reflector lasers," *Optical Engineering*, vol. 37, no. 4, pp. 1169–1174, 1998.

[52] C. W. Wilmsen *et al*., *Vertical-cavity surface-emitting lasers: design, fabrication, characterization, and applications*, vol. 24. Cambridge University Press, 2001.

[53] C.-C. Shen *et al.*, "Design and fabrication of the reliable GaN based vertical-cavity surface-emitting laser via tunnel junction," *Crystals*, vol. 9, no. 4, p. 187, 2019.

[54] J. L. Jewell *et al*., "Vertical-cavity surface-emitting lasers: design, growth, fabrication, characterization," *IEEE Journal of Quantum Electronics*, vol. 27, no. 6, pp. 1332–1346, 1991.

[55] H. K. H. Choy *et al*., "Design and fabrication of distributed Bragg reflectors for vertical-cavity surface-emitting lasers," PhD Thesis, Massachusetts Institute of Technology, 1998.

[56] W. W. Chow *et al*., "Design, fabrication, and performance of infrared and visible vertical-cavity surface-emitting lasers," *IEEE Journal of Quantum Electronics*, vol. 33, no. 10, pp. 1810–1824, 1997.

[57] R.-J. Essiambre *et al*., "Capacity Limits of Optical Fiber Networks," *Journal of Lightwave Technology*, vol. 28, no. 4, pp. 662–701, Feb. 2010, doi: 10.1109/JLT.2009.2039464.

[58] B. R. Saltzberg *et al*., "Comparison of single-carrier and multitone digital modulation for ADSL applications," *IEEE Communications Magazine*, vol. 36, no. 11, pp. 114–121, Nov. 1998, doi: 10.1109/35.733485.

[59] L. Plissonneau *et al*., "Analysis of Peer-to-Peer Traffic on ADSL," in *Passive and Active Network Measurement*, C. Dovrolis, Ed., in Lecture Notes in Computer Science. Berlin, Heidelberg: Springer, 2005, pp. 69–82. doi: 10.1007/978-3-540-31966-5_6.

[60] J. A. C. Bingham *et al*., *ADSL, VDSL, and Multicarrier Modulation*. in Wiley Series in Telecommunications and Signal Processing. New York, USA: John Wiley & Sons, Inc., 2000. doi: 10.1002/0471200727.

[61] N.-N. Dao *et al.*, "Survey on Aerial Radio Access Networks: Toward a Comprehensive 6G Access Infrastructure," *IEEE Communications Surveys & Tutorials*, vol. 23, no. 2, pp. 1193–1225, 2021, doi: 10.1109/COMST.2021.3059644.

[62] M. Yao *et al*., "Artificial Intelligence Defined 5G Radio Access Networks," *IEEE Communications Magazine*, vol. 57, no. 3, pp. 14–20, Mar. 2019, doi: 10.1109/MCOM.2019.1800629.

[63] P. Arnold *et al*., "5G radio access network architecture based on flexible functional control / user plane splits," in *2017 European Conference on Networks and Communications (EuCNC)*, Jun. 2017, pp. 1–5. doi: 10.1109/EuCNC.2017.7980777.

[64] Y. Yamao *et al*., "Radio access network design concept for the fourth generation mobile communication system," in *VTC2000-Spring. 2000 IEEE 51st Vehicular Technology Conference Proceedings (Cat. No.00CH37026)*, May 2000, pp. 2285–2289 vol.3. doi: 10.1109/VETECS.2000.851680.

[65] H. Holma *et al*., *WCDMA for UMTS: Radio Access for Third Generation Mobile Communications*. John Wiley & Sons, 2005.

[66] P. E. G. Jr *et al*., *Fiber to the Home: The New Empowerment*. John Wiley & Sons, 2005.

[67] S. Sugumaran *et al*., "An Overview of FTTH for Optical Network," in *Advances in Smart Communication and Imaging Systems*, R. Agrawal, C. Kishore Singh, and A. Goyal, Eds., in Lecture Notes in Electrical Engineering. Singapore: Springer, 2021, pp. 41–51. doi: 10.1007/978-981-15-9938-5_6.

[68] P. W. Shumate *et al*., "Fiber-to-the-Home: 1977–2007," *Journal of Lightwave Technology*, vol. 26, no. 9, pp. 1093–1103, May 2008, doi: 10.1109/JLT.2008.923601.

[69] S. Verbrugge *et al.*, "Research approach towards the profitability of future FTTH business models," in *2011 Future Network & Mobile Summit*, Jun. 2011, pp. 1–10.

[70] G. Kramer *et al*., "IPACT a dynamic protocol for an Ethernet PON (EPON)," *IEEE Communications Magazine*, vol. 40, no. 2, pp. 74–80, Feb. 2002, doi: 10.1109/35.983911.

[71] S.-J. Park *et al*., "Fiber-to-the-Home Services Based on Wavelength-Division-Multiplexing Passive Optical Network," *J. Lightwave Technol., JLT*, vol. 22, no. 11, p. 2582, Nov. 2004.

[72] G. Kramer *et al*., "Ethernet passive optical network (EPON): building a next-generation optical access network," *IEEE Communications Magazine*, vol. 40, no. 2, pp. 66–73, Feb. 2002, doi: 10.1109/35.983910.

[73] C. F. Lam *et al*., *Passive optical networks: principles and practice*. Elsevier, 2011.

[74] M. Ridolfi *et al*., "Analysis of the Scalability of UWB Indoor Localization Solutions for High User Densities," *Sensors*, vol. 18, no. 6, Art. no. 6, Jun. 2018, doi: 10.3390/s18061875.

[75] G. Kramer *et al*., "The problem of upstream traffic synchronization in Passive Optical Networks," *Davis, CA*, vol. 95616, 1999.

[76] H. Ishio *et al*., "Review and status of wavelength-division-multiplexing technology and its application," *Journal of lightwave technology*, vol. 2, no. 4, pp. 448–463, 1984.

[77] Y. Shachaf *et al*., "Multi-PON access network using a coarse AWG for smooth migration from TDM to WDM PON," *Opt. Express*, vol. 15, no. 12, p. 7840, 2007, doi: 10.1364/OE.15.007840.

[78] D. T. H. Tan *et al*., "Towards 100 channel dense wavelength division multiplexing with 100GHz spacing on silicon," *Opt. Express*, vol. 22, no. 9, p. 10408, May 2014, doi: 10.1364/OE.22.010408.

[79] K. Iwatsuki *et al*., "Access and Metro Networks Based on WDM Technologies," *J. Lightwave Technol., JLT*, vol. 22, no. 11, p. 2623, Nov. 2004.

[80] D. Sadot *et al*., "Tunable optical filters for dense WDM networks," *IEEE Communications Magazine*, vol. 36, no. 12, pp. 50–55, Dec. 1998, doi: 10.1109/35.735877.

[81] M. Wu *et al*., "Fiber Nonlinearity Limitations in Ultra-Dense WDM Systems," *J. Lightwave Technol., JLT*, vol. 22, no. 6, p. 1483, Jun. 2004.

[82] A. Banerjee *et al.*, “Wavelength-division-multiplexed passive optical network (WDM-PON) technologies for broadband access: a review [Invited],” *J. Opt. Netw.*, vol. 4, no. 11, p. 737, 2005, doi: 10.1364/JON.4.000737.

[83] “G.989.2 : 40-Gigabit-capable passive optical networks 2 (NG-PON2): Physical media dependent (PMD) layer specification.” Accessed: Oct. 31, 2022. [Online]. Available: https://www.itu.int/rec/T-REC-G.989.2-201902-I/en

[84] K. Singhal *et al*., “Walsh Codes, PN Sequences and their role in CDMA Technology”.

[85] Zhang, Chongfu *et al*.. "Passive optical network based on optical-code-division multiple access." *SPIE Newsroom* 45 (2010).

[86] B. Ahn *et al*., “A symmetric-structure CDMA-PON system and its implementation,” *IEEE Photonics Technology Letters*, vol. 14, no. 9, pp. 1381–1383, Sep. 2002, doi: 10.1109/LPT.2002.801066.

[87] J. Armstrong *et al*., “OFDM for optical communications,” *Journal of lightwave technology*, vol. 27, no. 3, pp. 189–204, 2009.

[88] Sector, ITU-T. Standardization. "A broadband optical access system with increased service capability by wavelength allocation." *ITU-T Recommendation G. 983.3* (2001).

[89] Rec, I. T. U. T. "G. 983.1–“Broadband Optical Access Systems Based on Passive Optical Networks (PON)”." (1998).

[90] G. Kramer *et al*., “Ethernet passive optical network (EPON): Building a next-generation optical access network,” *IEEE Communications magazine*, vol. 40, no. 2, pp. 66–73, 2002.

[91] “IEEE P802.3av 10GEPON Task Force - Baseline Proposals.” Accessed: Oct. 31, 2022. [Online]. Available: https://www.ieee802.org/3/av/public/baseline.html

[92] I. Cale *et al*., “Gigabit Passive Optical Network - GPON,” in *2007 29th International Conference on Information Technology Interfaces*, Jun. 2007, pp. 679–684. doi: 10.1109/ITI.2007.4283853.

[93] ITU, G. "984.1: Gigabit-capable passive optical networks (gpon): General characteristics." *ITU-T, March* (2008).

[94] S. Jain *et al.*, “World’s first XG-PON field trial,” *Journal of lightwave technology*, vol. 29, no. 4, pp. 524–528, 2011.

[95] ITU-T G, ITU-T. Recommendation. "987.1,“10-Gigabit-capable passive optical networks (XG-PON): General requirements,”." *International Telecommunication Union: Geneve, Switzerland* (2016).

[96] F. J. Effenberger *et al.*, “Next-generation PON-part III: System specifications for XP-PON,” *IEEE Communications Magazine*, vol. 47, no. 11, pp. 58–64, 2009.

[97] B. N. Mells *et al.*, “Frequency-stable semiconductor laser for DWDM,” in *Novel In-Plane Semiconductor Lasers*, SPIE, 2002, pp. 107–118.

[98] Y. Chang *et al.*, “Highly stable multi-wavelength fiber laser based on hybrid enclosed two-armed fiber filter,” *Optical Fiber Technology*, vol. 71, p. 102894, 2022.

[99] M. Abe *et al.*, “1-GHz-spaced 16-channel arrayed-waveguide grating for a wavelength reference standard in DWDM network systems,” *Journal of lightwave technology*, vol. 20, no. 5, p. 822, 2002.

[100] N. Solihah *et al.*, “DEVELOPMENT OF MULTICAST SERVICE TECHNICAL REQUIREMENTS REGULATION ON XG-PON OLT EQUIPMENT,” *Jurnal Penelitian Pos dan Informatika*, vol. 10, no. 1, pp. 59–72, 2020.

[101] F. J. Effenberger *et al.*, “The XG-PON system: Cost effective 10 Gb/s access,” *Journal of lightwave technology*, vol. 29, no. 4, pp. 403–409, 2011.

[102] Bonk, R., *et al*. "40-Gigabitcapable passive optical networks (NGPON2): Physical media dependent (PMD) layer specification." *ITU-T, G* 989 (2012).

[103] Recommendation, I. T. U. T. G. "9804.3,“50-Gigabitcapable passive optical networks (50G-PON): Physical media dependent (PMD) layer specification,”." *International Telecommunication Union* (2021).

[104] D. Zhang *et al*., “Progress of ITU-T higher speed passive optical network (50G-PON) standardization,” *J. Opt. Commun. Netw.*, vol. 12, no. 10, p. D99, Oct. 2020, doi: 10.1364/JOCN.391830.

[105] “World Internet Users Statistics and 2022 World Population Stats.” Accessed: Oct. 28, 2022. [Online]. Available: https://www.internetworldstats.com/stats.htm

[106] “Miyamoto *et al*.*,* "Space Division Multiplexing Optical Transmission T.pdf.” Accessed: Oct. 28, 2022. [Online]. Available: https://www.ntt-review.jp/archive/ntttechnical.php?contents=ntr201706fa1.pdf&mode=show_pdf".

[107] Y. Miyamoto *et al*., “Space Division Multiplexing Optical Transmission Technology to Support the Evolution of High-capacity Optical Transport Networks,” vol. 15, no. 6, 2017.

[108] S. Matsuo *et al*., “Design Optimization of Trench Index Profile for the same dispersion characteristics with SMF,” in *OFC/NFOEC 2007 - 2007 Conference on Optical Fiber Communication and the National Fiber Optic Engineers Conference*, Mar. 2007, pp. 1–3. doi: 10.1109/OFC.2007.4348404.

[109] C.-H. Yeh *et al*., “Using OOK Modulation for Symmetric 40-Gb/s Long-Reach Time-Sharing Passive Optical Networks,” *IEEE Photonics Technology Letters*, vol. 22, no. 9, pp. 619–621, May 2010, doi: 10.1109/LPT.2010.2043353.

[110] Bogoni, Antonella *et al.,* "OTDM-based optical communications networks at 160 Gbit/s and beyond." *Optical Fiber Technology* 13.1 (2007): 1-12.

[111] Md. N. H. Prince *et al*., “Performance Limitations of an Optical TDM Transmission Link Caused by Fiber Chromatic Dispersion,” in *2020 FORTEI-International Conference on Electrical Engineering (FORTEI-ICEE)*, Sep. 2020, pp. 130–133. doi: 10.1109/FORTEI-ICEE50915.2020.9249807.

[112] M. Bouda *et al.*, “Compact High-Power Wavelength Selectable Lasers for WDM Applications,” in *Optical Fiber Communication Conference (2000), paper TuL1*, Optica Publishing Group, Mar. 2000, p. TuL1. Accessed: Feb. 07, 2023. [Online]. Available: https://opg.optica.org/abstract.cfm?uri=OFC-2000-TuL1

[113] M. Funabashi *et al.*, “Recent advances in DFB lasers for ultradense WDM applications,” *IEEE Journal of Selected Topics in Quantum Electronics*, vol. 10, no. 2, pp. 312–320, Mar. 2004, doi: 10.1109/JSTQE.2004.826576.

[114] S.-M. Lee *et al.*, “Dense WDM-PON based on wavelength-locked Fabry-Pe/spl acute/rot laser diodes,” *IEEE Photonics Technology Letters*, vol. 17, no. 7, pp. 1579–1581, Jul. 2005, doi: 10.1109/LPT.2005.848558.

[115] J. Kani *et al.*, “Enabling Technologies for Future Scalable and Flexible WDM-PON and WDM/TDM-PON Systems,” *IEEE Journal of Selected Topics in Quantum Electronics*, vol. 16, no. 5, pp. 1290–1297, Sep. 2010, doi: 10.1109/JSTQE.2009.2035640.

[116] D. Zhao *et al.*, “Multiple wavelength load balancing in TWDM-PON,” in *2015 Opto-Electronics and Communications Conference (OECC)*, Jun. 2015, pp. 1–3. doi: 10.1109/OECC.2015.7340070.

[117] N. Cheng *et al.*, “Flexible TWDM PONs,” in *OFC 2014*, Mar. 2014, pp. 1–3. doi: 10.1364/OFC.2014.W1D.2.

[118] M. R. Phillips *et al.*, “Crosstalk due to optical fiber nonlinearities in WDM CATV lightwave systems,” *J. Lightwave Technol.*, vol. 17, no. 10, pp. 1782–1792, Oct. 1999, doi: 10.1109/50.793751.

[119] D. Marcuse *et al.*, “Effect of fiber nonlinearity on long-distance transmission,” *Journal of Lightwave Technology*, vol. 9, no. 1, pp. 121–128, Jan. 1991, doi: 10.1109/50.64931.

[120] M. Wu *et al.*, “Fiber Nonlinearity Limitations in Ultra-Dense WDM Systems,” *J. Lightwave Technol.*, vol. 22, no. 6, pp. 1483–1498, Jun. 2004, doi: 10.1109/JLT.2004.829222.

[121] C. H. Lin *et al.*, “Cascade self-induced holography: a new grating fabrication technology for DFB/DBR lasers and WDM laser arrays,” *IEEE Journal of Quantum Electronics*, vol. 32, no. 10, pp. 1752–1759, Oct. 1996, doi: 10.1109/3.538781.

[122] Q. Lu *et al.*, “Single mode lasers based on slots suitable for photonic integration,” *Opt. Express, OE*, vol. 19, no. 26, pp. B140–B145, Dec. 2011, doi: 10.1364/OE.19.00B140.

[123] W.-H. Guo *et al.*, “Integrable Slotted Single-Mode Lasers,” *IEEE Photonics Technology Letters*, vol. 24, no. 8, pp. 634–636, Apr. 2012, doi: 10.1109/LPT.2012.2184745.

[124] A. Abdullaev *et al.*, “Linewidth Characterization of Integrable Slotted Single-Mode Lasers,” *IEEE Photonics Technology Letters*, vol. 26, no. 22, pp. 2225–2228, Nov. 2014, doi: 10.1109/LPT.2014.2350772.

[125] P. Ma *et al.*, “30-Gbps Directly Modulated Semiconductor Lasers Based on Surface High-Order Gratings,” *IEEE Photonics Technology Letters*, vol. 33, no. 4, pp. 197–200, Feb. 2021, doi: 10.1109/LPT.2021.3049859.

[126] B. Kelly *et al.*, “Discrete mode laser diodes with very narrow linewidth emission,” *Electronics Letters*, vol. 43, no. 23, 2007.

[127] N. P. Kelly *et al.*, “Regrowth-Free Single Mode Laser Based on Dual Port Multimode Interference Reflector,” *IEEE Photonics Technology Letters*, vol. 29, no. 3, pp. 279–282, Feb. 2017, doi: 10.1109/LPT.2016.2637565.

[128] P. E. Morrissey *et al.*, “Coupled Cavity Single-Mode Laser Based on Regrowth-Free Integrated MMI Reflectors,” *IEEE Photonics Technology Letters*, vol. 28, no. 12, pp. 1313–1316, Jun. 2016, doi: 10.1109/LPT.2016.2541695.

[129] V. Tolstikhin *et al.*, “Distributed feedback lasers for regrowth-free multi-guide vertical integration in InP,” in *2010 23rd Annual Meeting of the IEEE Photonics Society*, Nov. 2010, pp. 521–522. doi: 10.1109/PHOTONICS.2010.5698990.

[130] L. Caro *et al.*, “An Integration-Friendly Regrowth-Free Tunable Laser,” *IEEE Photonics Technology Letters*, vol. 30, no. 3, pp. 270–272, Feb. 2018, doi: 10.1109/LPT.2017.2781799.

[131] R. M. Briggs *et al.*, “Regrowth-free single-mode quantum cascade lasers with power consumption below 1 W,” *Appl. Phys. Lett.*, vol. 105, no. 14, p. 141117, Oct. 2014, doi: 10.1063/1.4898003.

[132] “https://github.com/jtambasco/modesolverpy”.

[133] “https://camfr.sourceforge.net/”.

[134] M. Kamp *et al.*, “Lateral coupling – a material independent way to complex coupled DFB lasers,” *Optical Materials*, vol. 17, no. 1, pp. 19–25, Jun. 2001, doi: 10.1016/S0925-3467(01)00014-3.

[135] L. Hou *et al.* , “Laterally coupled dual-grating distributed feedback lasers for generating mode-beat terahertz signals,” *Opt. Lett., OL*, vol. 40, no. 2, pp. 182–185, Jan. 2015, doi: 10.1364/OL.40.000182.

[136] L. Liu *et al.*, “High-brightness single-mode double-tapered laser diodes with laterally coupled high-order surface grating,” *Optics Letters*, vol. 39, no. 11, pp. 3231–3234, 2014.

[137] Y.-L. Cao *et al.*, “Hybrid III–V/silicon laser with laterally coupled Bragg grating,” *Optics express*, vol. 23, no. 7, pp. 8800–8808, 2015.

[138] M. Müller *et al.* , “Wide-range-tunable laterally coupled distributed feedback lasers based on InGaAsP–InP,” *Applied Physics Letters*, vol. 79, no. 17, pp. 2684–2686, 2001.

[139] F. Pozzi *et al.*, “Dual-wavelength InAlGaAs–InP laterally coupled distributed feedback laser,” *IEEE photonics technology letters*, vol. 18, no. 24, pp. 2563–2565, 2006.

[140] J. A. Gupta *et al.*, “High-resolution methane spectroscopy using InGaAsSb/AlInGaAsSb laterally-coupled index-grating distributed feedback laser diode at 3.23 [mu] m,” *Electronics letters*, vol. 48, no. 7, p. 1, 2012.

[141] L. Bach *et al.*, “Laterally coupled DBR laser emitting at 1.55 μm fabricated by focused ion beam lithography,” *IEEE Photonics Technology Letters*, vol. 14, no. 8, pp. 1037–1039, 2002.

[142] Y. Wang *et al.*, “Narrow Linewidth Single-Mode Slotted Fabry–Pérot Laser Using Deep Etched Trenches,” *IEEE Photonics Technology Letters*, vol. 24, no. 14, pp. 1233–1235, Jul. 2012, doi: 10.1109/LPT.2012.2201711.

[143] Q. Lu *et al.*, “Slotted Single Mode Lasers Integrated With a Semiconductor Optical Amplifier,” *IEEE Photonics Technology Letters*, vol. 25, no. 6, pp. 564–567, Mar. 2013, doi: 10.1109/LPT.2013.2245645.

[144] Q. Lu *et al.*, “Design of Slotted Single-Mode Lasers Suitable for Photonic Integration,” *IEEE Photonics Technology Letters*, vol. 22, no. 11, pp. 787–789, Jun. 2010, doi: 10.1109/LPT.2010.2045888.

[145] W.-H. Guo *et al.*, “Integrable Slotted Single-Mode Lasers,” *IEEE Photonics Technology Letters*, vol. 24, no. 8, pp. 634–636, Apr. 2012, doi: 10.1109/LPT.2012.2184745.

[146] T. Yu *et al.*, “Single-mode and wavelength tunable lasers based on deep-submicron slots fabricated by standard UV-lithography,” *Opt. Express, OE*, vol. 20, no. 15, pp. 16291–16298, Jul. 2012, doi: 10.1364/OE.20.016291.

[147] M. J. Wallace *et al.*, “Athermal operation of multi-section slotted tunable lasers,” *Opt. Express, OE*, vol. 25, no. 13, pp. 14414–14426, Jun. 2017, doi: 10.1364/OE.25.014414.

[148] Q. Lu *et al.*, “Design of slotted single-mode lasers suitable for photonic integration,” *IEEE Photonics Technology Letters*, vol. 22, no. 11, pp. 787–789, 2010.

[149] X. Jinbiao *et al.*, "Full-vectorial mode solver for anisotropic optical waveguides using multidomain spectral collocation method." Optics Communications 283.14 (2010): 2835-2840.

[150] A. B. Fallahkhair *et al.*, “Vector finite difference modesolver for anisotropic dielectric waveguides,” *Journal of lightwave technology*, vol. 26, no. 11, pp. 1423–1431, 2008.

[151] P. Ma *et al.*, “Single-mode semiconductor lasers fabricated by standard photolithography for direct modulation,” *Opt. Express*, vol. 27, no. 4, p. 5502, Feb. 2019, doi: 10.1364/OE.27.005502.

[152] L. A. Coldren *et al.*, *Diode lasers and photonic integrated circuits*. John Wiley & Sons, 2012.

[153] H. Wenzel *et al.*, “A comparative study of higher order Bragg gratings: coupled-mode theory versus mode expansion modeling,” *IEEE Journal of Quantum Electronics*, vol. 42, no. 1, pp. 64–70, Jan. 2006, doi: 10.1109/JQE.2005.859910.

[154] S. O’Brien *et al.*, “Design, Characterization, and Applications of Index-Patterned Fabry–Pérot Lasers,” *IEEE Journal of Selected Topics in Quantum Electronics*, vol. 17, no. 6, pp. 1621–1631, Nov. 2011, doi: 10.1109/JSTQE.2011.2118192.

[155] H. Kogelnik *et al.*, “Coupled-wave theory of distributed feedback lasers,” *Journal of applied physics*, vol. 43, no. 5, pp. 2327–2335, 1972.

[156] Q. Y. Lu *et al.*, “Analysis of slot characteristics in slotted single-mode semiconductor lasers using the 2-D scattering matrix method,” *IEEE Photonics Technology Letters*, vol. 18, no. 24, pp. 2605–2607, 2006.

[157] P. Bienstman *et al.*, “Optical modelling of photonic crystals and VCSELs using eigenmode expansion and perfectly matched layers,” *Optical and Quantum Electronics*, vol. 33, no. 4, pp. 327–341, 2001.

[158] M. G. Moharam *et al.*, “Rigorous coupled-wave analysis of planar-grating diffraction,” *JOSA*, vol. 71, no. 7, pp. 811–818, 1981.

[159] W. Sun *et al.*, “Analysis of High-Order Slotted Surface Gratings by the 2-D Finite-Difference Time-Domain Method,” *Journal of Lightwave Technology*, vol. 35, no. 1, pp. 96–102, Jan. 2017, doi: 10.1109/JLT.2016.2627604.

[160] C. Ellmers *et al.*, “Measurement and calculation of gain spectra for (GaIn)As/(AlGa)As single quantum well lasers,” *Appl. Phys. Lett.*, vol. 72, no. 13, pp. 1647–1649, Mar. 1998, doi: 10.1063/1.121140.

[161] B. W. Hakki *et al.*, “cw degradation at 300 K of GaAs double-heterostructure junction lasers. II. Electronic gain,” *Journal of Applied Physics*, vol. 44, no. 9, pp. 4113–4119, 1973.

[162] H. Wang *et al.*, “Gain measurements of Fabry-Pe/spl acute/rot semiconductor lasers using a nonlinear least-squares fitting method,” *IEEE journal of quantum electronics*, vol. 41, no. 4, pp. 532–540, 2005.

[163] D. Hofstetter *et al.*, “Measurement of semiconductor laser gain and dispersion curves utilizing Fourier transforms of the emission spectra,” *IEEE Photonics Technology Letters*, vol. 11, no. 11, pp. 1372–1374, 1999.

[164] W.-H. Guo *et al.*, “Measurement of gain spectrum for Fabry-Perot semiconductor lasers by the Fourier transform method with a deconvolution process,” *IEEE journal of quantum electronics*, vol. 39, no. 6, pp. 716–721, 2003.

[165] W.-H. Guo *et al.*, “Fourier series expansion method for gain measurement from amplified spontaneous emission spectra of Fabry-Perot semiconductor lasers,” *IEEE journal of quantum electronics*, vol. 40, no. 2, pp. 123–129, 2004.

[166] A. Oster *et al.*, “Gain spectra measurements by a variable stripe length method with current injection,” *Electronics Letters*, vol. 33, no. 10, pp. 864–866, 1997.

[167] D. Pustakhod *et al.*, “Fast and Robust Method for Measuring Semiconductor Optical Amplifier Gain,” *IEEE Journal of Selected Topics in Quantum Electronics*, vol. 24, no. 1, pp. 1–9, Jan. 2018, doi: 10.1109/JSTQE.2017.2737581.

[168] G. Lippi *et al.*, "Analytical vs. numerical Langevin description of noise in small lasers." arXiv preprint arXiv:1903.08859 (2019). [169] G. Feng and X. Fernando, “Simulation and Analysis of Single Mode Semiconductor Laser”.

[170] “Homepage,” Nazca Design. Accessed: Aug. 12, 2023. [Online]. Available: https://nazca-design.org/

[171] “KLayout Layout Viewer And Editor.” Accessed: Aug. 12, 2023. [Online]. Available: https://www.klayout.de/build.html

[172] M. Chen *et al.*, “Ultra-narrow linewidth measurement based on Voigt profile fitting,” *Optics express*, vol. 23, no. 5, pp. 6803–6808, 2015.

[173] G. Poberaj *et al.*, “Lithium niobate on insulator (LNOI) for micro-photonic devices,” *Laser & photonics reviews*, vol. 6, no. 4, pp. 488–503, 2012.

[174] S. Koeber *et al.*, “Femtojoule electro-optic modulation using a silicon–organic hybrid device,” *Light: Science & Applications*, vol. 4, no. 2, pp. e255–e255, 2015.

[175] J. Liu *et al.*, “Waveguide-integrated, ultralow-energy GeSi electro-absorption modulators,” *Nature Photonics*, vol. 2, no. 7, pp. 433–437, 2008.

[176] J. Ozaki *et al.*, “High-speed modulator for next-generation large-capacity coherent optical networks,” *NTT Tech. Rev*, vol. 16, no. 4, pp. 1–8, 2018.

[177] M. G. Wood *et al.*, “Gigahertz speed operation of epsilon-near-zero silicon photonic modulators,” *Optica*, vol. 5, no. 3, pp. 233–236, 2018.

[178] G. T. Reed *et al.*, “Silicon optical modulators,” *Nature photonics*, vol. 4, no. 8, pp. 518–526, 2010.

[179] M. Li *et al.*, “Lithium niobate photonic-crystal electro-optic modulator,” *Nat Commun*, vol. 11, no. 1, Art. no. 1, Aug. 2020, doi: 10.1038/s41467-020-17950-7.

[180] E. L. Wooten *et al.*, “A review of lithium niobate modulators for fiber-optic communications systems,” *IEEE Journal of selected topics in Quantum Electronics*, vol. 6, no. 1, pp. 69–82, 2000.

[181] M. Seimetz, *High-order modulation for optical fiber transmission*, vol. 143. Springer, 2009.

[182] L. Arizmendi *et al.*, "Photonic applications of lithium niobate crystals," *physica status solidi (a)*, vol. 201, no. 2, pp. 253–283, 2004, doi: 10.1002/pssa.200303911.

[183] G. Breed *et al.*, "A tutorial introduction to optical modulation techniques," *High Frequency Electronics*, 2007.

[184] Y. Yacoby *et al.*, "High-frequency franz-keldysh effect," *Physical Review*, vol. 169, no. 3, p. 610, 1968.

[185] B. O. Seraphin *et al.*, "Franz-Keldysh effect of the refractive index in semiconductors," *Physical Review*, vol. 139, no. 2A, p. A560, 1965.

[186] H. I. Ralph *et al.*, "On the theory of the Franz-Keldysh effect," *Journal of Physics C: Solid State Physics*, vol. 1, no. 2, p. 378, 1968.

[187] D. A. B. Miller *et al.*, "Relation between electroabsorption in bulk semiconductors and in quantum wells: The quantum-confined Franz-Keldysh effect," *Physical Review B*, vol. 33, no. 10, p. 6976, 1986.

[188] A.-P. Jauho *et al.*, "Dynamical franz-keldysh effect," *Physical review letters*, vol. 76, no. 24, p. 4576, 1996.

[189] J. Liu *et al.*, "Waveguide-integrated, ultralow-energy GeSi electro-absorption modulators," *Nature photonics*, vol. 2, no. 7, pp. 433–437, 2008.

[190] E. Lach *et al.*, "Application of electroabsorption modulators for high-speed transmission systems," *Journal of Optical and Fiber Communications Reports*, vol. 2, no. 2, pp. 140–170, 2005.

[191] L. V. Keldysh *et al.*, "Behavior of non-metallic crystals in strong electric fields," *Soviet Journal of Experimental and Theoretical Physics*, vol. 6, p. 763, 1958.

[192] I. Bar-Joseph *et al.* "Quantum-confined Stark effect in InGaAs/InP quantum wells grown by organometallic vapor phase epitaxy," *Applied physics letters*, vol. 50, no. 15, pp. 1010–1012, 1987.

[193] M. Trajkovic *et al.*,"High speed electroabsorption modulator in the generic photonic integration platform," in *20th Annual Symposium of the IEEE Photonics Benelux Chapter*, OPERA-photonics, Brussels School of Engineering, 2015, pp. 75–78.

[194] M. E. Chin *et al.*, “Theoretical design optimization of multiple-quantum-well electroabsorption waveguide modulators,” *IEEE Journal of Quantum Electronics*, vol. 29, no. 9, pp. 2476–2488, Sep. 1993, doi: 10.1109/3.247705.

[195] D. Feng *et al.*, “High speed GeSi electro-absorption modulator at 1550 nm wavelength on SOI waveguide,” *Opt. Express, OE*, vol. 20, no. 20, pp. 22224–22232, Sep. 2012, doi: 10.1364/OE.20.022224.

[196] M.-H. Park *et al.*, “Low resistance Ohmic contact scheme (μØmega cm 2) to p-InP,” *Applied physics letters*, vol. 70, no. 1, pp. 99–101, 1997.

[197] Y. T. Hu *et al.*, “Broadband 10Gb/s graphene electro-absorption modulator on silicon for chip-level optical interconnects,” in *2014 IEEE International Electron Devices Meeting*, IEEE, 2014, pp. 5–6.

[198] D. Lavery *et al.*, “Digital coherent receivers for long-reach optical access networks,” *Journal of Lightwave Technology*, vol. 31, no. 4, pp. 609–620, 2012.

[199] S. Hein *et al.*, “Modulation Bandwidth and Linewidth Enhancement Factor of High-Speed 1.55-μ m Quantum-Dash Lasers,” *IEEE Photonics Technology Letters*, vol. 21, no. 8, pp. 528–530, Apr. 2009, doi: 10.1109/LPT.2009.2014076.

[200] S. M. Kim *et al.*, “High-frequency modulation characteristics of 1.3-μm InGaAs quantum dot lasers,” *IEEE Photonics Technology Letters*, vol. 16, no. 2, pp. 377–379, Feb. 2004, doi: 10.1109/LPT.2003.823088.

[201] C. M. Miller *et al.*, “Intensity modulation and noise characterization of high-speed semiconductor lasers,” *IEEE LTS*, vol. 2, no. 2, pp. 44–50, May 1991, doi: 10.1109/80.93288.

[202] O. Ozolins *et al.*, “100 GHz externally modulated laser for optical interconnects,” *Journal of Lightwave Technology*, vol. 35, no. 6, pp. 1174–1179, 2017.

[203] N. Andriolli *et al.*, “InP monolithically integrated transmitters based on high speed directly modulated DFB lasers,” *IEEE Journal of Selected Topics in Quantum Electronics*, vol. 26, no. 5, pp. 1–6, 2020.

[204] C. Ke *et al.*, “Design Optimization for 25Gbps DML InAlGaAs/InP SL-MQW Laser Diode,” in *Asia Communications and Photonics Conference*, Optica Publishing Group, 2016, pp. AF2A-62.

[205] L. Xie *et al.*, “24-GHz Directly Modulated DFB Laser Modules for Analog Applications,” *IEEE Photonics Technology Letters*, vol. 24, no. 5, pp. 407–409, Mar. 2012, doi: 10.1109/LPT.2011.2179026.

[206] C. B. Su *et al.*, “Effect of doping level on the gain constant and modulation bandwidth of InGaAsP semiconductor lasers,” *Applied physics letters*, vol. 45, no. 12, pp. 1302–1304, 1984.

[207] C.-H. Chang *et al.*, “Injection locking of VCSELs,” *IEEE Journal of Selected Topics in Quantum Electronics*, vol. 9, no. 5, pp. 1386–1393, Sep. 2003, doi: 10.1109/JSTQE.2003.819510.

[208] A. Villafranca *et al.*, “Precise characterization of the frequency chirp in directly modulated DFB lasers,” in *2007 Spanish Conference on Electron Devices*, IEEE, 2007, pp. 173–176.

[209] S. Mohrdiek *et al.*, “Chirp reduction of directly modulated semiconductor lasers at 10 Gb/s by strong CW light injection,” *Journal of Lightwave Technology*, vol. 12, no. 3, pp. 418–424, 1994.

[210] Y. Matsui *et al.*, “Chirp-managed directly modulated laser (CML),” *IEEE Photonics Technology Letters*, vol. 18, no. 2, pp. 385–387, 2006.

[211] D. Mahgerefteh *et al.*, “Error-free 250 km transmission in standard fibre using compact 10 Gbit/s chirp-managed directly modulated lasers (CML) at 1550 nm,” *Electron. Lett*, vol. 41, no. 9, pp. 543–544, 2005.

[212] T. L. Koch *et al.*, “Nature of wavelength chirping in directly modulated semiconductor lasers,” *Electronics letters*, vol. 20, no. 25, pp. 1038–1040, 1984.

[213] D. Mahgerefteh *et al.*, “Error-free 250 km transmission in standard fibre using compact 10 Gbit⁄s chirp-managed directly modulated lasers (CML) at 1550 nm,” *Electron. Lett.*, vol. 41, no. 9, p. 543, 2005, doi: 10.1049/el:20050631.

[214] Y. Matsui *et al.*, “Chirp-managed directly modulated laser (CML),” *IEEE Photonics Technology Letters*, vol. 18, no. 2, pp. 385–387, Jan. 2006, doi: 10.1109/LPT.2005.862358.

[215] J. Jian *et al.*, “High modulation efficiency lithium niobate Michelson interferometer modulator,” *Optics Express*, vol. 27, no. 13, pp. 18731–18739, 2019.

[216] P. O. Weigel *et al.*, "Bonded thin film lithium niobate modulator on a silicon photonics platform exceeding 100 GHz 3-dB electrical modulation bandwidth," *Optics express*, vol. 26, no. 18, pp. 23728–23739, 2018.

[217] A. J. Mercante *et al.*, "Thin film lithium niobate electro-optic modulator with terahertz operating bandwidth," *Optics express*, vol. 26, no. 11, pp. 14810–14816, 2018.

[218] A. Rao *et al.*, "Heterogeneous microring and Mach-Zehnder modulators based on lithium niobate and chalcogenide glasses on silicon," *Optics express*, vol. 23, no. 17, pp. 22746–22752, 2015.

[219] S. N. Malinowski *et al.*, "Heterogeneous Microring And Mach-Zehnder Modulators Based On Lithium Niobate And Chalcogenide Glasses On Silicon," *Thin-film Lithium Niobate Photonics for Electro-optics, Nonlinear Optics, and Quantum Optics on Silicon*, vol. 23, no. 17, p. 109, 2018.

[220] L. Chen *et al.*, "Hybrid silicon and lithium niobate electro-optical ring modulator," *Optica*, vol. 1, no. 2, pp. 112–118, 2014.

[221] L. Chen *et al.*, "12.5 pm/V hybrid silicon and lithium niobate optical microring resonator with integrated electrodes," *Optics express*, vol. 21, no. 22, pp. 27003–27010, 2013.

[222] A. Guarino *et al.*, "Electro–optically tunable microring resonators in lithium niobate," *Nature photonics*, vol. 1, no. 7, pp. 407–410, 2007.

[223] S. Yin *et al.*, "100-km DWDM Transmission of 56-Gb/s PAM4 per $\backslashlambda $ via Tunable Laser and 10-Gb/s InP MZM," *IEEE Photonics Technology Letters*, vol. 27, no. 24, pp. 2531–2534, 2015.

[224] K. Prosyk *et al.*, "Tunable InP-based optical IQ modulator for 160 Gb/s," in *European Conference and Exposition on Optical Communications*, Optica Publishing Group, 2011, p. Th-13.

[225] G. Letal *et al.*, "Low loss InP C-band IQ modulator with 40GHz bandwidth and 1.5 V Vπ," in *Optical Fiber Communication Conference*, Optica Publishing Group, 2015, pp. Th4E-3.

[226] R. A. Griffin *et al.*, “InP Mach–Zehnder modulator platform for 10/40/100/200-Gb/s operation,” *IEEE Journal of Selected Topics in Quantum Electronics*, vol. 19, no. 6, pp. 158–166, 2013.

[227] R. A. Griffin *et al.*, “Advances in InP optical modulators,” in *Asia Optical Fiber Communication and Optoelectronic Exposition and Conference*, Optica Publishing Group, 2008, p. SuF6.

[228] A. Aimone *et al.*, “DAC-free ultra-low-power dual-polarization 64-QAM transmission with InP IQ segmented MZM module,” in *Optical Fiber Communication Conference*, Optica Publishing Group, 2016, pp. Th5C-6.

[229] O. Ozolins *et al.*, “100 GHz externally modulated laser for optical interconnects,” *Journal of Lightwave Technology*, vol. 35, no. 6, pp. 1174–1179, 2017.

[230] G.-Y. Kim *et al.*, “The influence of chirp and extinction ratio on directly modulated DFB lasers,” in *Conference on Lasers and Electro-Optics/Pacific Rim*, Optica Publishing Group, 2001, p. P2_50.

[231] Y. Matsui *et al.*, “Transceiver for NG-PON2: Wavelength Tunablity for Burst Mode TWDM and Point-to-point WDM,” in *Optical Fiber Communication Conference (2016), paper Tu2C.1*, Optica Publishing Group, Mar. 2016, p. Tu2C.1. doi: 10.1364/OFC.2016.Tu2C.1.

[232] T. N. Duong *et al.*, “Very high bit rate transmission for NGPON using AMOOFDM direct modulation of linear laser,” in *Optical Fiber Communication Conference*, Optica Publishing Group, 2010, p. OTuO3.

[233] E.-G. Lee *et al.*, “16-channel tunable VCSEL array with 50-GHz channel spacing for TWDM-PON ONUs,” in *39th European Conference and Exhibition on Optical Communication (ECOC 2013)*, Sep. 2013, pp. 1–3. doi: 10.1049/cp.2013.1354.

[234] A. C. Bordonalli *et al.*, “High-performance phase locking of wide linewidth semiconductor lasers by combined use of optical injection locking and optical phase-lock loop,” *Journal of Lightwave Technology*, vol. 17, no. 2, p. 328, 1999.

[235] G. D. Villarreal *et al.*, “Performance of WDM-PON system based on optical frequency comb generation,” in *2013 IEEE Colombian Conference on Communications and*

Computing (COLCOM), May 2013, pp. 1–6. doi: 10.1109/ColComCon.2013.6564819.

[236] M. Bi *et al.*, "Power budget improvement of symmetric 40-Gb/s DML-based TWDM-PON system," *Optics express*, vol. 22, no. 6, pp. 6925–6933, 2014.

[237] L. Yi *et al.*, "Symmetric 40-Gb/s TWDM-PON with 39-dB power budget," *IEEE Photonics Technology Letters*, vol. 25, no. 7, pp. 644–647, 2013.

[238] Z. Zhou *et al.*, "Experimental demonstration of symmetric 100-Gb/s DML-based TWDM-PON system," *IEEE Photonics Technology Letters*, vol. 27, no. 5, pp. 470–473, 2014.

[239] A. Paśnikowska *et al.*, "Integrated transceivers for WDM-PON access systems," in *2018 Baltic URSI Symposium (URSI)*, IEEE, 2018, pp. 31–32.

[240] L. M. Augustin *et al.*, "InP-Based Generic Foundry Platform for Photonic Integrated Circuits," *IEEE Journal of Selected Topics in Quantum Electronics*, vol. 24, no. 1, pp. 1–10, Jan. 2018, doi: 10.1109/JSTQE.2017.2720967.

[241] G.-H. Duan *et al.*, "Hybrid III–V on Silicon Lasers for Photonic Integrated Circuits on Silicon," *IEEE Journal of Selected Topics in Quantum Electronics*, vol. 20, no. 4, pp. 158–170, Jul. 2014, doi: 10.1109/JSTQE.2013.2296752.

[242] Z. Liu *et al.*, "Optical injection locking: From principle to applications," *Journal of Lightwave Technology*, vol. 38, no. 1, pp. 43–59, 2020.

[243] H.-K. Sung *et al.*, "Optical single sideband modulation using strong optical injection-locked semiconductor lasers," *IEEE Photonics Technology Letters*, vol. 19, no. 13, pp. 1005–1007, 2007.

[244] R. T. Ramos *et al.*, "Optical injection locking and phase-lock loop combined systems," *Optics letters*, vol. 19, no. 1, pp. 4–6, 1994.

[245] Z. Liu *et al.*, "Homodyne OFDM with optical injection locking for carrier recovery," *Journal of Lightwave Technology*, vol. 33, no. 1, pp. 34–41, 2014.

[246] E. K. Lau *et al.*, "Strong optical injection-locked semiconductor lasers demonstrating> 100-GHz resonance frequencies and 80-GHz intrinsic bandwidths," *Optics Express*, vol. 16, no. 9, pp. 6609–6618, 2008.

[247] E. K. Lau *et al.*, “Enhanced modulation characteristics of optical injection-locked lasers: A tutorial,” *IEEE Journal of Selected Topics in Quantum Electronics*, vol. 15, no. 3, pp. 618–633, 2009.

[248] E. K. Lau *et al.*, “Frequency response enhancement of optical injection-locked lasers,” *IEEE Journal of Quantum Electronics*, vol. 44, no. 1, pp. 90–99, 2007.

[249] A. C. Bordonalli *et al.*, “Optical injection locking to optical frequency combs for superchannel coherent detection,” *Optics express*, vol. 23, no. 2, pp. 1547–1557, 2015.

[250] H.-K. Sung *et al.*, “Optical single sideband modulation using strong optical injection-locked semiconductor lasers,” *IEEE Photonics Technology Letters*, vol. 19, no. 13, pp. 1005–1007, 2007.

[251] S. Shao *et al.*, “Gain-Switched Optical Frequency Comb Source Using a Hybrid Integrated Self-Injection Locking DFB Laser,” *IEEE Photonics Journal*, vol. 14, no. 1, pp. 1–6, Feb. 2022, doi: 10.1109/JPHOT.2022.3141424.

[252] X. Zhang *et al.*, “Sideband Ampilification Injection Locking Effect in Integrated Mutual Injection DFB Laser,” in *2021 19th International Conference on Optical Communications and Networks (ICOCN)*, Aug. 2021, pp. 01–04. doi: 10.1109/ICOCN53177.2021.9563746.

[253] A. H. Perrott *et al.*, “Mutual Injection Locking of Lasers in a Photonic Integrated Circuit”.

[254] K. Balakier *et al.*, “Optical injection locking of monolithically integrated photonic source for generation of high purity signals above 100 GHz,” *Opt. Express, OE*, vol. 22, no. 24, pp. 29404–29412, Dec. 2014, doi: 10.1364/OE.22.029404.

[255] H.-K. Sung *et al.*, “Optical properties and modulation characteristics of ultra-strong injection-locked distributed feedback lasers,” *IEEE Journal of Selected Topics in Quantum Electronics*, vol. 13, no. 5, pp. 1215–1221, 2007.

[256] A. Hurtado *et al.*, “Polarization effects in Optically-Injected Long-Wavelength Vertical-Cavity Surface Emitting Lasers,” in *2011 13th International Conference on Transparent Optical Networks*, IEEE, 2011, pp. 1–4.

[257] X. Zhang *et al.*, “The design of bi-layer vertical grating coupler for the hybrid integration of VCSEL with stable polarization on silicon photonics,” in *Asia*

Communications and Photonics Conference, Optica Publishing Group, 2019, pp. M4A-273.

[258] S. Ristic *et al.*, "An Optical Phase-Locked Loop Photonic Integrated Circuit," *Journal of Lightwave Technology*, vol. 28, no. 4, pp. 526–538, Feb. 2010, doi: 10.1109/JLT.2009.2030341.

[259] A. H. Perrott *et al.*, "A Comparison between off and On-Chip Injection Locking in a Photonic Integrated Circuit," *Photonics*, vol. 6, no. 4, Art. no. 4, Dec. 2019, doi: 10.3390/photonics6040103.

[260] H.-K. Sung *et al.*, "Modulation bandwidth enhancement and nonlinear distortion suppression in directly modulated monolithic injection-locked DFB lasers," in *MWP 2003 Proceedings. International Topical Meeting on Microwave Photonics, 2003.*, IEEE, 2003, pp. 27–30.

[261] A. Tauke-Pedretti *et al.*, "Mutual injection locking of monolithically integrated coupled-cavity DBR lasers," *IEEE Photonics Technology Letters*, vol. 23, no. 13, pp. 908–910, 2011.

[262] G. P. Agrawal, *Fiber-optic communication systems*. John Wiley & Sons, 2012.

[263] E. K. Lau *et al.*, "Enhanced modulation characteristics of optical injection-locked lasers: A tutorial," *IEEE Journal of Selected Topics in Quantum Electronics*, vol. 15, no. 3, pp. 618–633, 2009.

[264] E. K. Lau *et al.*, "Frequency response enhancement of optical injection-locked lasers," *IEEE Journal of Quantum Electronics*, vol. 44, no. 1, pp. 90–99, 2007.

[265] E. K. Lau *et al.*, "Strong optical injection-locked semiconductor lasers demonstrating> 100-GHz resonance frequencies and 80-GHz intrinsic bandwidths," *Optics Express*, vol. 16, no. 9, pp. 6609–6618, 2008.

[266] A. Murakami *et al.*, "Cavity resonance shift and bandwidth enhancement in semiconductor lasers with strong light injection," *IEEE journal of quantum electronics*, vol. 39, no. 10, pp. 1196–1204, 2003.

[267] J. Stohs *et al.*, "Gain, refractive index change, and linewidth enhancement factor in broad-area GaAs and InGaAs quantum-well lasers," *IEEE Journal of Quantum Electronics*, vol. 37, no. 11, pp. 1449–1459, Nov. 2001, doi: 10.1109/3.958374.

[268] J. Z. Wilcox *et al.*, “Gain-and threshold-current dependence for multiple-quantum-well lasers,” *Journal of applied physics*, vol. 64, no. 11, pp. 6564–6567, 1988.

[269] R. Nagarajan *et al.*, “Effects of carrier transport on injection efficiency and wavelength chirping in quantum-well lasers,” *IEEE Journal of Quantum Electronics*, vol. 29, no. 6, pp. 1601–1608, Jun. 1993, doi: 10.1109/3.234411.

[270] A. Zadok *et al.*, “Spectral shift and broadening of DFB lasers under direct modulation,” *IEEE Photonics Technology Letters*, vol. 10, no. 12, pp. 1709–1711, 1998.

[271] K. Sato *et al.*, “Chirp characteristics of 40-Gb/s directly modulated distributed-feedback laser diodes,” *Journal of Lightwave technology*, vol. 23, no. 11, p. 3790, 2005.

[272] S. Mohrdiek *et al.*, “10-Gb/s standard fiber transmission using directly modulated 1.55-μm quantum-well DFB lasers,” *IEEE Photonics Technology Letters*, vol. 7, no. 11, pp. 1357–1359, 1995.

[273] T. L. Koch *et al.*, “Nature of wavelength chirping in directly modulated semiconductor lasers,” *Electronics letters*, vol. 20, no. 25, pp. 1038–1040, 1984.

[274] G. Yabre *et al.*, “Effect of relatively strong light injection on the chirp-to-power ratio and the 3 dB bandwidth of directly modulated semiconductor lasers,” *Journal of lightwave technology*, vol. 14, no. 10, pp. 2367–2373, 1996.

[275] S. Mohrdiek *et al.*, “Chirp reduction of directly modulated semiconductor lasers at 10 Gb/s by strong CW light injection,” *Journal of Lightwave Technology*, vol. 12, no. 3, pp. 418–424, 1994.

[276] S. Piazzolla *et al.*, “Small signal analysis of frequency chirping in injection-locked semiconductor lasers,” *IEEE Journal of Quantum Electronics*, vol. 22, no. 12, pp. 2219–2223, 1986.

[277] Y. Okajima *et al.*, “Experimental observation of chirp reduction in bandwidth-enhanced semiconductor lasers subject to strong optical injection,” *Optics Communications*, vol. 219, no. 1–6, pp. 357–364, Apr. 2003, doi: 10.1016/S0030-4018(03)01305-1.

[278] L. A. Coldren *et al.*, "Diode lasers and photonic integrated circuits". John Wiley & Sons, 2012.

[279] X. Shel *et al.*, “Reduced relative intensity noise of integrated DFB laser array under injection locking,” in *2020 Asia Communications and Photonics Conference (ACP) and International Conference on Information Photonics and Optical Communications (IPOC)*, IEEE, 2020, pp. 1–3.

[280] L. Chrostowski *et al.*, “Reduction of relative intensity noise and improvement of spur-free dynamic range of an injection locked VCSEL,” in *The 16th Annual Meeting of the IEEE Lasers and Electro-Optics Society, 2003. LEOS 2003.*, Oct. 2003, pp. 706–707 vol.2. doi: 10.1109/LEOS.2003.1252996.

[281] K. I. Kallimani *et al.*, “Relative intensity noise for laser diodes with arbitrary amounts of optical feedback,” *IEEE journal of quantum electronics*, vol. 34, no. 8, pp. 1438–1446, 1998.

[282] D. Liang *et al.*, “Hybrid integrated platforms for silicon photonics,” *Materials*, vol. 3, no. 3, pp. 1782–1802, 2010.

[283] M. J. Heck *et al.*, “Hybrid silicon photonic integrated circuit technology,” *IEEE Journal of Selected Topics in Quantum Electronics*, vol. 19, no. 4, pp. 6100117–6100117, 2012.

[284] Y. Arakawa *et al.*, “Silicon photonics for next generation system integration platform,” *IEEE Communications Magazine*, vol. 51, no. 3, pp. 72–77, 2013.

[285] U. Fischer *et al.*, “0.1 dB/cm waveguide losses in single-mode SOI rib waveguides,” *IEEE Photonics Technology Letters*, vol. 8, no. 5, pp. 647–648, May 1996, doi: 10.1109/68.491567.

[286] A. Bhardwaj *et al.*, “Low-Loss InGaAsP/InP Surface Ridge Waveguides for Photonic Integrated Circuits,” *IEEE Photonics Technology Letters*, vol. 28, no. 13, pp. 1403–1405, Jul. 2016, doi: 10.1109/LPT.2016.2543749.

[287] C. Sun *et al.*, “Modulation Characteristics Enhancement of Monolithically Integrated Laser Diodes Under Mutual Injection Locking,” *IEEE Journal of Selected Topics in Quantum Electronics*, vol. 21, no. 6, pp. 628–635, Nov. 2015, doi: 10.1109/JSTQE.2015.2478817.

[288] M. J. Wallace *et al.*, “Athermal operation of multi-section slotted tunable lasers,” *Optics Express*, vol. 25, no. 13, pp. 14414–14426, 2017.

[289] G. Jain *et al.*, “Directly modulated photonic integrated multi-section laser for next generation TWDM access networks,” in *45th European Conference on Optical Communication (ECOC 2019)*, IET, 2019, pp. 1–4.

[290] G. Jain *et al.*, “Directly modulated photonic integrated multi-section laser for next generation TWDM access networks,” in *45th European Conference on Optical Communication (ECOC 2019)*, Dublin, Ireland: Institution of Engineering and Technology, 2019, p. 389 (4 pp.)-389 (4 pp.). doi: 10.1049/cp.2019.1123.

[291] G. Jain *et al.*, “Design Optimization for Semiconductor Lasers With High-Order Surface Gratings Having Multiple Periods,” *Journal of Lightwave Technology*, vol. 36, no. 22, pp. 5121–5129, Nov. 2018, doi: 10.1109/JLT.2018.2869373.

[292] Y.-C. Xin *et al.*, “Characterization of the Static and Dynamic Parameters in a 1.3-μm Quantum Dot Mode-locked Laser,” in *2007 Conference on Lasers and Electro-Optics (CLEO)*, May 2007, pp. 1–2. doi: 10.1109/CLEO.2007.4452593.

[293] T. A. Heumier *et al.*, “Mode hopping in semiconductor lasers,” PhD Thesis, Montana State University-Bozeman, College of Letters & Science, 1992.

[294] F. Van Dijk, A. Accard *et al.*, “Monolithic dual wavelength DFB lasers for narrow linewidth heterodyne beat-note generation,” in *2011 International Topical Meeting on Microwave Photonics jointly held with the 2011 Asia-Pacific Microwave Photonics Conference*, IEEE, 2011, pp. 73–76.

[295] H. Ishii *et al.*, “Spectral linewidth reduction in widely wavelength tunable DFB laser array,” *IEEE Journal of Selected Topics in Quantum Electronics*, vol. 15, no. 3, pp. 514–520, 2009.

[296] M. Chen *et al.*, “Ultra-narrow linewidth measurement based on Voigt profile fitting,” *Optics express*, vol. 23, no. 5, pp. 6803–6808, 2015.

[297] F. van Dijk *et al.*, “Monolithic dual wavelength DFB lasers for narrow linewidth heterodyne beat-note generation,” in *2011 International Topical Meeting on Microwave Photonics jointly held with the 2011 Asia-Pacific Microwave Photonics Conference*, Oct. 2011, pp. 73–76. doi: 10.1109/MWP.2011.6088672.

[298] K. I. Kallimani *et al.*, “Relative intensity noise for laser diodes with arbitrary amounts of optical feedback,” *IEEE Journal of Quantum Electronics*, vol. 34, no. 8, pp. 1438–1446, Aug. 1998, doi: 10.1109/3.704337.

[299] W. V. Sorin *et al.*, “A simple intensity noise reduction technique for optical low-coherence reflectometry,” *IEEE Photonics Technology Letters*, vol. 4, no. 12, pp. 1404–1406, 1992.

[300] C. C. Rosa *et al.*, “Limitation of the achievable signal-to-noise ratio in optical coherence tomography due to mismatch of the balanced receiver,” *Applied optics*, vol. 43, no. 25, pp. 4802–4815, 2004.

[301] E. K. Lau *et al.*, “Enhanced Modulation Characteristics of Optical Injection-Locked Lasers: A Tutorial,” *IEEE Journal of Selected Topics in Quantum Electronics*, vol. 15, no. 3, pp. 618–633, May 2009, doi: 10.1109/JSTQE.2009.2014779.

[302] N. Schunk *et al.*, “Noise analysis of injection-locked semiconductor injection lasers,” *IEEE Journal of Quantum Electronics*, vol. 22, no. 5, pp. 642–650, May 1986, doi: 10.1109/JQE.1986.1073018.

[303] L. Chrostowski *et al.*, “Reduction of relative intensity noise and improvement of spur-free dynamic range of an injection locked VCSEL,” in *The 16th Annual Meeting of the IEEE Lasers and Electro-Optics Society, 2003. LEOS 2003.*, Oct. 2003, pp. 706–707 vol.2. doi: 10.1109/LEOS.2003.1252996.

[304] C. Sun *et al.*, “Modulation Characteristics Enhancement of Monolithically Integrated Laser Diodes Under Mutual Injection Locking,” *IEEE Journal of Selected Topics in Quantum Electronics*, vol. 21, no. 6, pp. 628–635, Nov. 2015, doi: 10.1109/JSTQE.2015.2478817.

[305] A. C. Bordonalli *et al.*, “High-performance phase locking of wide linewidth semiconductor lasers by combined use of optical injection locking and optical phase-lock loop,” *Journal of Lightwave Technology*, vol. 17, no. 2, p. 328, 1999.

[306] Z. Liu *et al.*, “Optical injection locking: From principle to applications,” *Journal of Lightwave Technology*, vol. 38, no. 1, pp. 43–59, 2020.

[307] H.-K. Sung *et al.*, “Optical Single Sideband Modulation Using Strong Optical Injection-Locked Semiconductor Lasers,” *IEEE Photonics Technology Letters*, vol. 19, no. 13, pp. 1005–1007, Jul. 2007, doi: 10.1109/LPT.2007.898760.

[308] R. T. Ramos *et al.*, “Optical injection locking and phase-lock loop combined systems,” *Optics letters*, vol. 19, no. 1, pp. 4–6, 1994.

[309] Z. Liu *et al.*, “Homodyne OFDM with optical injection locking for carrier recovery,” *Journal of Lightwave Technology*, vol. 33, no. 1, pp. 34–41, 2014.

[310] H.-K. Sung *et al.*, “Optical properties and modulation characteristics of ultra-strong injection-locked distributed,” *Issue: IEEE Journal of Selected Topics in Quantum Electronics, 13 (5)*, 2007.

[311] G. Yabre *et al.*, “Effect of relatively strong light injection on the chirp-to-power ratio and the 3 dB bandwidth of directly modulated semiconductor lasers,” *Journal of lightwave technology*, vol. 14, no. 10, pp. 2367–2373, 1996.

[312] S. Mohrdiek *et al.*, “Chirp reduction of directly modulated semiconductor lasers at 10 Gb/s by strong CW light injection,” *Journal of Lightwave Technology*, vol. 12, no. 3, pp. 418–424, 1994.

[313] R. A. Saunders *et al.*, “Wideband chirp measurement technique for high bit rate sources,” *Electronics Letters*, vol. 30, no. 16, pp. 1336–1338, 1994.

[314] P. Krehlik *et al.*, “Characterization of semiconductor laser frequency chirp based on signal distortion in dispersive optical fiber,” *Opto-Electronics Review*, vol. 14, no. 2, pp. 119–124, Jun. 2006, doi: 10.2478/s11772-006-0015-z.

[315] S. Tammela *et al.*, “Time-resolved frequency chirp measurement using a silicon-wafer etalon,” *IEEE Photonics Technology Letters*, vol. 9, no. 4, pp. 475–477, Apr. 1997, doi: 10.1109/68.559393.

[316] T. O. Bazarov *et al.*, “Chirp measurement with FM discriminator,” in *2020 International Conference Laser Optics (ICLO)*, Nov. 2020, pp. 1–1. doi: 10.1109/ICLO48556.2020.9285777.

[317] J.-G. Provost *et al.*, “Measuring the Chirp and the Linewidth Enhancement Factor of Optoelectronic Devices with a Mach–Zehnder Interferometer,” *IEEE Photonics Journal*, vol. 3, no. 3, pp. 476–488, Jun. 2011, doi: 10.1109/JPHOT.2011.2148194.

[318] F. Devaux *et al.*, “Simple measurement of fiber dispersion and of chirp parameter of intensity modulated light emitter,” *Journal of Lightwave Technology*, vol. 11, no. 12, pp. 1937–1940, Dec. 1993, doi: 10.1109/50.257953.

[319] A. Sharma *et al.*, “A Six-Section Photonic Integrated Transmitter With Chirp Control for Extension of the Transmission Reach,” *IEEE Photonics Journal*, vol. 14, no. 4, pp. 1–7, 2022.

[320] A. Sharma *et al.*, “A six-section photonic integrated transmitter with chirp control for transmission reach extension,” in *2021 27th International Semiconductor Laser Conference (ISLC)*, IEEE, 2021, pp. 1–2.

[321] C. E. Zah *et al.*, “1.5-μm GaInAsP angled-facet flared-waveguide traveling wave laser amplifiers,” in *Optical Fiber Communication (1990), paper THB3*, Optica Publishing Group, Jan. 1990, p. THB3. doi: 10.1364/OFC.1990.THB3.

[322] A. Sharma *et al.*, “A Six-Section Photonic Integrated Transmitter With Chirp Control for Extension of the Transmission Reach,” *IEEE Photonics Journal*, vol. 14, no. 4, pp. 1–7, Aug. 2022, doi: 10.1109/JPHOT.2022.3187073.

[323] A. Roy *et al.*, “Tunable Semiconductor Slotted Lasers for Near-Infrared Optical Coherence Tomography,” *IEEE Photonics Technology Letters*, vol. 33, no. 16, pp. 896–899, Aug. 2021, doi: 10.1109/LPT.2021.3098418.

[324] D. Mickus *et al.*, “Large Range Athermalisation of Multi-Section Surface Grating Lasers for DWDM-PONs,” in *2021 Conference on Lasers and Electro-Optics (CLEO)*, May 2021, pp. 1–2.

[325] J. Huang *et al.*, “Gain and saturation in semiconductor lasers,” *Opt Quant Electron*, vol. 25, no. 6, pp. 369–390, Jun. 1993, doi: 10.1007/BF00420579.

[326] M. Chen *et al.*, “Ultra-narrow linewidth measurement based on Voigt profile fitting,” *Opt. Express, OE*, vol. 23, no. 5, pp. 6803–6808, Mar. 2015, doi: 10.1364/OE.23.006803.

[327] A. D. McCoy *et al.*, “Experimental study on receiver filtering effects in a spectrum-sliced incoherent light WDM system using SOA based noise reduction,” 2003, Accessed: Sep. 28, 2023. [Online]. Available: https://eprints.soton.ac.uk/41602/

[328] A. J. Ward *et al.*, “Widely tunable DS-DBR laser with monolithically integrated SOA: Design and performance,” *IEEE Journal of selected topics in quantum electronics*, vol. 11, no. 1, pp. 149–156, 2005.

[329] N. Olsson *et al.*, “Chirp-free transmission over 82.5 km of single mode fibers at 2 Gbit/s with injection locked DFB semiconductor lasers,” *Journal of Lightwave Technology*, vol. 3, no. 1, pp. 63–67, 1985.

[330] Chang-Hee Lee *et al.*, “Transmission of directly modulated 2.5-Gb/s signals over 250-km of nondispersion-shifted fiber by using a spectral filtering method,” *IEEE Photon. Technol. Lett.*, vol. 8, no. 12, pp. 1725–1727, Dec. 1996, doi: 10.1109/68.544732.

[331] A. Villafranca *et al.*, “Precise characterization of the frequency chirp in directly modulated DFB lasers,” in *2007 Spanish Conference on Electron Devices*, IEEE, 2007, pp. 173–176.

[332] C. Lin, J. K. Andersen *et al.*, “Frequency chirp reduction in a 2.2 Gbit/s directly modulated InGaAsP semiconductor laser by CW injection,” *Electronics Letters*, vol. 2, no. 21, pp. 80–81, 1985.

[333] C. W. Chow *et al.*, “All-optical RZ to NRZ data format and wavelength conversion using an injection locked laser,” *Optics Communications*, vol. 223, no. 4–6, pp. 309–313, Aug. 2003, doi: 10.1016/S0030-4018(03)01691-2.

[334] B. Zhang *et al.*, “Adjustable chirp injection-locked 1.55-μm VCSELs for enhanced chromatic dispersion compensation at 10-Gbit/s,” in *OFC/NFOEC 2008-2008 Conference on Optical Fiber Communication/National Fiber Optic Engineers Conference*, IEEE, 2008, pp. 1–3. Accessed: Sep. 24, 2023. [Online]. Available: https://ieeexplore.ieee.org/abstract/document/4528779/

[335] J. C. Cartledge *et al.*, “Theoretical performance of multigigabit-per-second lightwave systems using injection-locked semiconductor lasers,” *Journal of lightwave technology*, vol. 8, no. 7, pp. 1017–1022, 1990.

[336] K. Nakahara *et al.*, “40-Gb/s Direct Modulation With High Extinction Ratio Operation of 1.3-μ InGaAlAs Multiquantum Well Ridge Waveguide Distributed Feedback Lasers,” *IEEE Photonics Technology Letters*, vol. 19, no. 19, pp. 1436–1438, 2007.

[337] M. Kuramoto *et al.*, “Reduction of Internal Loss and Threshold Current in a Laser Diode with a Ridge by Selective Re-Growth (RiS-LD),” *physica status solidi (a)*, vol. 192, no. 2, pp. 329–334, 2002, doi: 10.1002/1521-396X(200208)192:2<329::AID-PSSA329>3.0.CO;2-A.

[338] J. O’Carroll *et al.*, “Transmission over 50 km using a directly modulated integrated two-section discrete mode laser at 1550 nm,” in *2013 Conference on Lasers & Electro-Optics Europe & International Quantum Electronics Conference CLEO EUROPE/IQEC*, Munich, Germany: IEEE, May 2013, pp. 1–1. doi: 10.1109/CLEOE-IQEC.2013.6800721.

[339] “ITU.int.G.989.2, ‘40-Gigabit-capable passive optical networks 2 (NGPON2): Physical media dependent (PMD) layer specification,’ 2022. Accessed: Jul. 6, 2022. [Online]. Available: https://www.itu.int/rec/TREC-G.989.2-201902-I.”

[340] V. Houtsma *et al.*, “Investigation of 100G (4x25G) NG-PON2 Upgrade using a Burst Mode Laser based on a Multi-Electrode Laser to enable 100 GHz Wavelength Grid,” in *Optical Fiber Communication Conference*, San Diego, California: OSA, 2018, p. M1B.3. doi: 10.1364/OFC.2018.M1B.3.

[341] K. Asaka *et al.*, “High output power OLT/ONU transceivers for 40 Gbit/s symmetric-rate NG-PON2 systems,” in *2015 European Conference on Optical Communication (ECOC)*, Valencia, Spain: IEEE, Sep. 2015, pp. 1–3. doi: 10.1109/ECOC.2015.7341659.

[342] M. Gay *et al.*, “Frequency Drift Reduction in a Four-Laser Array for TWDM PON Applications,” *IEEE Photon. Technol. Lett.*, vol. 30, no. 14, pp. 1345–1348, Jul. 2018, doi: 10.1109/LPT.2018.2848115.

[343] T. Pfau *et al.*, “Coherent optical communication: Towards realtime systems at 40 Gbit/s and beyond,” *Optics express*, vol. 16, no. 2, pp. 866–872, 2008.

[344] J. Zhang *et al.*, “Flexible and adaptive coherent PON for next-generation optical access network [Invited],” *Optical Fiber Technology*, vol. 75, p. 103190, Jan. 2023, doi: 10.1016/j.yofte.2022.103190.

[345] Mohamed, Ali *et al.*, "DSP-based dispersion compensation: Survey and simulation." *2017 International Conference on Communication, Control, Computing and Electronics Engineering (ICCCCEE)*. IEEE, 2017.

[346] Y. Yamamoto *et al.*, "Coherent optical fiber transmission systems," *IEEE Journal of Quantum Electronics*, vol. 17, no. 6, pp. 919–935, 1981.

[347] K. Kikuchi *et al.*, "Digital coherent optical communication systems: Fundamentals and future prospects," *IEICE Electronics Express*, vol. 8, no. 20, pp. 1642–1662, 2011.

[348] K. Kikuchi *et al.*, "Coherent optical communication systems," *Optical Fiber Telecommunications VB*, pp. 95–129, 2008.

[349] E. Ip, A. P. T. Lau *et al.*, "Coherent detection in optical fiber systems," *Optics express*, vol. 16, no. 2, pp. 753–791, 2008.

[350] S. Weinstein *et al.*, "Data transmission by frequency-division multiplexing using the discrete Fourier transform," *IEEE transactions on Communication Technology*, vol. 19, no. 5, pp. 628–634, 1971.

[351] L. Cimini *et al.*, "Analysis and simulation of a digital mobile channel using orthogonal frequency division multiplexing," *IEEE transactions on communications*, vol. 33, no. 7, pp. 665–675, 1985.

[352] T. Takahara *et al.*, "Discrete Multi-Tone for 100 Gb/s Optical Access Networks," in *Optical Fiber Communication Conference (2014), paper M2I.1*, Optica Publishing Group, Mar. 2014, p. M2I.1. doi: 10.1364/OFC.2014.M2I.1.

Appendix A

List of publications

The following is the list of publications included in this work.

A. Referred Journals

A.1. **Ankit Sharma**, Aleksandra Maria Kaszubowska-Anandarajah, Mohab Nabil Hammad, Michael Wallace, Jules Braddell, Frank Smyth, Prince M. Anandarajah, "A Six-Section Photonic Integrated Transmitter With Chirp Control for Extension of the Transmission Reach," in IEEE Photonics Journal, vol. 14, no. 4, pp. 1-7, Aug. 2022, Art no. 1540107, doi: 10.1109/JPHOT.2022.3187073.

A.2. **Ankit Sharma**, Aleksandra Maria Kaszubowska-Anandarajah, Michael Wallace, Gaurav Jain, Jules Braddell, Frank Smyth, Prince M. Anandarajah, "A Wavelength Tunable Multi-Section PIC as an Upstream Transmitter for TWDM Networks," in Journal of Lightwave Technology, vol. 41, no. 14, pp. 4672-4679, 15 July15, 2023, doi: 10.1109/JLT.2023.3244363.

A.3. Marcos Troncoso Costas, Ahmed Galib Reza, Hima Putta, **Ankit Sharma**, Gaurav Jain, Mark Smyth, Frank Smyth, John MacDougall, Colm Browning, Francisco Diaz Otero, and Liam Barry, "30 Gbit/s PAM4 transmission using an 8-GHz directly modulated multi-section laser," Opt. Express 30, 20194-20202 (2022)

B. Referred Conferences

B.1. **Ankit Sharma**, Mohab N. Hammad, Aleksandra Kaszubowska-Anandarajah, Gaurav Jain, Michael Wallace, Jules Braddell, Frank Smyth, Prince M. Anandarajah, "A six-section photonic integrated transmitter with chirp control for transmission reach extension," 2021 27th International Semiconductor Laser Conference (ISLC), Potsdam, Germany, 2021, pp. 1-2, doi: 10.1109/ISLC51662.2021.9615884.

B.2. **Ankit Sharma**, Aleksandra Kaszubowska-Anandarajah, Michael J Wallace, Gaurav Jain, Frank Smyth, Jules Braddell, Prince Anandarajah, "Wavelength Tunable Directly Modulated Laser for TWDM Applications," 2021 European Conference on Optical Communication (ECOC), Bordeaux, France, 2021, pp. 1-4, doi: 10.1109/ECOC52684.2021.9606065.

C. Other publications

C.1. M. Srivastava, M. N. Hammad, S. T. Ahmad, **A. Sharma**, A. Kaszubowska-Anandarajah, P. Landais, and P. M. Anandarajah, "Noise Figure and Saturation Characteristics of Multi-section Semiconductor Optical Amplifier for Data Center Networks," in Conference on Lasers and Electro-Optics, Technical Digest Series (Optica Publishing Group, 2022), paper JTh3B.3.

C.2. Aleksandra Kaszubowska-Anandarajah, Syed Tajammul Ahmad, Chris G. H. Roeloffzen, Paulus W. L. van Dijk, **Ankit Sharma**, Manas Srivastava, Prajwal D. Lakshmijayasimha, M. Deseada Gutierrez Pascual, Frank Smyth, Jules Braddell, Prince M. Anandarajah, “Reconfigurable photonic integrated transmitter for metro-access networks," in Journal of Optical Communications and Networking, vol. 15, no. 3, pp. A92-A102, March 2023, doi: 10.1364/JOCN.470113.

C.3. Manas Srivastava, Syed Tajammul Ahmad, **Ankit Sharma**, Prajwal Doddaballapura Lakshmijayasimha, M. Deseada Gutierrez Pascual, Frank Smyth, Prince M. Anandarajah, Aleksandra Kaszubowska-Anandarajah,

"Monolithically Integrated Optical Frequency Comb Generator Based on Mutually Injection Locked Gain Switched Lasers," in IEEE Journal of Selected Topics in Quantum Electronics, vol. 29, no. 5: Terahertz Photonics, pp. 1-8, Sept.-Oct. 2023, Art no. 6101608, doi: 10.1109/JSTQE.2023.3305829.

Appendix B

CAMFR code for slot optimization

Extraction of reflection coefficient vs slot width and depth

```
#!/usr/bin/env python2
# -*- coding: utf-8 -*-
"""
Created on Wed Mar 18 14:43:00 2020

@author: Ankit Sharma
"""
import numpy as np
import pylab as plt
from camfr import *

# Problem 4b
# Repeat problem 4 but this time choose your grating period based on the Bragg
condition. Refer to ..\papers\p1.pdf for help
# (Try set slot width to 1 and period order m to 37)

"""
      STACK
 SLAB1      SLAB2       SLAB1       SLAB2
```

```
   n0

_______          _________

      |_________|         |_____________ . . . X 5

   n1

_____________________________________________ . . .

___n2_____________________________________________ . . .


___n3_____________________________________________ . . .

"""


s=np.arange(0.15,1.55,0.1)

E=np.arange(0.15,1.55,0.1)


r=np.zeros(len(s))

t=np.zeros(len(s))


z = np.zeros((len(s), len(E)))

y = np.zeros((len(s), len(E)))


for j,etch in enumerate(E):

    bragg_wavelength = 1.545

    # Step 0 - Set simulation parameters

    set_lambda(bragg_wavelength)

    set_lower_PML(-0.1)

    set_upper_PML(-0.1)  # These pml values normally work well.
```

```
set_N(60)  # Number of Modes to consider. As we have introduce a perturbation in the index we can expect some loss.
           # As such we need to consider higher order radiating modes to accurately account for losses.

# Step 1 - Import data.
data = np.loadtxt("index_profile_new.txt", delimiter = ",", skiprows = 1)
n1 = data[:, 0] # Refractive indexes
d1 = data[:, 1] # Height of each layer

print(n1)
print(d1)

n2 = copy(n1)
d2 = copy(d1)

#etch = E[i]
d2[0] += etch # Add height to air layer
d2[1] -= etch # Remove height from cladding layer

# Step 2a - define SLAB1 in camfr

layer_n1 = [] # Empty list to contain material objects.
for i in range(len(n1)):
    layer_n1.append(Material(n1[i])) # Makes a list of Material objects
```

```
    for i in range(len(d1)):
        if i == 0:
            slab_list1 = (layer_n1[len(d1)-1](d1[i])) # Sets height of each Material object
in layer_n.
        else:
            slab_list1 = slab_list1 + (layer_n1[i](d1[i]))  # Sets height of each Material
object in layer_n.
    slab1 = Slab(slab_list1) # Make slab object

    # Step 2b - define SLAB2 in camfr

    layer_n2 = [] # Empty list to contain material objects.
    for i in range(len(n2)):
        layer_n2.append(Material(n2[i])) # Makes a list of Material objects

    for i in range(len(d2)):
        if i == 0:
            slab_list2 = (layer_n2[i](d2[i])) # Sets height of each Material object in
layer_n.
        else:
            slab_list2 = slab_list2 + (layer_n2[i](d2[i]))  # Sets height of each Material
object in layer_n.
    slab2 = Slab(slab_list2) # Make slab object

    # Step 3 - Create Stack. (Extend from 1D to 2D in propogation direction)
    slab1.calc()
```

```
    slab2.calc()

    neff1 = slab1.mode(0).n_eff().real
    neff2 = slab2.mode(0).n_eff().real

    period_order = 42
    dp = period_order * bragg_wavelength /  (2.0 * neff1) # Period is half integer
multiples of the mode wavelength.
    for k,ds in enumerate(s):
        print ds,etch
        #ds = 1.4
        dw = dp - ds

        #print(dp, "Grating period")
        #print(dw, "slot")

        slot_N = 10
        # slab(d) adds section of length = d. d = 0 projects section to infinity.
        stack_pert = Stack(slab1(0) + slot_N*(slab1(dw) + slab2(ds)) + slab2(0))

        # Set incident field and calculate stack.
        inc = zeros(N())
        inc[0] = 1
        stack_pert.set_inc_field(inc)

        stack_pert.calc()
```

```
        # Do some interactive plotting.
        #stack_pert.plot()

        r[k]=np.abs(stack_pert.R12(0, 0));
        t[k]=np.abs(stack_pert.T12(0, 0));
        # print scattering parameters of stack.
        r0 = np.abs(stack_pert.R12(0, 0));
        #print(r0)
        t0 = np.abs(stack_pert.T12(0, 0));

    z[:,j]=r
    y[:,j]=t


np.savetxt('r_data.csv',z,delimiter=',')
np.savetxt('t_data.csv',y,delimiter=',')
```

Extraction of reflectance band

```
#!/usr/bin/env python2
# -*- coding: utf-8 -*-
"""
Created on Wed Mar 18 14:43:00 2020

@author: pilot
"""
```

```
import numpy as np
import pylab as plt
from camfr import *

# Problem 5
# Continuing from problem 5. Create a grating composed of three sub-gratings of
varying dp, each satisfying the Bragg condition for 1.55 microns.
# Calculate the Reflectivity spectrum, including the FSR peaks.
# Refer to ../papers/p2.pdf when doing this. Do you results match up?


"""
      STACK
 SLAB1      SLAB2        SLAB1        SLAB2
   n0
_________              ____________
       |____________|          |_____________ . . . X 20
   n1
_____________________________________________________ . . .
___n2_____________________________________________________ . . .

___n3_____________________________________________________ . . .

"""
```

```
# Step 0 - Set simulation parameters
#s=np.array([0.2,0.3,0.4,0.5,0.6,0.7,0.8,0.9,1.0,1.1,1.2,1.3,1.4])
s=np.array([0.3])

for m,slw in enumerate(s):

    print('solving for '+str(s[m]))



    set_lower_PML(-0.1)
    set_upper_PML(-0.1)  # These pml values normally work well.
    set_N(60)  # Number of Modes to consider. As we have introduce a perturbation in the index we can expect some loss.
                # As such we need to consider higher order radiating modes to accurately account for losses.
    set_solver(series)  #

    # Step 1 - Import data.

    data = np.loadtxt("index_profile_new.txt", delimiter = ",", skiprows = 1)
    n1 = data[:, 0] # Refractive indexes
    d1 = data[:, 1] # Height of each layer

    n2 = copy(n1)
    d2 = copy(d1)
```

```
etch = 1.35
d2[0] += etch # Add height to air layer
d2[1] -= etch # Remove height from cladding layer

# Step 2a - define SLAB1 in camfr

layer_n1 = [] # Empty list to contain material objects.
for i in range(len(n1)):
    layer_n1.append(Material(n1[i])) # Makes a list of Material objects

for i in range(len(d1)):
    if i == 0:
        slab_list1 = (layer_n1[i](d1[i])) # Sets height of each Material object in
layer_n.
    else:
        slab_list1 = slab_list1 + (layer_n1[i](d1[i]))  # Sets height of each Material
object in layer_n.
slab1 = Slab(slab_list1) # Make slab object

# Step 2b - define SLAB2 in camfr

layer_n2 = [] # Empty list to contain material objects.
for i in range(len(n2)):
    layer_n2.append(Material(n2[i])) # Makes a list of Material objects

for i in range(len(d2)):
```

```
        if i == 0:
            slab_list2 = (layer_n2[i](d2[i])) # Sets height of each Material object in
layer_n.
        else:
            slab_list2 = slab_list2 + (layer_n2[i](d2[i]))  # Sets height of each Material
object in layer_n.
    slab2 = Slab(slab_list2) # Make slab object



    # Step 3 - Create Stack. (Extend from 1D to 2D in propogation direction)
    bragg_wavelength = 1.545
    set_lambda(bragg_wavelength)

    slab1.calc()
    slab2.calc()

    neff1 = slab1.mode(0).n_eff().real
    neff2 = slab2.mode(0).n_eff().real

    #period_order = np.array([37, 42, 47])
    period_order = np.array([42])
    slot_width = np.array([slw])
    slot_N = [10]

    dw = np.zeros(len(period_order), dtype=np.float64)
    ds = np.zeros(len(period_order), dtype=np.float64)
```

```
dp = np.zeros(len(period_order), dtype=np.float64)

for i in range(len(period_order)):
    dp[i] = (period_order[i])  * bragg_wavelength / (2.0*neff1)
    ds[i] = slot_width[i]
    dw[i] = dp[i] - ds[i]



wavesweep = np.linspace(1.50, 1.60, 100)
r_array = np.zeros_like(wavesweep)
t_array = np.zeros_like(wavesweep)s
f_ = []
for i in range(len(slot_N)):
    f_.append(slot_N[i] * ( slab1(dw[i]) + slab2(ds[i])))

stack_pert = Stack(slab1(0) + sum(f_) + slab1(0))

for i, wave in enumerate((wavesweep)):
    print i, wave
    set_lambda(wave)

    # slab(d) adds section of length = d. d = 0 projects section to infinity.
    stack_pert.calc()

    r_array[i] = np.abs(stack_pert.R12(0, 0))
```

```
        t_array[i]= np.abs(stack_pert.T12(0, 0))

    plt.plot(wavesweep, r_array)

    g_spetra=[wavesweep,r_array, t_array]

    g_spetra=np.transpose(g_spetra)

    dir=r'C:\Users\ASharma\Desktop\grating_order_37_0.3um\\'

    np.savetxt(dir+str(s[m])+'um_gspectra.csv',g_spetra,delimiter=',')

plt.plot(wavesweep, t_array)
plt.xlabel("Wavelength micorns")
plt.ylabel("Amplitude")
plt.show()
```

Appendix C

MATLAB code of rate equation model

Code

```
clear all
close all
clc

format short

Fs=4e11;
%tsam=1e-12;
tsam = 1/Fs
NFFT = 2^12;%2e11

%tfinal=1e-8;
tfinal=NFFT*tsam;

tspan = [0 tfinal]

ts=linspace(0,tfinal,NFFT/2);

%p_mw=6.62607015e-34*3e8*W*d*ng*cf/1.550e-6;
```

```
I=30*1e-3; % supply current
L=380e-4;  % dimension in cm

%y0 = [0 0 0 0 0 0 0 0 0 0 0 0 0 0 0 0 0 0];

y0 = [1e-9 1e-9 1e-9 1e-9 1e-9 1e-9 1e-9 1e-9 1e-9 1e-9 1e-9 0 0 0 0 0];

[t,y] = ode45(@(t,y) reqm13(t,y,I,L,tsam), ts, y0);
disp('first interation complete');

y0 = [1e-9 1e-9 1e-9 1e-9 1e-9 1e-9 1e-9 1e-9 1e-9 1e-9 1e-9 0 0 0 0 0];

for k=7:11
p=polyfit(t,y(:,k),1);
y0(k+5)=-p(1);
y0(k)=-p(2);
end

[t,y] = ode45(@(t,y) reqm13(t,y,I,L,tsam), ts, y0);


plot(t,y(:,1),'-','Linewidth',2)

% plotting time trace of photons

figure

subplot(5,1,1)
plot(t,y(:,2),'-','Linewidth',2)
```

```
subplot(5,1,2)
plot(t,y(:,3),'-','Linewidth',2)

subplot(5,1,3)
plot(t,y(:,4),'-','Linewidth',2)

subplot(5,1,4)
plot(t,y(:,5),'-','Linewidth',2)

subplot(5,1,5)
plot(t,y(:,6),'-','Linewidth',2)

%ylim=[0 2e15];

% plotting time trace of phase
figure

subplot(5,1,1)
plot(t,y(:,7),'-','Linewidth',2)

subplot(5,1,2)
plot(t,y(:,8),'-','Linewidth',2)

subplot(5,1,3)
plot(t,y(:,9),'-','Linewidth',2)

subplot(5,1,4)
plot(t,y(:,10),'-','Linewidth',2)

subplot(5,1,5)
```

```
plot(t,y(:,11),'-','Linewidth',2)

a=sqrt(y(:,2)).*exp(j*y(:,7));
b=sqrt(y(:,3)).*exp(j*y(:,8));
c=sqrt(y(:,4)).*exp(j*y(:,9));
d=sqrt(y(:,5)).*exp(j*y(:,10));
e=sqrt(y(:,6)).*exp(j*y(:,11));
k=[0.7744 0.7815 0.7733 0.7879 0.7714]; % 0.3um slot
%k=[0.6168 0.6280 0.6044 0.6385 0.5821]; % 1.0um slot
%k=[0.7 0.7 0.7 0.7 0.7];

a=a.*k(1);
b=b.*k(2);
c=c.*k(3);
d=d.*k(4);
e=e.*k(5);

X1=abs(fftshift(fft(a,NFFT)));
X2=abs(fftshift(fft(b,NFFT)));
X3=abs(fftshift(fft(c,NFFT)));
X4=abs(fftshift(fft(d,NFFT)));
X5=abs(fftshift(fft(e,NFFT)));
%
X1=X1.*conj(X1);
X2=X2.*conj(X2);
X3=X3.*conj(X3);
X4=X4.*conj(X4);
X5=X5.*conj(X5);

%
```

```
Xa=abs(X1)./max(abs(X1));
Xb=abs(X2)./max(abs(X1));
Xc=abs(X3)./max(abs(X1));
Xd=abs(X4)./max(abs(X1));
Xe=abs(X5)./max(abs(X1));

df=linspace(-Fs/2,Fs/2,length(Xa));
%
figure
hold on
plot(df,Xa,'Linewidth',3);
plot(df,Xb,'Linewidth',3);
plot(df,Xc,'Linewidth',3);
plot(df,Xd,'Linewidth',3);
plot(df,Xe,'Linewidth',3);
%
set(gca,'FontSize',20,'LineWidth',3,'FontWeight','Bold');

hold off
n_dbm_0  = 10.*log10(abs(Xa));
n_dbm_m1 = 10.*log10(abs(Xb));
n_dbm_p1 = 10.*log10(abs(Xc));
n_dbm_m2 = 10.*log10(abs(Xd));
n_dbm_p2 = 10.*log10(abs(Xe));

figure
plot(df,n_dbm_0,'Linewidth',1);
xlabel('Frequency (GHz)','FontSize',20,'LineWidth',3,'FontWeight','Bold');
ylabel('Power (dBm)','FontSize',20,'LineWidth',3,'FontWeight','Bold');
set(gca,'FontSize',20,'LineWidth',3,'FontWeight','Bold');
```

```
xlim([-Fs/2 Fs/2]);

hold on

plot(df,n_dbm_m1,'Linewidth',1);
xlabel('Frequency (GHz)','FontSize',20,'LineWidth',3,'FontWeight','Bold');
ylabel('Power (dBm)','FontSize',20,'LineWidth',3,'FontWeight','Bold');
set(gca,'FontSize',20,'LineWidth',3,'FontWeight','Bold');
xlim([-Fs/2 Fs/2]);
plot(df,n_dbm_p1,'Linewidth',1);
xlabel('Frequency (GHz)','FontSize',20,'LineWidth',3,'FontWeight','Bold');
ylabel('Power (dBm)','FontSize',20,'LineWidth',3,'FontWeight','Bold');
set(gca,'FontSize',20,'LineWidth',3,'FontWeight','Bold');

plot(df,n_dbm_m2,'Linewidth',1);
xlabel('Frequency (GHz)','FontSize',20,'LineWidth',3,'FontWeight','Bold');
ylabel('Power (dBm)','FontSize',20,'LineWidth',3,'FontWeight','Bold');
set(gca,'FontSize',20,'LineWidth',3,'FontWeight','Bold');
xlim([-Fs/2 Fs/2]);

plot(df,n_dbm_p2,'Linewidth',1);
xlabel('Frequency (GHz)','FontSize',20,'LineWidth',3,'FontWeight','Bold');
ylabel('Power (dBm)','FontSize',20,'LineWidth',3,'FontWeight','Bold');
set(gca,'FontSize',20,'LineWidth',3,'FontWeight','Bold');

xlim([-Fs/2 Fs/2]);

% SMSR calculation
smsr1=10*log10(y(end,2)/y(end,3))
smsr2=10*log10(y(end,2)/y(end,4))
```

```
smsr3=10*log10(y(end,2)/y(end,5))
smsr4=10*log10(y(end,2)/y(end,6))
```

Function

```
function dy = reqm13(t,y,I,L,tsam)

  dy = zeros(16,1);

  dwc0=y(12);
  dwc1=y(13);
  dwc2=y(14);
  dwc3=y(15);
  dwc4=y(16);

  e=1.6e-19;
  N0=2.05e18;
  c=2.99792458e10;

  L=350e-4;
  W=2e-4;
  d=0.03e-4;
  V=L*W*d;
  ng = 3.19;
  mode_spacing=(c/2*ng*L);
  vg = c / ng;
  R1 = 0.95;
```

```
%R1 = 0.3;

e  = 1.6E-19;
%alphain = 30;
alphain = 40;

gain=[2.1382e-17 2.1181e-17 2.1000e-17 2.0842e-17 2.0705e-17];

%gain=[9e-16 8.9e-16 8.9e-16 8.8e-16 8.8e-16]; % modal gain coefficient; % modal gain coefficient

gama=0.05;%
beta=3.2e-5;
%beta=0.2e-3;
eta=5e-17;
%tp=2e-12;

%tp= 1/vg/(alphain + 1/(2*L)*log(1/(R1*R2))); % photon lifetime
R2=[0.2738 0.2228 0.2251 0.1285 0.1228]; % 0.3 um slot
%R2=[0.2714 0.2130 0.2331 0.1159 0.1912];%1.0um slot
%R2=[0.3 0.3 0.3 0.3 0.3];

tp1= 1/vg/(alphain + 1/(2*L)*log(1/(R1*R2(1))));
tp2= 1/vg/(alphain + 1/(2*L)*log(1/(R1*R2(2))));
tp3= 1/vg/(alphain + 1/(2*L)*log(1/(R1*R2(3))));
tp4= 1/vg/(alphain + 1/(2*L)*log(1/(R1*R2(4))));
tp5= 1/vg/(alphain + 1/(2*L)*log(1/(R1*R2(5))));

alpha_h=2;
```

```
  AA=gain.*vg.*49;%49
  %AA=gain;

%   Ak  = 0.06E9;
%   Bk  = 1.4E-10;
%   Ck = 1E-28;

  Ak  = 0.1E9;
  Bk  = 1E-10;
  Ck = 3.5E-29;

  lambda=1550e-7;
  h=6.62607015e-34;
  nu=h*c/lambda;

  Nk= Ak*y(1) + Bk*y(1)^2 + Ck*y(1)^3;

  Rsp=gama*beta*Bk*y(1)^2;

  Dpp1=Rsp*y(2); % this is strength of the noise associated to photon density, please have a look in Section 1.5 of the Eq_v2.pdf
  Dnn1=Dpp1/gama+Nk/V; % Langevin force for the carriers
  Dphi1=Rsp/(4*y(2)); % last one for the phase

  Dpp2=Rsp*y(3); % this is strength of the noise associated to photon density, please have a look in Section 1.5 of the Eq_v2.pdf
  Dnn2=Dpp2/gama+Nk/V; % Langevin force for the carriers
  Dphi2=Rsp/(4*y(3)); % last one for the phase
```

```
  Dpp3=Rsp*y(4); % this is strength of the noise associated to photon density, please have
a look in Section 1.5 of the Eq_v2.pdf
  Dnn3=Dpp3/gama+Nk/V; % Langevin force for the carriers
  Dphi3=Rsp/(4*y(4)); % last one for the phase

  Dpp4=Rsp*y(5); % this is strength of the noise associated to photon density, please have
a look in Section 1.5 of the Eq_v2.pdf
  Dnn4=Dpp4/gama+Nk/V; % Langevin force for the carriers
  Dphi4=Rsp/(4*y(5)); % last one for the phase

  Dpp5=Rsp*y(6); % this is strength of the noise associated to photon density, please have
a look in Section 1.5 of the Eq_v2.pdf
  Dnn5=Dpp5/gama+Nk/V; % Langevin force for the carriers
  Dphi5=Rsp/(4*y(6)); % last one for the phase


  %% multimode laser rate equation
  dy(1) = I/(e*V)...
       -AA(1)*(y(1)-N0)*(y(2)/(1+eta*y(2)))...
       -AA(2)*(y(1)-N0)*(y(3)/(1+eta*y(3)))...
       -AA(3)*(y(1)-N0)*(y(4)/(1+eta*y(4)))...
       -AA(4)*(y(1)-N0)*(y(5)/(1+eta*y(5)))...
       -AA(5)*(y(1)-N0)*(y(6)/(1+eta*y(6)))...
       -Nk...

+sqrt((2*Dnn1/tsam)+(2*Dnn2/tsam)+(2*Dnn3/tsam)+(2*Dnn4/tsam)+(2*Dnn5/tsam))*ra
ndn;
%       +(sqrt(2*Dnn1/tsam)...
%       +sqrt(2*Dnn2/tsam)...
%       +sqrt(2*Dnn3/tsam)...
```

```
%        +sqrt(2*Dnn4/tsam)...
%        +sqrt(2*Dnn5/tsam)...
%     )*randn;


  dy(2) = AA(1)*gama*(y(1)-N0)*(y(2)/(1+eta*y(2)))-y(2)/tp1 +
gama*beta*Nk+sqrt(2*Dpp1/(tsam))*randn;
  dy(3) = AA(2)*gama*(y(1)-N0)*(y(3)/(1+eta*y(3)))-y(3)/tp2 +
gama*beta*Nk+sqrt(2*Dpp2/(tsam))*randn;
  dy(4) = AA(3)*gama*(y(1)-N0)*(y(4)/(1+eta*y(4)))-y(4)/tp3 +
gama*beta*Nk+sqrt(2*Dpp3/(tsam))*randn;
  dy(5) = AA(4)*gama*(y(1)-N0)*(y(5)/(1+eta*y(5)))-y(5)/tp4 +
gama*beta*Nk+sqrt(2*Dpp4/(tsam))*randn;
  dy(6) = AA(5)*gama*(y(1)-N0)*(y(6)/(1+eta*y(6)))-y(6)/tp5 +
gama*beta*Nk+sqrt(2*Dpp5/(tsam))*randn;

  dy(7) = 0.5*alpha_h*(AA(1)*gama*(y(1)-N0)-1/tp1)+ dwc0 +
sqrt(2*Dphi1/(tsam))*randn; % phase equation for mode 0
  dy(8) = 0.5*alpha_h*(AA(2)*gama*(y(1)-N0)-1/tp2)+ dwc1 +
sqrt(2*Dphi2/(tsam))*randn; % phase equation for mode 0
  dy(9) = 0.5*alpha_h*(AA(3)*gama*(y(1)-N0)-1/tp3)+ dwc2 +
sqrt(2*Dphi3/(tsam))*randn; % phase equation for mode 0
  dy(10) = 0.5*alpha_h*(AA(4)*gama*(y(1)-N0)-1/tp4)+ dwc3 +
sqrt(2*Dphi4/(tsam))*randn; % phase equation for mode 0
  dy(11) = 0.5*alpha_h*(AA(5)*gama*(y(1)-N0)-1/tp5)+ dwc4 +
sqrt(2*Dphi5/(tsam))*randn; % phase equation for mode 0

end
%%
```

Appendix D

RF Generator design and implementation

RF generator unit is designed to achieve multiple objectives such as modulation and gain switching. The gain switching is a renowned technique to generate ultrashort optical pulses by supplying high power (typically 25 dBm) RF signal. When considered in the frequency domain, the generated optical pulses correspond to an optical frequency comb (OFC). This RF unit can generate frequency signal from 100 MHz to 28 GHz at power of 30 dBm. The high-quality RF signal (spur of -90dBc) for gain switching is critical for generation of high-quality OFC.

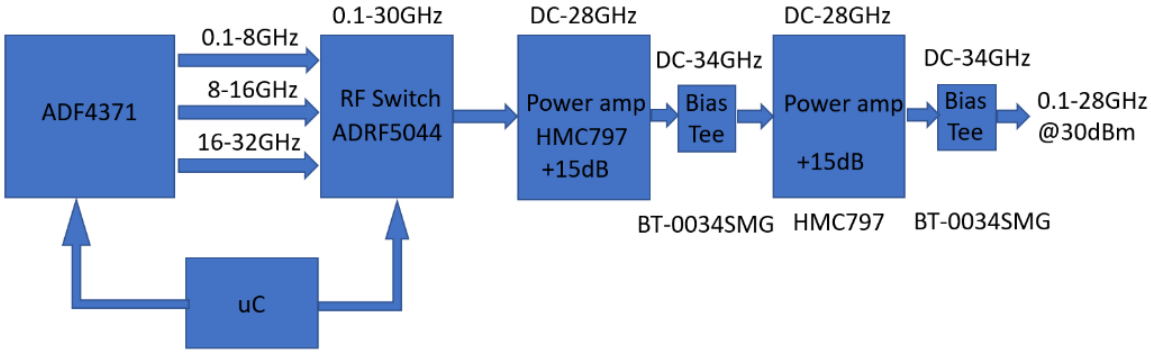

Figure D.1. Block diagram of RF generator unit.

Figure D.1 shows the block diagram of the manufactured RF unit. First, a frequency synthesizer integrated circuit having phase lock loop (PLL) and voltage controller oscillator is used. It has three output channels, and each port can be access through differential RF signal pins of IC. Channel-1, channel-2, and channel-3 have output frequency ranges 100 MHz to 8 GHz, 8 GHz to 16 GHz, and 16 GHz to 32 GHz, respectively. The output frequency and power of the channel are defined by firmware. The power level can be set to -4 dBm, -1 dBm, 2 dBm, and 5 dBm. To initialize the chip, a 64-byte word need to be transferred through the serial peripheral interface (SPI) and to update the frequency, 9 bytes must be loaded to

specific addresses of the chip's flash memory. The following formula is used to calculate the frequency of the generated signal:

$$f_{RFOUT} = INT + \frac{FRAC1 + \frac{FRAC2}{MOD2}}{MOD1} \times \frac{f_{PFD}}{RF\ Divider}$$

$$f_{PFD} = REF_{IN} \times ((1 + D)/(R \times (1 + T)))$$

where: -

f_{RFOUT} is the RF output frequency.

INT is the integer division factor.

FRAC1 is the fractionality.

FRAC2 is the auxiliary fractionality.

MOD1 is the fixed 25-bit modulus.

MOD2 is the auxiliary modulus.

REFIN is the reference frequency input.

D is the REFIN doubler bit.

R is the reference division factor.

T is the reference divide by 2 bit (0 or 1).

To obtain a single port capable of operating over the entire frequency range, a 4-way RF switch ADRF5044 shown in Figure D.2 and operating from the DC to 30 GHz, is used. A microcontroller is connected to handle the operation of SPI transfer and control RF switch. The operation of digital switch is described in Table D.1 and a schematic diagram is shown in Figure D.3.

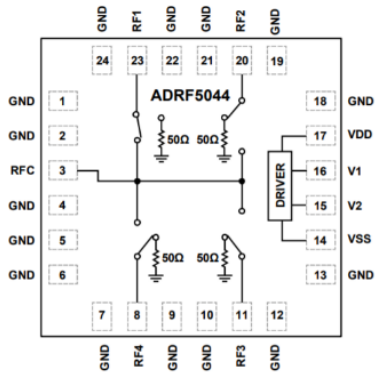

Figure D.2. Architecture of RF switch.

Digital Control Input		RF Paths			
V1	V2	RF1 to RFC	RF2 to RFC	RF3 to RFC	RF4 to RFC
Low	Low	Insertion loss (on)	Isolation (off)	Isolation (off)	Isolation (off)
High	Low	Isolation (off)	Insertion loss (on)	Isolation (off)	Isolation (off)
Low	High	Isolation (off)	Isolation (off)	Insertion loss (on)	Isolation (off)
High	High	Isolation (off)	Isolation (off)	Isolation (off)	Insertion loss (on)

Table D.1. Description of operating condition of RF switch

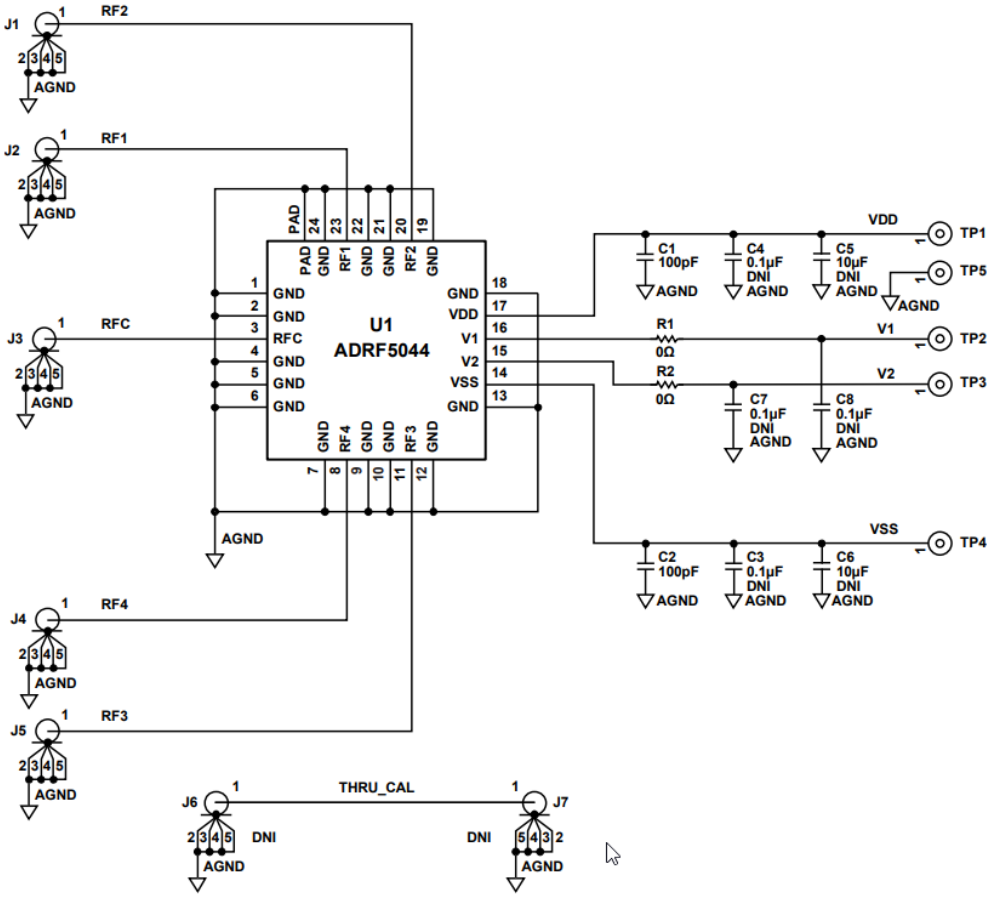

Figure D.3. Schematic diagram of ADRF5044.

The output signal of the switch is then amplified, using two stage power amplifiers (DC-28 GHz) with +15 dB to achieve an output power up to 30 dBm. The two-stage amplifier is built by cascading two HMC994 IC provided by Analog devices. The schematic of amplifier is shown in Figure D.4.

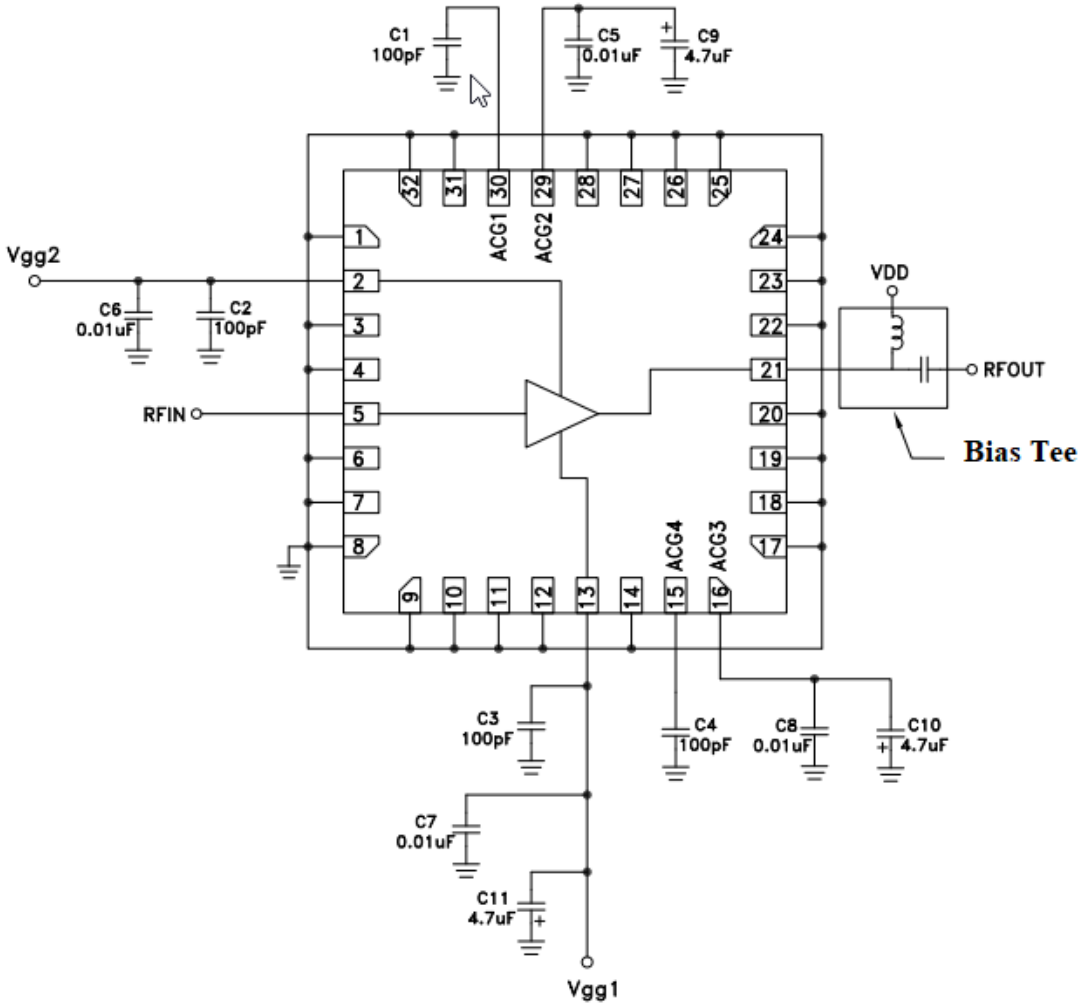

Figure D.4. RF power amplifier.

The BT used at the output stage of the amplifier is BT-0034SMG. The bandwidth of the bias is from 500 kHz to 34 GHz. A combined schematic is created in the Altium software as shown in Figure D.5. Subsequently, the PCB is design lay out is generated on Altium software. The PCB drawing is divided into three main sections: power supply for digital and RF circuits, USB communication circuit for PC interface, and RF circuits. A four-layer stack of the board is used to design circuit to enable shortest path for ground and VCC signal.

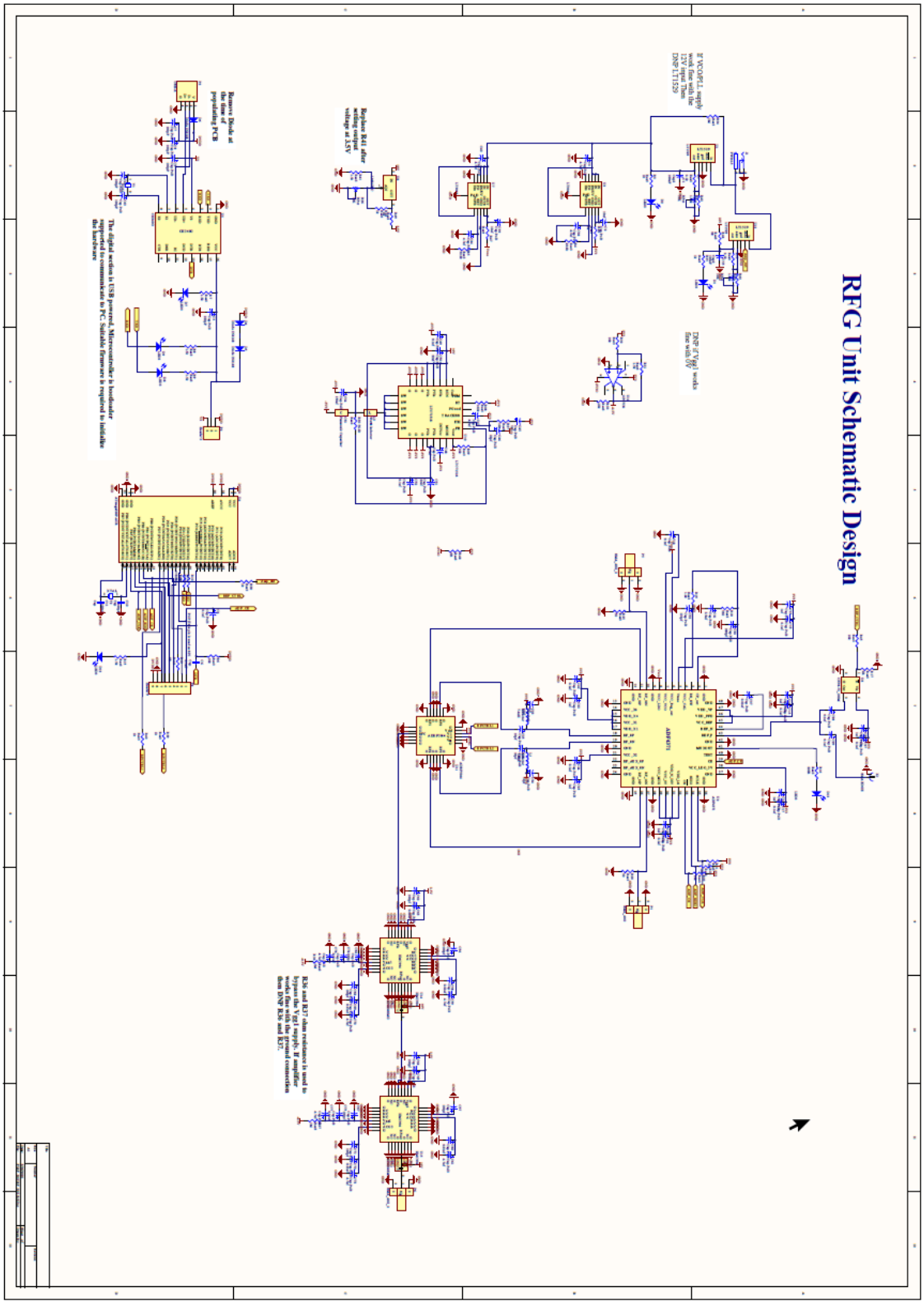

Figure D.5. Schematic diagram of RFGU.

Appendix E

Development of in-house chip packaging system

The bare PIC is tested by biasing all the sections, and a lens fiber collects the optical signal. In traditional testing, the tungsten probes connected to the current source are landed on the contact pads of the PIC. These probes are manually aligned and positioned to supply the current on the respective sections. Operating a bare chip on a traditional test station is time-consuming. Therefore, the chips are packaged to reduce the testing time and effort. In the packaging process of the PIC, the chip is wire-bonded to the contact pin of the packaging case, and the output facet is fiber coupled. The standard packaging of the PIC is expensive and requires a longer lead time. Hence, this project aimed to establish an in-house chip packaging facility to enable quick testing of bare chips at a reduced cost. The chip packaging process involves three main steps: subcarrier preparation, fiber coupling, and metal casing.

Subcarrier preparation

The subcarrier PCB is designed using two layered fiber reinforced-4 (FR-4) material. The subcarrier is divided into three regions: DC, RF, and thermal sensing. The DC section comprises DC track and DC contact pads. DC pads and tracks are designed to supply DC to PIC. The DC tracks are drawn on the top copper layer of the PCB (as shown in Figure E.1.1). A ribbon-copper wire is soldered on the DC contact pads and connected to the DC source to supply current. In the second section, a 50 Ω ground-signal-ground (G-S-G) RF track and pad are implemented for supplying RF signal. To design a 50 Ω G-S-G track, the width of the track and the gap between the ground and signal are determined using Spok online calculators. After that, the design is fabricated using an external PCB fabrication lab. To finalize the subcarrier, an SMA connector at one end and a matching resistance at another are soldered. In the last section, a thermal pad on the PCB is designed to maintain the

temperature of PIC. The PIC is epoxied on the thermal pad. The PCB is placed on top of the cold surface of the thermos-electric cooler (TEC). In addition, a thermistor is placed near the thermal pad is soldered to monitor the temperature of the PIC. Finally, the contact pads of the epoxied PIC are wire bonded to the contact pad of the subcarrier. Figure E.1.2 and Figure E.1.3 show the wire bond connecting the contact pad of the PCB to the PIC and finalized version of the subcarrier PCB.

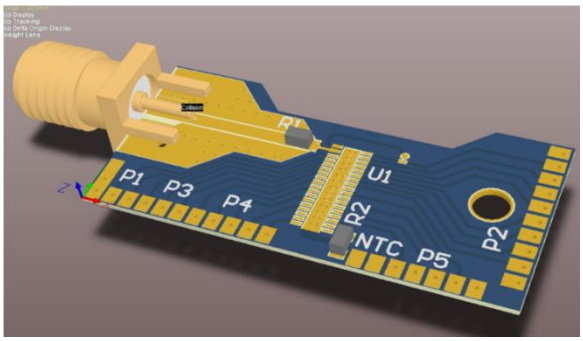

Figure E.1.1. Three-dimensional picture of designed subcarrier PCB.

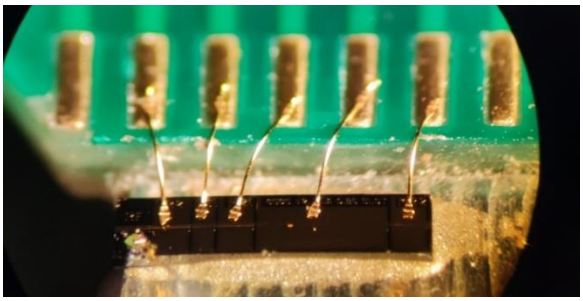

Figure E.1.2. Wire-bonded PIC on subcarrier PCB.

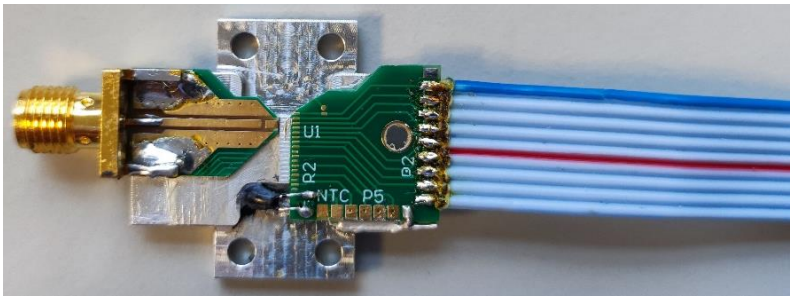

Figure E.1.3. Finalized version of the subcarrier.

Fiber alignment and coupling

In the next stage, the fiber alignment and coupling setup is built to align and couple the fiber. As shown in Figure E.2.1, the setup is divided into four blocks: camera, ultra-violet lamp, TEC mount, and fiber mount. First, the camera is mounted on an ‘x’ and ‘y’ linear translation stage to see the top view of the subcarrier-mounted chip. Next, the ‘z’ height of the camera is manually adjusted. Next, the UV lamp is placed near the fiber mount to flash the light on the UV-activated glue to cure it. The third part of the setup is the TEC mount, where the subcarrier is screwed. The TEC mount can be moved in the x, y, and z directions with the help of the three-axis translation stage. Finally, a fiber mount is designed to mount and align the fiber. The fiber mount is prepared by placing a fiber holder (specially designed metalwork for mounting a fiber) on top of the three-axis stage.

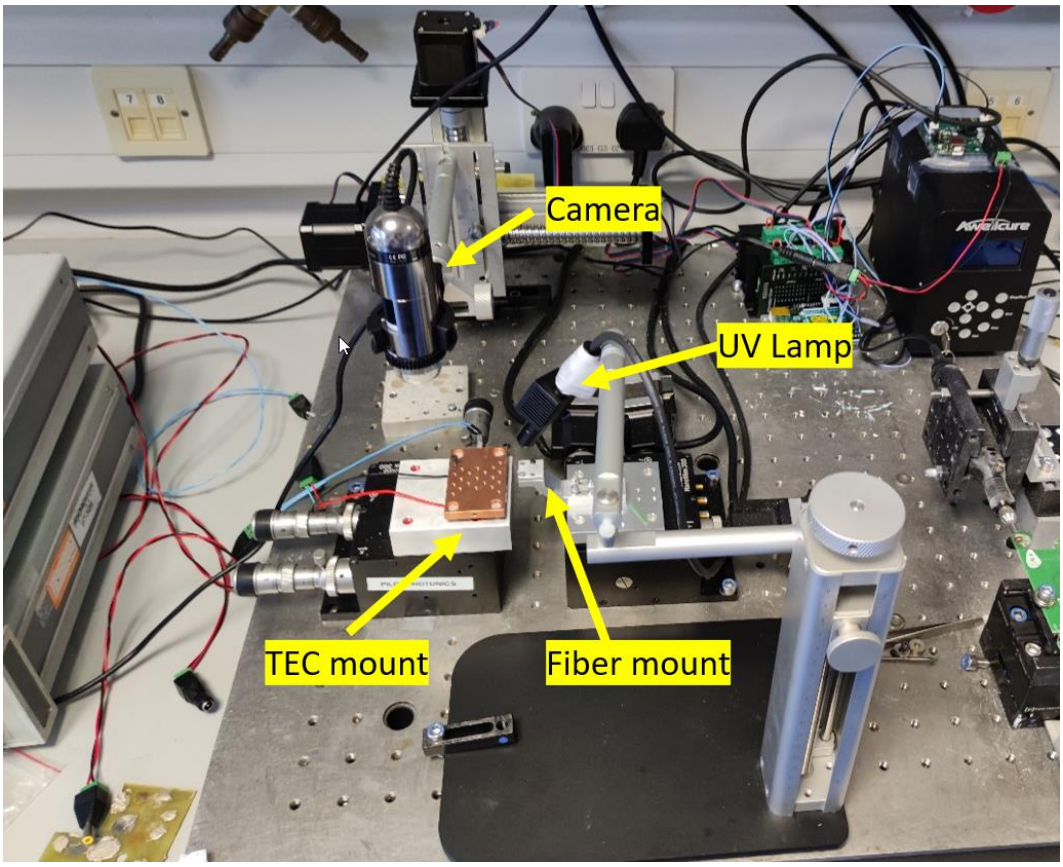

Figure E.2.1. Fiber coupling setup.

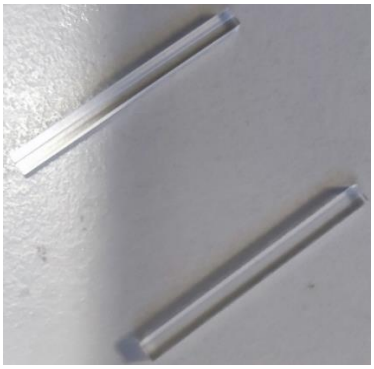

Figure E.2.2. Fiber supporters.

Initially, the fiber alignment and coupling, a fiber supporter (depicted in Figure E.2.2), was first fabricated on Perspex material. The fiber supporter protects the fiber from any stretch and strain forces. In addition, fiber supporter allows multiple attempts for fiber alignment without damaging the fiber. The Perspex material is preferred because the material is transparent, lightweight, and has an excellent thermal isolator. UV light passes through the material due to the transparency of Perspex. In addition, the thermal isolation property reduces the effect of thermal expansion/contraction that restricts fiber movement due to temperature changes.

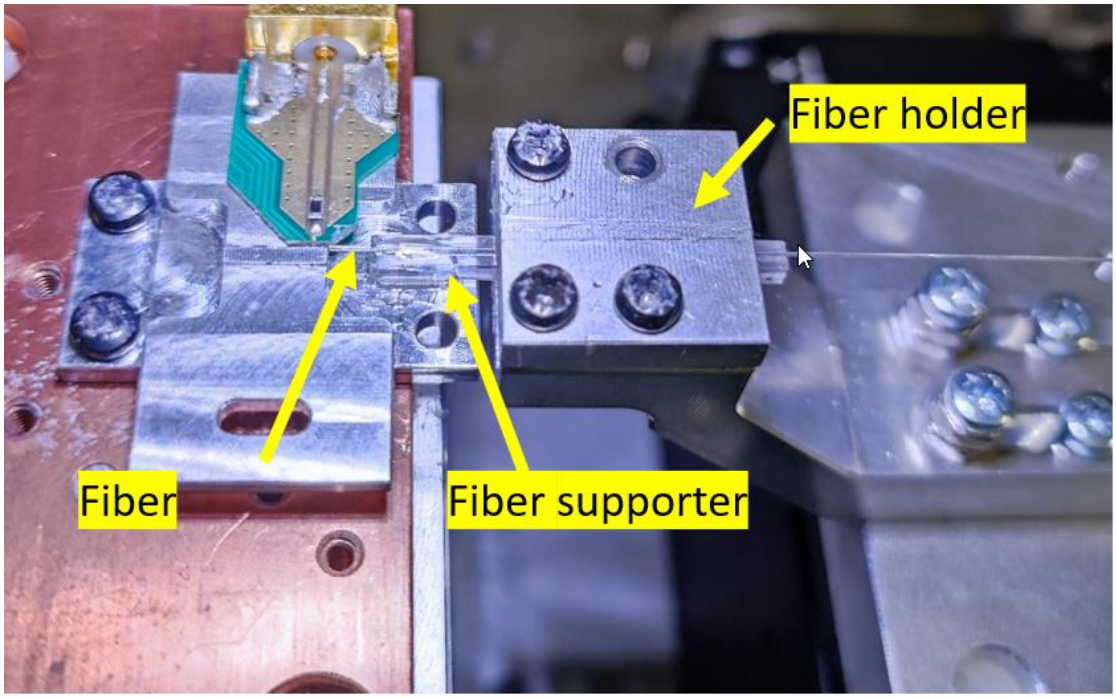

Figure E.2.3. Fiber mounting and alignment.

Initially, a high numerical aperture (HNA) fiber pigtail is mounted on the V-groove of the fiber supporter. The fiber facet is placed 2 mm ahead of the front corner of the fiber supporter (as shown in Figure E.2.3). Then, the fiber is glued on the fiber supporter by a UV-cured epoxy resin. After that, the fiber supported mounted with fiber is clamped on the fiber holder. On the other side, the subcarrier with mounted and wire-bonded PIC is screwed on the copper plate of the TEC mount. Next, the current is supplied to the PIC, and the lasing is confirmed by using an infrared detector card. Subsequently, the fiber is aligned by adjusting the x, y, and z-axis positions. An optical power meter monitors the maximum power coupled through the high NA fiber. The fiber's x, y, and z position is kept stationary, and the low shrinkage glue is dispensed into the gap between the subcarrier baseplate and the fiber supporter. Finally, the glue is slowly cured by shining toggled (on-off) UV light. The duty cycle of the on-off UV lap is set to 30%. Then the fiber-coupled subcarrier is removed from the TEC mount (as shown in Figure E.2.4).

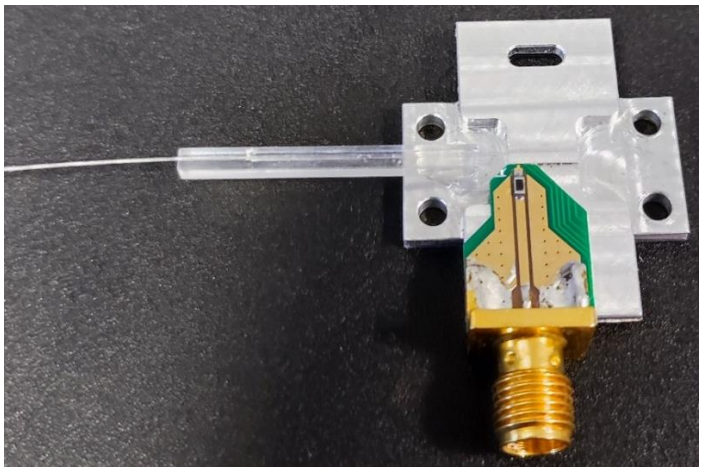

Figure E.2.4. Fiber coupled subcarrier.

Packaging case

A metal case is designed to protect the fiber-coupled subcarrier from damage in the next phase. An aluminum metal case is designed on Solid Works software. Figure E.3.1 (a) and (b) is the picture of a hollow metal case designed on Solidworks where the fiber-attached subcarrier can be placed. The subcarrier can be screwed on the four M2.5 threaded holes. A

cutout at the right wall of the metal case is given to keep the RF connector outside of the package. A multi-pin connector is screwed at the left wall of the case for the DC connection.

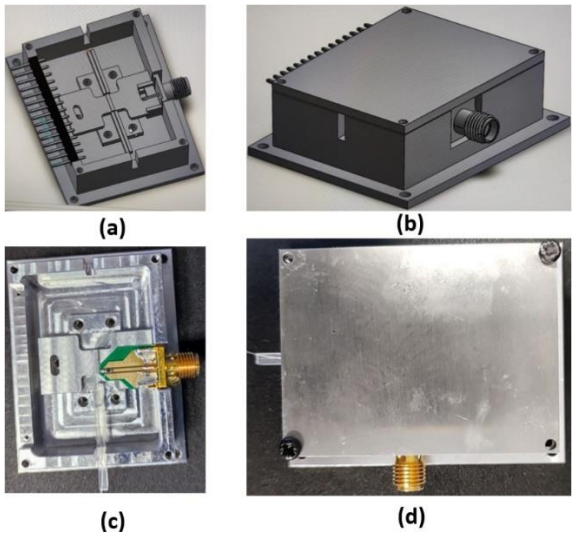

Figure E.3.1. (a) and (b) are designs made on Solidworks. (c) and (d) are fabricated metal works.

Figure E.3.1 (c) and (d) shows manufactured aluminum metal case. First, a thermal paste is applied under the subcarrier and screwed it on the metal case. The ribbon cable supplying DC current and RF connector is placed at the left and right side of the metal case. The fiber is pulled out from the front wall of the case. Finally, the metallic cover is screwed on the top to close the package shown in Figure E.3.2.

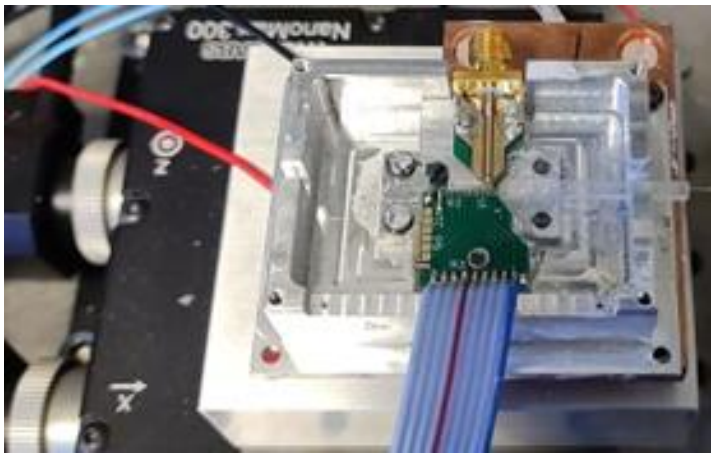

Figure E.3.2. Packaged subcarrier.